



**UNIVERSITÄT
DES
SAARLANDES**

Department of Neuroanatomy,
Institute of Anatomy and Cell Biology,
Faculty of Medicine, Saarland University,
Homburg (Saar), Germany

**Characterization of RIBEYE knock-in mice to
analyze the role of RIBEYE B-domain for the
assembly of the synaptic ribbon**

Ph.D. Thesis

A Thesis Submitted to the Faculty of Medicine in Fulfilment of the
Requirements for the Degree of
Doctor of Philosophy (Ph.D.)

Submitted by

Soni Shankwar

Germany 2022

Supervisor:

Co-supervisor:

Tag der Promotion: 23. August 2022

Dekan: Univ.-Prof. Dr. med. Michael D. Menger

Berichterstatter: Prof. Dr. Gerald Thiel
Prof. Dr. Frank Schmitz
PD Dr. Stephan Philipp

Declaration

I hereby declare that the Ph.D. thesis entitled “**Characterization of RIBEYE knock-in mice to analyze the role of RIBEYE B-domain for the assembly of the synaptic ribbon**” is a presentation of my original research work. All external sources of information have been acknowledged. No portion of this thesis work has been submitted in support of any other degree or qualification.

Homburg, Germany

21.02.22

Soni Shankhwar

*Dedicated to my parents, husband,
brother, sister, and in-laws*

Acknowledgements

It is a great pleasure to convey my gratitude to those who had contributed directly or indirectly to the completion of my thesis in my courteous acknowledgements.

Foremost, I would like to express deep and sincere gratitude to my Ph.D. supervisor Prof. Dr. med. Frank Schmitz for giving me an opportunity to do research work in his laboratory and providing invaluable guidance, support, motivation to me throughout my Ph.D. work. His dynamic vision, sincerity, passion for science have deeply inspired me. I wish to thank Dr. Karin Schwarz for her constant support and valuable suggestions during lab meetings. I would also like to extend my thanks to Prof. Jens Rettig, Prof. Dieter Brun's for their insightful comments, suggestions, and discussions during synapse club seminars. I also express my gratitude to Dr. Bianca Schrul for access to the Li-Cor Odyssey system, Dr. Elmer Krause, for the SR-SIM microscope, and Dr. Keerthana Ravichandran for introducing me to the SR-SIM microscope for my experiments. I would also like to thank Dr. Martin Jung for generating invaluable peptide arrays.

A special token of appreciation goes to my lab mates and colleagues for making my stay in the lab easier and unforgettable. My sincere thanks extend to Dr. Rashmi Katiyar, Dr. Mayur Dembla, Dr. Ekta Dembla, Dr. Shweta Suiwal, Dr. Ajay Kesharwani, Dr. Amrita Mukherjee, for their suggestions, scientific discussions, and help in the laboratory. Special thanks to Julia Jaffal, Amer Al Khalifa, Sofia Maragkou, Manish Yadav, Praveen Kumar, Swarnali Kundu for providing the happiest and friendly environment in the laboratory.

I also would like to thank all the technicians for their efficient and constant support: Sylvia Brundader for excellent administrative support, Gabi Kiefer for providing semithin and ultrathin sections and helping with the transmission electron microscope, Sabine Schmidt and Ines Krüger for their help at the animal house, Tamara Brück for her cordial nature and technical laboratory support.

I would like to express my thanks to my colleagues and collaborators, who shared authorship in my publication: Dr. Martin Jung, Dr. Stephan Maxeiner, Prof. Thomas C. Südhof.

I convey my special thanks to Dr. Stephan Maxeiner and Dr. Karin Schwarz for proofreading the "Zusammenfassung" of the thesis.

I want to gratefully acknowledge, Deutsche Forschungsgemeinschaft (Schm797/8-1), Dr. Rolf M.Schwiete foundation (2020-002) for financial supporting my entire Ph.D. work.

I would like to pay my special regards to Prof. MR Rajeshwari, AIIMS; Prof. Mulayam Singh Gaur, HCST; Prof. Bhupendra Singh, SGI; Prof. Pratibha Mehta Luthra, ACBR; Prof. Satendra Singh; ANDC to work under esteemed guidance and for their motivation.

I would like to thank my friends, Deepti, Gauri, Dr. Sushant, Dr. Hemlata, Dr. Himanshu, Dr. Jayvardhan for the wonderful cherishable moments, support, and encouragement. I am also thankful to my friends from Homburg Rashmi, Priya for their help, support, and good memories throughout my Ph.D.

I must express my profound gratitude to my mother Late Bitoli Shankhwar for her love and care in my childhood and my father Late Suraj Pal Shankhwar for his love, care, constant support, and encouragement in every step since childhood to make me in the present stage, especially after my mother's demise. I am extremely thankful for my parents-in-law, uncle, and aunty for their moral support, hope, inspiration. Most importantly, I would like to render my warmest thanks to the most important person in my life, my husband Mr. Subhash Kumar for his unconditional support, help, and sharing of difficult times during this period. I express my thanks to brothers Megh Singh and Man Singh and lovely sister Sapna, sister-in-law, and brother-in-law for being supportive and caring. Last, not least I also thank all my family members for giving me strength.

I am thankful to the almighty God for constant blessings and for giving me strength.

Table of Contents

ABSTRACT	1
ZUSAMMENFASSUNG.....	3
1. INTRODUCTION.....	6
1.1 The anatomy of the mammalian eye	6
1.2 Retinal anatomy and function.....	7
1.3 Photoreceptor cells	8
1.4 Bipolar cells.....	10
1.5 Horizontal cells and amacrine cells.....	11
1.6 Ganglion cells.....	12
1.7 Glial cells.....	12
1.8 Structure of the ribbon synapses.....	13
1.9 Proteins associated with synaptic ribbons	17
1.10 L-type calcium channels.....	19
1.11 Exocytosis and trafficking of vesicles	21
1.12 Endocytosis	21
1.13 RIBEYE- a major component of the synaptic ribbon.....	22
1.14 Function of RIBEYE	26
1.15 Generation of RIBEYE knock-in and RIBEYE knock-out mice	27
2. AIM OF THE STUDY	29
3. MATERIALS AND METHODS.....	30
3.1 Materials.....	30
3.1.1 Antibodies	30
3.1.1.1 Primary antibodies.....	30
3.1.1.2 Secondary antibodies.....	31
3.1.2 Reagents and chemicals.....	31
3.1.3 Buffers and solutions.....	34
3.1.4 Laboratory instruments and consumables	37
3.2 Methods.....	38
3.2.1 Animal care	38
3.2.2 RIBEYE knock-in mice.....	39
3.2.3 Genotyping of mice	39
3.2.3.1 Extraction of genomic DNA as PCR template for genotyping.....	39
3.2.3.2 Primer for genomic PCR	39
3.2.3.3 PCR program for genotyping	40

3.2.3.4 Genomic PCR and agarose gel electrophoresis for genotyping	40
3.2.4 Isolation of mouse retina	41
3.2.5 Light microscopic analyses	42
3.2.5.1 Embedding of retinal samples for immunocytochemistry on semi-thin sections (0.5 μm and 1.5 μm)	42
3.2.5.2 Immunolabeling of 0.5 μm and 1.5 μm thin retinal resin sections	42
3.2.5.3 Confocal Laser Scanning Microscopy	43
3.2.5.3.1 Principle and methodology	43
3.2.5.3.2 Confocal Microscopy Image Acquisition	43
3.2.5.3.3 Quantification of RIBEYE immunofluorescence signals in the OPL	43
3.2.5.3.4 RIBEYE puncta count in the OPL of 0.5 μm immunolabeled retinal sections	44
3.2.5.3.5 Quantification of RIBEYE immunofluorescence signals and RIBEYE puncta count in the IPL	45
3.2.5.4 Super-Resolution Structured Illuminated Microscopy (SR-SIM)	46
3.2.5.4.1 Principle and methodology	46
3.2.5.4.2 Measurement and quantification of ribbon contour length from 3D SR-SIM images	46
3.2.5.5 Preparation of cryostat sections from the mouse retina	47
3.2.5.5.1 Immunolabeling of cryostat sections of the mouse retina	47
3.2.5.6 Isolation of mouse cochlea	47
3.2.5.6.1 Isolation of mouse cochlea and whole-mount immunostaining of cochlear turn	47
3.2.5.6.2 Immunolabeling of whole mount organ of Corti	48
3.2.6 Transmission Electron Microscopy	48
3.2.6.1 EM embedding procedure	48
3.2.6.2 Ethanolic Phosphotungstic Acid (E-PTA) staining of retina samples for TEM	49
3.2.6.3 London Resin (LR)- Gold post embedding immunogold microscopy	49
3.2.6.4 Post embedding immunogold labeling	50
3.2.6.5 Preparation of ultrathin retina section for TEM	50
3.2.6.6 Transmission Electron Microscope	50
3.2.6.6.1 Principle and methodology	50
3.2.6.7 Transmission electron microscope Image Acquisition	51
3.2.6.8 Quantification of the number of synaptic ribbons in rod photoreceptor synapses and measurement of ribbon height using TEM	51
3.2.7 SDS PAGE and western blotting	52
3.2.7.1 Preparation of retinal lysate for SDS page	52
3.2.7.2 Measurement of protein concentration	52
3.2.7.3 SDS-PAGE	53
3.2.7.3.1 Background	53

3.2.7.3.2 SDS gel electrophoresis and electroblotting.....	53
3.2.7.3.3 Western blot analysis.....	54
3.2.7.3.4 Stripping and reprobing of immunoblot.....	55
3.2.7.3.5 Determination of concentration of 6F4 (RIBEYE A-domain) monoclonal antibody	55
3.2.8 Peptide arrays for epitope mapping of 6F4 (RIBEYE A-domain) monoclonal antibody	55
3.2.8.1 Stripping of pepspot membrane.....	56
3.2.9 Statistical analysis	56
4. RESULTS.....	57
4.1 RIBEYE deletion does not affect the overall organization of the retina	57
4.2 RIBEYE B-domain immunosignals are absent in the photoreceptor synapses of RBE ^{KI/KI} mice	59
4.3 RIBEYE B-domain puncta at high magnification in the OPL was unchanged between RBE ^{WT/WT} and RBE ^{WT/KI} and absent from RBE ^{KI/KI} mice	61
4.4 RIBEYE A-domain immunosignals are absent in the photoreceptor synapse of RBE ^{KI/KI} mice.	62
4.5 Corroboration of the absence of RIBEYE A-domain immunolabeling in RBE ^{KI/KI} retina using novel mouse monoclonal antibody against RIBEYE A-domain (6F4)	64
4.6 RIBEYE A-domain puncta at high magnification in the OPL was unchanged between RBE ^{WT/WT} and RBE ^{WT/KI} and absent from RBE ^{KI/KI} mice	66
4.7 Synaptic ribbon is absent from the ultrastructural rod photoreceptor synapse of RBE ^{KI/KI}	68
4.8 Length of synaptic ribbons immunostained with RIBEYE B-domain antibody is shorter in RBE ^{WT/KI} retina (3D SR-SIM analyses).....	70
4.9 Length of synaptic ribbons immunostained with RIBEYE A-domain antibody is shorter in RBE ^{WT/KI} retina (3D SR-SIM analyses).....	71
4.10 Synaptic ribbon height is shorter in the ultrastructure of rod photoreceptor synapses of RBE ^{WT/KI} mice (TEM analyses).....	73
4.11 Synaptic ribbon is lacking from the cone synapses and bipolar cell synapses of RBE ^{KI/KI} and RIBEYE immunofluorescence signals and RIBEYE puncta was reduced in the IPL of RBE ^{WT/KI} retina.....	74
4.12 Western blot analyses of RIBEYE expression	76
4.13 Synaptic ribbons are absent in the inner ear of RBE ^{KI/KI} mice	78
5. DISCUSSION.....	81
5.1 RIBEYE knock-in causes loss of synaptic ribbons	81
5.2 Synaptic ribbon was smaller in the OPL of heterozygous RIBEYE knock-in mice	82
5.3 RIBEYE immunofluorescence and puncta was less in the IPL of RBE ^{WT/KI} mice in comparison to RBE ^{WT/WT} and bipolar cells of RBE ^{KI/KI} mice lacking synaptic ribbons	83
5.4 RIBEYE expression was downregulated in RIBEYE knock-in retina.....	83
6. CONCLUSION.....	84
7. REFERENCES	85
8. LIST OF FIGURES.....	98

9. LIST OF ABBREVIATIONS.....	100
10. CV AND PUBLICATIONS	104

ABSTRACT

Ribbon synapses are specialized chemical synapses that transmit a wide range of sensory information in the visual and auditory systems. Ribbon synapses are tonically active and continuously release neurotransmitters at the synapse in response to graded changes of membrane potential. Continuous synaptic transmission at ribbon synapses requires a presynaptic electron-dense specialization, the synaptic ribbon. The synaptic ribbons immobilize a large number of release-ready vesicles near the release site (active zone) to promote continuous exocytosis. It is a large proteinaceous structure anchored to the active zone of ribbon synapses.

The synaptic ribbon mainly consists of the RIBEYE protein (Schmitz et al., 2000). RIBEYE contains a unique amino-terminal RIBEYE A-domain and a carboxy-terminal B-domain. The B-domain of RIBEYE shows sequence identity to the transcriptional co-repressor CtBP2 and binds with NAD(H). NAD(H) regulates the interaction between RIBEYE A- and RIBEYE B-domain (Schmitz et al., 2000; Magupalli et al., 2008). NAD(H) also promotes the assembly of CtBP2 dimers into tetramers (Bellesi et al., 2018). Transfection experiments suggested that the RIBEYE A-domain plays a structural role due to the formation of electron-dense protein aggregates (Magupalli et al., 2008). Consequently, the deletion of the RIBEYE A-domain in RIBEYE knock-out mice has revealed a complete loss of retinal and inner ear synaptic ribbons (Maxeiner et al., 2016; Jean et al., 2018). To date, it is unclear whether the RIBEYE A-domain alone is sufficient for synaptic ribbon formation or whether the RIBEYE B-domain is also required for the assembly of synaptic ribbons.

To address the role of the RIBEYE B-domain in ribbon formation, I analyzed RIBEYE knock-in mice (RBE^{KI/KI}). In these RIBEYE knock-in mice, the RIBEYE B-domain was replaced with the calcium sensor GCaMP3. RBE^{KI/KI} mice contain only the RIBEYE A-domain fused to GCaMP3 and consequently lack the RIBEYE B-domain.

Morphological analysis of RBE^{KI/KI} by immunofluorescence microscopy and transmission electron microscopy (TEM) showed the complete absence of synaptic ribbons in retinal synapses, both in rod and cone photoreceptor synapses in the OPL as well as in ribbon synapses formed by bipolar cell synapses in the IPL. Similarly, synaptic ribbons were completely absent in outer and inner hair cells of the organ of Corti from homozygous RBE^{KI/KI} mice.

In heterozygous RIBEYE knock-in mice (RBE^{WT/KI}), the overall fluorescence intensity of RIBEYE A- and RIBEYE B-domain immunosignals in the outer plexiform layer (OPL) was significantly reduced in comparison to littermate wild-type mice. In contrast, the average number of RIBEYE (RIBEYE A- and

ABSTRACT

RIBEYE B-domain) puncta was unaffected in the OPL. I investigated the reason for the decreased RIBEYE fluorescence intensity in heterozygous RIBEYE knock-in mice by using super-resolution structured illuminated microscopy (SR-SIM) to measure the contour length of synaptic ribbons. Using transmission electron microscopy (TEM) I further assessed the height of synaptic ribbons. Both analyses showed a significant reduction in the size of synaptic ribbons in RBE^{WT/KI} compared to littermate wild-type control mice. Interestingly, I also observed a decreased expression of RIBEYE in heterozygous RBE^{WT/KI} mice by quantitative western blot analyses raising the possibility that the level of RIBEYE expression is important to control the size of the synaptic ribbon.

In the IPL, I observed a similar though slightly differing result. In the inner plexiform layer (IPL) of RBE^{WT/KI} mice, both average RIBEYE fluorescence intensity (RIBEYE A- and RIBEYE B-domain), as well as average RIBEYE puncta, were significantly reduced compared to littermate wild-type control mice. The reduction in IPL RIBEYE puncta was further analyzed by ultrastructural analysis of rod bipolar cell synapses using TEM which showed the absence of synaptic ribbons in RBE^{KI/KI} mice. Thus, the reduction in RIBEYE fluorescence intensity and RIBEYE puncta in the IPL of RBE^{WT/KI} mice could be due to a loss of synaptic ribbons in bipolar cell synapses. Synaptic ribbons in bipolar cell synapses are smaller in size compared to photoreceptor synapses. Therefore, further reduction in ribbon size can more easily lead to the disappearance of synaptic ribbons in bipolar cell synapses than in photoreceptor synapses.

Collectively, the present data showed that the RIBEYE A-domain alone cannot form synaptic ribbons in the retina and inner ear of RIBEYE knock-in mice (RBE^{KI/KI}). Therefore, these findings strongly suggest that the RIBEYE B-domain is essential for the synaptic ribbon formation. Since RIBEYE B-domain also binds to NAD(H), it can be speculated that RIBEYE B-domain forms a tetramer under the control of NAD(H).

ZUSAMMENFASSUNG

Ribbonsynapsen/Bandsynapsen (engl.: ribbon synapse; im deutschen häufig auch als „Bandsynapse“ bezeichnet) sind spezialisierte chemische Synapsen, die ein breites Spektrum sensorischer Informationen im visuellen und akustischen System übermitteln. Ribbonsynapsen sind tonisch aktive Synapsen und setzen an der präsynaptischen Endigung kontinuierlich Neurotransmitter als Antwort auf abgestufte Änderungen des Membranpotentials frei. Die kontinuierliche Neurotransmitterausschüttung mittels Exozytose benötigt auffällige präsynaptische Strukturspezialisierungen, die als Synaptic Ribbons bezeichnet werden. Synaptic Ribbons binden eine große Anzahl von Freisetzungsbereiten synaptischen Vesikeln und stellen sie der aktiven Zone für eine kontinuierliche Vesikelexozytose zur Verfügung. Der Synaptic Ribbon ist eine große, Protein-dichte Struktur, die an der aktiven Zone der Ribbonsynapse/Bandsynapse verankert ist.

Der Synaptic Ribbon besteht im Wesentlichen aus dem Protein RIBEYE, das spezifisch für die Ribbonsynapsen/Bandsynapsen ist (Schmitz et al., 2000). RIBEYE besteht sich aus einer charakteristischen aminoterminalen A-Domäne und einer carboxyterminalen B-Domäne. Die B-Domäne von RIBEYE ist von der Primärstruktur weitgehend identisch mit dem ubiquitär exprimierten transkriptionelle Co-Repressor CtBP2. CtBP2 und die B-Domäne von RIBEYE binden NAD(H). NAD(H) reguliert die Interaktion zwischen RIBEYE A-Domäne und RIBEYE B-Domäne (Magupalli et al., 2008 et al., Schmitz et al., 2000). Außerdem stimuliert NAD(H) die Assemblierung von CtBP2-Dimeren zu Tetrameren (Belleis et al., 2018). Heterologe Transfektionsexperimente legten nahe, dass die RIBEYE A-Domäne eine wichtige Rolle bei der Ausbildung von elektronendichten Proteinaggregaten besitzt. Diese Befunde deuten auf eine mögliche strukturelle Bedeutung der A-Domäne von RIBEYE hin (Magupalli et al., 2008). Folgerichtig führt das Fehlen der RIBEYE A-Domäne in RIBEYE Knock-out Mäusen zu einem kompletten Verlust der Synaptic Ribbons in der Retina und im Innenohr (Maxeiner et al., 2016; Jean et al., 2018). Bis heute ist allerdings unklar, ob die RIBEYE A-Domäne alleine ausreichend ist, um Synaptic Ribbons entstehen zu lassen, oder ob auch die RIBEYE B-Domäne einen Beitrag für die Assemblierung der Synaptic Ribbons leistet.

Um die Rolle der RIBEYE B-Domäne für die Bildung der Synaptic Ribbons zu untersuchen, habe ich RIBEYE Knock-In Mäuse (RBE^{KI/KI}) verwendet. In diesen Knock-in Mäusen wurde die RIBEYE B-Domäne durch den Calcium-sensor GCaMP3 ausgetauscht. RBE^{KI/KI} Mäuse exprimieren anstelle von RIBEYE ein Fusionsprotein, bestehend aus der aminoterminalen RIBEYE A-Domäne, welche mit GCaMP3 fusioniert ist und folglich keine RIBEYE B-Domäne besitzt.

ZUSAMMENFASSUNG

Morphologische Untersuchungen der RBE^{KI/KI} Mäuse mittels Immunfluoreszenzmikroskopie und Transmissionselektronenmikroskopie (TEM) zeigten ein vollständiges Fehlen von Synaptic Ribbons in den Ribbonsynapsen/Bandsynapsen der Retina (sowohl in Stäbchen- und Zapfen-Photorezeptoren in der äußeren plexiformen Schicht, OPL als auch in den Ribbonsynapsen, die von den Bipolarzellen in der inneren plexiformen Schicht, IPL, der Netzhaut gebildet werden). Weiterhin fehlen die Synaptic Ribbons im homozygoten RIBEYE Knock-in (RBE^{KI/KI}) auch in den äußeren und inneren Haarzellen des Innenohrs.

In heterozygoten Knock-in Mäusen (RBE^{WT/KI}) war die Intensität der Immunfluoreszenzsignale von RIBEYE A- und B-Domäne in den Photorezeptorsynapsen der OPL signifikant reduziert. Die durchschnittliche Anzahl/Dichte von RIBEYE Signalen (Anzahl der Synaptic Ribbons in der äußeren plexiformen Schicht) war allerdings zwischen Wildtyp-Kontrolle und heterozygoten Knock-In Mäusen unverändert. Die Abnahme der Intensität der RIBEYE Immunfluoreszenzsignale in der OPL von heterozygoten Knock-In Mäusen wurde weiter mittels SR-SIM Mikroskopie (super-resolution structured illuminated microscopy) untersucht, indem die Konturlänge der Synaptic Ribbons mit dieser hochauflösenden Methode bestimmt wurde. Weiterhin wurde die Höhe der Synaptic Ribbons (Ausdehnung des „Bandes“ von der aktiven Zone bis in die Zelle hinein) mittels Transmissionselektronenmikroskopie ausgemessen. Beide Untersuchungen zeigten übereinstimmend eine signifikante Reduktion der Größe der Synaptic Ribbons in Photorezeptorsynapsen von heterozygoten RBE^{WT/KI} Mäusen gegenüber Wildtyp-Kontrollmäusen aus dem gleichen Wurf. Interessanterweise beobachtete ich mit Hilfe von quantitativen Western Blot-Untersuchungen, dass die Menge an exprimiertem RIBEYE Protein in heterozygoten Knock-in-Tieren deutlich geringer war als in Wildtypkontrollen. Dies deutet darauf hin, dass Expressionsspiegel von RIBEYE wichtig für die Steuerung der Größe der Synaptic Ribbons sein könnte.

Im Gegensatz zu den Ergebnissen, die in der äußeren plexiformen Schicht beobachtet wurden, zeigten sich in der inneren plexiformen Schicht sowohl die Fluoreszenzintensität als auch die Anzahl/Dichte der fluoreszierenden Signale in heterozygoten RBE^{WT/KI} Mäusen gegenüber Wildtyp-Kontrollmäusen signifikant abgemindert. Die Reduktion der Immunfluoreszenzsignale in der inneren plexiformen Schicht wurde weiter an Stäbchen-Bipolarzellen in homozygoten RBE^{KI/KI} Mäusen ultrastrukturell mittels TEM untersucht und festgestellt, dass dort Synaptic Ribbons komplett fehlten. Eine Reduktion der RIBEYE Fluoreszenzintensität und der Anzahl der RIBEYE Immunsignale könnte in heterozygoten RBE^{WT/KI} Mäusen durch die physiologischerweise kleineren Synaptic Ribbons in Bipolarzellsynapsen bedingt sein. Die Ribbons in Bipolarzellen sind deutlich kleiner als in den Photorezeptoren. Folglich

ZUSAMMENFASSUNG

könnte daher eine weitere Reduktion der Ribbongröße in Bipolarzellen leichter zu einem kompletten Verlust der Synaptic Ribbons führen als in den Photorezeptoren.

Zusammenfassend zeigen die hier präsentierten Daten, dass die Ausbildung von Synaptic Ribbons in der Netzhaut und im Innenohr nicht allein durch die RIBEYE A-Domäne bewerkstelligt werden kann. Die A-Domäne ist ja noch in RIBEYE Knock-in (RBE^{KI/KI}) Mäusen vorhanden, die keine Synaptic Ribbons ausbilden. Meine Ergebnisse zeigen, dass die RIBEYE B-Domäne ebenfalls für die Ausbildung der Synaptic Ribbons essenziell ist. Ohne die Anwesenheit der B-Domäne von RIBEYE kommt es zu keiner Ausbildung von Synaptic Ribbons. Die Bindung von NAD(H) an die RIBEYE B-Domäne führt wahrscheinlich zu oligomeren Komplexen (Tetrameren), die möglicherweise verschiedene RIBEYE Untereinheiten zusammenhalten und damit die Ausbildung der Synaptic Ribbons ermöglichen.

1. INTRODUCTION

In humans, primates, and simpler organisms such as zebra fish, the visual system is extremely developed, combining the sensory organ (the eye) and elements of the central nervous system (the photoreceptor cells, the optic nerve, the optic tract, and the visual cortex). The visual system imparts the ability to receive and process visual details. The eye, a sensory organ, receives visible radiation from its environment then transmits and focuses onto the neural retina, where photoreceptors transduce the light stimuli into electrical signals. Neuronal cells circuit processes the absorbed optical signals and transmitted to the midbrain and thalamus by optical nerves for making the perception of vision (Sung and Chuang, 2010).

1.1 The anatomy of the mammalian eye

The eyes of vertebrates are the main organ of the visual system. It is a fluid-filled, slightly asymmetrical sphere and three-layered tissue. The outermost layer consists of the sclera at the posterior end, and it turned into the light permissive cornea at the front of the eye. The middle layer is composed of two parts: the anterior (iris and ciliary body) and posterior (choroid). The innermost layer is the retina, the sensory part of the eye that processes light (Figure 1).

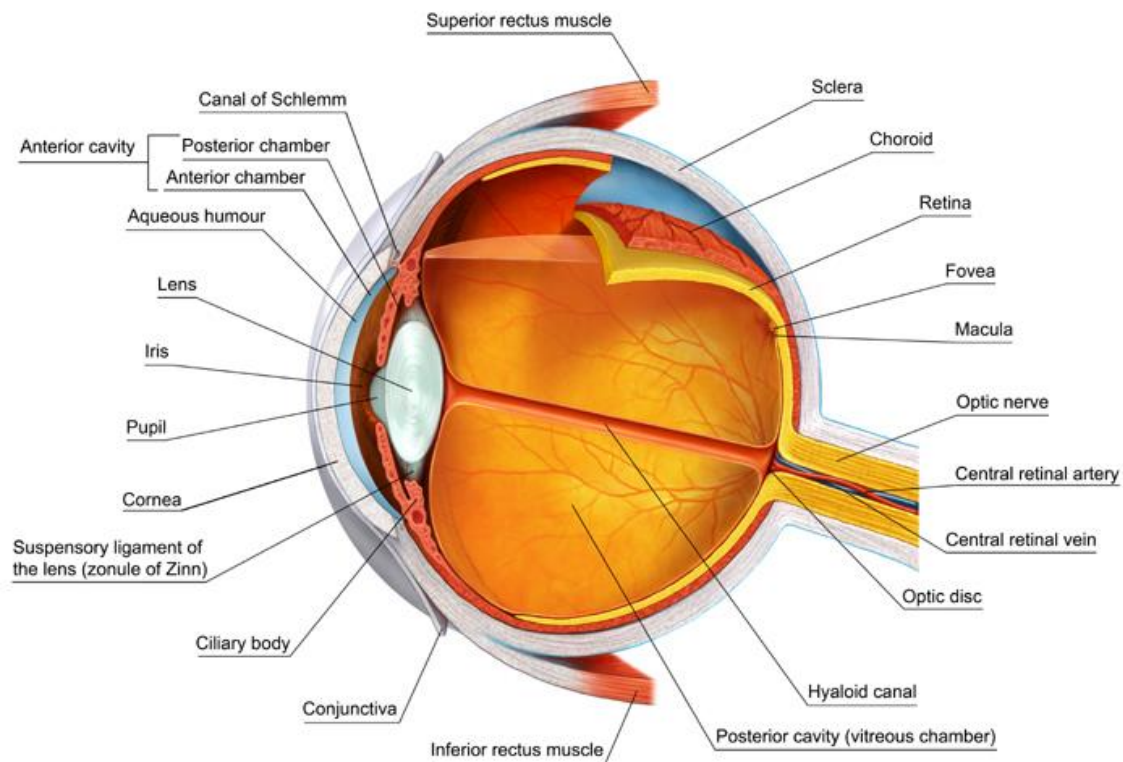


Figure 1. Drawing of a sagittal section through the adult human eye adapted from (virtual medical centre.com)

INTRODUCTION

The space of the eye is filled with two fluids: aqueous humor and vitreous humor. The aqueous humor is located between the cornea and lens. It is produced by the ciliary processes which are located on the posterior eye cup. The vitreous humor (a gelatinous substance) fills the cavity between the lens and the retina which make up about 80 % of the volume of the eye (Figure 1).

When light rays strike the eyes, they are first received by the cornea then pass through the pupil, and the crystalline lens, and finally reach the retina. The corneas refract, converge, and transmit the light onto the retina via crystalline lens. The photon received by the photoreceptor of the retina is translated into an electrical signal which stimulates all the succeeding neurons of the retina. These signals reach the higher brain center via optic nerve where the final image is generated (Zhu et al., 2012; Kolb, 2005; Purves et al., 2004).

1.2 Retinal anatomy and function

The mature mammalian retina is a thin, delicate, ~ 0.2 mm thick transparent sheet that is derived from the neuroectoderm. The neuronal cells of the retina are organized in layers. The photoreceptors are responsible for light reception and transmit signals via bipolar cells to ganglion cells then ganglion cells transmit visual information to the brain (Purves et al., 2004; Kolb, 2005). The retina comprises the retinal pigmented epithelium and five types of neuronal cells: Photoreceptors, bipolar cells, amacrine cells, horizontal cells, and ganglion cells (Figure 2) that are arranged in a manner such as nuclei and processes which are separated into an alternate and anatomically distinctive layer (Purves et al., 2004; Kolb, 2005).

The retinal pigment epithelium (RPE) is a melanin-containing structure that absorbs scattered light or light unabsorbed by the photoreceptors. The RPE is also important for photopigments regeneration.

The cell bodies of the photoreceptors (rods and cones) are located in the outer nuclear layer (ONL). The cell bodies of the bipolar cell, horizontal cell, and amacrine cells as well as the cell bodies of the Müller glial cells are located in the inner nuclear layer (INL). The cell bodies of the ganglion cells and the displaced amacrine cells are located in the ganglion cell layer. The first neuropil of the retina is the outer plexiform layer (OPL) which has a synaptic connection between photoreceptors (rods and cones) and vertically running bipolar cells and horizontal cells. The second neuropil of the retina is the inner plexiform layer (IPL) where axons of bipolar cells synapse onto the ganglion cells and dendrites of the amacrine cells also synapse in this zone (Figure 2). The IPL is responsible for processing visual information, such as motion detection, changes in brightness and contrast (Gupta et al., 2016; Kolb, 2005; Purves et al., 2004; Mashige and Oduntan, 2016).

INTRODUCTION

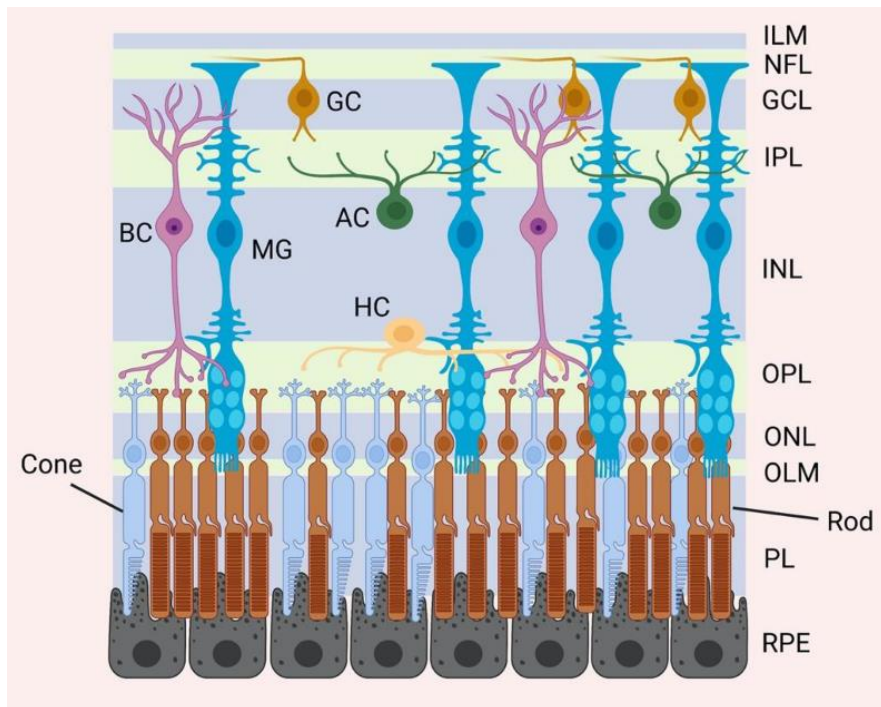


Figure 2. Schematic illustration of major retinal layers and cells of the adult human retina

Three neuronal cells chain: photoreceptors (rod and cones), bipolar cells, and ganglion cells make a direct route to transmitting visual information to the brain. Abbreviations: AC-amacrine cells, BC-bipolar cells, Cone- cone photoreceptor cells, GC-ganglion cells, GCL-ganglion cell layer, HC-horizontal cells, ILM-Inner limiting membrane, INL-inner nuclear layer, IPL-inner plexiform layer, MG-Müller glial cells, NFL-nerve fiber layer, ONL-outer nuclear layer, OPL-outer plexiform layer, OS-outer segments, OLM-outer limiting membrane, Rod-rod photoreceptor cells, RPE-retinal pigment epithelium. Adapted from (Salman et al., 2021).

1.3 Photoreceptor cells

The retina of the eyes includes two kinds of photoreceptors: rod and cones. Rod photoreceptors are very sensitive to light and operate in scotopic light (Figure 3A). Rod photoreceptors are very sensitive and can activate a photon. Humans have ~ 130 million photoreceptors, approximately 120 million are cylindrical rod photoreceptors which outnumber cones ~ 20-fold throughout the retina except for the fovea. On the other hand, cone photoreceptors are shorter, thicker, and become active only in bright light (larger number of a photon (photopic light)), including color vision (Zhu et al., 2012; Sung and Chuang, 2010; Moser et al., 2020) (Figure 3B).

Rods and cones consist of the outer segment, inner segment, cell body, and synaptic terminal. The outer segment is a modified cilium composed of a membranous disk that encloses light-sensitive photopigment (rhodopsin in rods and cone opsin in cones) and is constantly renewed. In the inner segment metabolism, biosynthesis and endocytosis take place (Sung and Chuang, 2010) (Figure 3A, B).

INTRODUCTION

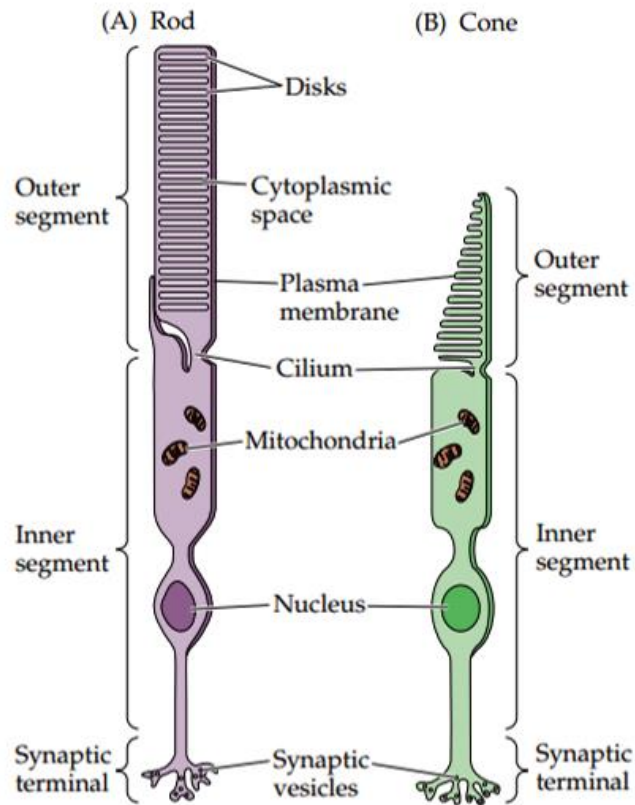


Figure 3. Structural differences between rod and cone photoreceptors

(A) Rod and (B) cone, these photoreceptor cells differ in their shape, size, and arrangement of the membranous disks in the outer segments. Adapted from (Purves et al., 2004).

Rhodopsin is a membranous protein composed of opsin and chromophore. It encompasses 95% of the total disc proteins. The phototransduction process occurs in the outer segment, this cascade is initiated by absorption of a photon by opsin (11- *cis*-retinal) which causes its isomerization (all-*trans*-retinal) (Figure 4A). The photoactivated rhodopsin activates the G protein (transducin) by catalyzing the exchange of GDP to GTP. Then α -subunit dissociates from transducin and activates cGMP (cyclic guanosine monophosphate), phosphodiesterase which quickly hydrolyzes the cGMP of the cytoplasm. This causes a decrease in cGMP concentration and closes cGMP gated channels. As a result, photoreceptor cells become hyperpolarized and release fewer neurotransmitters to the secondary neurons (bipolar cells) which leads to a decrease in the internal Ca^{2+} concentration (Figure 4A).

After light activation, reversal of activation step is required for the photoreceptors to return to their resting state. For this recovery, timely inactivation of activated rhodopsin and phosphodiesterase as well as resynthesis of cGMP are required. Low Ca^{2+} in the photoreceptor increases the activity of guanyl cyclase (cGMP synthesizing enzyme), leading to an increase in cGMP levels (Shichida and Matsuyama, 2009; Purves et al., 2004; Chen and Sampath, 2013). This triggers the opening of cGMP gated channels.

INTRODUCTION

The all-*trans*-retinal dissociated from opsin, which is converted to all-*trans*-retinol in OS, then diffuses into the pigment epithelium, where it is converted to 11- *cis* retinal by appropriate enzymes (Sung and Chuang, 2010; Shichida and Matsuyama, 2009; Purves et al., 2004; Chen and Sampath, 2013) (Figure 4B).

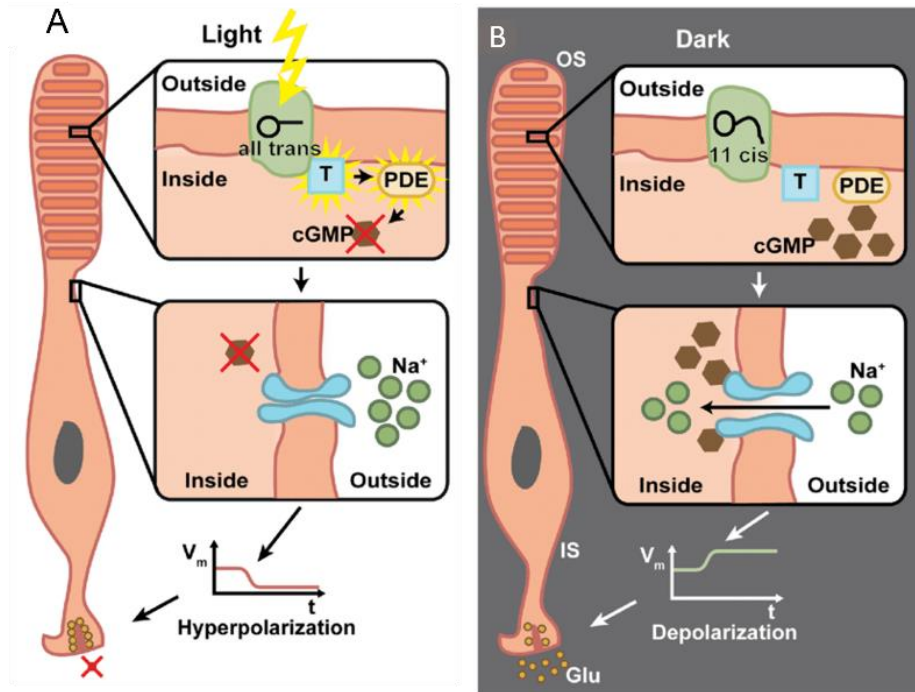


Figure 4. The phototransduction cascade in vertebrate photoreceptors

(A) This cascade initiates in the outer segment when a photon of light strikes the visual pigment, rhodopsin in rods, promotes conformational changes of 11-*cis*-retinals to all-*trans*-retinal (active state). The active rhodopsin activates transducin which in turn activates PDE (phosphodiesterase). PDE hydrolyzes the cGMP efficiently and lowers the concentration of cGMP, which leads to the closure of cyclic nucleotide-gated channels. This interrupts the flow of Na⁺, Ca²⁺ into the photoreceptor and hyperpolarizes the membrane potential which stops the glutamate exocytosis. (B) In dark, 11-*cis* retinal binds to rhodopsin which is present on the disc membrane of outer segments. As a consequence, inactivation of G-protein transducin and PDE occurs. Resynthesized cGMP triggers the opening of CNG channels which mediates Na⁺, and Ca²⁺ influx. This, in turn, depolarizes the membrane potential of inner segments and triggers glutamate release from photoreceptor synapses. Abbreviations: PDE- phosphodiesterase, cGMP- cyclic guanosine monophosphate, T- transducin, OS-outer segment, IS-inner segment, Na⁺-Sodium, Ca²⁺- calcium, Glu-glutamate. Adapted from (Klapper et al., 2016)

1.4 Bipolar cells

The bipolar cells are the second-order neurons and link the outer retina (OPL) to the inner retina (IPL). The 15 different types of bipolar cells make a parallel information pathway and transmit photoreceptor signals to the IPL. The IPL is thicker than OPL and subdivided into five equal-thickness strata. The first two strata (1, 2) are known as sublamina-a so-called OFF lamina while strata 3-5 are known as sublamina-b so-called ON lamina (Kolb, 1997; Euler et al., 2014). The cell bodies of bipolar cells reside

INTRODUCTION

in the inner nuclear layer (INL). Whereas terminal of bipolar cells and process of amacrine, ganglion cells are residing in the different strata of IPL (Figure 2 & 5). At the synapse, bipolar cell terminals connect to processes of amacrine cells and dendrites of ganglion cells termed as a dyad (Dowling and Werblm, 1971; Kolb, 1997; Euler et al., 2014).

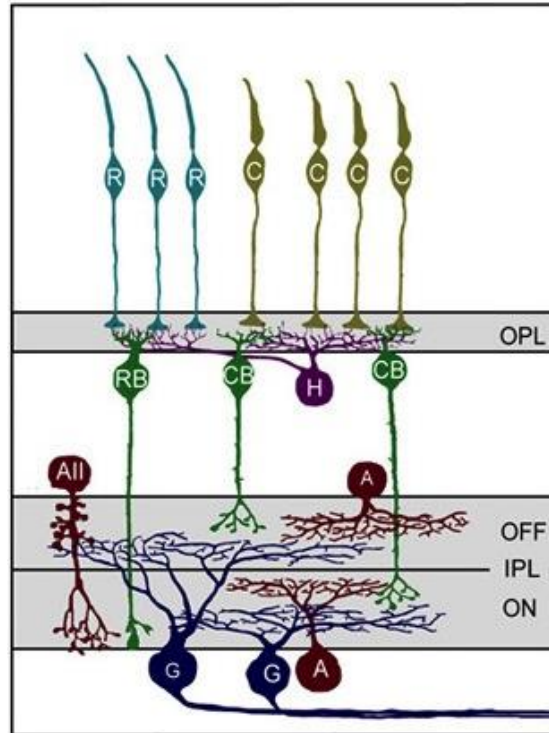


Figure 5. Schematic representation of primary cells and their connection patterns in the mouse retina
In OPL rods (blue) and cones (yellowish) make synapse with horizontal cells (H, purple) and bipolar cells (green). Amacrine cells also make synapse with bipolar cells as well as ganglion cells in the IPL. Bipolar cells terminals make synapse with dendrites of ganglion cells in different stratified layers of the IPL. A solid black line through the IPL indicates sublaminae, the upper layer (sublamina a) contains terminal of OFF bipolar cells and dendrites of OFF ganglion cell, and lower layer (sublamina b) contains terminal of ON bipolar cells and dendrites of ON ganglion cell. Abbreviation: R-rod, C-cone, OPL-outer plexiform layer, RB-rod bipolar cells, CB-cone bipolar cells, H-horizontal cell, A-amacrine cells, G-ganglion cells. adapter from (<http://webvision.med.utah.edu/>).

1.5 Horizontal cells and amacrine cells

Horizontal and amacrine cells are the interconnecting neurons. At the first synapse in the outer plexiform layer (OPL), processes of horizontal cells and dendrites of ON-bipolar cells invaginate into photoreceptor terminal and make triad where visual information transfers and processing initiates. The horizontal cells make a lateral connection between the photoreceptor cells and the bipolar cells and connect to the neighboring cells by gap junctions known as a triad (Masland, 2012). A single horizontal cell connects to more than one photoreceptor. Therefore, bipolar cells receive the

INTRODUCTION

signal from several photoreceptor cells. These cells enhance the contrast between light and dark regions and also lateral inhibitory feedback to the photoreceptors (Wässle and Boycott, 1991; Zhu et al., 2012). Amacrine cells are laterally computing in the IPL. The IPL contains different types of amacrine cells which conduct lots of different functions. Amacrine cells mediate ganglion cells activity likewise motion and direction selectivity (Tsukamoto and Omi, 2017; Kolb, 1997) (Figure 2 & 5).

1.6 Ganglion cells

The ganglion cells are the last neuron of the network which are located in the ganglion cell layer of the retina. This layer also contains displaced amacrine cells, Müller cell bodies, and astroglial cells (Mashige et al., 2016) (Figure 2 & 5). Ganglion cells collect visual information from bipolar cells and amacrine cells in the form of chemical messages. These chemical responses are transformed into an electrical signal by the transmembrane receptor. After integration, this information is digitized in the ganglion cells axons. The ganglion axons converge and form an optic nerve then this optic nerve transmits visual information in the form of an electrical message to the visual centers of the brain (Zhu et al., 2012; Nelson, 2021).

1.7 Glial cells

Glial cells are the supportive cells of the retinal neurons. There are some basic glial cells in the human retina. The most important types are Müller glia cells. However, microglia cells and astrocytes are also present.

Müller's cells are the main support cells. They make an architectural support structure and limit the retina at the outer (OLM) and the inner limiting membrane (ILM) (Figure 2). The outer limiting membrane is formed from the adherent junctions between Müller cells and photoreceptor inner segments and forms a barrier between subretinal space. The inner limiting is formed by laterally contacting conical end feet of Müller cells and the basement membrane. The ILM serves as a diffusion barrier between the retina and the vitreous humor. The cell bodies of the Müller cells reside in the INL (Kolb, 2001; Zhu et al., 2012).

Astrocytes are usually present in the vascular retina and enter from the brain through developing optic nerve in developing retina. Astrocytes are functionally active in the GCL and the nerve fiber layer (NFL). Astrocyte cells together with Müller cells and blood vessels form ILM (Kolb, 2005 & 2001; Zhu et al., 2012).

Microglial cells are mesodermal in origin. These cells infiltrate the retina via retinal vasculature during late embryogenesis. These cells are found in all retinal layers. These cells are engaged in phagocytosis

INTRODUCTION

and tissue repair. After the injury, these cells can be stimulated to behave as macrophage cells (Kolb, 2005 & 2001; Zhu et al., 2012).

The nerve fiber layer (NFL) is unmyelinated and composed of axons of ganglion cells before converging at the optic disk. These nerve fibers are myelinated after exiting from the eyeball. NFL is thickest near the optic disk (Airaksinen et al., 2008) (Figure 2).

1.8 Structure of the ribbon synapses

The ribbon synapse of a vertebrate is a specialized chemical synapse formed by the photoreceptors and the bipolar cells. Ribbon synapses are found in the retina as well as in the sensory neurons such as hair cells in the cochlea, vestibular organ, and pineal gland. The synaptic ribbons at the ribbon synapse are responsible for the sustained and graded release of the vesicles at the active zone (Moser et al., 2020; Lagnado and Schmitz, 2015) (Figure 6A, B).

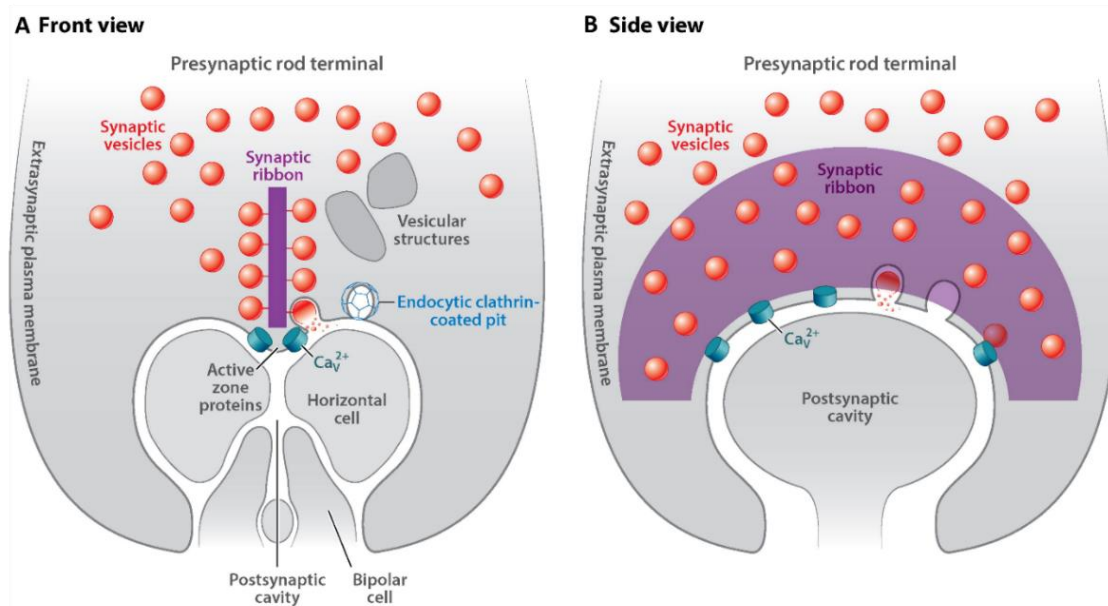


Figure 6. Schematic diagram of rod photoreceptor synapse

(A) Front view of bar-shaped synaptic ribbon in cross-sections, (B) side view of synaptic ribbon reveals horseshoe-shaped plate-like structure with L-type Cav voltage-gated channel at the active zone. Adapted from (Lagnado and Schmitz, 2015)

The synaptic ribbon is a specialized proteinaceous structure at the presynaptic active zone of the photoreceptor cells and the bipolar cells (second-order neurons) which are linked with a large number of vesicles. Synaptic ribbons are the electron-dense plate-like structure with a large surface area that extends into the presynaptic cytoplasm from the site of neurotransmitter release (Figure 6A). The shape

INTRODUCTION

of the synaptic ribbons and the number of tethered vesicles are different in the photoreceptors and the bipolar cells (tom Dieck and Brandstätter, 2006) (Figure 6A).

Microscopically, the cross-section of the synaptic ribbon at the photoreceptor synapse appeared bar-shaped (Figure 6A). From the 3D construction it looks like a planar structure (approximately 30 nm) with a large surface area of approximately $0.77 \mu\text{m}^2$. The rod photoreceptor terminal is small ($\sim 2 \mu\text{m}$ in length) and usually contains a large single ribbon that is perpendicular to the plasma membrane and $\sim 200 \text{ nm} - 1000 \text{ nm}$ in length. Synaptic ribbon anchors at the plasma membrane by an electron-dense arciform density. From the side view, the synaptic ribbon appears like a horseshoe shape ($1-2 \mu\text{m}$) because of banded arciform density (Figure 6B). The arciform density is approximately 50 nm in diameter with a tough or ball-shaped structure (Moser et al., 2020; Sterling and Matthews, 2005) (Figure 6 A & 7A).

The presynaptic membrane invaginating inside the presynaptic terminal forms a cavity called the postsynaptic cavity which contains dendrites of horizontal cells (HC) and bipolar cells (BC) (Figure 7A). The dendritic tip of the invaginating rod bipolar cells contains metabotropic (mGluR6) glutamate receptor in rod bipolar cells and ionotropic AMPA glutamate receptors and kainate glutamate receptor in horizontal cells (Lagnado and Schmitz, 2015) (Figure 9).

Synaptic vesicles ($\sim 40 \text{ nm}$ diameter) are physically attached to the entire surface of the synaptic ribbon by several fine filaments ($\sim 5 \text{ nm}$ thick, 40 nm long) (Sterling and Matthews, 2005). These attached vesicles are called tethered vesicles. The vesicles row at the base of the synaptic ribbon which is directly contacted with the plasma membrane is called docked vesicles (Figure 7A, B). The docked vesicles release first during exocytosis. The pool of these vesicles is making up a readily releasable pool (RRP). The number of tethered vesicles to docked vesicles is roughly 5:1 for the rod-shaped ribbon and 10:1 for the spherical ribbon. The many vesicles which are attached to the ribbon at a more distant position in the cytoplasm are called reserve pool vesicles that replenish the readily reserve pool upon its depletion (Lagnado and Schmitz, 2015) (Figure 7A, B).

The number of vesicles attached to the ribbon in the presynaptic terminal depends on the number of ribbons, size, and shape. The vesicles are loaded with the neurotransmitter glutamate. Mammalian rod photoreceptor terminals (rod spherules) possess a single ribbon per terminal which has approximately 770 tethered vesicles and 130 docked vesicles (Lagnado and Schmitz, 2015; Wan and Heidelberger, 2011) (Figure 7A, B).

INTRODUCTION

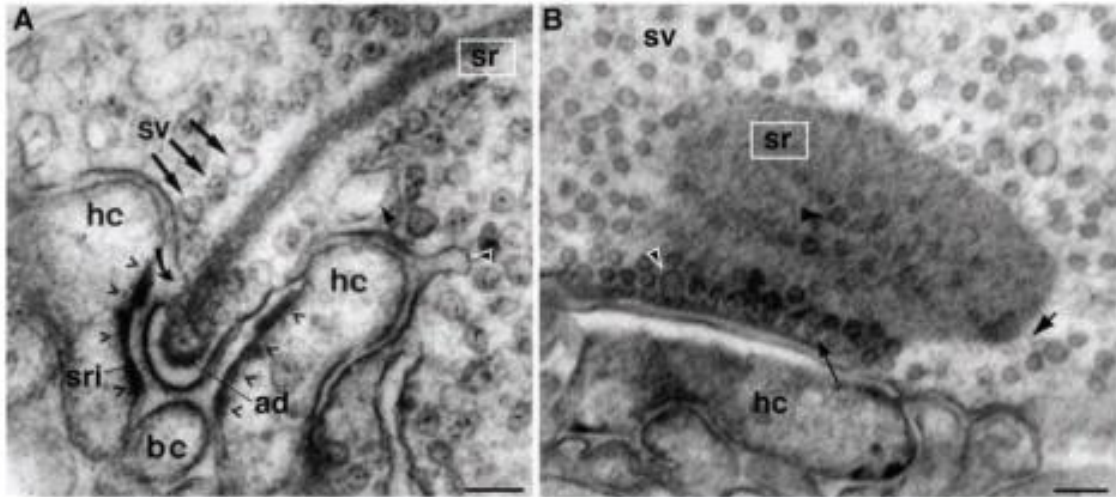


Figure 7. Ultrastructure of rod photoreceptor ribbon synapse

(A) Rod photoreceptor synapse electron micrograph of goldfish retina. The bar-shaped synaptic ribbon (sr) which is anchored at arciform density (ad) extends into the cytoplasm. Arciform density is located within small synaptic ridge-like (sri) evagination of the presynaptic plasma membrane. The active zone which is a hot spot for exocytosis (curved arrow) is found at the plasma membrane, anchored at the base of the ribbon (curved arrow). A large number of vesicles (SV, arrow) are tethered to the synaptic ribbon and filled the synaptic terminal. Opposite to the active zone, dendritic tips of bipolar cells (bc) pair sandwiched between pair of horizontal cells (hc) and dendritic tips of bipolar cells are located in the postsynaptic cavity. Open black arrowheads showed postsynaptic density. (B) Plate-like synaptic ribbon (sr) is tangentially cut. Tethered vesicles are associated with it in a more distal position (black arrowhead). Docked vesicles physically connected to the presynaptic plasma membrane (long black arrow). White arrowhead shows fusion vesicles docked at the base of synaptic ribbons. Adapted from (Schmitz, 2009).

Cone terminals (cone pedicels) are usually bigger in size (3-5 μm diameter) than rod spherules and possess more synaptic ribbons (Figure 8b). The cone ribbons are shorter in length than rod ribbons, but their total surface is larger in contrast to rods which allowed to tether more vesicles. Due to a large number of vesicles cones encode light intensity with finer resolution than rods. Cone synapse also makes triad synapse as rod photoreceptor (HC-ON-bipolar cell- HC processes) as described above. In addition, cone photoreceptors make synapses with OFF-bipolar cells at the base of their terminal. This synapse occurs at the other side of the HC processes. This synapse comprises two or five kinds of OFF-bipolar cells, one or two ON-bipolar cells, and two HC (Moser et al., 2020; Lagnado and Schmitz, 2015) (Figure 8b).

The synaptic ribbon of the retinal bipolar cells is bar-shaped to ellipsoid and typically smaller than those in rods and cones (Figure 8c). The bipolar cell ribbons are ~ 50 nm thick, 125 nm high and 175 nm long. Bipolar cells terminal in the inner retina has different sizes. The goldfish rod bipolar cells terminal can be 10 μm diameter which contains 45-65 ribbons, ~ 110 tethers, and ~ 22 docked vesicles. Therefore,

INTRODUCTION

~ 6000 are the total ribbon-associated vesicles and ~ 1200 are the total docked vesicles (von Gersdorff, 2001).

The hair cell's synaptic ribbons vary in, number, shape, and size. In a hair cell, the number of synaptic ribbons is very few in outer hair cells (OHC) and dozens in inner hair cells (IHC). Synaptic ribbons range from ~ 0.1 to ~ 0.4 μm in length and can be ellipsoid, plate-like, spherical, or barrel-shaped. 20 to 400 vesicles tethered to it depending on the cell type. The ribbon synapses of hair cells are found to differ in postsynaptic structure from retinal synapses (LoGuidice and Matthews, 2007; Moser et al., 2020) (Figure 8a).

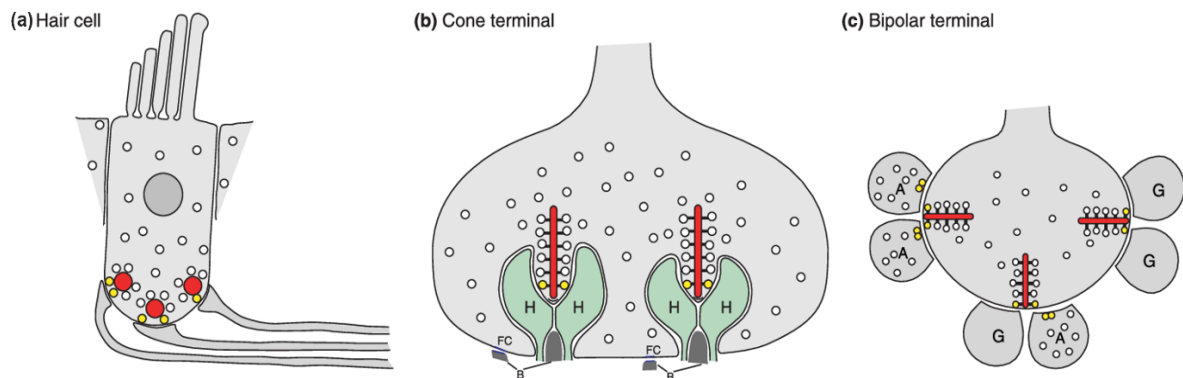


Figure 8. Diversity of the ribbon synapse in the retina and the inner ear

(a) In hair cells, ribbons (red) are located at the basal pole with numerous tethered vesicles (white and yellow, yellow are docked vesicles) near the presynaptic plasma membrane. A hair cell contains 10-20 ribbons. (b) The Cone terminal contains more ribbons that are shorter than rod ribbons and makes a triad with postsynaptic processes. (c) Rod bipolar cells make many presynaptic boutons, containing multiple small ribbons, and make a dyad, comprising of two ganglion cell dendrites (G), two amacrine cell processes, or one ganglion and amacrine cell processes. Abbreviation: H-horizontal cells, B-bipolar cells, A-amacrine cells, G-ganglion cells. Adapted from (Sterling and Matthews, 2005).

At the conventional synapse, approximately 100 vesicles are clustered at the active zone near the plasma membrane. Therefore, the number of vesicles in the ribbon terminals are more than the conventional synapses. The neurons of ribbon synapses are tonically active and transmit visual information as graded changes in membrane potential. In contrast, in brain neurotransmitter release is sparked by an action potential (Morgans, 2000; Lagnado and Schmitz, 2015; Heidelberger et al., 2005). The presynaptic density connects to the postsynaptic intersection of a pair of amacrine cell processes (AII and A17), dendrites of bipolar, and processes of amacrine or rarely pair of ganglion cells (Matthews and Fuchs, 2010; Lagnado and Schmitz, 2015; Moser et al., 2020). In bipolar cells, the arciform density is lacking at the synaptic ribbon in contrast to the photoreceptor which approaches the ribbon closer to the plasma

INTRODUCTION

membrane. Therefore, vesicles that are located at the base of the ribbon have contact with the plasma membrane as well as the synaptic ribbon (Heidelberger et al., 2005) (Figure 8c).

1.9 Proteins associated with synaptic ribbons

The active zone is located as an electron-dense region beneath of plasma membrane. This electron-dense structure is ultra-structurally composed of cytoskeleton meshwork (cytomatrix). The cytomatrix at the active zone (CAZ) is extended into the cytoplasm as synaptic bouton and synaptic vesicles tethered to it. Therefore, CAZ involves in the docking and priming of synaptic vesicles at the active zone (Deguchi-Tawarada et al., 2006). CAZ is composed of a set of multidomain proteins which interact with other proteins via protein-protein interaction or protein-lipid interaction (tom Dieck et al., 2005).

CAZ proteins are set apart into two presynaptic compartments at the ribbon synapse. The ribbon-associated compartment comprises RIBEYE/CtBP2, CtBP1/BARS, RIM1, KIF3A (motor protein), and Piccolo. The active zone compartment comprises RIM2, ubMunc 13-2, ERC2/CAST1 and L-type calcium channel (Lagnado and Schmitz, 2015; tom Dieck et al., 2005; tom Dieck and Brandstätter, 2006; Sterling and Matthews, 2005) (Figure 9).

RIBEYE (~ 120 kDa), a major component of the synaptic ribbon was first identified, characterized, and cloned by Schmitz et al., 2000. It is composed of proline-rich RIBEYE A-domain and C-terminal B-domain which is identical to CtBP2 (Figure 9). CtBP proteins have a role in transcriptional regulation. RIBEYE is homologous to CtBP1/BARS (C-terminal binding protein/ brefeldin A adenosine diphosphate ribosylated substrate) (Figure 9). These proteins are present at both photoreceptor synapses and conventional synapses. These proteins play a role in the function and molecular assembly at conventional synapses. CtBP2 Knock-out leads to embryonic lethality at embryonic day 10.5 because of uncompensated CtBP2 nuclear function whereas CtBP1 null mice were viable and fertile (tom Dieck et al., 2005; Hildebrand and Soriano, 2002; Vaithianathan et al., 2019).

Bassoon and piccolo/Aczonin are the large structural multidomain CAZ scaffolding protein (400 kDa and 550 kDa respectively). These proteins are ubiquitously expressed at conventional synapses and work as docking modules for CAZ proteins (Moser et al., 2020; tom Dieck and Brandstätter, 2006) (Figure 9).

Piccolino, a piccolo variant present at the ribbon synapse of the eye and the ear cannot interact with other CAZ proteins due to c-terminal truncation. Therefore, piccolino is independent from the CAZ protein network (Regus-Leidig et al., 2013; Moser et al., 2020). It is expressed at both the photoreceptor

INTRODUCTION

ribbons as well as bipolar ribbons. Piccolo knock-out mice led to severe visual problems but did not cause any hearing problems. In the retina of piccolo knock-out mice floating ribbons and changes in related proteins were observed (Li et al., 2021; Müller et al., 2019). Piccolo knock-out mice show the phenotype of retinitis pigmentosa (Li et al., 2021).

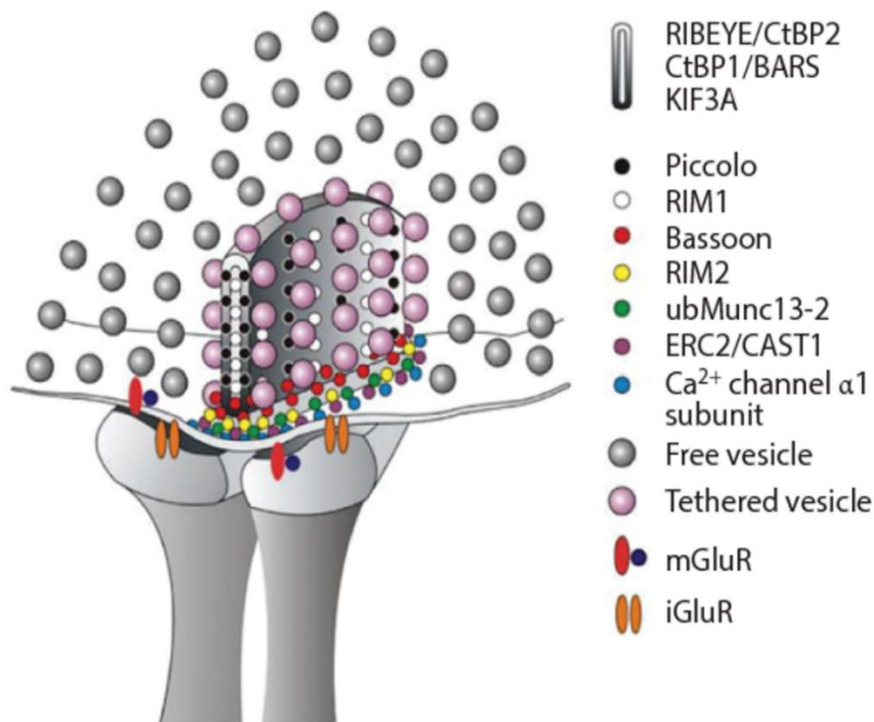


Figure 9. Retinal ribbon synapse associated proteins

CAZ (cytomatrix at the active zone) proteins are located on two presynaptic compartments at the ribbon synapse. Ribbon associated compartment comprises RIBEYE/CtBP2, CtBP1/BARS, KIF3A, Piccolo, and RIM 1. While the active zone compartment comprises RIM2, ubMunc 13-2, ERC2/CAST1, and L-type calcium channel. Bassoon localized at the border between two compartments at the photoreceptor synapse. Modified image from (tom Dieck and Brandstätter, 2006).

The bassoon is located ultra-structurally to the arciform density at the active zone, which suggests its crucial role in the anchoring of ribbons at the active zone (Figure 9). At ribbon synapse bassoon interacts physically with both the ribbons and RIM binding proteins (Davydova et al., 2014; Dick et al., 2001 & 2003). The bassoon is expressed at the ribbon of the photoreceptors but not at the bipolar cells ribbon. Whereas in IPL bassoon immunoreactivity was found only at conventional synapses made by amacrine cells onto bipolar cell terminals (Brandstätter et al., 1999). In contrast to conventional synapse absence of bassoon leads to a free-floating (non-anchored) ribbon in the cytoplasm of photoreceptor terminals, deformed calcium channel clusters, and impaired vesicles attachment to the plasma membrane. The absence of piccolo and bassoon does not affect the ultrastructure of the synaptic terminal (Moser et al., 2020; Ackermann et al., 2015).

INTRODUCTION

Rab3 is a neuronal ATP binding protein that negatively regulates synaptic vesicles fusion (Heidelberger et al., 2005). RIMs, a putative Rab3 effector protein, are the central element at the presynaptic active zone in conventional synapses because they bind to other synaptic proteins. RIM proteins play a major role in calcium channel immobilization, recruitments of synaptic vesicles, and vesicle priming (Morgans, 2000; Lagnado and Schmitz, 2015; Südhof, 2014). RIM1 is localized to the ribbon body whereas RIM2 is present at the active zone. Rim proteins interact with ubMunc13-2 in the photoreceptor terminal and exert vesicle priming. ELKS has homology to CAST. CAST (cytomatrix associated structural protein), a CAZ protein forms a ternary complex with RIM1 and ubMunc13-2 by direct interaction with RIM1. CAST1/ERC2 also interacts with RIM2 at the base of the ribbon. CAST protein also makes direct interaction with piccolo and bassoon (Deguchi-Tawarada et al., 2006). ERC2/CAST1 is also localized to the ribbon body where it interacts with RIM1. Therefore, the interaction of these proteins regulates the size of the active zone at the photoreceptor synapse (Lagnado and Schmitz, 2015; Mercer and Thoreson, 2011; Moser et al., 2020). ERC2/CAST1/ELKS2 proteins interact with several β subunits of voltage-gated calcium channels (Lagnado and Schmitz, 2015) (Figure 9).

KIF3A, a Kinesin motor protein enriched at the ribbon suggests the movement of vesicles along with the ribbon by active transport to the release site at the plasma membrane (Morgans, 2000; Lagnado and Schmitz, 2015; tom Dieck and Brandstätter, 2006).

Synapsin (synaptic vesicle-associated proteins), a synaptic vesicle membrane protein implicated in the vesicle recruitment to the active zone of the conventional synapse is absent from ribbon synapse. But ribbon synapse expresses synaptic vesicles proteins SV2 and synaptophysin (tom Dieck and Brandstätter, 2006; Mandell et al., 1990 & 1992).

Calcium binding protein 4 (CaBP4), a calmodulin-like calcium binding protein of photoreceptor which colocalizes with L-type Cav1.4 calcium channel and modulates its activity (tom Dieck and Brandstätter, 2006).

1.10 L-type calcium channels

Calcium channels are ubiquitously express in nervous and non-nervous animal cells. The calcium channel mediates calcium entry into the presynaptic nerve terminal which is essential for neurotransmitter release (Zamponi, 2003; Davies and Zamponi, 2008; Matthews and Fuchs, 2010). Voltage - activated calcium channel is a complex of heteromeric proteins which contains $\alpha 1$ pore-forming subunit, regulatory β subunit, and $\alpha 2\delta$ subunit. According to voltage range activation, high voltage activated channels comprises L (Cav1), P/Q (Cav2.1), N (Cav2.2), and R (Cav2.3) whereas low

INTRODUCTION

voltage activated channel comprises T (Cav3). The Cav1.4 and Cav1.3, L- type voltage gated channels are located at the ribbon synapse of photoreceptor cells and hair cells respectively (Pangrsic et al., 2018; Ramakrishnan et al., 2012) (Figure 6A, B). In the photoreceptor active zone L-type Ca^{2+} channels consist of $\alpha 1$ pore-forming subunit, regulatory $\beta 2$ subunit, and $\alpha 2\delta 4$ subunit (Morgans, 2000; Lagnado and Schmitz, 2015). These L-type channels are sensitive to dihydropyridine (DHP). These channels show very less or no calcium dependent inactivation but undergo voltage dependent inactivation very slowly. Therefore, voltage gated calcium channels open upon depolarization of the membrane and give rise to calcium influx to the cells (Ramakrishnan et al., 2012; Lagnado and Schmitz, 2015; Heidelberger et al., 2005).

The vesicle fusion machinery is similar to the conventional synapse in the retinal ribbon synapses. They utilize the following SNARES (soluble N-ethylmaleimide-sensitive fusion protein attachment protein receptor) protein receptors: v-SNAREs (vesicle-associated SNARE protein), t-SNAREs (presynaptic plasma membrane protein) (Ramakrishnan et al., 2012; Mercer and Thoreson, 2011).

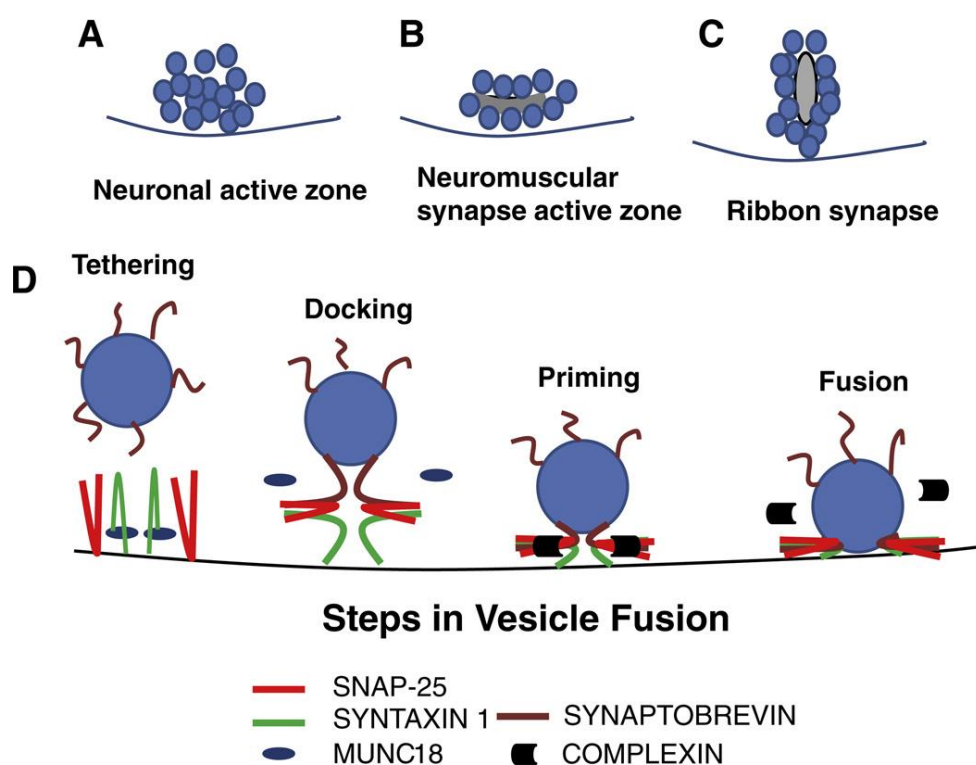


Figure 10. The vesicles fusion machinery in neuronal and sensory cells

The organization of vesicles in various types of synapses and steps in vesicle fusion. (A) Clustering of synaptic vesicles in the presynaptic terminal of the neuronal active zone. (B) Organization of vesicles in ridge shaped at the neuromuscular junction synapse. (C) Organization of synaptic vesicles around a ribbon like or spherical structure at the presynaptic terminal of sensory cells ribbon synapse. (D) Steps of vesicle fusion, tethering, docking, priming, fusion. Adapted from (Ramakrishnan et al. 2012).

INTRODUCTION

The t-SNAREs are syntaxin and SNAP-25. SNAP-25 may promote vesicle priming and compound fusion before synaptic release. The difference between photoreceptors and neurons is the presence of syntaxin 3 rather than syntaxin 1 and complexins 3 and 4 rather than complexins 1 and 2. The SNARE and its associated proteins play a critical role in vesicle docking, priming, fusion, and synchronization of neurotransmitter release (Ramakrishnan et al., 2012) (Figure 10).

1.11 Exocytosis and trafficking of vesicles

Synaptic transmission is initiated at the synaptic terminal because of neurotransmitter release triggered by graded potential. The generation of graded potential causes the opening of calcium channels result in Ca^{2+} channel exocytosis. The sensory neurons of the visual, auditory and vestibular systems transmit the signal to the neighboring cells by graded changes in neurotransmitter release. The rate of fusion of vesicles increases and decreases with depolarizing and hyperpolarizing changes in membrane potential (Lagnado and Schmitz, 2015) The ribbon, a specialized electron-dense structure increased the pool of readily releasable pool which replenished rapidly.

Electrophysiological analysis demonstrates two different kinetic components of vesicle exocytosis: fast and slow sustained components. The fast component of exocytosis releases docked vesicles at the base of the ribbon in contact with the plasma membrane within a few milliseconds after the opening of the calcium channel (Neves and Lagnado, 1999; Mennerick and Matthews, 1996). Upon strong depolarization this rapidly releasable pool (RRP) can be exhausted within a few milliseconds then vesicles move from the ribbon down to the docking site to limit the release rate (Zenisek et al., 2000; Lagnado and Schmitz, 2015). The tethered vesicles which are attached to the ribbon at the distal position are released with slower released kinetics within several hundreds of milliseconds at maximal stimulation. The nonribbon attached vesicles are called reserve vesicles that could replenish empty docking sites at the ribbon (Schmitz, 2009).

This high rate of exocytosis must be balanced by endocytosis. Therefore, after exocytosis, synaptic vesicles subsequently undergo exocytosis, recycle and refill with neurotransmitters for another round of exocytosis (Südhof, 2004; LoGiudice and Matthews, 2007).

1.12 Endocytosis

A large amount of exocytosis due to sustained release of neurotransmitters requires balanced endocytosis. Electrophysiological capacitance measurement in retinal bipolar cells revealed two modes of endocytosis with different kinetics. Fast endocytosis occurs within 1-2 seconds and slow endocytosis occurs in 10-20 seconds (von Gersdorff and Matthews, 1994; Schmitz, 2009; LoGiudice and Matthews, 2007). The slow endocytosis occurs in clathrin and dynamin dependent but Ca^{2+} independent manner

INTRODUCTION

after strong stimulation of presynaptic terminal (Jockusch et al., 2005). Whereas fast endocytosis is clathrin independent, regulated by presynaptic Ca^{2+} , and selectively inhibited by the high level of intracellular chloride (Llobet et al., 2011).

1.13 RIBEYE- a major component of the synaptic ribbon

The RIBEYE is only the known ribbon specific protein which is the major component of the synaptic ribbon (Schmitz et al., 2000). RIBEYE gene is located on chromosomes 7 and 10 in mice and humans respectively. RIBEYE is composed of a unique amino-terminal proline-rich A-domain (563 residues) specific for ribbon in all ribbon synapses and carboxy-terminal B-domain (425 residues) which is identical to the nuclear protein CtBP2 (except for first 20 amino acids) together with transcriptional repressor CtBP1 (Figure 11). RIBEYE A-domain is proposed to have a structural role whereas B-domain on the ribbon facing towards the cytoplasm where it binds to NAD(H) (Schmitz., 2009; Schmitz et al., 2000; Magupalli et al., 2008).

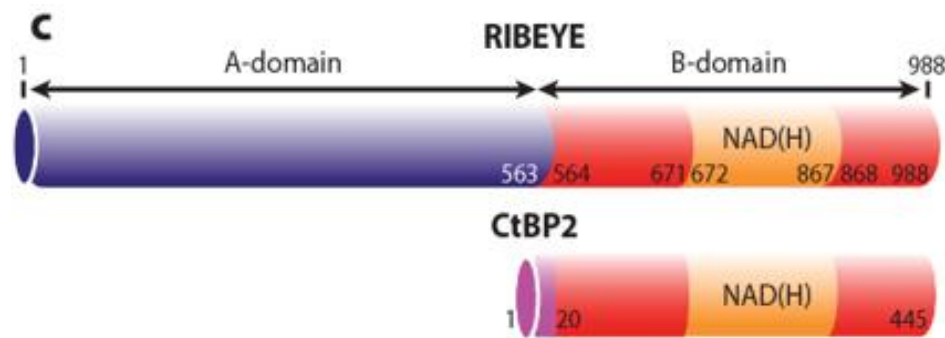


Figure 11. Schematic domain structure of RIBEYE and CtBP2

RIBEYE consists of a proline-rich amino terminal A-domain and NADH binding B-domain. RIBEYE B- domain is nearly identical to CtBP2 (C-terminal binding protein) except for unique 20 N-terminal amino acid. Adapted from (Lagnado and Schmitz, 2015)

RIBEYE and CtBP2 are encoded in the same gene. N-terminal sequences of RIBEYE and CtBP2 are encoded in a single 5' exon (exon 1) whereas their C-terminal sequences are encoded by eight common exons (exon 2-9) (Figure 12a). In the retina, RIBEYE is expressed in the tissue specific promoter within intron 1 of RIBEYE/CtBP2 whereas CtBP2 is ubiquitously expressed using different 5' promoters for transcription control (Piatigorsky, 2001; Schmitz et al., 2000) (Figure 12a, b). Exon 1 which encoded CtBP2 N-terminal sequence is not expressed when RIBEYE is produced by the RIBEYE/CtBP2 gene. CtBP2 is produced by alternative RNA splicing of the RIBEYE A-domain.

INTRODUCTION

The 5' intron which contains exon 1 of RIBEYE in the CtBP2 gene is absent from the *Drosophila* genome sequence. Therefore, a protein similar to RIBEYE is not generated by an alternative promoter in *Drosophila* which reveals that synaptic ribbons and RIBEYE are innovated in vertebrates evolutionary (Schmitz et al., 2000). The structure of RIBEYE and its gene reveals that it is a hybrid protein in which pre-existing CtBP2 and novel N-terminal RIBEYE domain was joined to make up a fusion protein for a new function (Schmitz et al., 2000). RIBEYE A mRNA was detected only in the retina, but RIBEYE B mRNA was detected ubiquitously in most of the tissues at variable levels (Schmitz et al., 2000) (Figure 12b).

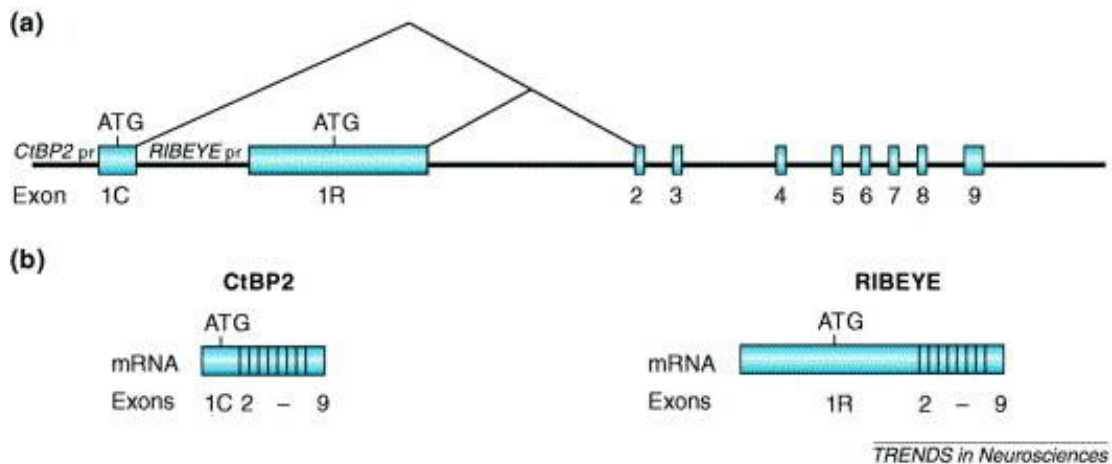


Figure 12. Diagrammatic representation of RIBEYE/CtBP2 gene

(a) RIBEYE and CtBP2 are transcribed from the independent promoter in the same gene by alternate RNA splicing. The unique N-terminal sequence of each protein (exon 1) is encoded by eight common 3' exons (exon 2-9). The CtBP2 promoter (pr) is ubiquitously active in most of the cells, whereas the RIBEYE promoter (pr) is active only in neurons that make ribbon synapse and RIBEYE and CtBP2 differ in their N-terminal regions. (b) Exon 1C is used exclusively for the expression of CtBP2 and exon 1R only for the expression of RIBEYE. Adapted from (Piatigorsky, 2001).

RIBEYE A-domain and the RIBEYE B-domain contain five distinct sites for RIBEYE- RIBEYE interactions. Three docking sites in the RIBEYE A-domain mediate homotypic interactions with other RIBEYE molecules. This interaction is essential for the formation of synaptic ribbon scaffold (Magupalli et al., 2008; Schmitz, 2009; Moser et al., 2020) (Figure 13). In addition, two docking sites in RIBEYE B-domain mediate the homotypic interaction and the heterotypic interaction between RIBEYE A- and RIBEYE B-domains which is regulated by NAD(H). Heterologous interaction between RIBEYE A- and RIBEYE B-domains is inhibited by a low physiological concentration of NADH, suggesting that inhibition of the heterotypic interaction is a potential mechanism for regulation synaptic ribbon aggregation (Schmitz et al., 2000; Magupalli et al., 2008; Sheets et al., 2014) (Figure 13B, C).

INTRODUCTION

The RIBEYE B-domain is exposed on the ribbon surface towards the cytoplasm therefore it binds to various cytosolic proteins.

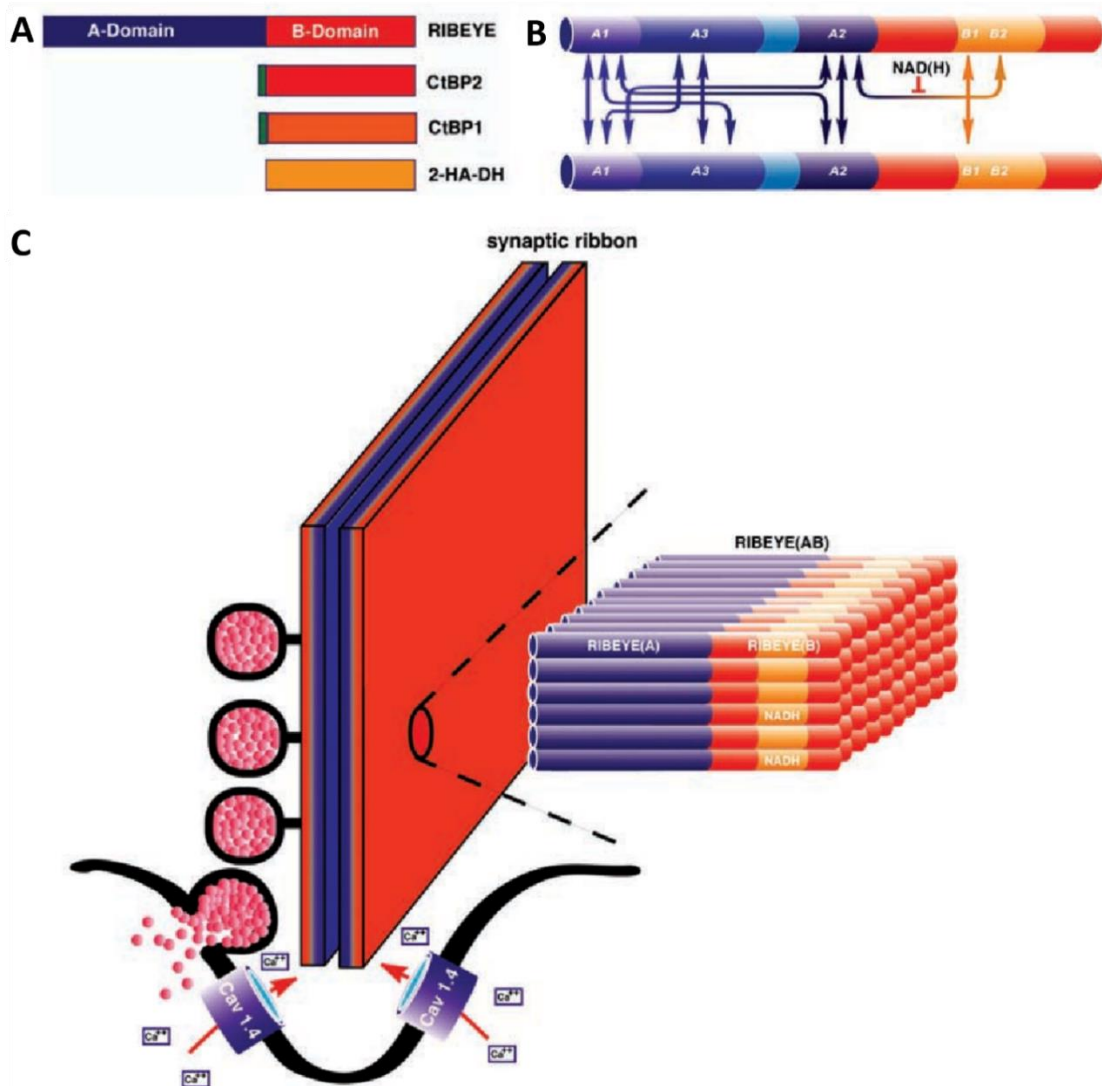


Figure 13. RIBEYE is a main structural protein of the synaptic ribbons

(A) RIBEYE B-domain/CtBP2 is structurally related to CtBP1 and binds to NAD(H). RIBEYE B-domain/CtBP2 and CtBP1 evolutionary developed from the D-isomer specific 2-hydroxy acid dehydrogenases (D2-HDH) (B) Multiple interaction sites are present in RIBEYE A-(A1, A2, A3) and RIBEYE B-domain (B1, B2) which allows multiple homotypic and heterotypic interaction shown by arrows. Heterotypic interactions (between RIBEYE A- and RIBEYE B-domain) are inhibited by NAD(H). (C) A simplified hypothetical diagram elucidates the formation of the synaptic ribbon by RIBEYE subunits. The model showing RIBEYE- RIBEYE interaction together builds the RIBEYE scaffold. The L- type voltage gated calcium channel clustered at the base of ribbon and Cav1.4 subunit of these channels form pores in rod synapses. Adapted from (Schmitz, 2009).

CtBP (C-terminal binding protein) protein has been known as a 48 kDa cellular phosphoprotein that binds to the C-terminal region of the adenovirus E1A oncoprotein known as CtBP1. CtBPs proteins bind

INTRODUCTION

with consensus pentapeptide motif PXDLS (X is generally leucine or valine) in DNA binding proteins. CtBPs act as a protein bridge between histone deacetylases and DNA bound factor because it binds to the PXDLS motif of histone deacetylases (Nardini et al., 2003; Chinnadurai, 2003 & 2002). CtBP has multiple biological roles in development because it binds to a diverse array of transcriptional regulators (Hildebrand and Soriano, 2002).

CtBP family proteins are conserved among vertebrates (CtBP1 and CtBP2) and invertebrates. CtBP1 proteins are present in higher amounts in the nucleus and with a significant amount in the cytosol (Hildebrand and Soriano, 2002). CtBP1 gene is located on chromosomes 4 and 5 of humans and mice respectively (Lagnado and Schmitz, 2015; Chinnadurai, 2007 & 2003) (Figure 13A).

The CtBP protein function as a transcriptional corepressor in the nucleus in conjugation with various DNA binding repressors (Chinnadurai, 2007). Transcriptional regulatory activity of CtBP is regulated by NADH and the cell's metabolic status. Homology search states that CtBP1 has striking homology to D-isomer-specific 2-hydroxy acid dehydrogenase, potentially showing another molecular enzymatic strategy for repression (Chinnadurai, 2007; Kumar et al., 2002). CtBP proteins are ADP- ribosylated by the fungal toxin brefeldin A and serve as a redox sensor that is metabolically regulated by NADH (Fjeld et al., 2003; Chinnadurai, 2003; Moser et al., 2020). Human CtBP1 sequence (except for approximately 90 N-terminal residues) are identical to NAD⁺-dependent dehydrogenases which include D-glycerate dehydrogenase and D-lactate dehydrogenase among others (Kumar et al., 2002; Goldberg et al., 1994; Stoll et al., 1996). CtBP1 is not essential for the structure and function of the synaptic ribbon, but it binds to the piccolo and bassoon. In the conventional synapses, CtBP1 proteins shuttle between the presynaptic terminal and nucleus and regulate their gene expression in activity-dependent manner (Moser et al., 2020).

CtBP consists of three domains: (i) substrate binding domain comprising PXDLS binding cleft. (ii) central nucleotide binding domain that binds to NAD(H). (iii) C-terminal motif that is intrinsically unsaturated (Nardini et al., 2009). In the presence of low NAD(H) level CtBP2 makes dimer whereas an increasing level of NAD(H) leads to oligomerization of CtBP2 that is necessary for transcriptional activities (Bellesis et al., 2018; Shi et al., 2003). Multi angle light scattering (MALS) studies have shown that NAD(H) binding promotes the assembly of two CtBP dimers into tetramer which is stabilized by hydrophilic and hydrophobic interactions (Bellesis et al., 2018). The absence of NAD(H), conformational change induces the decline in homodimerization efficiency and repression activity of CtBP (Nardini et al., 2009; Madison et al., 2013) (Figure 14).

INTRODUCTION

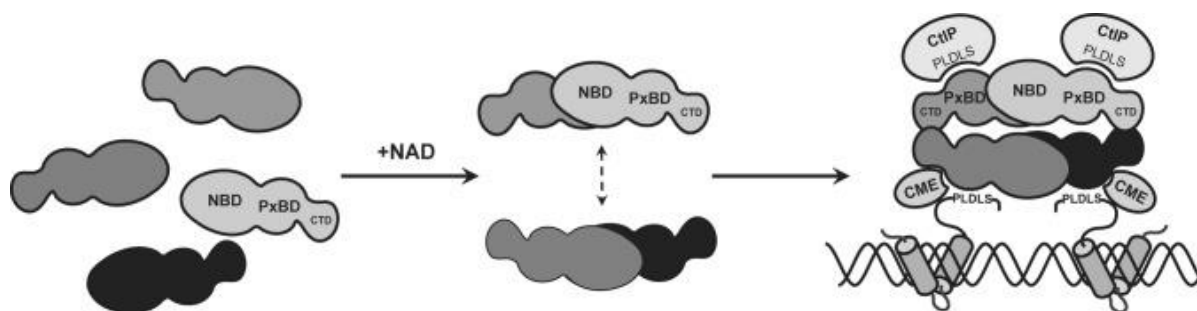


Figure 14. Schematic representation of CtBP tetramerization

The binding of NAD^+ at nucleotide binding domain (NBD) within CtBP1 monomers leads to dimerization of two CtBP1 monomers (dark gray-light gray; dark gray-black). Then each monomer binds with PXDLS containing protein bound to DNA through its PXDLS-binding domain at the N-terminus (PxBD). Each carboxyterminal domain (CTD) recruited additional CtBP1 dimer pairs to stabilize a homotetramer that can attract multiple chromatin modifying enzymes (CME). Other proteins such as CtIP (C-terminal interacting protein) can recruit additional PXDLS binding domains. The assembly order and activity of the dehydrogenase domain are not known in this model. Adapted from (Madison et al., 2013)

1.14 Function of RIBEYE

Previous studies have examined the heterologous expression of RIBEYE(A) and RIBEYE(B) and RIBEYE(AB) in R28 cells. The cells transfected with RIBEYE-A alone and with RIBEYE-AB make ribbon like rounded punctate aggregates in contrast to a bar shaped or plate shaped ribbons. (Schmitz, 2009; Magupalli et al., 2008; Sheets et al., 2014). These rounded electron dense aggregates resemble the spherical synaptic ribbon of inner hair cells revealing that spherical ribbons are the basal type of synaptic ribbons and probably additional scaffolding proteins are needed for bar shapes ribbons. RIBEYE-A alone transfection in cells forms spherical ribbon aggregates which supports the role of the RIBEYE(A) domain as an aggregation domain. In contrast, RIBEYE(B) transfection showed a diffusely distribution. Whereas co-transfection of RIBEYE(B) with RIBEYE(A) showed a redistribution of RIBEYE(B) from diffuse to spot like distribution (Magupalli et al., 2008).

The teleosts fish, Fugu, and zebrafish have two homologs of mammalian RIBEYE A- and RIBEYE B-domain. RIBEYE A-domain expression was found in photoreceptors, bipolar cells in the retina as well as in the inner ear and pineal gland. Whereas RIBEYE B-domain expression was found in the inner ear, but it is absent from the bipolar cells. Diminishing of RIBEYE (A) by morpholino antisense oligos in embryos results in shorter photoreceptor ribbons, fewer bipolar ribbons, and smaller synaptic terminals. RIBEYE A-domain deficiency in the teleosts fish inhibits ribbon assembly, impairs visual function, arrest development, and induces apoptosis in bipolar cells (Wan et al., 2005).

The RIBEYE knock-out mice which are lacking RIBEYE A-domain showed a complete absence of synaptic ribbon from the retina and inner ear (Maxeiner et al., 2016). In these RIBEYE KO mice, the

INTRODUCTION

presynaptic terminal of the retina was unaltered at the ultrastructural level except for the absence of ribbon, and the number of synaptic vesicles present at and close to the active zone was reduced (Figure 15). Cav1.4 channels were also less enriched at AZ. The pre and postsynaptic recordings from the rod bipolar cells/AII amacrine cell synapses reveal that ablation of synaptic ribbons causes a strong reduction in fast stimulus synchronous release, as well as slower, sustained release. This suggested that synaptic ribbons are assembled from the RIBEYE and ribbon is required to establish the normal number of the release ready vesicles (RRP) and to intact SV replenishment of RRP (Maxeiner et al., 2016). Damage of the ribbon by fluorophore assisted light inactivation (FALI) also showed the role of synaptic ribbon in vesicles priming (Snellman et al., 2011).

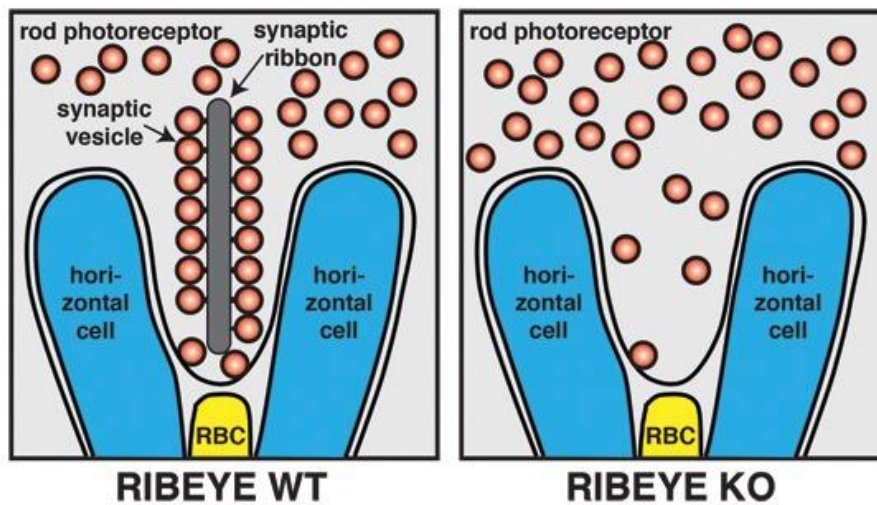


Figure 15. Schematic diagram of the absence of synaptic ribbon in RIBEYE KO mice
Deletion of synaptic ribbon reduces the docked vesicles, causes loss of fast and sustained release, and distorted nanodomain coupling in RIBEYE-KO mice. Adapted from (Maxeiner et al., 2016).

1.15 Generation of RIBEYE knock-in and RIBEYE knock-out mice

RIBEYE conventional Knock-in mice (KI) and knock-out mice (KO) were generated as described previously (Maxeiner et al., 2016). The RIBEYE KO in which RIBEYE specific A-domain was deleted, resulting in a complete absence of the synaptic ribbon in the retina compared with wildtype (WT) (Maxeiner et al., 2016) (Figure 15). The RIBEYE WT mice contain both the RIBEYE A- and RIBEYE B-domain (Figure 15 & 16A) in which synaptic ribbons with tethered vesicles are present.

In contrast, in RIBEYE knock-in mice RIBEYE B-domain is replaced by the calcium sensor GCaMP3 (Figure 16A). The RIBEYE knock-in mice express, a fusion protein of the amino terminal RIBEYE A-domain with the genetically encoded GCaMP3 calcium indicator (Tian et al., 2009) as a reporter for expression of RIBEYE via the endogenous RIBEYE promoter (Figure 16A). To investigate the function of the RIBEYE B-domain RIBEYE knock-in mice were generated (Maxeiner et al., 2016).

INTRODUCTION

The strategy for generating mice is shown in Figure 16B. The targeting vector contains the RIBEYE A-domain fused in frame to GCaMP3 calcium sensor cDNA, followed by stop codon (posttranscriptional regulatory element WPRE of woodchuck hepatitis virus) (Lee et al., 2005) and a neomycin selection cassette flanked by frt site. The neomycin selection cassette was removed after the homologous recombination into the RIBEYE locus ($RBE^{KI} + neo$) by flp recombinase. As a result, RIBEYE knock-in was generated. This mouse constitutively expressed RIB-G3 fusion protein under the control of endogenous RIBEYE promoter (Figure 16B). The entire RIBEYE A-domain with GCaMP3- Ca^{2+} sensor flanked by a loxP site was removed by Cre recombinase to generate RIBEYE KO mice (Figure 16B).

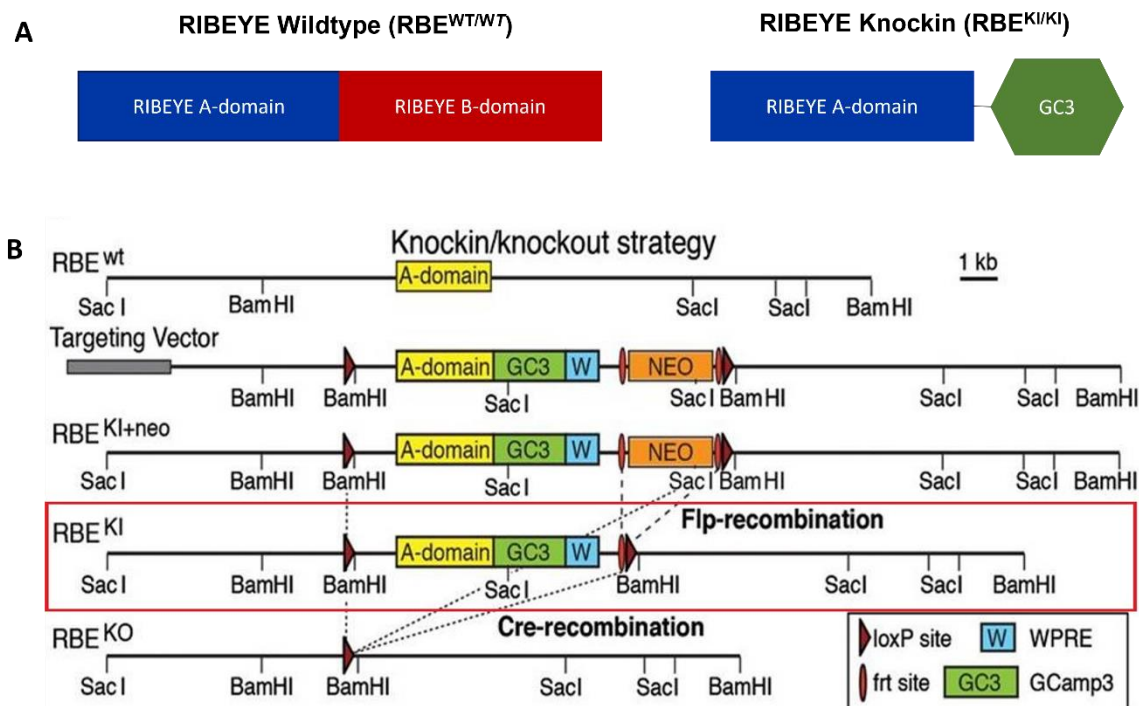


Figure 16. Schematic representation of targeting vector

(A) Schematic representation of RIBEYE wildtype and RIBEYE knock-in mice. (B) In targeting vector RIBEYE A-domain (yellow) is fused with GCaMP3 Ca^{2+} calcium sensor (green) followed by stop codon and woodchuck hepatitis virus posttranscriptional regulatory element (WPRE, blue) and frt flanked (red ovals) PGK-neomycin selection cassette (orange). The loxP site (dark red triangle) flanked the entire DNA sequence. Flp-recombinase excises neomycin cassette after homologous recombination in RIBEYE locus (RBE^{KI+neo}) to generate RBE^{KI} . Subsequently, the entire RIBEYE A-domain with a Ca^{2+} calcium sensor is removed by Cre-recombinase to generate RBE^{KO} . Adapted from (Maxeiner et al., 2016).

2. AIM OF THE STUDY

The ribbon synapses are unique chemical synapses with a specialized active zone that contains synaptic ribbons. These synapses tonically release neurotransmitters, a process that is promoted by the synaptic ribbon (Heidelberger et al., 2005; Schmitz, 2009; Sterling and Matthews, 2005; Matthews and Fuchs, 2010). In vertebrates, ribbon synapses are found in the retina, inner ear, and pineal gland (Lagnado and Schmitz, 2015; Moser et al., 2020).

The RIBEYE is the only known, major ribbon specific protein, which was first identified, characterized, and cloned by Schmitz et al., 2000. This protein is present in the ribbon synapse of all vertebrates (Schmitz et al., 2000; Zenisek et al., 2000; Khimich et al., 2005). The RIBEYE protein is composed of novel aminoterminal, proline-rich A-domain, and carboxyterminal B-domain, which is identical to the transcriptional repressor, C-terminal binding protein (CtBP2) except for 20 residues at aminoterminal (Schmitz et al., 2000; Schmitz, 2009; Wan et al., 2005).

The synaptic ribbon is a large, plate-like three-dimensional presynaptic structure that is composed of RIBEYE protein. Both RIBEYE A-domain and RIBEYE B-domain have multiple binding sites for other RIBEYE proteins, but the contribution of both RIBEYE A- and RIBEYE B-domain in the assembly of synaptic ribbon is still unclear. The results of RIBEYE transfection in cells suggest the structural role of the RIBEYE A-domain in the building of scaffold of synaptic ribbon (Schmitz et al., 2000; Magupalli et al., 2008). But it is unknown whether RIBEYE A-domain alone is sufficient for assembly of synaptic ribbon *in situ* or whether the RIBEYE B-domain is required for it.

To address whether RIBEYE B-domain has a role in the assembly of synaptic ribbons, I used RIBEYE knock-in mice (KI) made by Maxeiner et al., 2016. In these RIBEYE knock-in mice, RIBEYE B-domain has been replaced with the GCaMP3 calcium sensor, therefore these mice are the ideal tool to understand the role of RIBEYE B-domain in the assembly of synaptic ribbon.

3. MATERIALS AND METHODS

3.1 Materials

3.1.1 Antibodies

3.1.1.1 Primary antibodies

Antibody	Source	Reference	Dilution
RIBEYE A-domain (6F4), mouse monoclonal IgG1 antibody (stock≈0.8mg/ml)	Generated in the present study	Raised against a GST fusion protein encoding mouse RIBEYE(A): amino acids 83-211 (NP001164215)	1:100 (IF, WB) 1:500 (Cryo) 1:50 (EM)
RIBEYE(A), rabbit polyclonal (Tau)	Lab-made	Maxeiner et al., 2016	1:500 (IF)
RIBEYE(A)/ SySy, rabbit polyclonal	Synaptic Systems; Göttingen, Germany; 192103	Kerov et al., 2018	1:500 (Licor)
RIBEYE B-domain (2D9), mouse monoclonal IgG2b antibody	Lab-made	Dembla et al., 2018	1:200 (IF, Licor, WB)
Rhodopsin 1D4, mouse monoclonal	Gift: Dr. RS Molday	Hodges et al., 1988	1:100 (IF)
PSD95, rabbit polyclonal (L667)	Gift: Dr. TC Südhof	Irie et al., 1997	1:500 (IF)
Calbindin-D-28K (KD-15), rabbit polyclonal	Sigma; Darmstadt, Germany; C7354	Park et al., 2019	1:100 (IF)
Glial Fibrillary Acidic Protein (GFAP), rabbit polyclonal	DaKo; Glostrup, Denmark; Z0334	Gruber et al., 2021	1:500 (IF)
SV2, mouse monoclonal	Develop. Studies Hybridoma Bank; Univ. Iowa; Iowa City, IA, USA	Buckley and Kelly, 1985	1:20 (IF)
GFP, rabbit polyclonal	Abcam; Cambridge, UK; ab290	Yuan et al., 2021	1:2,000 (Licor)

MATERIALS AND METHODS

Actin, mouse monoclonal (clone C4)	Millipore; Molsheim, France (MAB1501)	Lessard, 1988; Mukherjee et al., 2020	1:3,000 (WB, Licor)
PMCA2 ATPase, rabbit polyclonal	Thermo Fisher; Rockford, USA; PA1-915	Lin et al., 2021	1:500 (IF)

3.1.1.2 Secondary antibodies

Antibodies	Source	Dilution
Donkey anti-mouse Alexa 568	Invitrogen; Karlsruhe, Germany; A-10037	1:1,000 (IF)
Chicken anti-rabbit Alexa 488	Invitrogen; Karlsruhe, Germany; A-21441	1:500 (IF)
Donkey anti-rabbit IRDye 800CW	LI-COR Biosciences; Bad Homburg, Germany; #92532213	1:5,000 (Licor)
Donkey anti-mouse IRDye 680LT	LI-COR Biosciences; Bad Homburg, Germany; #92568022	1:5,000 (Licor)
Goat anti-mouse peroxidase-conjugate (POX)	Sigma; Taufkirchen, Germany; A3673	1:3,000 (WB)
Goat anti-mouse conjugated to 10 nm colloidal gold	Sigma; Taufkirchen, Germany; G7652	1:100 (EM)

Miscellaneous reagents: Chameleon pre-stained protein ladder (Li-Cor Biosciences; Bad Homburg, Germany; #978-16526); Lectin PNA conjugated to Alexa 568 (Invitrogen; Karlsruhe, Germany; L32458).

3.1.2 Reagents and chemicals

Name	Company
Absolute Ethanol	Fischer Chemical
Acetic acid	Roth
Acetone	Roth
Amido Black	Merck
APS	Applichem
Agarose	Genaxxon Bioscience

MATERIALS AND METHODS

Benzil	Science Services
Betaine	Sigma-Aldrich
Bovine serum albumin	Sigma
Bromophenol blue	Serva
Cacodylic acid	Roth
Cellulose membrane for Peptide array	Intavis Bioanalytical Instruments
Cellulose acetate membrane for protein quantification	GE Healthcare
Chameleon pre-stained protein ladder for Licor blot	Li-Cor Biosciences
Coomassie Brilliant Blue R 250	TCI
Di Sodium hydrogen phosphate	Roth
Dimethylsulfoxide (DMSO)	Roth
Dodecanyl Succinic Anhydride (DDSA)	Electron Microscopy Sciences
dNTP's PCR-grade	Roth
Ethidiumbromide	Roth
EDTA	Roth
Epoxy embedding medium (Epon 812)	Fluka-Sigma-Aldrich
Ethanol	ZCHL
Formic acid	Merck
Glutaraldehyde, 25 %	Sigma Aldrich
Glycerol	Sigma
Hydrogen peroxide	Roth
Hydrochloric acid	VWR Chemicals
LR-Gold	London Resin Company
Low range protein standard Roti marker	Roth
Luminol	Roth
Magnesium Chloride PCR	Peqlab
Maleic Acid	Fulka
Mercaptoethanol	Roth
Methanol	ZCHL

MATERIALS AND METHODS

Methyl-5-Norbornene-2,3-Dicarboxylic Anhydride (MNA)	Electron Microscopy Sciences
Methyl Butane	Roth
Non-fat dry milk powder	Supermarket
Nonidet P 50 NPG (n- Propylgallate)	Sigma
dNTP	Meridian Bioscience
Nitrocellulose membrane	Millipore
Osmium tetroxide	Serva
Para-hydroxy Coumarin Acid (PCA)	Roth
Paraformaldehyde	Sigma-Aldrich
Posphotungstic acid	VWR
Ponceau S-stain	Roth
Potassium chloride	Grussing GmbH
Potassium dihydrogen phosphate	Roth
Potassium ferrocyanide (K4)	Merck
Propylene Oxide	Aldrich
Proteinase K	Meridian Bioscience
Rotiphorese Gel30(29% acrylamide,0.8% bisacrylamide)	Roth
Roti-Mark protein Standard	Roth
Sodium chloride	VWR
Sodium hydroxide	Grussing GmbH
Sodium methylate	Merck
TEMED	Roth
Trichloroacetic acid	Roth
Triton X-100	Sigma - Aldrich
TRIZMA BASE	Roth
2,4,6-Tri(dimethylaminomethyl)phenol (DMP-30)	Electron Microscopy Sciences
Uranyl acetate	Merck
Xylol	Roth
Whatman filter paper	Roth

MATERIALS AND METHODS

3.1.3 Buffers and solutions

Name	Composition
Agarose gel electrophoresis buffer (TAE) 50X Stock	242.0 g Tris base 0.37 g EDTA 57.1 ml glacial acetic acid Make up to 1 liter with ddH ₂ O
Amido black staining solution (I stain)	0.5% Amido black 45% Methanol 45% Distilled water 10% Acetic acid
Amido black washing solution (I wash)	47.5% Methanol 47.5% Distilled water 5% Acetic acid
Amido black dissolution solution (I diss)	8% Formic acid 10% Acetic acid 10 g Trichloroacetic acid
Blocking and permeabilization buffer for immunohistochemistry (inner ear)	0.5% BSA and 1% Triton-X100 in PBS
Binding buffer pepspot	50 mM Tris-HCl, pH 7.5 150 mM NaCl, 0.1% Triton X-100
Cacodylate buffer (100 mM)	21.4 g Cacodylic acid /L ddH ₂ O pH 7.4
Cacodylate buffer (200 mM)	42.8 g Cacodylic acid /L ddH ₂ O pH 7.4
Coomassie staining solution for SDS gel	3 g/L Brilliant blue R250 45% Methanol 45% ddH ₂ O 10% glacial acetic acid
Destaining Solution	50 ml Glacial acetic acid 75 ml Ethanol 100% Make up volume up to 1000 ml with ddH ₂ O
ECL-solution (Chemiluminescence detection system)	1:1 v/v ECL I and ECL II ECL I:

MATERIALS AND METHODS

	<p>5 ml Tris 1M pH 8.5</p> <p>0.5 ml Luminol stock</p> <p>220 μl Para-hydroxy Coumarin acid (PCA)</p> <p>Make up volume up to 50 ml with ddH₂O</p> <p>ECL II:</p> <p>5 ml Tris 1M pH 8.5</p> <p>32 μl H₂O₂</p> <p>Make up volume up to 50 ml with ddH₂O</p>
EPON embedding medium	<p>6.5 g Epoxyembedding medium (Epon 812)</p> <p>2.75 g Dodecanyl Succinic Anhydride (DDSA)</p> <p>4 g Methyl-5-Norborene-2,3-Dicarboxylic Anhydride (MNA)</p> <p>0.1 g of 2,4,6-Tri (dimethyl aminomethyl)phenol</p>
Laird buffer	<p>12.1 g (0.1 M) Tris</p> <p>1.86 g (5 mM) EDTA</p> <p>11.69 g (0.2 M) NaCl</p> <p>20 ml (0.2%) SDS solution (10%)</p> <p>Make up volume 1 liter ddH₂O, pH 8.5</p>
Luminol stock	<p>0.885 g Lum (3-Aminophthalhydrazide) (250 mM) in 20 ml Dimethyl sulfoxide (DMSO)</p> <p>1 ml Aliquot stored at -20°C</p>
Maleate buffer (0.05 M)	<p>5.80 g Maleic Acid</p> <p>42 ml of 0.2 NaOH, pH 5</p> <p>Make up volume 1 liter with ddH₂O</p>
Osmium stock	<p>2 % Osmium in ddH₂O</p>
5x PBS	<p>40 g NaCl</p> <p>1 g KCl</p> <p>7.2 g Na₂HPO₄</p> <p>1.2 g KH₂PO₄</p> <p>Make up volume 1 liter with ddH₂O</p>
p-Coumaric acid (PCA) stock	<p>0.296 g p-Coumaric acid (90 mM) in 20 ml DMSO</p>
10x PCR buffer	<p>500 mM KCl</p>

MATERIALS AND METHODS

	<p>100 mM Tris-HCl, pH 9.0</p> <p>1% Triton X-100</p>
Polyacrylamide 10% Separating gel	<p>1.5 ml ddH₂O</p> <p>1.9 ml 1 M Tris pH 8.8</p> <p>2.5 ml 30% Acrylamide</p> <p>75 µl 10% SDS</p> <p>1.5 ml 50% glycerol</p> <p>38 µl 10% APS</p> <p>5 µl TEMED</p>
Polyacrylamide Stacking gel	<p>2.4 ml ddH₂O</p> <p>940 µl 0.5 M Tris pH 6.8</p> <p>500 µl 30% Acrylamide</p> <p>50 µl 10% SDS</p> <p>50 µl 10% APS</p> <p>10 µl TEMED</p>
Ponceau S-stain	<p>30 g Trichloroacetic acid</p> <p>5 g Ponceau S</p> <p>Make up volume 1 liter with ddH₂O</p>
SDS-PAGE electrophoresis buffer	<p>3.03 g Tris</p> <p>14.4 g Glycine</p> <p>1.0 g SDS</p> <p>Make up volume 1 liter with ddH₂O</p>
SDS loading buffer	<p>1.6 g SDS</p> <p>4 ml β-mercaptoethanol</p> <p>2 ml Glycerol</p> <p>2 ml 1 M Tris pH 7</p> <p>4 mg Bromophenol Blue</p> <p>2 ml ddH₂O</p> <p>Store at -20°C</p>
Stripping buffer for pepspot	<p>Buffer A:</p> <p>8 M Urea</p> <p>50 mM Tris-HCl, pH 7</p> <p>1% SDS</p> <p>0.5% Mercaptoethanol</p> <p>Buffer B:</p>

MATERIALS AND METHODS

	50% Ethanol 10% Acetic acid 40% ddH ₂ O
Stripping buffer of Western blot	110 µl β-mercaptoethanol 2 % Sodium dodecyl sulfate 0.1 M Tris-HCl, pH 8.5
Taq DNA Polymerase	Lab made
Transfer buffer (Western blot)	15.125 g Tris 72.05 g Glycine 1 liter Methanol Make up volume up to 5 liters with ddH ₂ O
1 M Tris buffer, pH 8.8	12.11 g Tris dissolved in 50-60 ml ddH ₂ O, pH 8.8 Make up volume up to 100 ml with ddH ₂ O
0.5 M Tris buffer, Ph 6.8	6.05 g Tris dissolved in 50-60 ml ddH ₂ O, pH 6.8 Make up volume up to 100 ml with ddH ₂ O
Xylol/Methanol	1 Xylol : 1 Methanol

3.1.4 Laboratory instruments and consumables

Name	Company
Adjustable pipettes	Eppendorf
Axiovert 200, AxioCam MRm (Camera)	Carl Zeiss
Agarose gel electrophoresis	Biozym
Autoclave	Tuttnauer Systec5050ELCV
Biofuge fresco	Heraeus
Biofuge primo R	
Biofuge Stratos	
Chemidoc XRSsystem	Bio-Rad
Confocal laser scanning microscope	Nikon
Dry bath system	Star lab
Fluorescence microscope	Axiovert 200 M, Carl Zeiss
Freezer -80°C	Heraeus
Glass slides	Roth

MATERIALS AND METHODS

Glass coverslips	Roth
Gold grid 100-mesh	Plano, Wetzlar, Germany
Hot air oven	Heraeus
Incubator for Epon resin Embedding (28°C)	Heraeus
Incubator for polymerization of Epon resin (60 °C)	Memmert 854 Schwabach sterilisator
Magnetic stirrer (Complete Set)	Neolab
pH meter	Inolab
Mini Vertical Electrophoresis Unit (MiniVE)	Hoefer
Powerpack for gel system	Amersham Biosciences
Overhead rotator	Neolab
PCR master cyclor	Bioer Genetouch
Refrigerated incubator shaker Innova 4320	New Brunswick Scientific
Super-resolution structured illumination microscope	Carl Zeiss
Thermomixer compact	Eppendorf
Ultracut Microtome (UltraCut S)	Leica
Ultrasound bandelin sonoplus	Bandelin Electronic, Berlin
Vortex	VWR International
Vacuum Pump	Duran
24 well plate	Greiner-CELLSTAR
Western blot transfer apparatus	Hoefer Scientific Instruments
Weighing balance CP64	Sartorius

3.2 Methods

3.2.1 Animal care

All animal experiments were performed in accordance with German legislation for the protection of animals. They were approved by the animal welfare and ethics committee of the Saarland's Institutional Animal Care and the local authorities. Mice were kept in a controlled and pathogen free environment. The standard light/dark cycle and provision of standard food and water ad libitum. Littermate mice 4 to 20 weeks old were used in this study.

3.2.2 RIBEYE knock-in mice

RIBEYE knock-in mice were generated by Maxeiner et al., 2016 (described in the introduction section, see section 1.15). All genotypes RBE^{WT/WT}, RBE^{WT/KI}, and RBE^{KI/KI} were used for comparative study as indicated in the respective experiments. To get all resulting genotypes of mice used in this study [RIBEYE Wildtype (RBE^{WT/WT}); RIBEYE heterozygous (RBE^{WT/KI}); and RIBEYE knock-in (RBE^{KI/KI})] heterozygous breeding was performed (Figure 17A). All experimental studies were performed blindly on littermate mice. Before organ collection, mice were anesthetized with isoflurane and killed by cervical dislocation in ambient light.

3.2.3 Genotyping of mice

3.2.3.1 Extraction of genomic DNA as PCR template for genotyping

For DNA extraction, ear or tail biopsy was taken from mice and digested for 2 hrs at 55°C in 400 µl Laird buffer containing 5 µl of 20 mg/ml proteinase K solution (Bioline; BIO-37085). Samples were centrifuged at 13,000 rpm, 4°C for 5 min. DNA was precipitated from the supernatant with 300 µl isopropanol and centrifuged at 13,000 rpm, 4°C for 10 min. The precipitated DNA was washed with 300 µl of 70% ethanol and centrifuged again at 13,000 rpm, 4°C for 5 min. The pellet was dried at 65°C for 15 minutes and resuspended in 50 µl dH₂O.

3.2.3.2 Primer for genomic PCR

Specific primers (11611 and 11626) were used for genotyping by PCR. The following primers, PCR reaction conditions, and PCR programs were used for genotyping.

Oligo 1: 11611

(5'- CTT GTG GCT GTG TAC AGT TAG CT -3')

Oligo 2: 11626

(5'- TAT GGG TTA GGA CCT GGA ATT CT -3')

Table 1. PCR reaction

PCR reaction ingredients	Stock	PCR reaction mixture for one reaction (µl)
10x buffer	10x	12.32
MgCl ₂	25mM	2.5
BSA	10mg/ml	2
Betaine	5M in H ₂ O	0.25
DMSO	100%	5

MATERIALS AND METHODS

dNTPs	25 mM	0.83
Oligo 1	100 μ M	0.2
Oligo 2	100 μ M	0.2
Taq polymerase	Lab made	0.5
DNA	50 -100 ng/ul	1
Total reaction volume		25

3.2.3.3 PCR program for genotyping

95°C for 5 min - initial denaturation of the template (and primers) plus activation of the Taq polymerase

95°C for 30 sec - cycling denaturation step

63°C for 30 sec - primer annealing step

72°C for 45 sec - product extension step

} 40 cycles

72°C for 2 min - terminal extension step (to ensure all products are maximally extended)

12°C forever - storage step

3.2.3.4 Genomic PCR and agarose gel electrophoresis for genotyping

The PCR reaction product was separated by electrophoresis on 1% agarose gel containing EtBr to distinguish the genotypes of the mice [homozygous Wildtype (RBE^{WT/WT}); heterozygous knock-in (RBE^{WT/KI}) and homozygous knock-in (RBE^{KI/KI}) allele].

The PCR reaction shown in Table 1 was used to discriminate between all RIBEYE genotypes. Wildtype DNA produced a band at approximately 250 bp and a knock-in allele at 340 bp with the above mentioned PCR conditions. Wildtype DNA was used as positive control and PCR reaction without DNA was used as a negative control. PCR amplification was performed as described above (see section 3.2.3.3). After completion of PCR reaction, 6x loading dye was added in each vial containing amplified DNA. Then DNA samples were resolved at 100 volts, 1 hour on 1% agarose in 1 x TAE gel containing ethidium bromide fluorescent dye. DNA fragment size was determined by comparison with known molecular weight standards (DNA ladder, 0.1-10 kb). DNA bands were visualized under UV light and images were captured by the Chemi Gel Doc XRS system. The resulting PCR gives the following product, RBE^{WT/WT}: 250 bp, RBE^{WT/KI}: 250 bp and 340 bp, RBE^{KI/KI}: 340 bp (Figure 17B).

MATERIALS AND METHODS

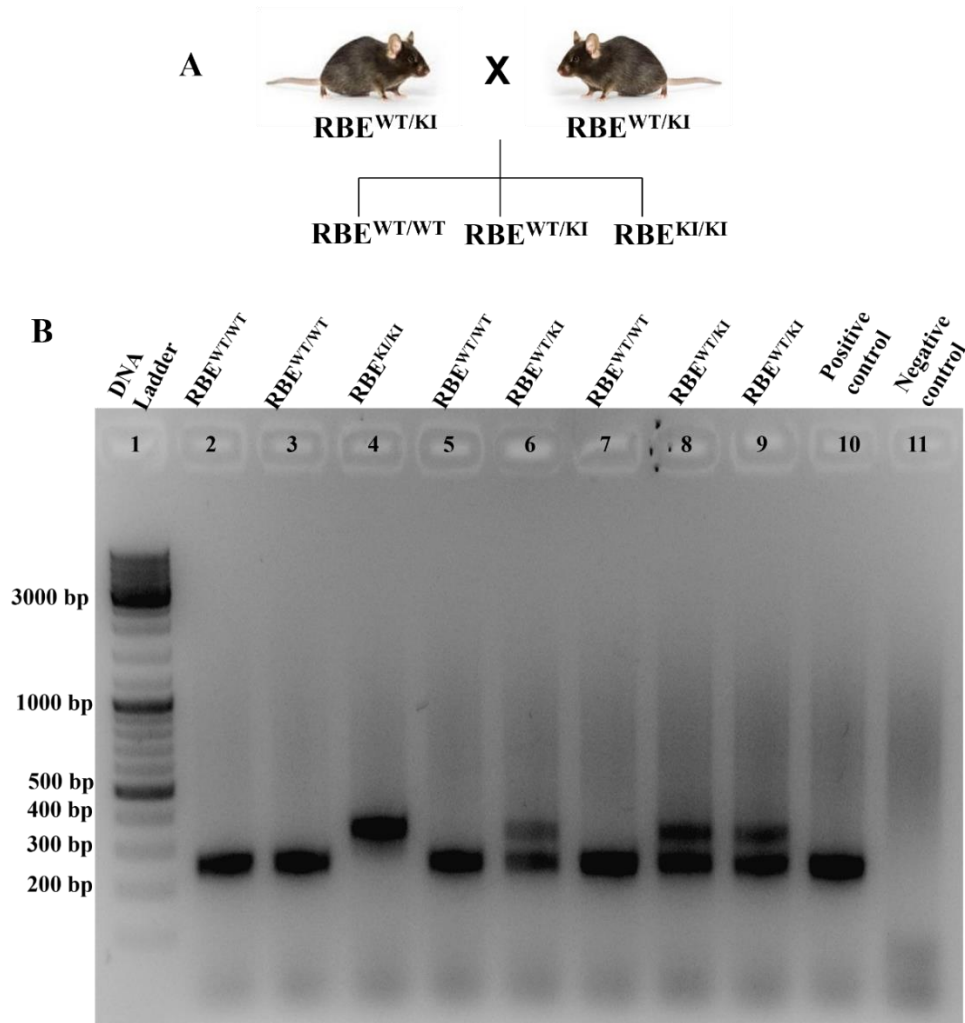


Figure 17. Diagrammatic representation of heterozygous mice breeding and genotyping
(A) Schematic diagram of breeding of heterozygous mice which gives all the three genotypes ($RBE^{WT/WT}$, $RBE^{WT/KI}$, and $RBE^{KI/KI}$). (B) Electrophoresis of PCR product for the comparison of genotypes. A single band of 250 bp represents homozygous RIBEYE wildtype (lane 2,3,5,7), two bands of 250 bp and 340 bp represent heterozygous knock-in (lane 6,8,9), and a single band of 340 bp represents homozygous knock-in (lane 4). Lane 10 is positive control and lane 11 is negative control. DNA ladder (0.1-10 kb) was loaded in lane 1.

3.2.4 Isolation of mouse retina

Mice were deeply anesthetized with isoflurane and sacrificed by cervical dislocation. Eyes were enucleated within 5 min *post-mortem* and placed into cold PBS. Under the dissecting microscope, the eye was positioned to see the posterior eyecup with the optic nerve pointing up. The eye was punctured at the equatorial plane with a sharp needle and the anterior eye cup was removed (white ring separating the posterior eye from the anterior) with spring scissors (Fine Science Tolls; F.S.T 15024-10). The lens was removed from the posterior eyecup. For the preparation of Epon, E-PTA, LR-Gold embeddings, posterior eyecup with attached retina was used and processed according to the embedding procedures as described below (see section 3.2.5 & 3.2.6).

3.2.5 Light microscopic analyses

3.2.5.1 Embedding of retinal samples for immunocytochemistry on semi-thin sections (0.5 μm and 1.5 μm)

Embedding of mice retinal tissue in Epon resin was performed as described by Wahl et al., 2013. This procedure is a modification from the procedure described by Drenckhahn and Franz (1986). Eyes were dissected as described above and for Epon embedding preparation, posterior eyecup with attached retina was flash-frozen in liquid nitrogen-cooled isopentane. Then, as a modification from the original procedure, lyophilization of the frozen tissue was performed for ≈ 48 hrs. The lyophilization of the retina tissue was performed in the vacuum of $\approx 10^{-7}$ mbar using a TCP270 turbo molecular pump (Arthur-Pfeiffer-Vacuumtechnik, Wetzlar/Aßlar) controlled by a PKG020 Pirani-gold cathode gauge control unit and an oil diffusion pump as a prepumping unit (type DUO 004B, Arthur-Pfeiffer-Vacuumtechnik, Wetzlar/Aßlar). Next, Epon was added to the lyophilized tissue and allow to infiltrate on the rotor (≈ 10 rpm) at 28°C for ≈ 24 hrs. The infiltrated tissue was degassed for 30 min and transferred to silica mold containing Epon then polymerized at 60°C for approximately 24 hrs.

3.2.5.2 Immunolabeling of 0.5 μm and 1.5 μm thin retinal resin sections

Immunolabeling was performed on Epon resin retinal semithin sections. For this purpose, 0.5 μm and 1.5 μm semithin sections were collected on glass coverslips and heat fixed after cutting with a Reichert ultramicrotome. The resolution of semithin sections is higher in comparison with paraffin sections and cryosections (Punge et al., 2008). Before immunolabeling Epon resin was removed from the 0.5 μm semithin sections by incubating them in the following solutions: sodium methanolate (30% solution in methanol; Sigma-Aldrich) for 10 minutes; xylol: methanol mixture (1:1) for 10 minutes each; acetone two times 10 minutes each; H_2O for 10 minutes; and PBS for 10 minutes.

For super-resolution microscopy (3D SR-SIM) (see section 3.2.5.4) 1.5 μm Epon resin sections were used. For removal of Epon resin 1.5 μm , thin sections were incubated in sodium methanolate for 12 minutes instead of 10 minutes.

After removal of resin, 0.5 μm semithin sections were double immunolabeled simultaneously with two primary antibodies (generated from different species; mouse and rabbit) diluted in PBS. The primary antibodies were added to the sections and incubated overnight at 4°C . The next day, sections were washed several times with PBS and incubated with corresponding secondary antibodies for 3 hrs at RT. Then sections were washed several times with PBS and mounted by antifade solution N-propyl gallate (NPG). For the control immunofluorescence experiment, sections were incubated with secondary antibodies, and the rest of the procedure was the same, no primary antibody was used in this case. No immunofluorescence was observed in the control sections.

3.2.5.3 Confocal Laser Scanning Microscopy

3.2.5.3.1 Principle and methodology

The basic principle of confocal laser scanning microscope (CLSM) was first introduced by Minsky (1961, 1988). Confocal microscopy is a powerful tool that produces sharp images of fluorescent specimens up to 100 μm thick. Images produced by a conventional microscope appear blurry when examined under the microscope. Unlike conventional wide-field microscopes, confocal microscopes exclude most of the light from the specimen that is not from the microscope's focal plane. In confocal microscopes laser of light is adjusted by neutral density filters then reflected by a dichromatic mirror in x-y direction and fully scanned the fluorescent specimen in a defined focal plane. The secondary fluorescence emitted by the specimens passes back through the objective lens and dichromatic mirror to the pinhole to reach the detector. A pinhole eliminates the fluorescence that befalls above and below the focal plane (out-of-focus areas). Therefore, only the focused beam of the laser that passes through the pinhole is detected by a photomultiplier tube (PMT). Photomultiplier tubes amplify the light signal and convert it to an electrical signal without noise and the output from the PMT is built into an image and displayed by the computer. In computers, analog electrical signals are converted the digital numbers. Confocal microscopy was performed exactly as previously described using the Nikon setup (Wahl et al., 2013). Images were taken with a 60x Plan-Apochromat oil immersion objective (numerical aperture of 1.4), and a 60x water objective (Nikon NR Apo 60X/1.0W DIC N2) with excitation wavelengths of 488 nm, and 561 nm.

3.2.5.3.2 Confocal Microscopy Image Acquisition

The images of immunolabeled retinal semithin sections were acquired using confocal NIS Elements AR 3.2 software. Images were acquired with 60x/1.40 N.A. oil objective for semithin sections of the retina and 60x water objective (Nikon NR Apo 60X/1.0W DIC N2) for the whole mount inner ear using laser excitation lines 488 nm and 561 nm under the control of the NIS Elements software (NIS Elements AR 3.2, 64 bit; Nikon). The confocal images were acquired at identical settings and conditions using the "re-use" settings option of NIS Elements software for the comparative analyses of the different genotypes ($\text{RBE}^{\text{WT}/\text{WT}}$, $\text{RBE}^{\text{WT}/\text{KI}}$, and $\text{RBE}^{\text{KI}/\text{KI}}$). Image acquisition was performed in a blinded manner without knowing the identity of the samples.

3.2.5.3.3 Quantification of RIBEYE immunofluorescence signals in the OPL

For quantification of RIBEYE immunofluorescence intensity, images acquired by confocal microscopy were exported and analyzed by using Fiji Image J software.

The acquired confocal images of immunolabeled retinal semithin sections were analyzed with Fiji ImageJ software. To analyze fluorescence intensity of RIBEYE immunosignals in the outer plexiform

MATERIALS AND METHODS

layer (OPL), images were opened in Fiji ImageJ software, and a rectangular region of interest (ROI) was made around SV2 and PSD95 immunosignals as a reference for OPL. SV2 and PSD95 are well known markers of photoreceptor synapses (Koulen et al., 1998; Maxeiner et al., 2016).

The ROI was drawn using Analyze-Tool-ROI Manager in Fiji ImageJ (NIH) software. The fluorescence intensity of the immunostained synaptic ribbon was measured as integrated density. The identical ROI was made in the OPL on all images from all genotypes. The average integrated density values were normalized. For analysis wildtype ($RBE^{WT/WT}$) integrated density values set to 100% and heterozygous ($RBE^{WT/KI}$), and homozygous ($RBE^{KI/KI}$) integrated values were compared with $RBE^{WT/WT}$ values. Normalized integrated density of all genotypes was analyzed with Microsoft Excel and their individual data points were plotted as box and whisker plots in Origin Pro 2019b software. Quantification was done blindly.

The statistical analysis was performed as described below (see section 3.2.9) using Origin Pro 2019b and GraphPad Prism 8.4.3 software. For comparison of RIBEYE B-domain immunosignals between $RBE^{WT/WT}$ and $RBE^{WT/KI}$ Student's t-test was done because data was normally distributed. The Kolmogorov-Smirnov test was done for comparison between $RBE^{WT/WT}/RBE^{KI/KI}$ and $RBE^{WT/KI}/RBE^{KI/KI}$ as data were non-normally distributed.

The RIBEYE A-domain immunosignals statistical analysis was performed by Mann-Whitney U-test and Kolmogorov-Smirnov test because data were non-normally distributed.

3.2.5.3.4 RIBEYE puncta count in the OPL of 0.5 μm immunolabeled retinal sections

The number of RIBEYE puncta was counted in the outer plexiform layer (OPL) in the acquired confocal images of all genotypes. The RIBEYE puncta were counted per μm of OPL for that OPL length was derived from the confocal NIS Elements software. The confocal images were opened in Image J and the same OPL-ROI that was used for integrated density was used and duplicated the image. Then automatic counting of RIBEYE puncta was performed using Process/Find Maxima plugin (prominence 25, output/point selection including edge maxima). The average number of RIBEYE puncta of $RBE^{WT/WT}$, $RBE^{WT/KI}$, and $RBE^{KI/KI}$ mice sections were plotted per 100 μm of OPL in Microsoft Excel and their individual data points were plotted as box and whisker plots in Origin Pro 2019b software.

The Mann-Whitney U-test and Kolmogorov-Smirnov test were performed for statistical significances of RIBEYE B-domain puncta as data were non-normally distributed.

For the statistical significance of RIBEYE A-domain puncta, Student's t-test was performed for $RBE^{WT/WT}/RBE^{WT/KI}$ comparison (as data was normally distributed) and Kolmogorov-Smirnov test was performed for $RBE^{WT/WT}/RBE^{KI/KI}$ and $RBE^{WT/KI}/RBE^{KI/KI}$ comparison (as data was non-normally distributed).

3.2.5.3.5 Quantification of RIBEYE immunofluorescence signals and RIBEYE puncta count in the IPL

The RIBEYE immunofluorescence intensity in the inner plexiform layer (IPL) was measured as integrated density on the acquired confocal images. To quantify the integrated density and puncta count, the ROI of the IPL was selected by considering SV2 and PSD95 immunosignals as described above (3.2.5.3.3). As a reference of IPL, rectangular ROI was drawn around the SV2/PSD95 immunosignals and integrated density was calculated as described above. The same IPL-ROI was also used for the RIBEYE puncta count in IPL. The IPL is thicker than the OPL because it has five equal-thickness strata (Kolb, 1997; Euler et al., 2014). Therefore, RIBEYE puncta were counted per μm^2 area of the IPL. For this purpose, the area of IPL was calibrated using known distance length that is derived from the confocal NIS Elements software. The same IPL ROI was used for all genotypes.

The values of average integrated densities of RIBEYE A- and RIBEYE B-domain immunosignals of all genotypes were normalized. For analysis wildtype ($\text{RBE}^{\text{WT}/\text{WT}}$) integrated values set to 100% and heterozygous ($\text{RBE}^{\text{WT}/\text{KI}}$), and homozygous ($\text{RBE}^{\text{KI}/\text{KI}}$) integrated values were compared with $\text{RBE}^{\text{WT}/\text{WT}}$ values. Normalized integrated density of all genotypes was analyzed with Microsoft Excel and their individual data points were plotted as box and whisker plots in Origin Pro 2019b software. Quantification was done blindly.

The RIBEYE A- and RIBEYE B-domain immunostained puncta in the IPL were counted automatically using the Process/Find Maxima plugin in Fiji ImageJ software as described above for the OPL. The RIBEYE A/B puncta were counted in a $3,000 \mu\text{m}^2$ rectangular area of immunolabeled retina cross-sections. The average RIBEYE puncta values of $\text{RBE}^{\text{WT}/\text{WT}}$, $\text{RBE}^{\text{WT}/\text{KI}}$, and $\text{RBE}^{\text{KI}/\text{KI}}$ retina sections were analyzed with Microsoft Excel and their individual data points were plotted as box and whisker plots in Origin Pro 2019b software.

The statistical analysis of the integrated density of all comparisons was performed by Mann-Whitney U-test in Origin Pro 2019b or online Mann-Whitney U-test.

For statistical analysis of RIBEYE B-domain puncta count, Student's t-test was performed for $\text{RBE}^{\text{WT}/\text{WT}}/\text{RBE}^{\text{WT}/\text{KI}}$ comparison (as data was normally distributed) and Mann-Whitney U-test was performed for $\text{RBE}^{\text{WT}/\text{WT}}/\text{RBE}^{\text{KI}/\text{KI}}$ and $\text{RBE}^{\text{WT}/\text{KI}}/\text{RBE}^{\text{KI}/\text{KI}}$ comparison (as data was non normally distributed).

For statistical analysis of RIBEYE A-domain puncta count, Mann-Whitney U-test was performed for $\text{RBE}^{\text{WT}/\text{WT}}/\text{RBE}^{\text{WT}/\text{KI}}$, $\text{RBE}^{\text{WT}/\text{WT}}/\text{RBE}^{\text{KI}/\text{KI}}$ comparisons, and Kolmogorov-Smirnov test was performed for $\text{RBE}^{\text{WT}/\text{KI}}/\text{RBE}^{\text{KI}/\text{KI}}$ (because data was non normally distributed).

3.2.5.4 Super-Resolution Structured Illuminated Microscopy (SR-SIM)

3.2.5.4.1 Principle and methodology

Fluorescence microscopy is widely used for fluorescently labeled samples but it has a limitation of resolution of approximately 200 nm in the laterals (x,y) dimension and 500 nm in axial (z) dimension. SR-SIM microscopy overcomes the limitation of spatial resolution by spatially structured illumination light (Schermelleh et al., 2010).

SR-SIM microscopy utilizes the grating to generate three coherent beams, which is applied to the sample. When it applies to sample, it makes an illumination pattern that varies axially and laterally. The high-resolution information created by excitation intensity is encoded in images by mixing the spatial frequency. The 3D-SR-SIM increases two-fold axial (z) resolution as well as lateral (x,y) resolution. SR-SIM microscopy also increases the possibility of using standard protocols by using a wide range of fluorescent dyes (Schermelleh et al., 2010).

The 3D SR-SIM microscopy resolves the objects beyond the diffraction limit of light (Schermelleh et al., 2010). For the measurement of contour length of the synaptic ribbon by 3D SR-SIM, 1.5 μm sections of RIBEYE^{WT/WT} and RIBEYE^{WT/KI} were prepared from the Epon embedded retina of these mice. Epon removal and immunolabeling were performed as described above (see section 3.2.5.2).

The 1.5 μm - thin sections, that were processed for 3D SR-SIM, were labeled only with a single primary antibody [anti RIBEYE B-domain (2D9) or anti-RIBEYE A-domain (6F4)]. For detection of primary antibodies fluorophore-conjugated donkey anti-mouse Alexa 568 secondary antibody was used as described above (see section 3.2.5.2). The high-resolution images were acquired by structured illuminated microscopy (SR-SIM) using the ELYRA PS1 setup (Carl Zeiss Microscopy GmbH).

OPL Images of synaptic ribbons labeled with RIBEYE antibodies were acquired with 63X/1.4 NA oil (DIC) objective using excitation light 561 nm and collected through an Andor iXon EM-CCD camera at 100 ms exposure time. The z-stack images of RIBEYE immunostained sections were taken at 125 nm intervals, using Zen 2012 software (black version-Zeiss). The whole thickness of the retinal section was scanned, and images were acquired. Afterward, images were processed for structured illumination for better resolution (Gustafsson et al., 2008).

3.2.5.4.2 Measurement and quantification of ribbon contour length from 3D SR-SIM images

The contour length of RIBEYE [anti RIBEYE B-domain (2D9) or anti-RIBEYE A-domain (6F4)] immunostained synaptic ribbon was measured using ZEN 2.3 SP1 software (black version). The RIBEYE^{WT/WT} and RIBEYE^{WT/KI} sections were used for this purpose. First, an individual synaptic ribbon was cropped from the z-stack images and scanned completely to ensure the immunostained ribbon is completely captured. Then the 3D image was created in transparent mode from z-stacks and 2D

MATERIALS AND METHODS

maximum projection images were made from the 3D image. The polyline tool was used to draw a line along the contour length of the ribbon in ZEN 2.3 SP1 software. The given values were exported to Microsoft Excel and average value of contour length was calculated. Their individual data points were plotted as box and whisker plots in Origin Pro 2019b software.

For statistical analysis of RIBEYE B- and RIBEYE A-domain immunostained synaptic ribbon Mann-Whitney U-test and Kolmogorov-Smirnov test was used respectively.

3.2.5.5 Preparation of cryostat sections from the mouse retina

Freshly isolated eyes of RBE^{WT/WT} and RBE^{KI/KI} mice were flash-frozen in liquid nitrogen-cooled isopentane. The frozen eyes were embedded in a tissue embedding medium (NEG-50) on a block for 5-10 minutes inside precooled cryostat (-23°C). After solidification of the embedding medium, the block of medium with the embedded eye was fixed on a specimen holder. Cryosectioning of the retina isolated from RBE^{WT/WT} and RBE^{KI/KI} mice was done by Leica cryostat. 10 µm-thick cryosections of the retina were cut with a microtome and thawed on glass slides. Cryosections on the glass slides were heat fixed at 50°C for 10 min. The heat fixed sections were kept at -20°C until used for immunostaining.

3.2.5.5.1 Immunolabeling of cryostat sections of the mouse retina

The fluorescent lectin PNA Alexa 568 was used on 10 µm thick retinal cryosections of RBE^{WT/WT} and RBE^{KI/KI} mice for visualization of cone synapses as previously described (Grabner et al., 2015). For immunolabeling, the first cryosections were heat fixed at 55°C for 10 mins. Then incubated with 0.5% BSA in PBS (blocking buffer) for 1 hr, RT to block unspecific binding sites. Next, RIBEYE A-domain (6F4, 1:500) primary antibody diluted in blocking buffer was applied on the retina sections and incubated overnight at 4°C. The unbound primary antibody was removed by several washes with PBS and simultaneously secondary antibody donkey anti-mouse Alexa 488 (1:1000) and PNA Alexa 568 (1:200) was applied to the sections and incubated for 3 hrs at RT. Then section was washed several times and mounted with NPG as described above (see section 3.2.5.2).

3.2.5.6 Isolation of mouse cochlea

3.2.5.6.1 Isolation of mouse cochlea and whole-mount immunostaining of cochlear turn

4-8 weeks old RBE^{WT/WT} and RBE^{KI/KI} mice were used for the isolation of cochlea. Mice were deeply anesthetized with isoflurane and sacrificed by cervical dislocation. Then, the mice were decapitated, and head of the mice was cooled on ice for 15 mins. The cochlea was isolated as described previously (Montgomery and Cox, 2016; Fang et al., 2019). First, mice skull bone was cut off by making cut along the sagittal suture and brain tissue was removed. The cranial nerves were scrapped away using anatomical forceps (Schreiber Instrument, Fridingen Germany; SI Line; SI-14-1531) and manually

MATERIALS AND METHODS

removed the petrous part of the temporal bone. The isolated temporal bone was transferred to the 2 ml microcentrifuge tube containing 4% cold PFA (PFA in PBS, pH 7.4) and incubated overnight for fixation at 4°C on an orbital shaker. The next day, temporal bone was washed several times with PBS and decalcified with 120 mM ethylene-diamine-tetraacetic acid (EDTA, in PBS, pH 7.4) at 4°C for 3 days. EDTA was changed two times, approximately after 8 hrs in a day. Decalcified temporal was washed several times with PBS and transferred to a petri dish containing cold PBS for dissection under a microscope. Hold the vestibular part of the temporal bone with a forcep and was cut away by making cut along oval and round window. The cochlea was placed in another petri dish by placing basal turn toward the bottom and cochlear turns were dissected. The dissected apical, middle, and basal turns of the cochlea were placed in 24 well plates containing cold PBS for immunostaining and stored at 4°C.

3.2.5.6.2 Immunolabeling of whole mount organ of Corti

After dissection of RBE^{WT/WT} and RBE^{KI/KI} cochlea, for immunolabeling, cochlea samples were incubated in 300 µl of blocking and permeabilization solution (0.5% BSA, 1% Triton in PBS) for 1 hr 30 min at RT on mild shaking. Then simultaneously two primary antibodies originating from different species (mouse and rabbit) were applied to the samples and incubated overnight at 4°C for double immunolabeling. The next day, samples were washed several times with PBS and incubated with corresponding secondary antibodies for 3 hrs at RT. For immunolabeling antibodies were diluted in a blocking/permeabilization solution. After secondary antibody incubation whole mount sections were washed several times with PBS and z-stacks images were acquired with 60x water objective (Nikon NR Apo 60X/1.0W DIC N2) using confocal microscopy. Afterward acquired images were processed for maximum intensity projection.

3.2.6 Transmission Electron Microscopy

3.2.6.1 EM embedding procedure

For the comparative ultrastructural analyses of retinal synapses of all genotypes by transmission electron microscopy (TEM), RBE^{WT/WT} wild-type mice, RBE^{WT/KI} heterozygous, and RBE^{KI/KI} homozygous littermate mice were used. The embedding was prepared as described by Maxeiner et al., 2016. For embedding, retina was dissected as described above (see section 3.2.4) and the posterior cup with attached retina was fixed with 4% paraformaldehyde (PFA in PBS, pH 7.4), and 2.5% glutaraldehyde (in PBS) overnight at 4°C on mild shaking subsequently (12 hrs for each fixation). Next, retina samples were postfixed in OsO₄, 1.5 % (wt/vol) K₄[Fe(CN)₆] × 3H₂O (1:1) in 100 mM cacodylate buffer (pH 7.4) for 1 hr at 4°C on rotating shaker. The samples were washed 3 times with 100 mM cacodylate buffer (pH 7.4), H₂O, and 50 mM Na-Maleate buffer (pH 5.0) subsequently. Next samples were contrasted with 2% uranyl acetate (in 50 mM Na-Maleate buffer, pH 5.0) for 3 hrs at 4°C on a rotating shaker.

MATERIALS AND METHODS

After contrasting samples were washed several times with 50 mM Na-Maleate buffer (pH 5.0) and H₂O subsequently. Then samples were dehydrated with ascending series of ethanol (30%, 50%, 70%, 80%, 90%, 99%) and pure acetone for 15 min each at RT. Afterward, acetone was gradually replaced by increasing volumes of Epon (3:1, 1:1, 1:3 (v/v)), 3 hrs each at RT. Finally, samples were infiltrated with pure Epon overnight at RT. Then infiltrate samples were transferred to the silica embedding molds and polymerized at 60°C for approximately 24 hrs. Ultrathin sections from the Epon embedding were used for transmission electron microscopy.

3.2.6.2 Ethanolic Phosphotungstic Acid (E-PTA) staining of retina samples for TEM

Ethanolic phosphotungstic acid staining of retinal samples was performed as described previously (Bloom and Aghajanian, 1968; Limbach et al., 2011) with some modification for ultrastructural analysis by TEM. For E-PTA embedding, 4-5 months old littermate (RBE^{WT/WT}, RBE^{WT/KI}, and RBE^{KI/KI}) mice were used. The posterior eyecup with retina was fixed in 4% paraformaldehyde, pH-7.4 overnight at 4°C. The next day, retina samples were washed several times with PBS and dehydrated with increasing concentrations of ethanol (30%, 50%, 70%, 80%, 90%, 99%), 15 mins (each step) on rotator at RT. Then samples were dehydrated with absolute ethanol (100%), 10 min at RT. After dehydration samples were stained with 1% phosphotungstic acid (w/v) in absolute ethanol containing 5 drops of 95% absolute ethanol for 10 ml of staining solution and kept on a rotator for 1.5 hrs, RT. After staining, E-PTA solution was replaced with ice-cold propylene oxide to avoid strong exothermic reaction (Fry and Spira, 1980). Propylene oxide was changed once and incubated the samples in propylene oxide for 30 mins at RT on a rotator. Afterward, samples were infiltrated with pure Epon overnight and polymerized at 60°C, ≈ 24 hrs as described above (see section 3.2.6.1).

3.2.6.3 London Resin (LR)- Gold post embedding immunogold microscopy

The LR Gold tissue embedding was performed as described previously (Schmitz et al., 2000; Wahl et al., 2013) with some modification. For embedding preparation, RBE^{WT/WT} wild-type, homozygous RBE^{KI/KI}, heterozygous RBE^{WT/KO}, and homozygous RBE^{KO/KO} mice were used. The freshly isolated posterior eyecup with attached retina was fixed in 2% paraformaldehyde (in PBS, pH 7.4) overnight at 4°C on the shaker. Next, sections were washed 3x with PBS then dehydrated with ascending series of ethanol (30% ethanol 4°C for 10 min, pre-cooled 50%, 70%, 80%, 90%, 99% ethanol; 1 hr each at -20°C on rotator). Afterward, ethanol was gradually replaced with the increasing volume of LR gold (2/1, 1/2 (v/v), 1 hr each, -20°C). Next, samples were infiltrated with pure London Resin (LR)-Gold overnight at -20°C. Finally, LR-Gold resin solution was replaced with LR-Gold containing 0.1% benzil and polymerized the samples under UV light ≈ 48 hrs at -20°C. In post embedding protocols, no osmium

MATERIALS AND METHODS

tetroxide can be used to enhance membrane contrast. In LR-Gold method, lipid-rich membrane compartments (i.e., synaptic vesicles) remain largely invisible.

3.2.6.4 Post embedding immunogold labeling

Ultrastructural analysis of immunogold labeling was performed on LR-Gold ultrathin sections of RBE^{WT/WT} wild-type, homozygous RBE^{KI/KI}; heterozygous RBE^{WT/KO}, and homozygous RBE^{KO/KO} mice. For immunogold staining, ultrathin sections were incubated in 0.5% Bovine serum albumin (BSA in PBS pH 7.4) for 45 mins at RT to block unspecific binding. Then, RIBEYE A-domain (6F4) primary antibody diluted (1:50) in 0.5% BSA was applied on the section and incubated overnight at 4°C. Next, sections were washed several times with PBS and secondary antibody goat anti-mouse conjugated to 10 nm gold nanoparticles (1:100 in blocking buffer) was applied on the sections for 1 hr at RT. Then sections were washed several times with PBS and immune complexes were post-fixed with 2.5% glutaraldehyde (in PBS), 15 min, RT. Afterward, sections were washed several times with H₂O and contrasted with 2% uranyl acetate (in H₂O) 15 min, RT. Next, sections were washed several times with H₂O and dried at RT then analyzed by transmission electron microscopy. In negative control incubation, all the labeling procedure was the same only primary antibody was omitted.

3.2.6.5 Preparation of ultrathin retina section for TEM

For ultrastructural analysis of ribbon synapse by transmission electron microscopy retinal ultrathin sections were used. Ultrathin sections (≈ 70 nm thick) were cut from the Epon and LR Gold polymerized tissue block of mice (RBE^{WT/WT}, RBE^{WT/KI}, RBE^{KI/KI}; RBE^{WT/KO}, RBE^{KO/KO}) retina. The retina tissue blocks were trimmed in a trapezoid-shaped pyramid with a small area. For ultrathin sectioning, Reichert ultramicrotome (Ultracut S, Leica Microsystem) with a diamond knife having a boat to fill with water (Ultra diamond knife 45°, Diatome AG; Beil, Switzerland, 6° sectioning angle) was used. The ultrathin sections ≈ 70 nm were made with a diamond knife and picked carefully then mounted on 100 mesh copper grids. The grid having sections was dried completely and stained with Reynold's lead acetate (Reynolds, 1963) for 2 mins at RT.

3.2.6.6 Transmission Electron Microscope

3.2.6.6.1 Principle and methodology

Transmission electron microscopy (TEM) is a very important tool in cell biology. This technique was first used in the early 1940s. The TEM operates on the same basic principles as the light microscope but uses electrons instead of light. The wavelength of the electron is much shorter than the light therefore TEM achieves ≈ 0.1 nm resolution that is a thousand times more in contrast to light microscopy. For imaging of tissues ultrathin section, the electron beam produced from the electron gun is focused into a

MATERIALS AND METHODS

small, thin, coherent beam by a condenser lens. The condenser aperture excludes high angle electrons. Then the focused beam is transmitted through a very thin specimen. The objective aperture that absorbed, scattered, and transmitted the beam that is projected by projector lens after being corrected by an intermediate lens on the phosphor screen. The image strikes on the phosphor screen produce light therefore images are visible for users (Kannan, 2018; Winey et al., 2014).

3.2.6.7 Transmission electron microscope Image Acquisition

The images from the retinal ultrathin sections of $RBE^{WT/WT}$, $RBE^{WT/KI}$, $RBE^{KI/KI}$, $RBE^{WT/KO}$, $RBE^{KO/KO}$ littermate mice were acquired with a Tecnai Biotwin12 digital transmission electron microscope (TEM) equipped with a Megaview III digital camera (Gatan) and controlled by iTEM acquisition software (Olympus, Hamburg, Germany). The transmission electron microscope was operated at 100 kV. The retinal rod photoreceptor synapse in the outer plexiform layer was clearly identified by their typical triad ultrastructural appearance. In mice retina, 95% of synapses are rod photoreceptor synapses. The rod photoreceptor synapses consist of a large synaptic ribbon anchored at the active zone. Cone synapses are bigger in size and possess multiple active zones with smaller synaptic ribbons. The inner plexiform layer also has presynaptic rod bipolar ribbon synapse. The rod bipolar ribbon synapses are larger in size and also have multiple active zones with smaller synaptic ribbons.

The transmission electron micrograph of rod photoreceptor ribbon synapse in the outer plexiform layer was acquired at 43,000x - 60,000x and the electron micrograph of the rod bipolar cell ribbon synapse in IPL was acquired at 26,500x.

3.2.6.8 Quantification of the number of synaptic ribbons in rod photoreceptor synapses and measurement of ribbon height using TEM

The quantification of the number of ribbons per rod terminal and ribbon height in the x-y direction was performed on ultrastructural images acquired by transmission electron microscopy. The cross-sectioned rod terminals of $RBE^{WT/WT}$, $RBE^{WT/KI}$, $RBE^{KI/KI}$ with clearly visible active zone were used for the analysis of ribbon per rod terminal. The average values of ribbon per rod terminal were calculated and plotted in Microsoft Excel and their individual data points were plotted as box and whisker plots in Origin Pro 2019b software. For ribbon per rod terminal analysis, $RBE^{WT/WT}$ values were normalized to 1, and $RBE^{WT/KI}$, $RBE^{KI/KI}$ were compared with $RBE^{WT/WT}$ values. For statistical significance, Mann-Whitney U-test and Kolmogorov-Smirnov test was performed.

The ribbon height in the x-y direction was measured in the ultrastructural images of rod photoreceptor synapses of $RBE^{WT/WT}$, $RBE^{WT/KI}$ retinas. The rod photoreceptor synapses in the outer plexiform layer were clearly visualized by a typical postsynaptic configuration that comprises horizontal and bipolar cells (triad or tetrad). The ribbon height was measured by drawing a straight line from the base to the

top of the ribbon using iTEM software. The scale bar on the exported TEM images was used as a reference to calibrate ribbon height. For statistical significance, Kolmogorov-Smirnov test was performed.

3.2.7 SDS PAGE and western blotting

3.2.7.1 Preparation of retinal lysate for SDS page

For the preparation of retinal lysate of RBE^{WT/WT}, RBE^{WT/KI}, and RBE^{KI/KI} mice, the retina was isolated as described above (see section 3.2.4). For western blot retina was gently detached from the posterior eyecup by holding the posterior eyecup (sclera) with forceps and detached from the retina by rotating the posterior eyecup intact with the retina. The retinal lysate was prepared by adding 200 μ l of Laemmli buffer into a pair of retinas of adult, age-matched mice. Retinal protein lysates were solubilized by homogenization by up/down pipetting with the tip in Laemmli buffer and heated at 96°C for 10 mins. The protein lysates were stored at -20°C until used for the western blot experiment.

3.2.7.2 Measurement of protein concentration

The classical, widely used protocols for protein determination, such as the Lowry (Lowry et al., 1951) or Biuret (Weichselbaum, 1946) methods are limited to a few compatible buffers. In addition, these methods suffer from the limitation of being incompatible with certain buffers, high salt concentrations, and the presence of detergents. To avoid these difficulties the concept of staining protein spots on a solid support with Amido Black followed by elution and photometric quantification of the dye was introduced. Therefore, the concentration of protein dissolved in Laemmli buffer was estimated by an Amido Black-based quantification method (Dieckmann-Schuppert and Schnittler, 1997).

In brief various pieces of ≈ 1.5 cm² size cellulose acetate membrane were cut. Defined volumes, 10 μ l of BSA standard (0.25, 0.5, 1, 2, 3, 4 μ g/ μ l), and protein samples were applied on the membrane. The membrane only with PBS was served as the blank control. The membrane was dried for 15 min at room temperature (RT) and subsequently immersed in the staining solution I stain [0.5% (w/v) amido black 10B, 45% (v/v) each of methanol and water, and 10% glacial acetic acid] for 15 min. After staining membrane was washed three times with the solution I washed (47.5% each of methanol and water, and 5% glacial acetic acid) for 5 min each. Afterward, dissolution of the cellulose acetate pieces was performed in 1 ml dissolution solution I diss (80% formic acid, and 10% each of glacial acetic acid and trichloroacetic acid) by incubating at 50°C for 30 min under shaking. The absorbance of the resulting blue solution was read photometrically at 620 nm against the corresponding blank reagent and concentration was calculated using the absorbance of BSA standards.

3.2.7.3 SDS-PAGE

3.2.7.3.1 Background

One dimensional sodium dodecyl sulfate-polyacrylamide gel electrophoresis (SDS-PAGE) is used to separate proteins with relative molecular mass under denaturing conditions in the presence of 0.1 % SDS (Laemmli, 1970). SDS, an anionic detergent that denatures the protein by breaking the disulfide bonds of the polypeptide chain and imparts an even distribution of negative charge per unit mass so that the proteins lose their secondary, tertiary, or quaternary structure, therefore the proteins being covered by SDS are negatively charged. β -mercaptoethanol is also included in the sample buffer to cleave disulfide bonds within or between molecules, allowing molecules to adopt an extended monomeric form. When negatively charged protein is loaded onto a gel and placed in an electric field, it will migrate towards the anode (positively charged electrode) and separated by a molecular sieving effect based on size.

The polyacrylamide electrophoresis gel contains two layers: the lower running gel of higher concentration of acrylamide (5% -10%), pH 8.8, and the upper stacking gel, pH 6.8 to separate the proteins which run towards anode through a discontinuous Laemmli buffer. The proteins can be easily visualized by staining with a protein specific stain such as Coomassie Brilliant R 250. The background was subsequently reduced by soaking the gel in the acrylamide gel destaining solution to visualize the protein bands.

3.2.7.3.2 SDS gel electrophoresis and electroblotting

Western blot analysis was performed for the examination of the expression of RIBEYE-A (SySy), RIBEYE-B (2D9), GFP, and Actin antibody in the retina of RBE^{WT/WT}, RBE^{WT/KI}, and RBE^{KI/KI} mice. For this purpose, retina lysate of all three genotypes was heated at 96°C for 10 min and 50 μ g protein was loaded per well and separated by 10% acrylamide SDS PAGE. Solubilized protein components were resolved electrophoretically by running the gel at 100V, 4 hr at RT. After electrophoresis, stacking gel was discarded and the resolving gel proteins were electrotransferred to nitrocellulose membrane (Protran 0.45 μ m) at 50 V for 5 hrs (4°C). For fluorescence detection (Licor Blots) membrane was not stained with ponceau-S staining.

For fluorescence immunoblotting, western blot (WB) membrane was blocked in 5% skimmed milk (in PBS) for 1 hr at RT to block unspecific binding sites and washed several times with PBS. Then WB membrane was incubated with primary antibodies (diluted in 3% skimmed milk in PBS) overnight at 4°C. The next day, membrane was washed several times with PBS and incubated for 3 hrs at RT in secondary antibodies (donkey anti-rabbit IRDye 800 CW, donkey anti-mouse IRDye 680 LT), diluted 1: 5,000 in 3% skimmed milk in PBS. Following washing with PBS, western blot membrane was scanned with Odyssey Infrared scanner using Odysee software (Licor Biosciences, Bad Homburg,

MATERIALS AND METHODS

Germany) for detection of fluorescence signal. The size of the protein band was compared with a known molecular weight chameleon pre-stained protein ladder (8 kDa - 260 kDa).

To perceive the expression of RIBEYE A- (6F4), RIBEYE B-domain, and Actin antibodies in the retina of heterozygous knock-out $RBE^{WT/KO}$ and homozygous knock-out ($RBE^{KO/KO}$) mice, retinal lysate of respective genotypes were run on 10% SDS gel and electrotransferred as described above. After electroblotting nitrocellulose membrane was stained with ponceau-S dye to confirm the transfer of proteins. The membrane was washed several times with PBS until complete removal of ponceau-S staining. Then membrane was blocked and incubated with primary antibodies as described above. For chemiluminescence detection, after primary antibody incubation membrane was washed several times with PBS and incubated for 3 hrs at RT with HRP-conjugated goat anti-mouse secondary antibody prepared in 3% skimmed milk. Then membrane was washed several times with PBS and incubated with chemiluminescence's detection solution (ECL1 and ECL2 mixture, 1:1 (v/v)), and the signals were documented with the ChemiDoc™ XRS Gel Doc system (Bio-Rad; Feldkirchen, Germany) apparatus. For chemiluminescence SDS gel Roti-Mark protein Standard (T851.2, Roth; 14 kDa - 212 kDa) was used.

3.2.7.3.3 Western blot analysis

The band intensities of fluorescence blot were quantified by using densitometry in Image Studio Lite software (Image Studio Lite 5.2 software: Li-Cor). To analyze the band signal of proteins on the blot, a rectangle ROI was drawn to encompass the protein band in all the lanes which give the signal value according to band intensity. Signal values were used for quantitative analysis.

To compensate for any loading errors, band intensities of the targeted proteins [RIBEYE-A (SySy), RIBEYE-B (2D9), GFP] were normalized to the band signals of actin (housekeeping protein) in the same lane and average values were calculated. For quantification, $RBE^{WT/WT}$ western blot signals were set to 100% for RIBEYE-A (6F4) and RIBEYE-B band intensity, and $RBE^{WT/KI}$ and $RBE^{KI/KI}$ were compared with respective wildtype values. For quantification of GFP band signals, $RBE^{KI/KI}$ western blot signals were set to 100%, and $RBE^{WT/WT}$, $RBE^{WT/KI}$ were compared corresponding knock-in values. The average values were plotted in Microsoft Excel and their data distribution was plotted in Origin 2019b software.

The Pearson's correlation coefficient of all experimental incubations was calculated in Microsoft Excel. The correlation coefficient was high (Pearson's correlation coefficient ($r \geq 0.8$) between two groups therefore, according to De Winter, 2013 two sample Student's t-test for non-equal variance were performed to determine statistical significance.

3.2.7.3.4 Stripping and reprobing of immunoblot

After the first detection, the membrane was washed with PBS five times and submerged in preheated stripping buffer (110 μ l β -mercaptoethanol, 2% sodium dodecyl sulfate, 20 ml 0.1 M Tris-HCl, pH 8.5) at 55 °C for 30 min with occasional agitation manually. Then again washed with PBS and used for other primary antibodies incubation then secondary antibody as described above.

3.2.7.3.5 Determination of concentration of 6F4 (RIBEYE A-domain) monoclonal antibody

The concentration of IgG cut 6F4 RIBEYE A-domain monoclonal antibody was determined by running descending series of 10 μ l BSA standard (0.5, 0.25, 0.1, 0.05, 0.04, 0.03 mg/ml) and 6F4 antibody on 10% polyacrylamide gel at 100V, RT. After gel electrophoresis, gel was stained with Coomassie Brilliant R 250. Then gel was destained with the destaining solution to reduce the background for visualization of protein band.

3.2.8 Peptide arrays for epitope mapping of 6F4 (RIBEYE A-domain) monoclonal antibody

Peptide array screening is the approach for the analysis of the antibody binding site (epitope mapping). It is a fast, easy, and inexpensive approach. (Amartely et al., 2014; Hilpert et al., 2007). For peptide array process peptides are synthesized on cellulose membrane usually by 9fluorenylmethyloxycarbonyl (Fmoc) chemistry for protection of amino group in which hydroxyl group of cellulose esterified with a carboxyl group of Fmoc protected amino acid (Frank, 2002; Amartely et al., 2014; Hilpert et al., 2007). The peptide synthesis includes mainly the following steps: preparation of cellulose membrane, synthesis of overlapped peptides, and cleavage of the side chain protection group.

For peptide array screening of (6F4) RIBEYE A-domain monoclonal antibody, the peptide of RIBEYE A-domain covering amino terminus (amino acid 83-211) with a length of 20 amino acids each containing an overlap of 5 amino acids were synthesized on a cellulose membrane using ResPepSL-Synthesizer (Intavis Bioanalytical Instruments; Cologne, Germany) as previously described (Frank, 2002; Hilpert et al., 2007; Harsman et al., 2011).

For epitope mapping of 6F4 monoclonal antibody, the membrane with immobilized peptide was activated by incubating the membrane in methanol for 1 min at RT. The membrane was washed two times with H₂O and equilibrated with binding buffer (50 mM Tris-HCl, pH 7.5, 150 mM NaCl, 0.1% Triton X-100) for 2 hrs at RT with mild shaking. Then membrane was blocked for 1 hr at RT with a binding buffer containing 1 μ M bovine serum albumin to block unspecific protein binding. Afterward, membrane was incubated with 6F4 primary antibody (diluted 1:20,000 in binding buffer) overnight at 4°C. The next day, membrane was washed 3 times for 10 min each with binding buffer to remove the

MATERIALS AND METHODS

unbound antibody and probed the membrane with HRP-conjugated goat anti-mouse (diluted 1:10,000 in binding buffer) secondary antibody for 1 hr, RT. Then membrane was washed 3 x 10 min with binding buffer and visualized by chemiluminescence's detection solution ECL1 and ECL2 mixture (1:1 v/v), and the signals were documented. To visualize all the spots, membrane was illuminated by UV light with the ChemiDoc™ XRS Gel Doc system (Bio-Rad; Feldkirchen, Germany) apparatus.

3.2.8.1 Stripping of pepspot membrane

Pepspot membrane was washed 3 x 5 min with DMF (Dimethylformamide) in an ultrasonic bath then washed with water. Afterward, membrane was washed 4 x with buffer A in an ultrasonic bath for 5 min. Next, membrane was washed 3x with buffer B, and ethanol subsequently at RT on mild shaking. After that membrane was dried and stored at -20°C.

3.2.9 Statistical analysis

Statistical analyses were done using OriginPro 2019b software and GraphPad Prism 8.4.3. For all analyses, at least three independent experiments were performed for each experimental group, as indicated in the respective experiments.

First, I checked whether data could be pooled from individual experiments, for this purpose I checked normality using the Shapiro-Wilk test for the experimental group. According to the Shapiro-Wilk test result, for multiple comparisons, ANOVA with Bonferroni's post hoc tests was performed for normally distributed, and Kruskal- Wallis ANOVA test with Dunn's post hoc test was performed for non-normally distributed data (significance level 0.05). After this verification data were pooled when multiple comparisons within the same group were not significantly different. The mean values of the individual experiment were used when multiple comparisons within the same group were significantly different.

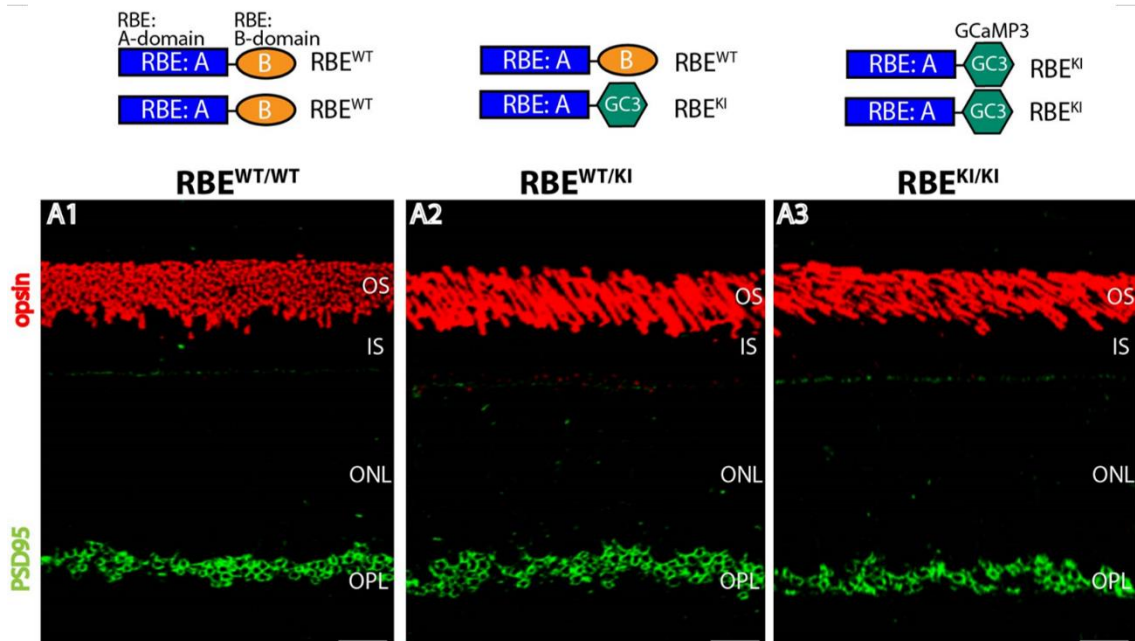
To check statistical significance between the two groups, the first normality was checked. When data of two groups were normally distributed, two sample Student's t-test was performed (with equal/non-equal variance) while Mann-Whitney U-test or Kolmogorov-Smirnov test was performed for non-normally distributed data. Online Mann-Whitney U-test was performed at (<https://astatsa.com/WilcoxonTest/>). The difference was considered statistically different with $p < 0.05$.

4. RESULTS

RIBEYE is a central building block of the synaptic ribbon (Schmitz et al., 2000; Maxeiner et al., 2016). Maxeiner et al., 2016 observed that deletion of RIBEYE A-domain abolished the formation of synaptic ribbons in the retina. The role of RIBEYE B-domain in the formation of ribbons remained to be elucidated. To answer this question, I made use of RIBEYE knock-in mice (Maxeiner et al., 2016). In RIBEYE knock-in (KI) mice RIBEYE B-domain was replaced by the cDNA of GCaMP3 so that RIBEYE knock-in mice consist of RIBEYE A-domain fused with Ca^{2+} sensor, GCaMP3 (Maxeiner et al., 2016). I first analyzed the overall organization of the retina in the RIBEYE knock-in mice.

4.1 RIBEYE deletion does not affect the overall organization of the retina

In the present study, I analyzed the RIBEYE KI mice in which RIBEYE B-domain is lacking. First, I checked whether the expression of the RIBEYE knock-in allele might alter the overall cellular organization of the retina. To check the consequence of RIBEYE B-domain deletion on the retina of $\text{RBE}^{\text{KI/KI}}$ mice in comparison to littermate control mice. I double immunolabeled retina semithin sections ($0.5 \mu\text{m}$) of all RIBEYE genotypes (wildtype: $\text{RBE}^{\text{WT/WT}}$, heterozygous knock-in $\text{RBE}^{\text{WT/KI}}$, and homozygous $\text{RBE}^{\text{KI/KI}}$) with following antibodies, including antibodies against opsin to label outer segments of rod photoreceptors (Figure 18A), PSD95 (Figure 18A) and SV2 (Figure 18B, C) to label photoreceptor synapse in the outer plexiform layer, calbindin (Figure 18B) to label horizontal cells, and GFAP (Figure 18C) to label Müller glial cells.



RESULTS

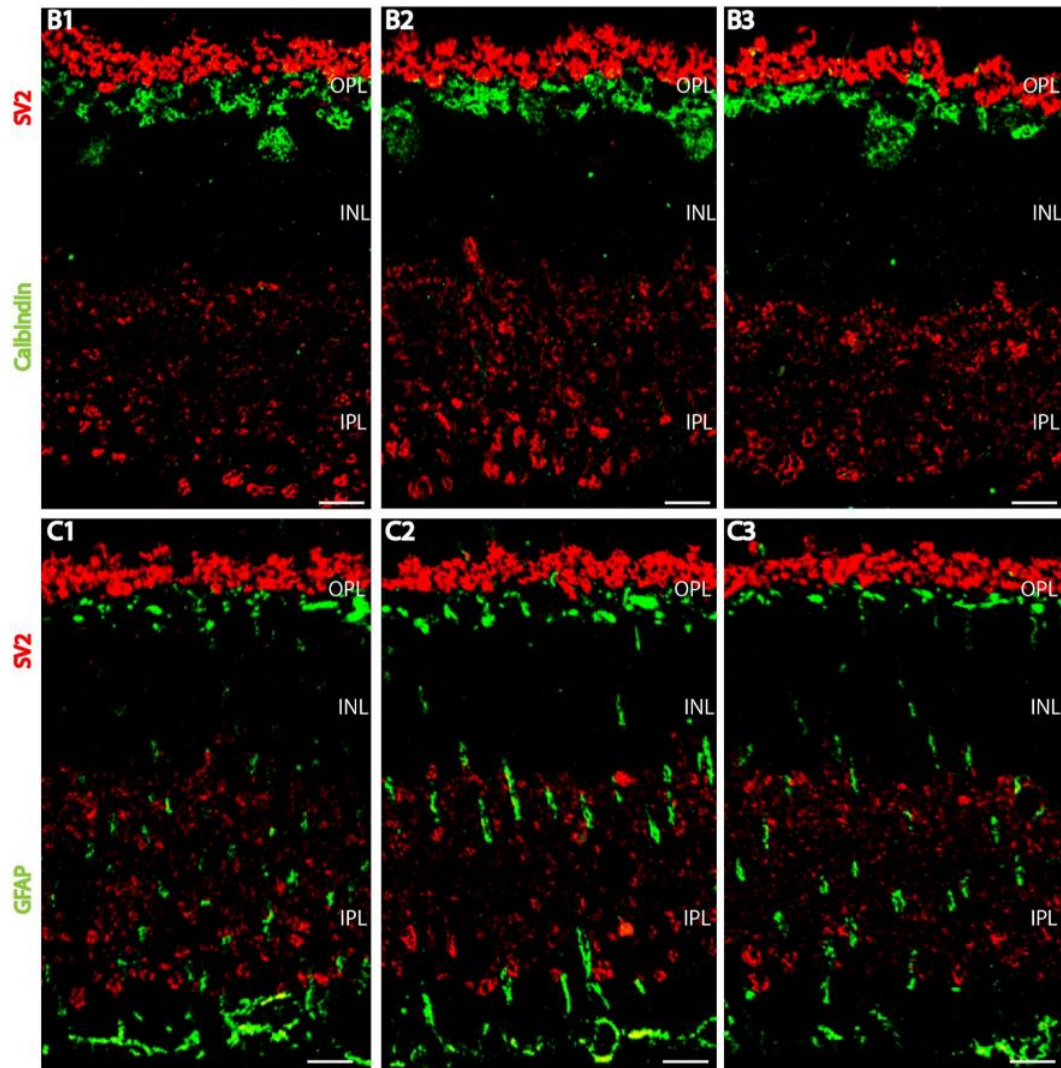


Figure 18. RIBEYE KI does not alter the organization of the retina

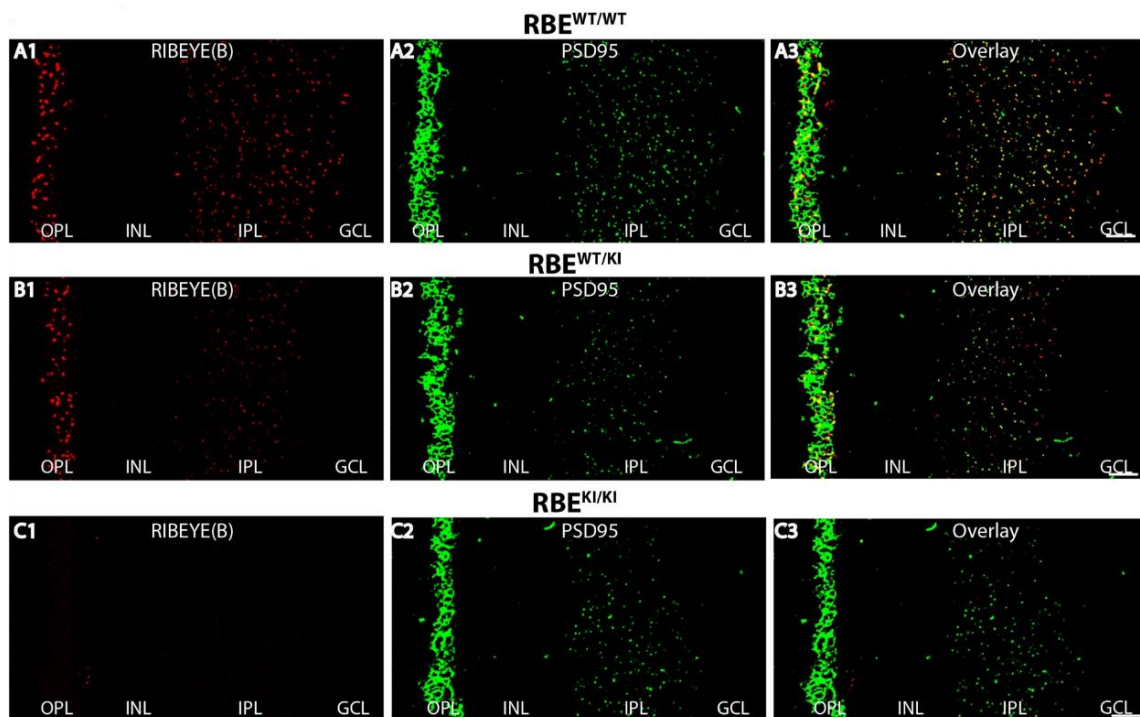
The top panel, schematic representation of analyzed all resulting genotypes ($RBE^{WT/WT}$, $RBE^{WT/KI}$, and $RBE^{KI/KI}$). (A) 0.5 μm retinal semi-thin sections of $RBE^{WT/WT}$, $RBE^{WT/KI}$, and $RBE^{KI/KI}$ mice double immunolabeled with antibodies against anti-rhodopsin (red, to label photoreceptor outer segments) and PSD95 (green, to label presynaptic photoreceptor terminals) in the OPL. (B) Retinal semithin sections of all genotypes double immunolabeled with antibodies against SV2 (red, to label synaptic vesicles) and calbindin (green, to label horizontal cells) in OPL. (C) Retinal semithin sections of all genotypes double immunolabeled with antibodies against SV2 (red, to label synaptic vesicles in OPL) and GFAP (green, to label Müller glial cells). Abbreviations OS, outer segments; IS, inner segments; ONL, outer nuclear layer; OPL, outer plexiform layer; INL, inner nuclear layer; IPL, inner plexiform layer; RBE, RIBEYE. Scale bar: 5 μm . Figure from Shankwar et al., 2022.

From the immunostaining with these protein markers of the retina, I did not observe any alterations in the organization of the retina of $RBE^{WT/WT}$, $RBE^{WT/KI}$, and $RBE^{KI/KI}$ mice. This confirms that RIBEYE knock-in allele does not affect the retinal organization. Likewise, RIBEYE knock-out mice retina in which RIBEYE protein was completely removed, did not show alterations in the retinal organization (Maxeiner et al., 2016).

RESULTS

4.2 RIBEYE B-domain immunosignals are absent in the photoreceptor synapses of RBE^{KI/KI} mice

Next, I examined the expression of RIBEYE B-domain in RIBEYE knock-in mice (Figure 19). For this purpose, I double immunolabeled 0.5 μm retinal semithin sections of different RIBEYE genotypes (wildtype: RBE^{WT/WT}; heterozygous knock-in: RBE^{WT/KI} and homozygous knock-in: RBE^{KI/KI}) with well characterized anti-RIBEYE B-domain monoclonal antibody (clone 2D9) (Dembla et al., 2018) and PSD95 antibody to label presynaptic photoreceptor terminal. From the confocal images of RBE^{WT/WT} and RBE^{WT/KI}, I observed punctate ribbon-like immunostaining of RIBEYE B-domain in both the outer plexiform layer (OPL) and inner plexiform layer (IPL) of the retina. RIBEYE B-domain immunosignals were completely absent in both synaptic layers, OPL and IPL of RBE^{KI/KI} mice retina (Figure 19 C). The absence of RIBEYE B-domain immunostaining was expected in RBE^{KI/KI} mice because RIBEYE B-domain was replaced by an unrelated Ca²⁺ sensor-GCaMP3. I observed strong RIBEYE B-domain immunosignals particularly in the OPL of RBE^{WT/WT} and RBE^{WT/KI} littermate mice because synaptic ribbons of rod photoreceptor synapses of the outer plexiform layer are larger than the IPL synaptic ribbon (Moser et al., 2020). Therefore, for quantitative analysis, I first focused on the OPL of the retina. Immunostaining of the presynaptic markers was identical in all genotypes, indicating that retinal synapses are unchanged in the RBE^{KI/KI} retina (Figure 19 A-C). In RIBEYE B-domain immunolabeled (Figure 19 E1) 0.5 μm resin sections of RBE^{WT/KI}, GCaMP3 moiety does not generate any direct fluorescence signals (Figure 19 E2).



Continued on next page.....

RESULTS

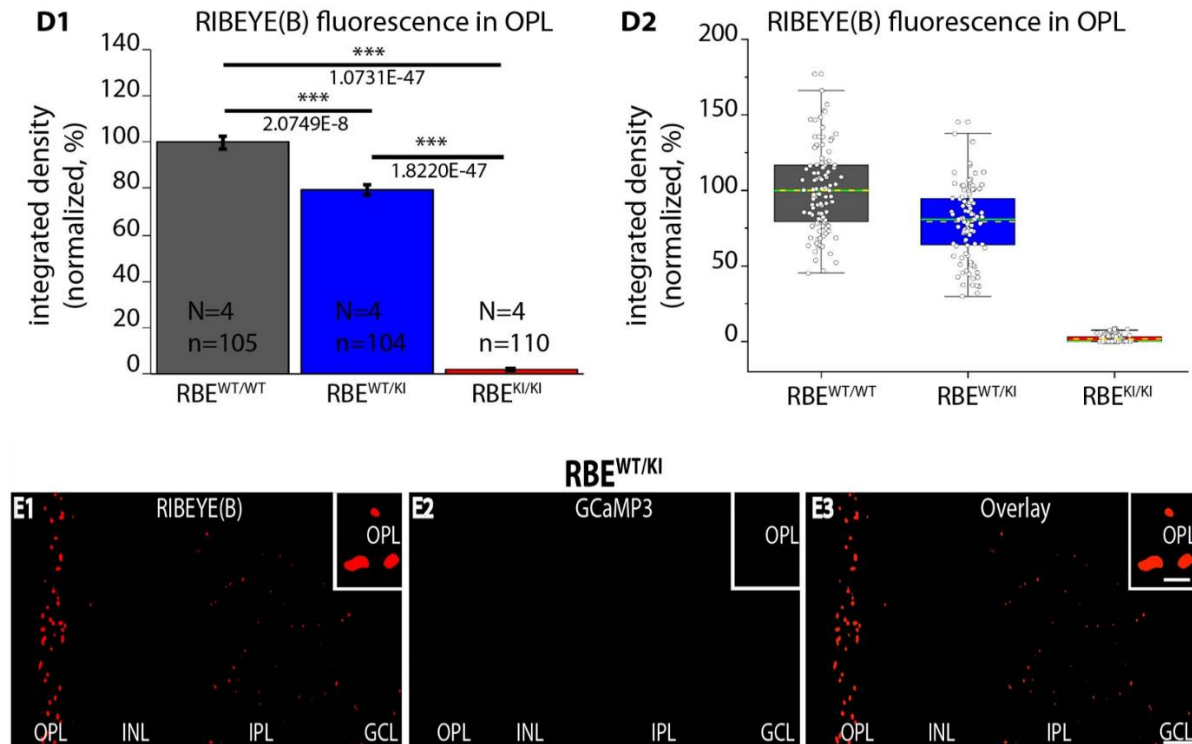


Figure 19. RIBEYE B-domain immunostaining is absent in the retinal semithin sections of RBE^{KI/KI} mice (A-C) Double immunostaining of retinal semi-thin sections (0.5 μ m) of RBE^{WT/WT}, RBE^{WT/KI}, and RBE^{KI/KI} mice with mouse monoclonal antibody (2D9) against RIBEYE B-domain (red) and rabbit polyclonal antibody against PSD95 to label postsynaptic body (green). (C1) Absence of RIBEYE B-domain immunosignals in both synaptic layers (OPL and IPL) in the retinal section of RBE^{KI/KI} mice. (D1) Quantification of RIBEYE B-domain average fluorescence integrated density in OPL, the bar graph represents mean \pm S.E.M (***) $P \leq 0.001$). In RBE^{WT/KI} RIBEYE B-domain immunosignals were significantly reduced than RBE^{WT/WT}. (D2) The Box and whisker plots of the data distribution from (D1), mean values, and median values are represented by yellow dotted line and solid green line respectively. The median represents the 50th percentile, the box represents the 25th -75th percentile, and whiskers represent 1.5 times of interquartile range. (E) Immunostaining of retinal semi-thin sections (0.5 μ m) of RBE^{WT/KI} mice with mouse monoclonal antibody (2D9) against RIBEYE B-domain (red). Inset shows high magnified synaptic ribbons. GCaMP3 direct immunosignals were absent in the green channel (E2) Abbreviations: OPL, outer plexiform layer; INL, inner nuclear layer; IPL, inner plexiform layer; GCL, ganglion cell layer; RBE, RIBEYE; S.E.M., standard error of the mean; N = number of mice; n = number of analyzed confocal images. Scale bar: 5 μ m. Figure from Shankhwar et al., 2022.

In the OPL, RIBEYE B-domain immunofluorescence signals were quantified as integrated density from 4 independent embeddings of RBE^{WT/WT}, RBE^{WT/KI}, and RBE^{KI/KI} mice (Figure 19D1, D2). Quantification showed that in the outer plexiform layer of RBE^{WT/KI} mice, RIBEYE B-domain immunosignals were weaker compared to littermate RBE^{WT/WT} and ~ 21% reduction was evident (p-value for RBE^{WT/WT} / RBE^{WT/KI} comparison: 2.0749E-8) (Students's t-test). RIBEYE B-domain immunosignals in the OPL were completely absent from RBE^{KI/KI} mice (p-value for RBE^{WT/WT} / RBE^{KI/KI} comparison: 1.0731E-47; for RBE^{WT/KI} / RBE^{KI/KI} comparison: 1.8220E-47) (Kolmogorov-Smirnov test) (Figure 19D1, D2).

RESULTS

4.3 RIBEYE B-domain puncta at high magnification in the OPL was unchanged between $RBE^{WT/WT}$ and $RBE^{WT/KI}$ and absent from $RBE^{KI/KI}$ mice

As mentioned, I observed weaker RIBEYE B-domain immunosignals in the retina of $RBE^{WT/KI}$ mice in comparison to littermate $RBE^{WT/WT}$ mice. To find the reason for this, I analyzed the puncta density of RIBEYE B-domain immunolabeled synaptic ribbons in the outer plexiform layer at higher magnification. I used 0.5 μm retina resin sections of $RBE^{WT/WT}$, $RBE^{WT/KI}$, and $RBE^{KI/KI}$ mice for clear identification of single puncta (Figure 20 A-C). The average RIBEYE B-domain positive puncta were quantified in 4 different embeddings.

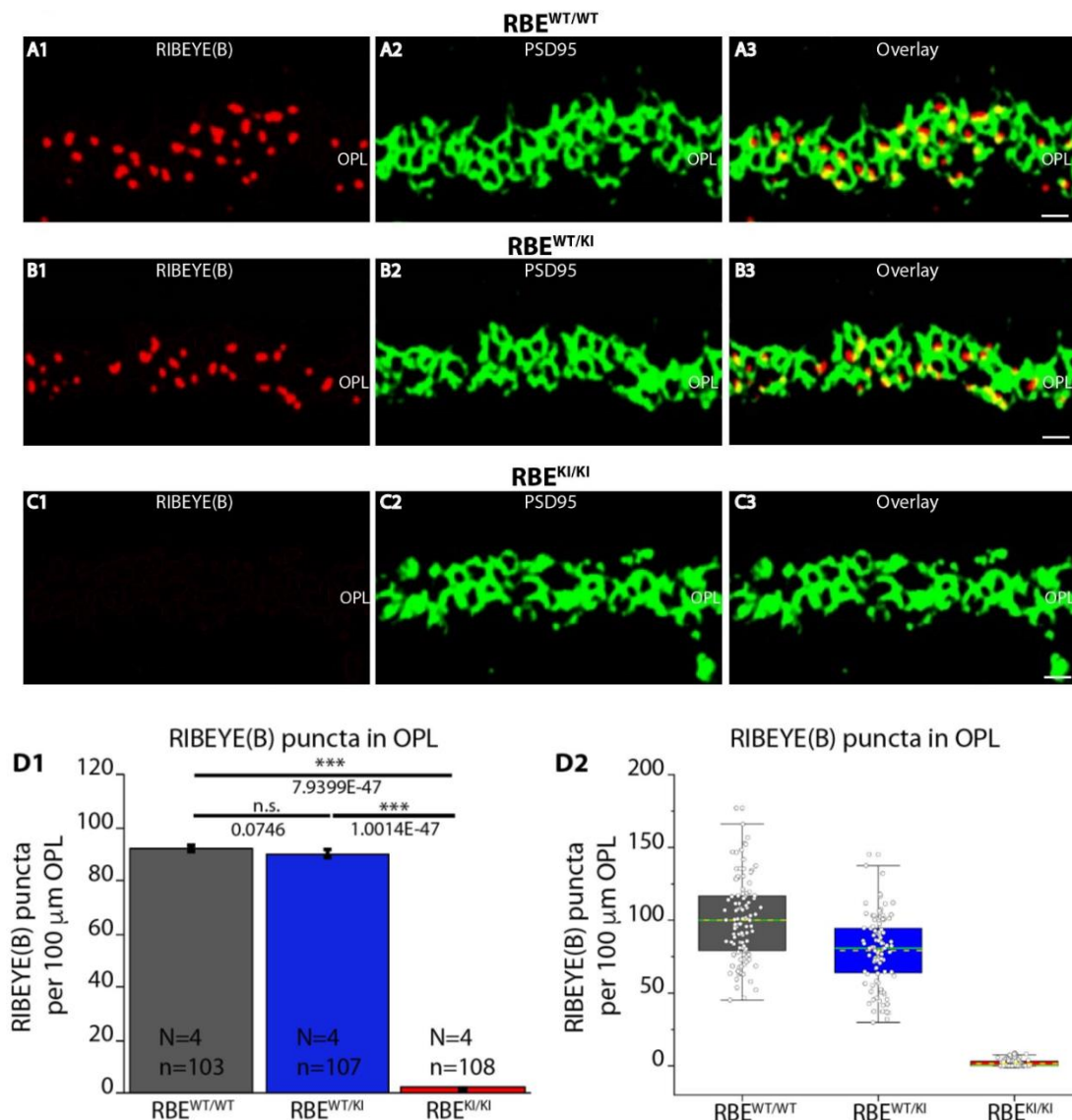


Figure 20. RIBEYE B-domain puncta in the OPL are unchanged between $RBE^{WT/WT}$ and $RBE^{WT/KI}$ (A-C) Double immunostaining of retinal semi-thin sections (0.5 μm) of $RBE^{WT/WT}$, $RBE^{WT/KI}$, and $RBE^{KI/KI}$ mice with mouse monoclonal antibody (2D9) against RIBEYE B-domain (red) and rabbit polyclonal antibody against PSD95 to label postsynaptic terminal of photoreceptor (green). (D1) Quantification of RIBEYE (B)

RESULTS

*puncta per 100 μm OPL showed puncta density is similar between $\text{RBE}^{\text{WT}/\text{WT}}$ and $\text{RBE}^{\text{WT}/\text{KI}}$ but completely absent in the OPL of $\text{RBE}^{\text{KI}/\text{KI}}$ mice. The bar graph represents mean \pm S.E.M (n.s. $P > 0.05$, *** $P \leq 0.001$). (D2) The Box and whisker plots of the data distribution from (D1), means values are represented by yellow dotted line and median values by green solid line. The median represents the 50th percentile, the box represents the 25th -75th percentile, and whiskers represent 1.5 times of interquartile range. Abbreviations: OPL, outer plexiform layer; RBE, RIBEYE; S.E.M., standard error of the mean; n.s. non-significant; N = number of mice; n = number of analyzed confocal images. Scale bar: 5 μm . Figure from Shankhwar et al., 2022.*

Interestingly, I found that the number of RIBEYE B-domain positive puncta in the outer plexiform layer were identical between $\text{RBE}^{\text{WT}/\text{WT}}$ and heterozygous $\text{RBE}^{\text{WT}/\text{KI}}$ mice (p-value for $\text{RBE}^{\text{WT}/\text{WT}}$ / $\text{RBE}^{\text{WT}/\text{KI}}$ comparison: 0.0746) (Mann-Whitney U-test). (Figure 20D1, D2). Whereas RIBEYE B-domain puncta were entirely absent from the OPL of $\text{RBE}^{\text{KI}/\text{KI}}$ mice (p-value for $\text{RBE}^{\text{WT}/\text{WT}}$ / $\text{RBE}^{\text{KI}/\text{KI}}$ comparison: 7.9399E-47; for $\text{RBE}^{\text{WT}/\text{KI}}$ / $\text{RBE}^{\text{KI}/\text{KI}}$ comparison: 1.0014E-47) (Kolmogorov-Smirnov test) as expected (Figure 20D1, D2).

4.4 RIBEYE A-domain immunosignals are absent in the photoreceptor synapse of $\text{RBE}^{\text{KI}/\text{KI}}$ mice

Next, I wanted to check whether the RIBEYE A-domain can still assemble into ribbons in the absence of the RIBEYE B-domain in RIBEYE knock-in mice. To verify this, I double immunolabeled 0.5 μm retinal semithin sections of $\text{RBE}^{\text{WT}/\text{WT}}$; $\text{RBE}^{\text{WT}/\text{KI}}$, and $\text{RBE}^{\text{KI}/\text{KI}}$ mice with a well-characterized polyclonal antibody against RIBEYE A-domain (Tau) (Maxeiner et al., 2016) to label synaptic ribbons and SV2 to label synaptic vesicles (Figure 21). As stated above, in RIBEYE knock-in mice RIBEYE A-domain is well present in contrast to RIBEYE B-domain that was replaced by GCaMP3.

Therefore, to visualize the synaptic ribbons in the retina I performed confocal microscopy. From the confocal imaging of $\text{RBE}^{\text{WT}/\text{WT}}$ and $\text{RBE}^{\text{WT}/\text{KI}}$ mice, I observed punctate ribbon like immunostaining of RIBEYE A-domain in both OPL and IPL of the retina (Figure 21 A-C). Surprisingly, immunostaining of RIBEYE A-domain was completely absent in both OPL and IPL of the $\text{RBE}^{\text{KI}/\text{KI}}$ mice retina (Figure 21 C). Immunostaining of anti-SV2 antibody in the OPL and IPL was similar in retina sections of all genotypes revealed that $\text{RBE}^{\text{KI}/\text{KI}}$ allele does not globally compromise ribbon synapses (Figure 21).

RIBEYE A-domain immunofluorescence signals in the OPL were quantified as integrated density from 3 different embeddings of $\text{RBE}^{\text{WT}/\text{WT}}$, $\text{RBE}^{\text{WT}/\text{KI}}$, and $\text{RBE}^{\text{KI}/\text{KI}}$ mice (Figure 21D1, D2). RIBEYE A-domain fluorescence signals were quantified as average integrated density. Quantification showed that RIBEYE A-domain immunosignals in the OPL were weaker in heterozygous $\text{RBE}^{\text{WT}/\text{KI}}$ mice compared to littermate wildtype $\text{RBE}^{\text{WT}/\text{WT}}$. In the outer plexiform layer, where photoreceptor synapses are located ~ 19% reduction in RIBEYE A-domain integrated density was observed in $\text{RBE}^{\text{WT}/\text{KI}}$ (p-value $\text{RBE}^{\text{WT}/\text{WT}}$ / $\text{RBE}^{\text{WT}/\text{KI}}$ comparison: 3.5333E-7) (Mann-Whitney U-test) when compared with $\text{RBE}^{\text{WT}/\text{WT}}$ mice. RIBEYE A-domain immunosignals were completely lacking in the OPL of $\text{RBE}^{\text{KI}/\text{KI}}$ mice (p-value for

RESULTS

$RBE^{WT/WT} / RBE^{KI/KI}$ comparison: $4.4408E-16$; for $RBE^{WT/KI} / RBE^{KI/KI}$ comparison: $13.7651E-54$) (Kolmogorov-Smirnov test and Mann-Whitney U-test respectively) (Figure 21D1, D2).

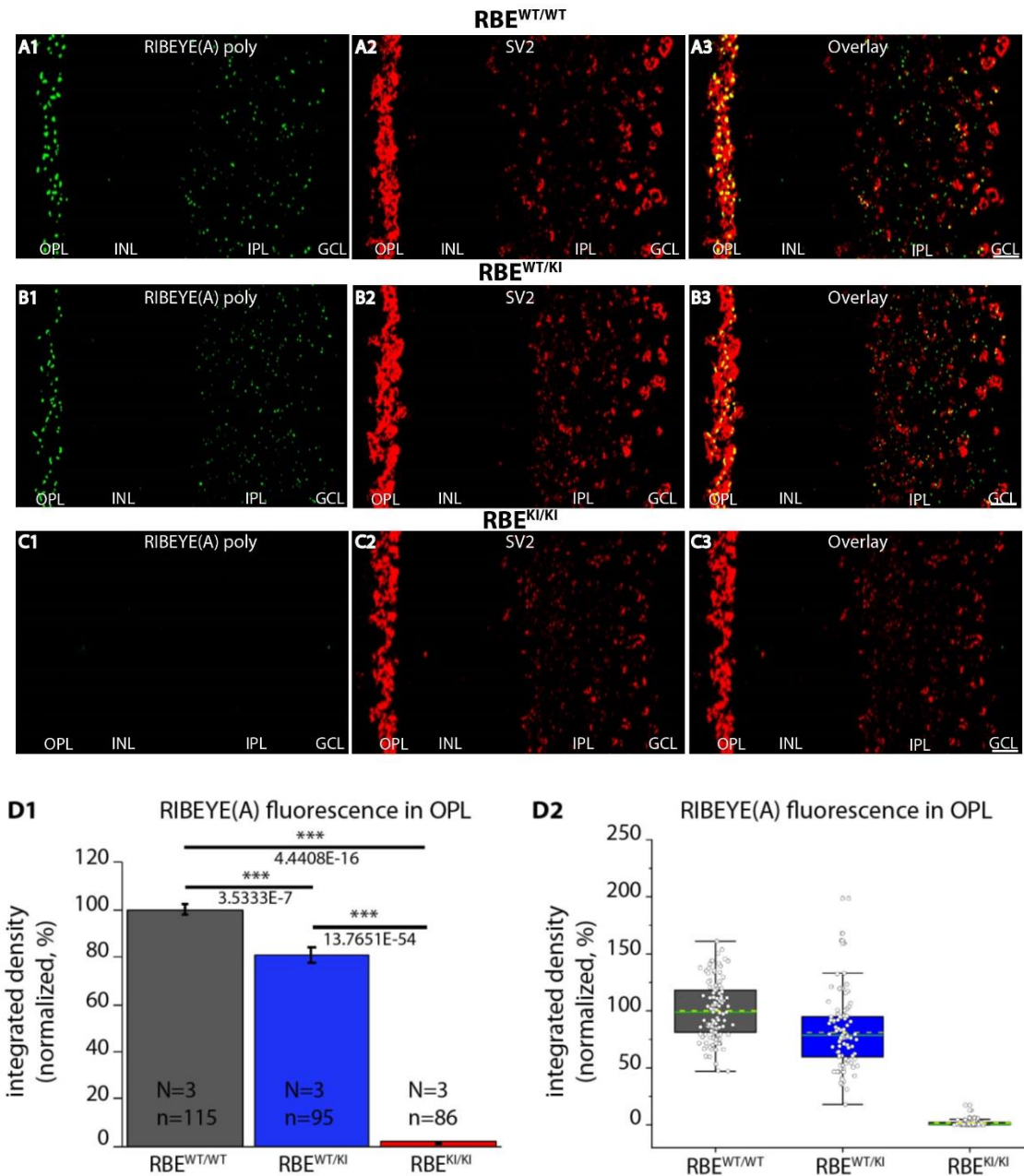


Figure 21. RIBEYE A-domain immunostaining is absent in the retina of $RBE^{KI/KI}$

(A-C) Double immunostaining of ($0.5 \mu\text{m}$) retinal semi-thin sections of $RBE^{WT/WT}$, $RBE^{WT/KI}$, and $RBE^{KI/KI}$ mice with mouse monoclonal antibody against SV2 (red, to label synaptic vesicles) and rabbit polyclonal antibody against Tau, Maxeiner et al., 2016 (green, to label RIBEYE A-domain synaptic ribbon). (C1) Absence of RIBEYE A-domain labeling in the retinal section of $RBE^{KI/KI}$ mice. (D1) Quantification of RIBEYE A-domain average integrated density in OPL, the bar graph represents mean \pm S.E.M ($***P \leq 0.001$). In $RBE^{WT/KI}$ RIBEYE A-domain immunosignals were significantly reduced than $RBE^{WT/WT}$. (D2) The Box and whisker plots of the data distribution from D1, mean values are represented by yellow dotted line and median values by green solid line. The median represents the 50th percentile, the box represents the 25th -75th percentile, and whiskers

RESULTS

represent 1.5 times of interquartile range. Abbreviations: OPL, outer plexiform layer; INL, inner nuclear layer; IPL, inner plexiform layer; GCL, ganglion cell layer; RBE, RIBEYE; S.E.M., standard error of the mean; N = number of mice; n = number of analyzed confocal images. Scale bar: 5 μ m. Figure from Shankhwar et al., 2022.

4.5 Corroboration of the absence of RIBEYE A-domain immunolabeling in RBE^{KI/KI} retina using novel mouse monoclonal antibody against RIBEYE A-domain (6F4)

Next, I verified the result which is obtained with the RIBEYE A-domain polyclonal antibody (Figure 21 A-C) using novel RIBEYE A-domain monoclonal antibody, clone 6F4 (Figure 22). For that retinal semithin sections of RBE^{WT/WT}, RBE^{WT/KI}, and RBE^{KI/KI} mice were double immunostained with 6F4 monoclonal antibody to label synaptic ribbons and PSD95 to label ribbon synapses. The immunostaining of synaptic ribbons with 6F4 RIBEYE A-domain antibody in RBE^{WT/WT}, and RBE^{WT/KI} retina sections was similar to the RIBEYE A-domain polyclonal antibody (Figure 22A1-B3). In contrast, no ribbon typical staining was observed in the OPL and IPL of RBE^{KI/KI} sections, which confirms the absence of synaptic ribbons as confirmed in the above experiments by RIBEYE A-domain polyclonal antibody (Tau) (Figure 22 C1).

The novel RIBEYE A-domain mouse monoclonal antibody 6F4 was directed against the peptide stretch in RIBEYE A-domain (aa 83- aa211). The specific binding site of the 6F4 antibody was determined by overlapping peptide array dot blot. The dot blot result showed that this antibody was raised against peptide spots #15 and #16 (Figure 22 F). The positive peptide spots were highlighted red in Figure 22F3. To further verify the specificity of the 6F4 monoclonal antibody, I performed western blotting (Figure 22D, E) and immunolabeling experiments (Figure 22G, H) on retina samples of RIBEYE heterozygous knock-out RBE^{WT/KO}, and homozygous knock-out RBE^{KO/KO} mice in which RIBEYE A-domain was completely removed (Maxeiner et al., 2016).

For western blotting RIBEYE A-domain 6F4 (Figure 22 D1) and RIBEYE B-domain 2D9 antibodies (Figure 22 E1) were used to check the expression of RIBEYE protein. Both antibodies detect full length RIBEYE protein ~ 120 kDa in retina lysates of RBE^{WT/KO}. But retina lysates of RBE^{KO/KO} do not detect the RIBEYE band as expected because it is lacking RIBEYE A-domain. The expression of CtBP2 does not affect by the deletion of RIBEYE A-domain in RBE^{KO/KO} mice (Figure 22 E1). Actin antibody was used as loading control for retina lysates which gives band ~ 43 kDa. The expression of actin was similar in both control and knock-out (Figure 22D2, E2). From the immunolabeling experiments, I found that a ribbon like immunostaining pattern was clearly present in RBE^{WT/KO} retina sections (Figure 22 G1) but absent from the RBE^{KO/KO} samples (Figure 22 H1). Ribbon synapses labeled with PSD95 were unaltered in both control and knock-out (Figure 22 G-H).

RESULTS

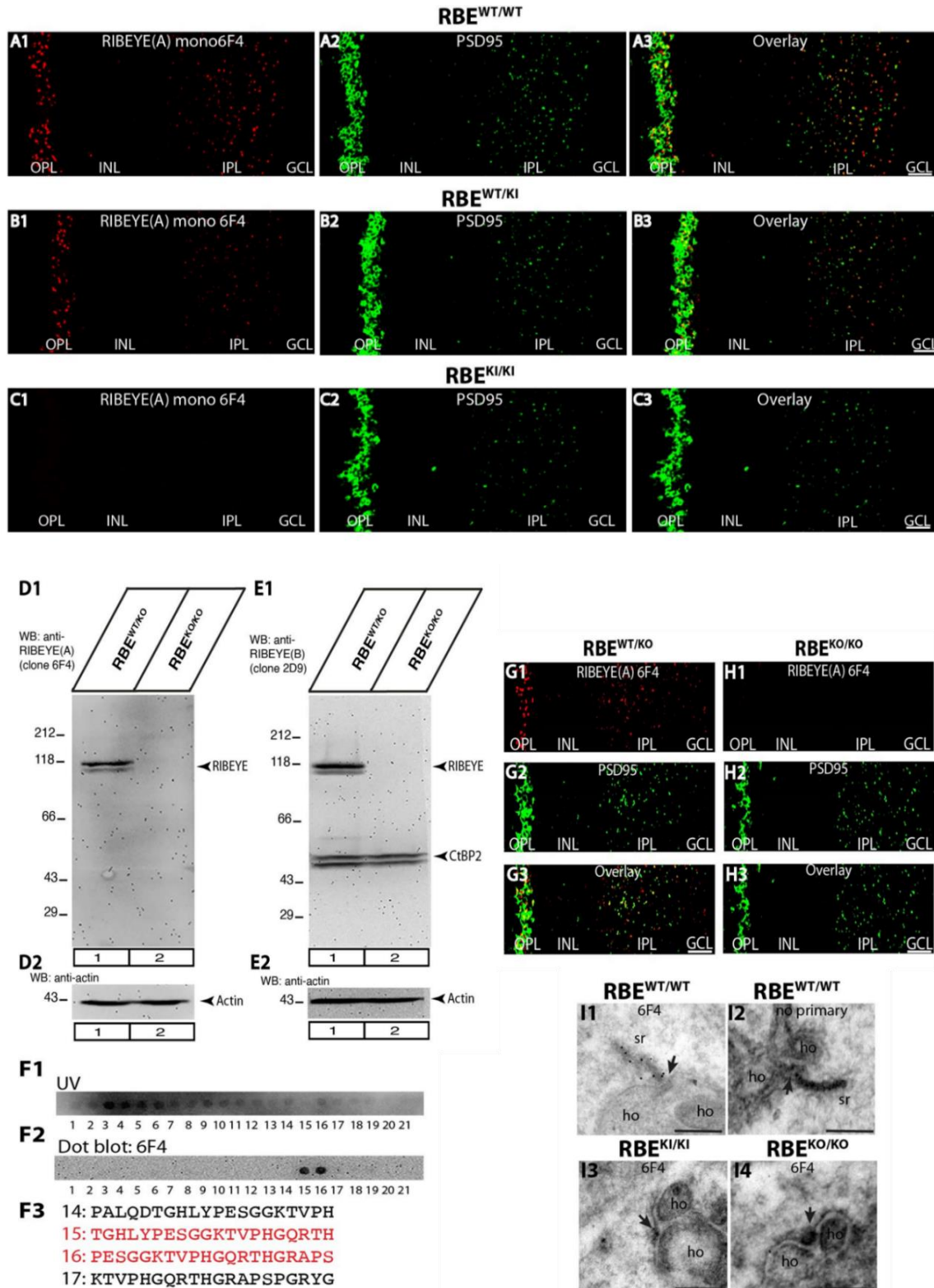


Figure 22. Verification of absence of RIBEYE A-domain immunoreactivity in $RBE^{KI/KI}$ retina, using novel mouse monoclonal antibody (6F4) against RIBEYE A-domain

(A-C) Double immunostaining of (0.5 μ m) retinal semi-thin sections of $RBE^{WT/WT}$, $RBE^{WT/KI}$, and $RBE^{KI/KI}$ mice with mouse monoclonal antibody (6F4) against RIBEYE A-domain (red) to label synaptic ribbon and rabbit polyclonal antibody against PSD95 to label postsynaptic terminal of photoreceptor (green). (C1) RIBEYE A-

RESULTS

domain immunoreactive signals were utterly absent in both synaptic layers (OPL and IPL) of $RBE^{KI/KI}$ mice. (D) Western blot of retinal lysates from $RBE^{WT/KO}$ and $RBE^{KO/KO}$ were probed with 6F4 mouse monoclonal antibody against RIBEYE A-domain and anti-actin antibody. (E) Western blot of retinal lysates from $RBE^{WT/KO}$ and $RBE^{KO/KO}$ were probed with 2D9 mouse monoclonal antibody against RIBEYE B-domain for comparison and anti-actin antibody as a loading control. (F1, F2) Cellulose membrane that contains synthetic overlapped peptide of RIBEYE A-domain fusion protein against which 6F4 antibody was generated. The membrane was probed with 6F4 monoclonal antibody for epitope mapping of 6F4 RIBEYE A-domain monoclonal antibody. (F1) UV transilluminated image of peptide spot membrane for visualization of all peptide spots. (F2) Immunodetection of peptide probed with anti-RIBEYE A-domain 6F4 antibody using enhanced chemiluminescence (spot numbers: #15 and #16). (F3) Overlapping peptide sequence of reactive peptide spots (spot: #15 and #16) displayed in red color. (G-H) Double immunostaining of (0.5 μ m) retinal semi-thin sections of $RBE^{WT/KO}$ and $RBE^{KO/KO}$ with anti-RIBEYE A-domain 6F4 antibody and anti-PSD95. (G1) 6F4 immunolabeled synaptic ribbons were present in the OPL and IPL of $RBE^{WT/KO}$ (H1) but not in the $RBE^{KO/KO}$ similar to rabbit polyclonal antibody, Tau. (I) Post embedding immunogold labeling of synaptic ribbon detected with goat anti-mouse conjugated 10 nm gold nanoparticles in rod photoreceptor synapses of (I1) $RBE^{WT/WT}$ but absent from the rod photoreceptor synapses of (I3) $RBE^{KI/KI}$, and (I4) $RBE^{KO/KO}$ retina. (I2) wildtype negative control, no primary antibody. Arrow represents the active zone where the synaptic ribbon is anchored. Abbreviations: OPL, outer plexiform layer; INL, inner nuclear layer; IPL, inner plexiform layer; GCL, ganglion cell layer; RBE, RIBEYE; sr, synaptic ribbons; ho, horizontal cells; Scale bar: 5 μ m (A-C, G-H); 300 nm (I). Figure from Shankhwar et al., 2022.

The uniqueness of the 6F4 monoclonal antibody was further confirmed by post embedding immunogold labeling of $RBE^{WT/WT}$, $RBE^{KI/KI}$, and $RBE^{KO/KO}$ ultrathin sections. This antibody labels synaptic ribbon in rod photoreceptor control mice retina (Figure 22 I1.), but synaptic ribbon immunogold labeling was clearly absent from the rod photoreceptor synapses of both RIBEYE knock-in (Figure 22 I3) and RIBEYE knock-out mice (Figure 22 I4). Negative control did not show any labeling (I2). These results confirm the specificity of 6F4 monoclonal antibody against RIBEYE A-domain.

4.6 RIBEYE A-domain puncta at high magnification in the OPL was unchanged between $RBE^{WT/WT}$ and $RBE^{WT/KI}$ and absent from $RBE^{KI/KI}$ mice

As I observed a decrease in RIBEYE A-domain fluorescent integrated intensity of $RBE^{WT/KI}$ retina sections in comparison to $RBE^{WT/WT}$. To further corroborate these findings, I determined RIBEYE A-domain puncta densities in the outer plexiform layer of $RBE^{WT/WT}$, $RBE^{WT/KI}$, and $RBE^{KI/KI}$ mice using RIBEYE A-domain immunolabeled 0.5 μ m retinal semithin sections at higher magnifications (Figure 23 A-C, E) as described above for RIBEYE B-domain.

From the quantification, I found that RIBEYE A-domain puncta were indistinguishable between $RBE^{WT/WT}$, and $RBE^{WT/KI}$ (Figure 23D), and there was no significant difference between them (p-value for $RBE^{WT/WT}$ / $RBE^{WT/KI}$ comparison: 0.0725) (Student's t-test). In contrast, RIBEYE A-domain immunostained puncta were completely absent from the outer plexiform layer of $RBE^{KI/KI}$ mice (p-value for $RBE^{WT/WT}$ / $RBE^{KI/KI}$ comparison: 5.5511E-16; for $RBE^{WT/KI}$ / $RBE^{KI/KI}$ comparison: 7.7715E-16) (Kolmogorov-Smirnov test) (Figure 23D1, D2). Immunolabeling result of RIBEYE A-domain

RESULTS

polyclonal antibody (Tau) was further confirmed by immunolabeling of retinal semithin sections with 6F4 RIBEYE A-domain monoclonal antibody (Figure 23 E) that also show the absence of RIBEYE A-domain puncta in the OPL of $RBE^{KI/KI}$ mice.

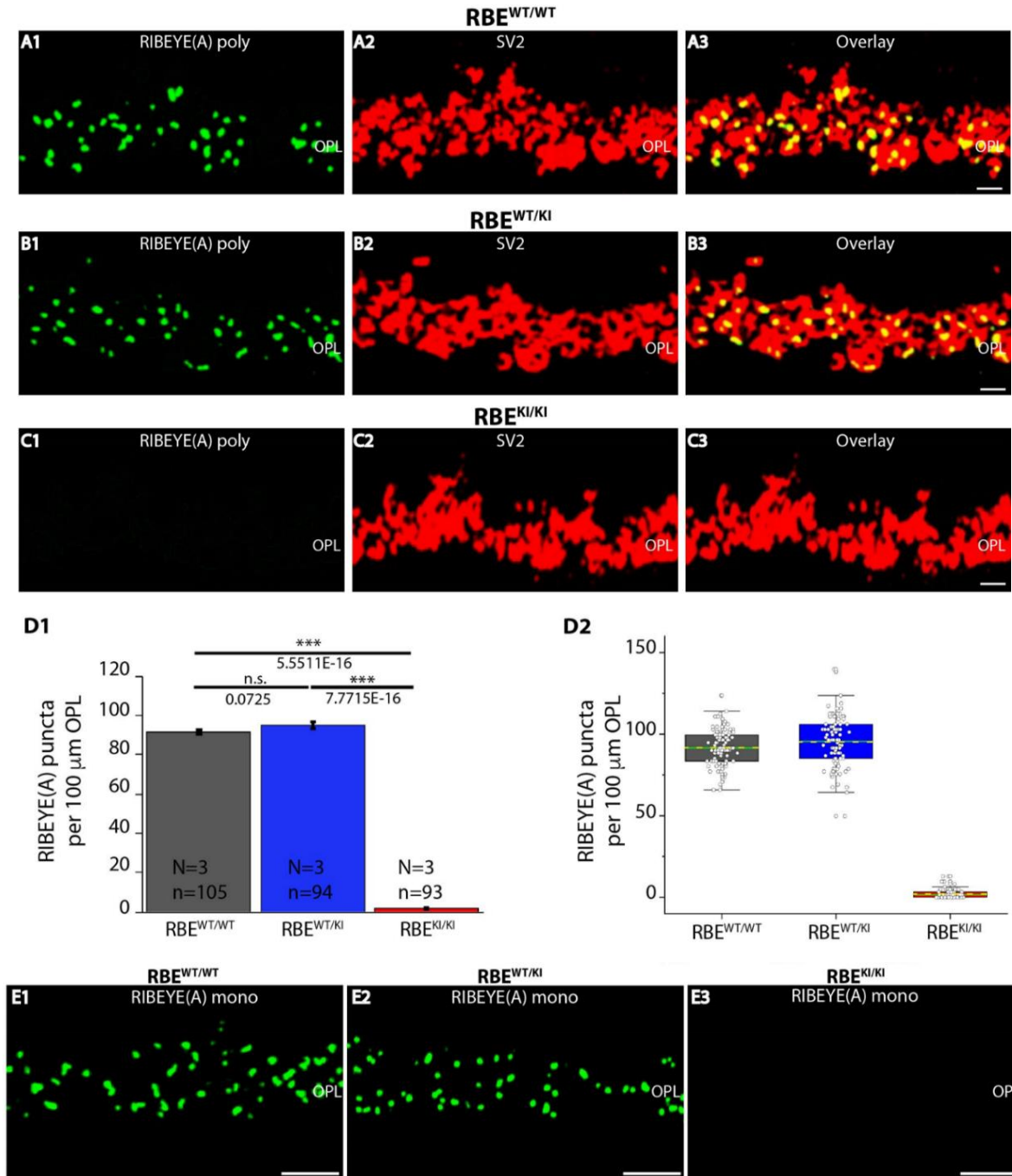


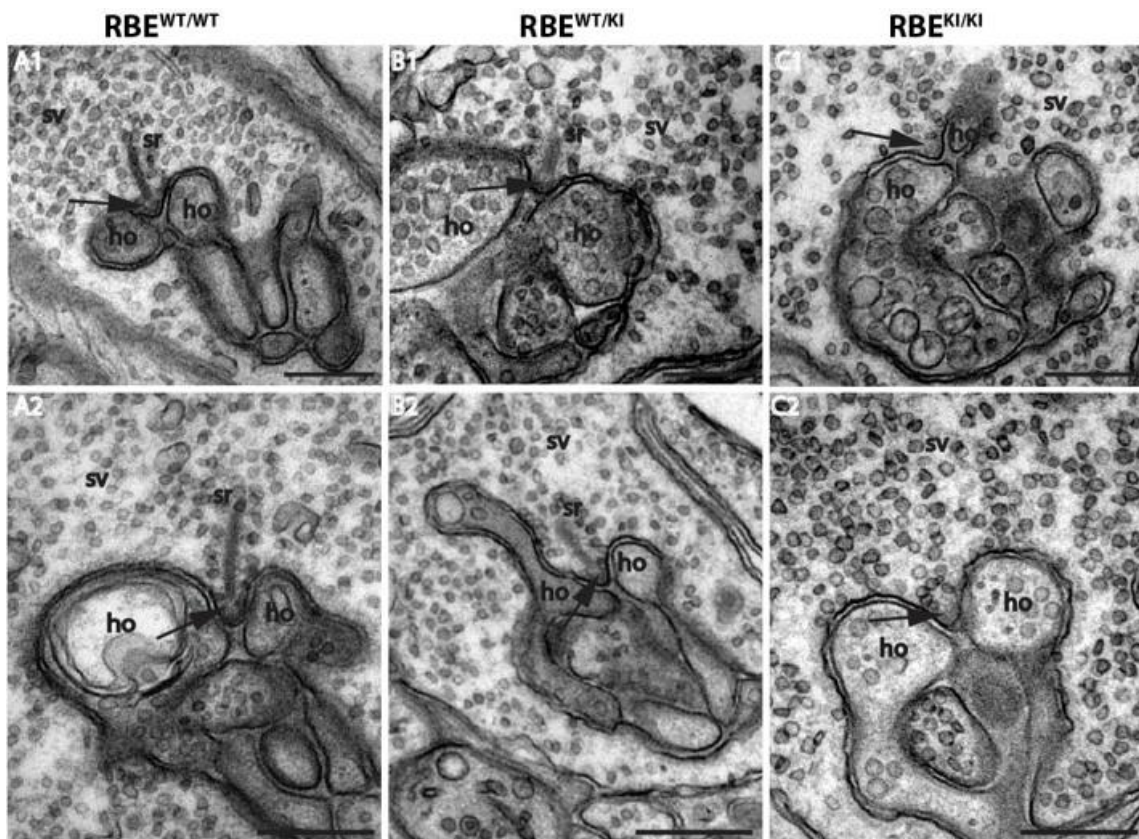
Figure 23. RIBEYE A-domain puncta in the OPL are unchanged between $RBE^{WT/WT}$ and $RBE^{WT/KI}$
 (A-C) Double immunostaining of (0.5 μm) retinal semi-thin sections of $RBE^{WT/WT}$, $RBE^{WT/KI}$, and $RBE^{KI/KI}$ with mouse monoclonal antibody SV2 (red, to label synaptic vesicles) and rabbit polyclonal antibody Tau (green, to label RIBEYE A-domain synaptic ribbon). (D1) Quantification of RIBEYE A-domain puncta per 100 μm OPL showed RIBEYE A-domain puncta density is similar between $RBE^{WT/WT}$, $RBE^{WT/KI}$ mice but completely absent

RESULTS

from the OPL of $RBE^{KI/KI}$ mice. The bar graph represents mean \pm S.E.M (n.s. $P > 0.05$, *** $P \leq 0.001$). (D2) The Box and whisker plots of the data distribution from (D1), means values, and median values are represented by yellow dotted line and green solid line respectively. The median represents the 50th percentile, the box represents the 25th -75th percentile, and whiskers represent 1.5 times of interquartile range. (E) Single immunolabeling of (0.5 μ m) retina semithin sections of $RBE^{WT/WT}$, $RBE^{WT/KI}$, and $RBE^{KI/KI}$ mice with anti-RIBEYE-A domain, 6F4 antibody. Abbreviations: OPL, outer plexiform layer; RBE, RIBEYE; S.E.M., standard error of the mean; n.s. non-significant; N = number of mice; n = number of analyzed confocal images. Scale bar: 5 μ m. Figure from Shankwar et al., 2022.

4.7 Synaptic ribbon is absent from the ultrastructural rod photoreceptor synapse of $RBE^{KI/KI}$

The immunolabeling results consistently show the complete absence of RIBEYE A- and RIBEYE B-domain immunolabeled puncta (Figure 19, 20 & Figure 21, 23) in the photoreceptor synapses of $RBE^{KI/KI}$ mice. To further corroborate these findings, I performed ultrastructural analyses of rod photoreceptor synapses in OPL by transmission electron microscopy. For this purpose, I used the retinal ultrathin section obtained from the retina of $RBE^{WT/WT}$, $RBE^{WT/KI}$, and $RBE^{KI/KI}$ littermate mice.



Continued on next page.....

RESULTS

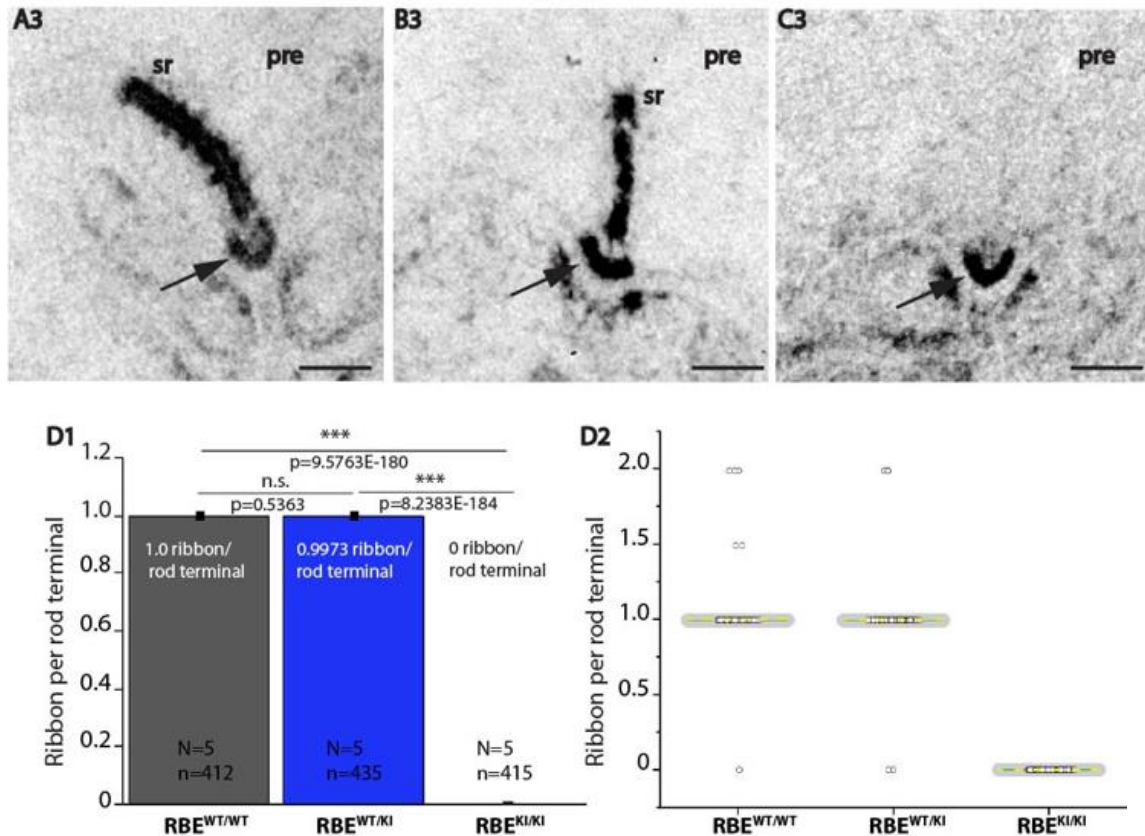


Figure 24. RIBEYE knock-in causes loss of synaptic ribbons at the active zone of rod photoreceptor terminal determined by transmission electron microscopy

(A-C) Representative ultra-structure images of rod photoreceptor terminal of RBE^{WT/WT}, RBE^{WT/KI}, and RBE^{KI/KI} mice. (C1, C2, C3) Demonstrate the absence of ribbon in presynaptic terminal of rod photoreceptor synapses of RBE^{KI/KI} mice but ultrastructure is comparable with control. Arrows indicate an active zone where synaptic ribbon is anchored. (A1, A2, B1, B2, C1, C2) Conventional TEM images, and (A3, B3, C3) E-PTA images of rod photoreceptor synapses of RBE^{WT/WT}, RBE^{WT/KI}, and RBE^{KI/KI} mice. (D1) Quantification of ribbon per rod terminal (mean \pm S.E.M, n.s. $P > 0.05$, *** $P \leq 0.001$). (D2) The Box and whisker of the data from D1, mean values, and median values are represented by yellow dotted line and green solid line respectively. The median represents the 50th percentile, the box represents the 25th -75th percentile, and whiskers represent 1.5 times of interquartile range. Abbreviations: sr, synaptic ribbon; ho, horizontal cells; SV, synaptic vesicles; pre, presynaptic; RBE, RIBEYE; S.E.M., standard error of the mean; n.s. non-significant; N = number of mice, n = number of analyzed images. Scale bar 200 nm. Figure from Shankhwar et al., 2022.

From the ultrastructural examination, as expected, I found that synaptic ribbons were evidently present in the rod photoreceptor synapses of RBE^{WT/WT} (Figure 24 A1, A2) and RBE^{WT/KI} (Figure 24 B1, B2). In contrast, synaptic ribbons were entirely absent from the active zone as well as from the presynaptic cytosol (no floating ribbon) (Regus-Leidig et al., 2014; Müller et al., 2019; Li et al., 2021) of rod photoreceptor synapses in RBE^{KI/KI} retina (Figure 24 C1, C2).

These results were also confirmed by the ultrastructural analysis of E-PTA stained retina samples. E-PTA stained synaptic ribbons were clearly present at the active zone (arrows) of rod photoreceptor

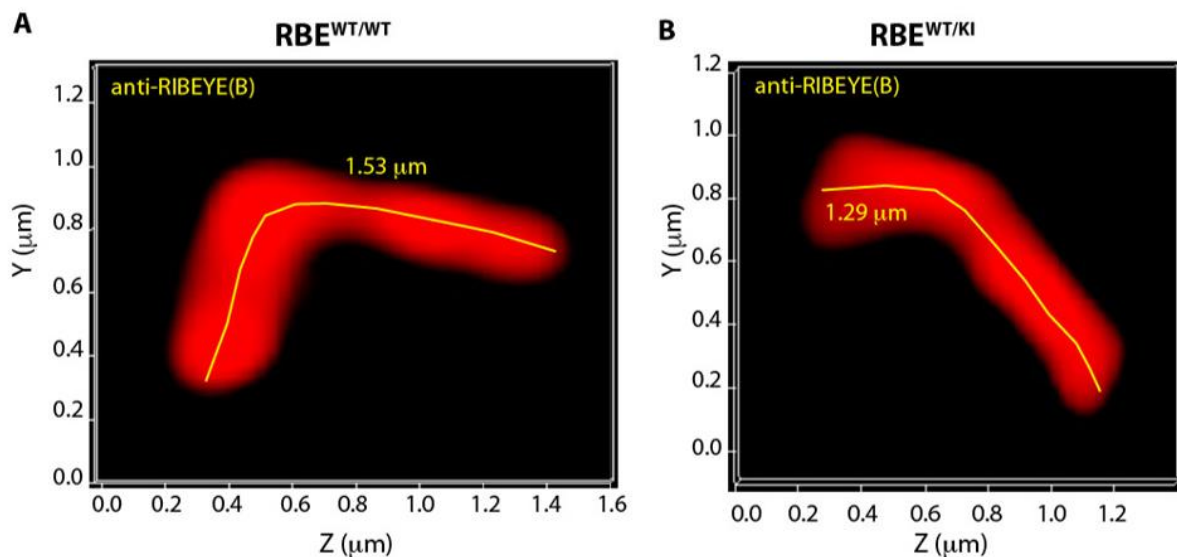
RESULTS

synapse in RBE^{WT/WT} (Figure 24 A3) and RBE^{WT/KI} (Figure 24 B3) but absent from the active zone of RBE^{KI/KI} mice (Figure 24 C3). Analysis from the 5 different embedding reveals that the ribbon per rod terminal (approximately 1 ribbon per terminal) was approximately similar between RBE^{WT/WT} and RBE^{WT/KI} mice (p-value for RBE^{WT/WT} / RBE^{WT/KI} comparison: 0.5363) (Mann-Whitney U-test) (Figure 24D1, D2).

In randomly analyzed 415 rod photoreceptor terminals, I did not find a single ribbon in RIBEYE knock-in retina (p-value for RBE^{WT/WT} / RBE^{KI/KI} comparison: 9.5763E-180; RBE^{WT/KI} / RBE^{KI/KI} comparison: 8.2383E-184) (Kolmogorov-Smirnov test) (Figure 24D1, D2). The ultrastructure of rod synapses (cytosolic vesicles and postsynaptic triad) of RIBEYE knock-in was comparable with control. These results confirm that RIBEYE B-domain is necessary for the formation of synaptic ribbons in photoreceptor synapses.

4.8 Length of synaptic ribbons immunostained with RIBEYE B-domain antibody is shorter in RBE^{WT/KI} retina (3D SR-SIM analyses)

As shown above, immunostaining of RIBEYE A- and RIBEYE B-domain in the outer plexiform layer were consistently weaker in RBE^{WT/KI} (Figure 19, 21) while ribbon density was similar (RIBEYE puncta) in the OPL (Figure 20, 23). To find the reason behind it I measured the contour length of individual rod synaptic ribbon in the OPL by 3D SR-SIM microscopy. The 1.5 μm thin Epon resin sections of RBE^{WT/WT} and RBE^{WT/KI} mice were immunolabeled with RIBEYE B-domain (2D9) monoclonal antibody and z-stack images were taken through 3D SR-SIM microscopy (Figure 25A, B).



Continued on next page.....

RESULTS

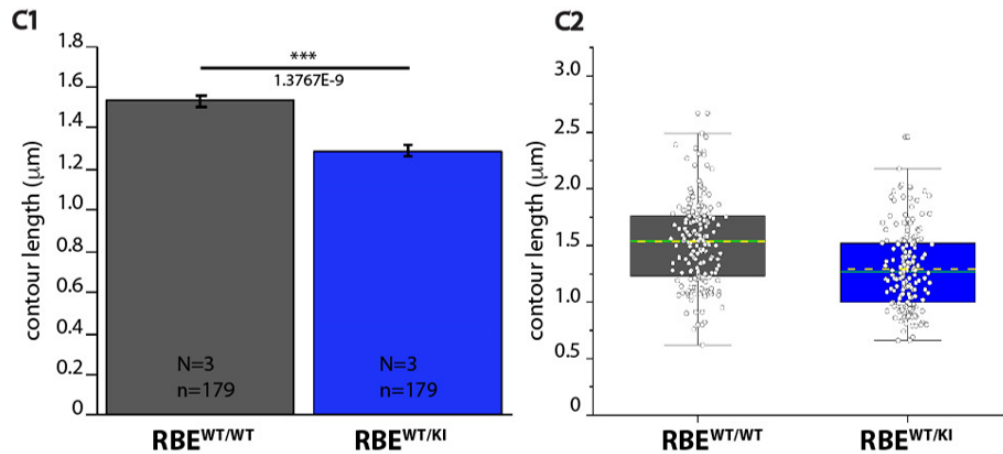


Figure 25. Contour length of synaptic ribbon labeled with anti-RIBEYE B-domain antibody is decreased in the photoreceptor synapses of $RBE^{WT/KI}$ mice in comparison to $RBE^{WT/WT}$ mice

(A, B) Single immunolabeling of (1.5 μm) retinal semithin sections of $RBE^{WT/WT}$ and $RBE^{WT/KI}$ with anti-RIBEYE B-domain antibody (2D9) and processed for 3D SR-SIM. Representative 3D SR-SIM images of RIBEYE B-domain immunostained synaptic ribbons in the OPL of (A) $RBE^{WT/WT}$ and (B) $RBE^{WT/KI}$. The yellow line in the middle of the synaptic ribbon represents the measurement of contour length. (C1) Contour length analysis of synaptic ribbons (mean \pm S.E.M, *** $P \leq 0.001$). (C2) Box and whisker plots of the data distribution from (C1), horizontal yellow dotted line represents mean and green solid line represents median. The median represents the 50th percentile, the box represents the 25th -75th percentile, and whiskers represent 1.5 times of interquartile range. Abbreviations: RBE, RIBEYE; S.E.M., standard error of the mean; N = number of mice; n = number of analyzed images. Figure from Shankwar et al., 2022.

From the analysis of contour length of individual ribbon, I found that average contour length of RIBEYE B-immunostained synaptic ribbon was approximately $1.5336 \pm 0.0281 \mu\text{m}$ in $RBE^{WT/WT}$ mice (Figure 25A), in case of $RBE^{WT/KI}$ it was $1.2908 \pm 0.0258 \mu\text{m}$ (Figure 25B). The reduction ($\sim 16\%$) of contour length was highly significant (p-value for $RBE^{WT/WT} / RBE^{WT/KI}$ comparison: $1.3767\text{E-}9$) (Mann-Whitney U-test) (Figure 25C1, C2). Thus, a decrease in ribbon contour length appears to be the main reason for the decreased RIBEYE B-domain immunofluorescence signals in the rod photoreceptor synapses of $RBE^{WT/KI}$ mice.

4.9 Length of synaptic ribbons immunostained with RIBEYE A-domain antibody is shorter in $RBE^{WT/KI}$ retina (3D SR-SIM analyses)

To further corroborate the above contour length results, 1.5 μm thin Epon resin sections of $RBE^{WT/WT}$ and $RBE^{WT/KI}$ were immunolabeled with RIBEYE A-domain (6F4) monoclonal antibody and z-stack images were taken through 3D SR-SIM microscopy (Figure 26A, B). Analysis of 3D SR-SIM images reveals that contour length of synaptic ribbon immunostained with RIBEYE A-domain antibody was significantly reduced ($\sim 22\%$) in $RBE^{WT/KI}$ (p-value for $RBE^{WT/WT} / RBE^{WT/KI}$ comparison: $4.2346\text{E-}17$) (Kolmogorov-Smirnov test) (Figure 26C1, C2). The average contour length of $RBE^{WT/WT}$ was observed $1.4569 \pm 0.0229 \mu\text{m}$ whereas in $RBE^{WT/KI}$ was observed $1.1343 \pm 0.0227 \mu\text{m}$.

RESULTS

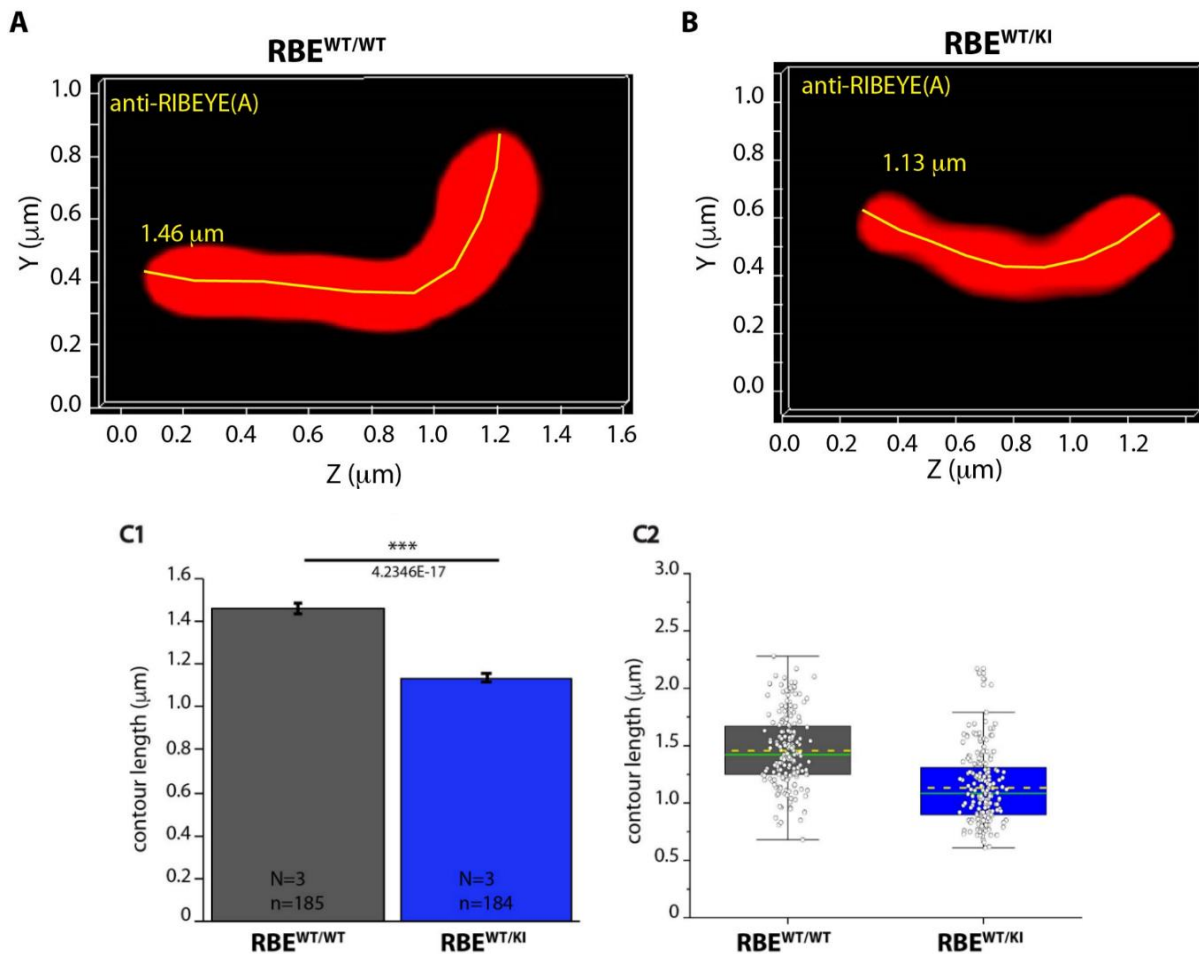


Figure 26. Contour length of synaptic ribbon labeled with anti-RIBEYE A-domain antibody is decreased in the photoreceptor synapses of $RBE^{WT/KI}$ mice in comparison to $RBE^{WT/WT}$ mice

(A, B) Single immunolabeling of ($1.5 \mu\text{m}$) retinal semithin sections of $RBE^{WT/WT}$ and $RBE^{WT/KI}$ with anti-RIBEYE A-domain antibody (6F4) and processed for 3D SR-SIM. Representative 3D SR-SIM images of RIBEYE A-domain immunostained synaptic ribbons in the OPL of (A) $RBE^{WT/WT}$ and (B) $RBE^{WT/KI}$. The yellow line in the middle of the synaptic ribbon represents the measurement of contour length. (C1) Contour length analysis of synaptic ribbon (mean \pm S.E.M, *** $P \leq 0.001$). (C2) The Box and whisker plots of the data from (C1), the yellow dotted line represents mean and green solid line represents median. The median represents the 50th percentile, the box represents the 25th -75th percentile, and whiskers represent 1.5 times of interquartile range. Abbreviations: RBE, RIBEYE; S.E.M., standard error of the mean; N = number of mice; n = number of analyzed images. Figure from Shankwar et al., 2022.

The decrease in contour length of the synaptic ribbon in $RBE^{WT/KI}$ was consistently observed from the two RIBEYE antibodies (2D9, 6F4) (Figure 25, 26). Interestingly, these results reveal that decrease of gene dosage of RIBEYE in $RBE^{WT/KI}$ leads to a decrease in ribbon size and also augments the exciting possibilities that the size of ribbon depends on RIBEYE concentration among others.

RESULTS

4.10 Synaptic ribbon height is shorter in the ultrastructure of rod photoreceptor synapses of RBE^{WT/KI} mice (TEM analyses)

To further investigate the light microscopic alteration of synaptic ribbon size in rod photoreceptor synapses of RBE^{WT/KI}, I performed ultrastructural analysis of RBE^{WT/WT} and RBE^{WT/KI} rod synapses by transmission electron microscopy (TEM). The ribbon height was measured in the X-Y direction from the acquired electron micrograph (Figure 27).

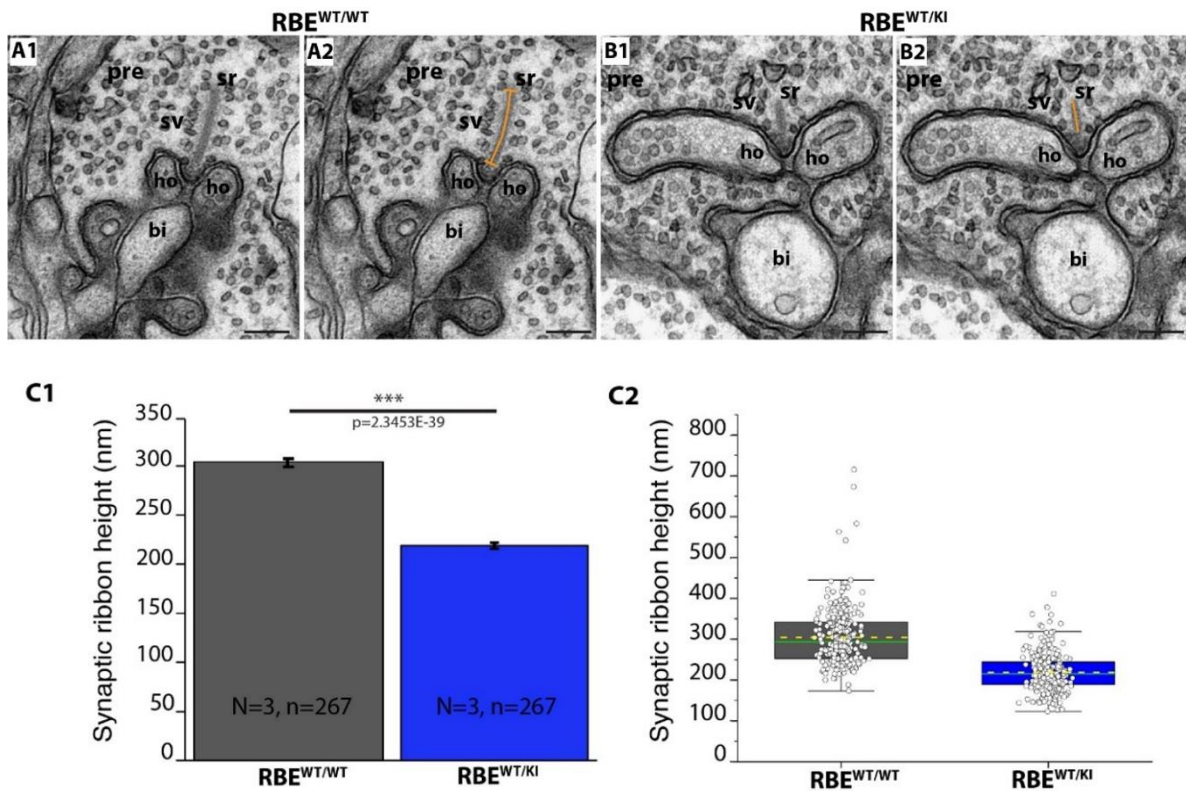


Figure 27. The height of the synaptic ribbon in rod photoreceptor synapses is shorter in RBE^{WT/KI} mice determined by transmission electron microscopy

(A, B) Representative ultrastructural micrographs of cross-sectioned rod photoreceptor synaptic ribbons from the retina of (A1, A2) RBE^{WT/WT} and (B1, B2) RBE^{WT/KI} mice. The orange line represents an outline of the measurement of ribbon height in the x-y direction. (C1) Quantification of ribbon height (mean \pm S.E.M, *** $P \leq 0.001$). (C2) The Box and whisker plot of data from (C1) mean values are marked by yellow dotted line and median values by green solid line. The median represents the 50th percentile, the box represents the 25th -75th percentile, and whiskers represent 1.5 times of interquartile range. Abbreviations: sr, synaptic ribbon; ho, horizontal cells; sv, synaptic vesicles; pre, presynaptic; bi, bipolar cell; RBE, RIBEYE; S.E.M., standard error of the mean; N = number of mice, n = number of analyzed images. Scale bar: 200 nm. Figure from Shankhwar et al., 2022.

I measured the ribbon height in the cross-sectioned synaptic ribbon from the base (anchored site at active zone) to the free cytosolic end of the synaptic ribbon. For examination of ribbon height, only rod photoreceptor synaptic ribbons with clearly visible active zone, opposed by clearly visible postsynaptic

RESULTS

triad (two lateral processes of horizontal cells and central one dendrite of bipolar cell) was used. The ribbon height measured in RBE^{WT/WT} and RBE^{WT/KI} was 304.6 nm ± 4.3 nm and 219.1 nm ± 2.9 nm respectively (Figure 27 C1, C2). The ribbon height was reduced ~ 28% in rod photoreceptor synapse of RBE^{WT/KI} than RBE^{WT/WT} and the difference was significant (p-value for RBE^{WT/WT} / RBE^{WT/KI} comparison: 2.3453E-39) (Kolmogorov-Smirnov test) (Figure 27 C1).

4.11 Synaptic ribbon is lacking from the cone synapses and bipolar cell synapses of RBE^{KI/KI} and RIBEYE immunofluorescence signals and RIBEYE puncta was reduced in the IPL of RBE^{WT/KI} retina

In previous experiments consistently I observed RBE^{KI/KI} mice lacking synaptic ribbons in rod photoreceptor synapses in the outer plexiform layer (OPL). Therefore, I thought to investigate whether synaptic ribbons are also absent in the cone synapses of RBE^{KI/KI} mice or not using confocal microscopy. As mentioned above, the mice retina is rod dominating and less enriched in cone synapse. To verify the cone synapses in the OPL, I double immunolabeled 10 µm retina cryosections of RBE^{WT/WT} and RBE^{KI/KI} mice with RIBEYE A-domain antibody (6F4) to label synaptic ribbon and lectin PNA agglutinin to label cone synapse in the OPL (Figure 28 A). From the confocal microscopy of RBE^{KI/KI} mice sections, I found PNA stained cone synapses but no RIBEYE A-domain stained synaptic ribbons in the OPL (Figure 28 B). In control (RBE^{WT/WT}) retina sections, ribbons are readily observed in cone synapses (Figure 28 A). These results suggest that RBE^{KI/KI} abolish synaptic ribbons from the cone synapse, like rod synapse in the retina of RBE^{KI/KI} mice.

Since I observed strong alteration in RIBEYE B-/RIBEYE A-domain immunostaining and RIBEYE B-/RIBEYE A-domain puncta in the outer plexiform layer (Figure 19-23), I thought to analyze synaptic ribbons in the inner retina (inner plexiform layer). To verify this, I made use of immunolabeled retinal sections (0.5 µm) that were used for the above immunofluorescence experiments (Figure 19, 21). As expected, similar to the outer plexiform layer I found a complete lack of RIBEYE B-domain (p-value for RBE^{WT/KI} / RBE^{KI/KI} comparison: 1.4089E-26; for RBE^{WT/WT} / RBE^{KI/KI} comparison: 1.8930E-25) (online Mann-Whitney U-test) and RIBEYE A-domain (p-value for RBE^{WT/KI} / RBE^{KI/KI} comparison: 9.6304E-35; for RBE^{WT/WT} / RBE^{KI/KI} comparison: 2.4220E-41) (online Mann-Whitney U-test) immunostained synaptic ribbon in the inner plexiform layer of RBE^{KI/KI} retina sections in comparison to RBE^{WT/WT} and RBE^{WT/KI} (Figure 28B1-E2). The RIBEYE B-/RIBEYE A-domain immunosignals and puncta were quantified from 3 different embeddings. Quantification of immunofluorescence signal in IPL showed approximately 33% and 26% significant reduction of RIBEYE B-domain (p-value for RBE^{WT/WT} / RBE^{WT/KI} comparison: 7.9100E-13) (Mann-Whitney U-test) and RIBEYE A-domain fluorescence integrated density respectively (p-value for RBE^{WT/WT} / RBE^{WT/KI} comparison: 9.5400E-4) in the retina of RBE^{WT/KI} in comparison to RBE^{WT/WT} (Figure 28B1, B2, D1, D2) (Mann-Whitney U-

RESULTS

test).

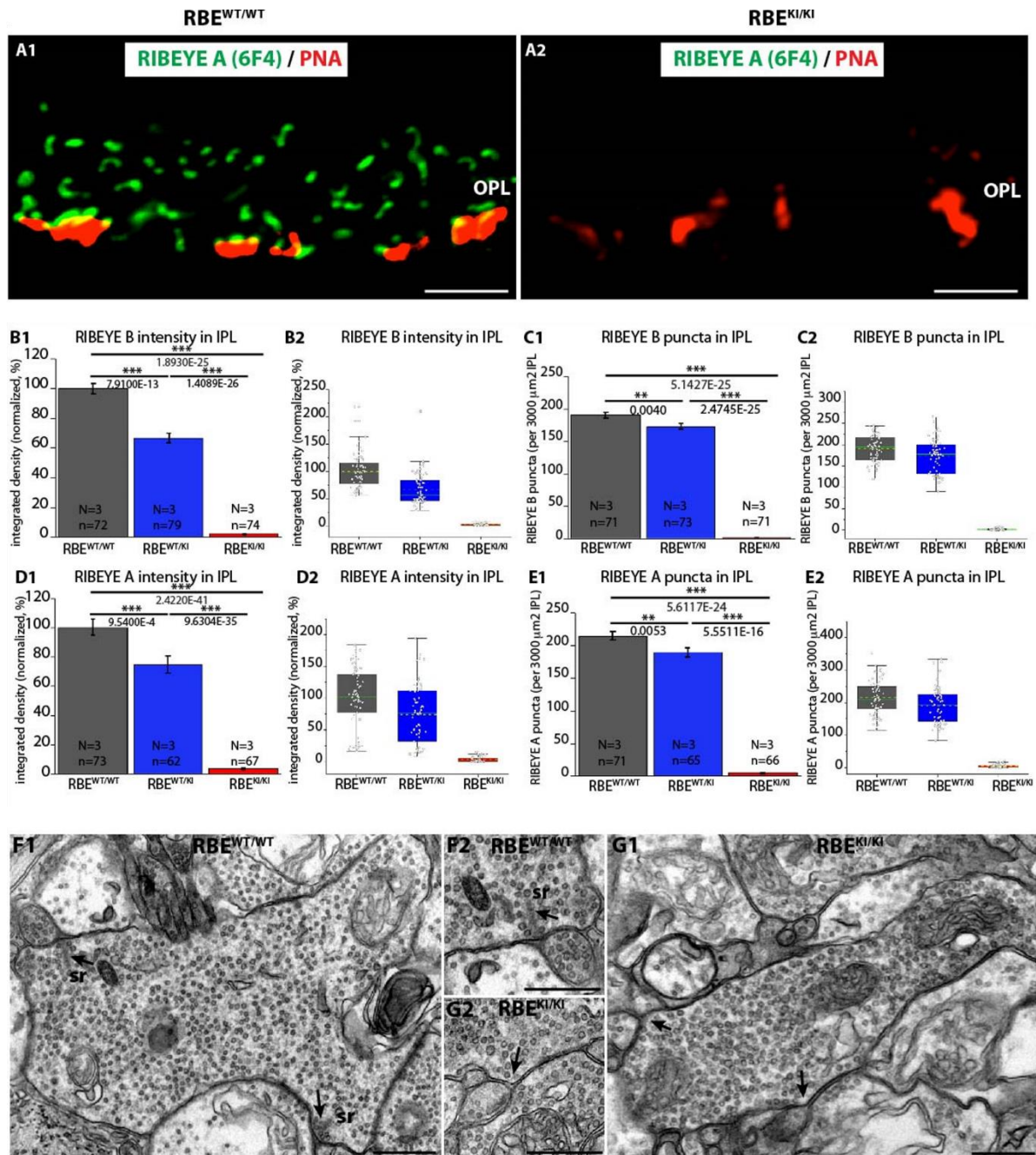


Figure 28. RIBEYE KI causes the absence of ribbons from the cone synapses and quantification of RIBEYE A-/ RIBEYE B-domain immunosignals and puncta in the IPL and ultrastructural analysis of rod bipolar cell terminals

(A-B) Immunolabeling of 10 μm retinal cryosections of RBE^{WT/WT} and RBE^{KI/KI} mice with anti-RIBEYE A-domain 6F4 monoclonal antibody to label synaptic ribbons and PNA lectin Alexa 568 to label cone synapses in the OPL. (A2) RIBEYE immunoreactive synaptic ribbons were absent in RBE^{KI/KI} sections even though cone synapses were well present similar to (A1) control. (B-E) Quantification of RIBEYE B-/RIBEYE A-domain fluorescence integrated density and RIBEYE B-/RIBEYE A-domain puncta. 0.5 μm retina semithin sections of RBE^{WT/WT}, RBE^{WT/KI}, RBE^{KI/KI} mice that were double immunolabeled with 2D9/PSD95 and Tau/SV2 (Figure 19, 20, 21, 23) respectively were used for analysis. (B-E) Immunosignals of RIBEYE B-/RIBEYE A-domain and puncta were completely absent from the IPL of RBE^{KI/KI}, whereas levels were less in RBE^{WT/KI} than RBE^{WT/WT}.

RESULTS

(B1, C1, D1, E1) Represents mean bar graph (mean \pm S.E.M, $**P \leq 0.01$, $***P \leq 0.001$). (B2, C2, D2, E2) The Box and whisker plots of the data from (B1, C1, D1, E1), mean represented by yellow dotted line and median by green solid line. The median represents the 50th percentile, the box represents the 25th -75th percentile, and whiskers represent 1.5 times of interquartile range. (F-G) Representative transmission electron micrograph of cross-sectioned synaptic ribbon from presynaptic bipolar cell synapses of (F1, F2) $RBE^{WT/WT}$ and (G1, G2) $RBE^{KI/KI}$ mice. (F2, G2) High magnified transmission electron micrograph of bipolar cells. Except for the absence of ribbon ultrastructure of rod bipolar cell synapses is comparable with $RBE^{WT/WT}$. Arrow indicates the site where ribbon anchors. Abbreviations: OPL, outer plexiform layer; sr, synaptic ribbon; S.E.M., standard error of the mean; N = number of mice, n = number of analyzed images. Scale bar: 500 nm. Figure from Shankwar et al., 2022.

Similar to immunofluorescence intensity in IPL, immunoreactive puncta of RIBEYE B-domain (p-value for $RBE^{WT/WT}$ / $RBE^{WT/KI}$ comparison: 0.0040) (Student's t-test) and RIBEYE A-domain (p-value for $RBE^{WT/WT}$ / $RBE^{WT/KI}$ comparison: 0.0053) (Mann-Whitney U-test) were also less intense but significantly reduced in $RBE^{WT/KI}$ retina in comparison to $RBE^{WT/WT}$ (Figure 28C1, C2, E1, E2).

In $RBE^{KI/KI}$ retina sections, I did not find any traces of immunoreactive RIBEYE B-domain (p-value for $RBE^{WT/KI}$ / $RBE^{KI/KI}$ comparison: 2.4745E-25; $RBE^{WT/WT}$ / $RBE^{KI/KI}$ comparison: 5.1427E-25) (online Mann-Whitney U-test) and RIBEYE A-domain (p-value for $RBE^{WT/KI}$ / $RBE^{KI/KI}$ comparison: 5.5511E-16; for $RBE^{WT/WT}$ / $RBE^{KI/KI}$ comparison: 5.6117E-24) (Kolmogorov-Smirnov test and online Mann-Whitney U-test respectively) puncta in comparison to $RBE^{WT/WT}$ and $RBE^{WT/KI}$ mice (Figure 28C1, C2, E1, E2).

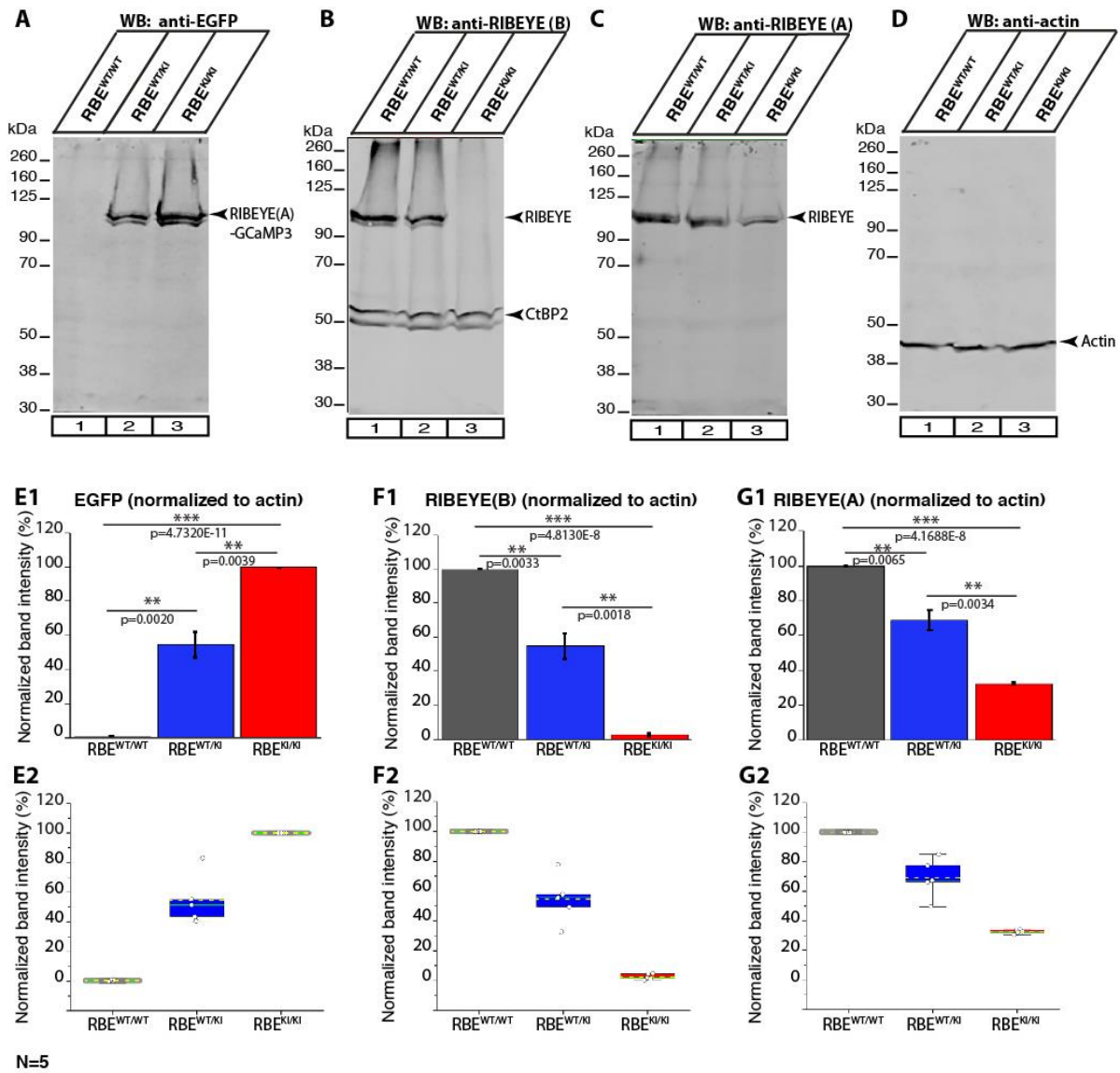
Hence, I did not detect any synaptic ribbons in photoreceptor synapses of $RBE^{KI/KI}$, I thought to examine synaptic ribbons in the ultrastructure of rod bipolar cell synapses by transmission electron microscopy. The inner plexiform layer of mice consists of 15 distinct types of bipolar cells. These bipolar cells make a morphologically and functionally heterogeneous population of ribbon synapses (Shekhar et al., 2016; Moser et al., 2020). The synaptic ribbons of the bipolar cell are smaller than the rod and cone ribbons and vary in size bar-shaped to ovoid (Moser et al., 2020). From the ultrastructure analysis I found, $RBE^{KI/KI}$ mice rod bipolar cell synapses were lacking synaptic ribbons (Figure 28G1, G2). In contrast, ribbons were present in rod bipolar cell synapses of $RBE^{WT/WT}$ mice (Figure 28 F1, F2). These results confirmed the entire absence of synaptic ribbons from the retina of $RBE^{KI/KI}$ mice.

4.12 Western blot analyses of RIBEYE expression

The above results depict, RIBEYE knock-in abolishes the synaptic ribbon in the retina. Further, I examined the effect of RIBEYE B-domain deletion on global protein expression in $RBE^{KI/KI}$ mice by western blotting. I processed retina lysates of $RBE^{WT/WT}$, $RBE^{WT/KI}$, and $RBE^{KI/KI}$ mice for RIBEYE A-domain, RIBEYE B-domain, GFP, and Actin primary antibodies for the Li-Cor system. Actin antibody was used as a loading control and signal intensities of each antibody were normalized with actin signals. The expression of RIBEYE A-GCaMP3 construct was detected by an antibody against GFP (Figure 29

RESULTS

A arrowhead, E1, E2). The GFP band ~ 112 kDa was absent from the retina lysate of $RBE^{WT/WT}$ (p-value for $RBE^{WT/WT} / RBE^{KI/KI}$ comparison: 4.7320E-11; p-value for $RBE^{WT/WT} / RBE^{WT/KI}$ comparison: 0.0020) (Student's t-test). In contrast, GFP band was observed in retina lysate of $RBE^{WT/KI}$, and $RBE^{KI/KI}$ because these mice contain RIBEYE A-GCaMP3 allele, but the expression of GFP in $RBE^{WT/KI}$ retina lysate was ~ 45% less than $RBE^{KI/KI}$ mice expression (p-value for $RBE^{WT/KI} / RBE^{KI/KI}$ comparison: 0.0039) (Student's t-test).



RESULTS

median represents the 50th percentile, the box represents 25th -75th percentile, and whiskers represent 1.5 times of interquartile range. Abbreviations: RBE, RIBEYE; S.E.M., standard error of the mean; N = number of littermate mice “triples” of respective genotypes. Figure from Shankhwar et al., 2022.

As expected, using the RIBEYE B-domain antibody (2D9) I did not find the RIBEYE band approximately 120 kDa in retina lysate of RBE^{KI/KI} mice because its lacked RIBEYE B-domain (p-value for RBE^{WT/WT} / RBE^{KI/KI} comparison: 4.8130E-8; for RBE^{WT/KI} / RBE^{KI/KI} comparison: 0.0018) (Student's t-test). But RIBEYE band is clearly present in retina lysate of RBE^{WT/WT}, and RBE^{WT/KI} mice although expression of RIBEYE B protein in RBE^{WT/KI} was ~ 45% less than RBE^{WT/WT} (p-value for RBE^{WT/WT} / RBE^{WT/KI} comparison: 0.0033) (Figure 29B arrowhead, F1, F2) (Student's t-test). The CtBP2 band was observed at ~55 kDa in all littermates and its expression did not differ significantly (Figure 29 B arrowhead).

RIBEYE A-domain positive band ~120 kDa was clearly observed in the retinal lysate of RBE^{KI/KI} using RIBEYE A-domain antibodies but the expression was less comparison to RBE^{WT/WT} (~ 67 %) and RBE^{WT/KI} (~36 %) (p-value for RBE^{WT/WT} / RBE^{KI/KI} comparison: 4.1688E-8; for RBE^{WT/KI} / RBE^{KI/KI} comparison: 0.0034) (Student's t-test). RIBEYE A-domain positive band in RBE^{WT/KI} retina lysate was ~31% less than RBE^{WT/WT} (p-value for RBE^{WT/WT} / RBE^{WT/KI} comparison: 0.0065) (Student's t-test) (Figure 12D arrowhead, G1, G2).

The western blot results indicate that RIBEYE A/GCaMP3 fusion protein may be unstable due to the absence of RIBEYE B-domain, therefore RIBEYE A/GCaMP3 fusion protein cannot assemble into synaptic ribbon. These outcomes reveal that RBE^{KI/KI} allele abolish synaptic ribbon in the retina not due to lack of protein synthesis, but rather due to the absence of RIBEYE B-domain.

4.13 Synaptic ribbons are absent in the inner ear of RBE^{KI/KI} mice

All retinal experiments confirm the entire absence of synaptic ribbon from the retina of RIBEYE knock-in mice. Further, I wanted to examine, is deletion of RIBEYE B-domain also causes loss of ribbon in the inner ear? To address this question, I performed whole-mount staining of the organ of Corti of RBE^{WT/WT} and RBE^{KI/KI} mice with RIBEYE B-domain (2D9), and RIBEYE A-domain (6F4) antibodies to label synaptic ribbons and PMCA2 to label stereocilia of outer hair cells (Figure 30) (Watson and Temple, 2013; Bortolozzi and Mammano, 2018; Lin et al., 2021).

The confocal images showed, synaptic ribbons immunostained with RIBEYE B-domain (Figure 30 A1-B4)/RIBEYE A-domain (Figure 30C1-D4) were clearly visible in inner hair cells (IHC) and outer hair cells (OHC) of RBE^{WT/WT} mice but completely absent from the IHC and OHC of RBE^{KI/KI} mice. PMCA2 labeling was appeared similar in both RBE^{WT/WT} and RBE^{KI/KI}.

RESULTS

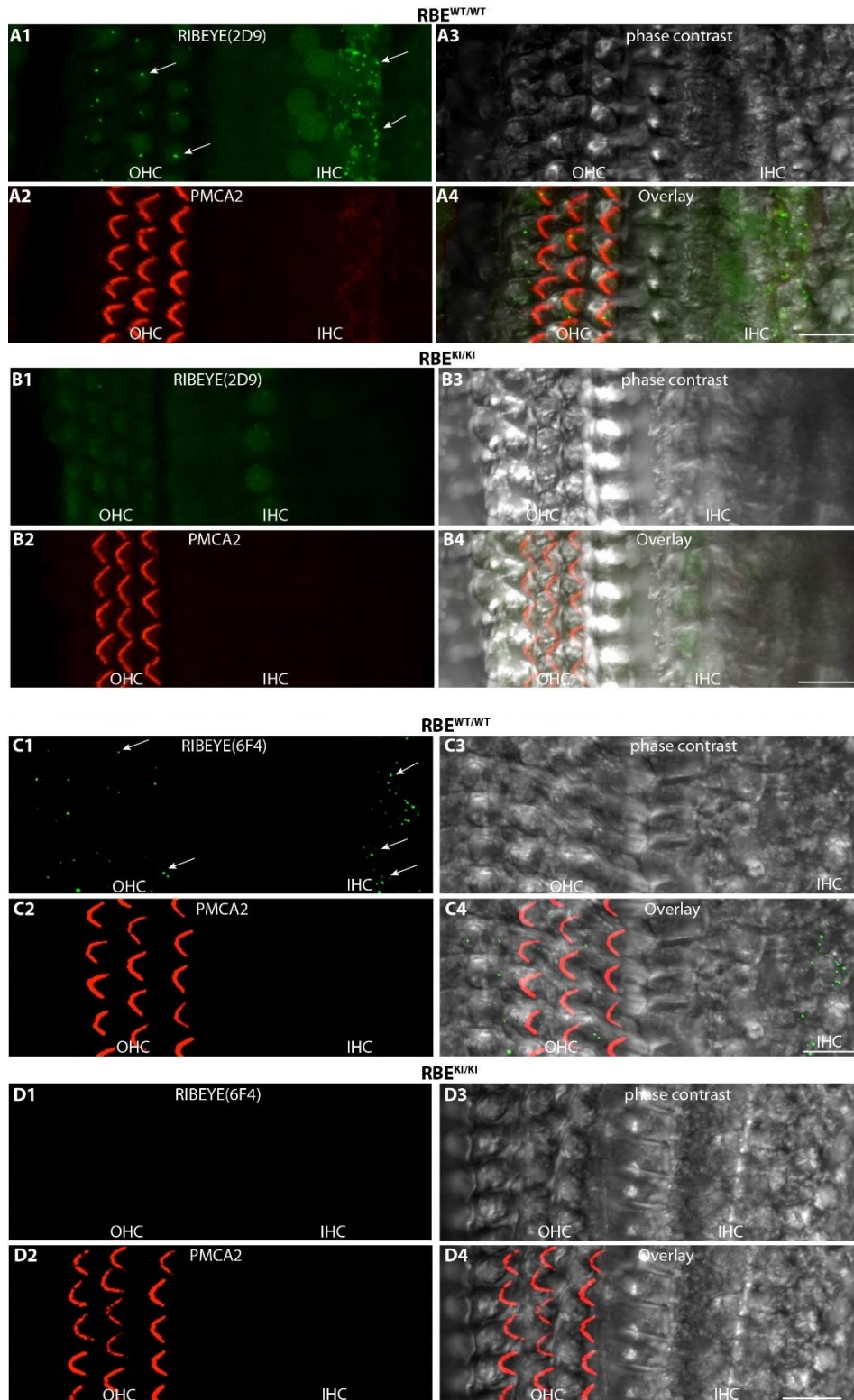


Figure 30. RIBEYE B-domain and RIBEYE A-domain immunosignal are absent in the inner ear of $RBE^{KI/KI}$ mice

(A-D) Whole-mount immunolabeling of organ of Corti (apical turn) of $RBE^{WT/WT}$, $RBE^{KI/KI}$ mice with (A, B) anti-RIBEYE B-domain 2D9, (C, D) anti-RIBEYE A-domain 6F4 to label synaptic ribbon (green) in outer hair cells (OHC) and inner hair cells (IHC) and rabbit polyclonal against PMCA2 (red) to visualize stereocilia of

RESULTS

outer hair cells. Immunolabeled synaptic ribbons were evident in OHC and IHC (arrows) of RIBEYE wildtype mice but not in RIBEYE knock-in mice. Abbreviations: OHC, outer hair cells; IHC, inner hair cells. Scale bar: 12 μ m. Figure from Shankhwar et al., 2022.

Hence, all the retinal and inner ear experiments showed the absence of synaptic ribbon constantly in the OPL and IPL as well as in the ribbon synapses of OHC and IHCs. Therefore, these findings confirm that RIBEYE A-domain alone is not sufficient to assemble into the synaptic ribbon, for that RIBEYE B-domain is required.

5. DISCUSSION

The synaptic ribbon, the name-giving characteristically presynaptic specialization of ribbon synapses plays an important role in rapid sustained synaptic vesicles exocytosis. RIBEYE is the only known ribbon-specific component that is essential for the scaffolding of synaptic ribbon (Schmitz et al. 2000; Schmitz, 2009; Sterling and Mathews 2005; Maxeiner et al., 2016; Moser et al., 2020).

RIBEYE is a scaffold protein that is made up of a unique amino-terminal RIBEYE A-domain and carboxyterminal B-domain that is identical to CtBP2, except for 20 amino acids. CtBP2 is a transcriptional co-repressor that is ubiquitously expressed in most of the tissues (Schmitz et al., 2000; Schmitz, 2009).

The role of RIBEYE in the scaffolding of synaptic ribbon was supported by the identification of multiple binding sites in RIBEYE A-domain for interaction with other RIBEYE proteins (Magupalli et al., 2008; Schmitz, 2009). It was shown that RIBEYE A-domain contains multiple binding sites for homolytic interaction with other RIBEYE A-domain as well as with RIBEYE B-domain (heterotypic interaction) and which may involve in the assembly of synaptic ribbon (Schmitz, 2000; Magupalli et al., 2008). From the transfection experiments, RIBEYE A-domain appears to serve as a structural component of the synaptic ribbon and RIBEYE B-domain interacts with cytoplasmic proteins (Schmitz, 2000; Magupalli et al., 2008). Moreover, it was shown NAD(H) binding promotes tetrameric assembly of CtBP (identical to RIBEYE B-domain) by an interaction between two dimers. Oligomerization of CtBP depends on NAD(H) interaction (Nardini et al., 2009; Madison et al., 2013; Bellesis et al., 2018; Kumar et al., 2002; Jecrois et al., 2021).

The central function of the RIBEYE in the assembly of synaptic ribbon has been finally shown with RIBEYE knock-out mice in which the exon that encodes RIBEYE A-domain was completely removed by genetic manipulation (Maxeiner et al., 2016). This study has shown that deletion of RIBEYE A-domain leads to complete loss of synaptic ribbon as well as impairment of neurotransmitter release in RIBEYE knock-out mice (Maxeiner et al., 2016; Jean et al., 2018; Becker et al., 2018). However, the role of RIBEYE B-domain in the assembly of synaptic ribbons remained unclear.

In the present study, I asked whether RIBEYE B-domain has a function in the assembly of the synaptic ribbons using RIBEYE knock-in mice in which RIBEYE B-domain is replaced by the calcium sensor GCaMP3.

5.1 RIBEYE knock-in causes loss of synaptic ribbons

My work was focusing on examining the consequences of deletion of RIBEYE B-domain in the retina of RIBEYE knock-in mice (RBE^{KI/KI}). From the immunostaining of synaptic ribbons with RIBEYE B-

DISCUSSION

/RIBEYE A-domain antibody, I did not observe any ribbon in the synaptic layers OPL and IPL of the retina of RBE^{KI/KI} mice in comparison to RIBEYE wildtype mice (RBE^{WT/WT}) and heterozygous RIBEYE knock-in mice (RBE^{WT/KI}) (Figure 19-23). Synaptic ribbons were also absent from the cone synapses of the RBE^{KI/KI} mice (Figure 28 A). Similarly, no RIBEYE immunostaining was observed in outer hair cells and inner hair cells of the organ of Corti in RBE^{KI/KI} mice (Figure 30). In contrast, immunostaining of all retinal markers was unchanged (Figure 18).

I confirmed the light microscopical findings by ultrastructural analyses of rod photoreceptor terminals by TEM analyses of photoreceptor ribbon synapses and other ribbon synapses. The ultrastructural analysis also confirmed the absence of synaptic ribbon from the rod photoreceptor synapses of RBE^{KI/KI} mice in comparison to RBE^{WT/WT} and RBE^{WT/KI} mice. The ribbon per rod terminal was similar in RBE^{WT/WT} and RBE^{WT/KI} mice (Figure 24).

Therefore, my finding demonstrates that deletion of the RIBEYE B-domain abolishes synaptic ribbon globally not only from the retina but also from the inner ear but does not alter the pre- and postsynaptic organization of ribbon synapses in RIBEYE knock-in mice. Hence, these outcomes confirm that RIBEYE functions universally in all ribbon synapses as suggested previously (Schmitz, 2009; Maxeiner et al., 2016; Jean et al., 2018; Becker et al., 2018). RIBEYE B-domain deletion in the RIBEYE knock-in causes a similar effect as complete RIBEYE A-domain deletion in RIBEYE knock-out mice (Maxeiner et al., 2016). Thus, these findings validate that RIBEYE B-domain is essential for ribbon assembly.

5.2 Synaptic ribbon was smaller in the OPL of heterozygous RIBEYE knock-in mice

Interestingly I found that a single genomic copy of the RIBEYE B-domain is sufficient for the assembly of synaptic ribbon using heterozygous RIBEYE knock-in mice (RBE^{WT/KI}). In the outer plexiform layer of RBE^{WT/KI} mice, I observed a significant reduction in immunosignals of RIBEYE B-domain and RIBEYE A-domain whereas immunolabeled puncta of RIBEYE B-domain and RIBEYE A-domain were unchanged (Figure 19, 20, 21, 23).

To find the reason behind it I measured the contour length of the synaptic ribbon by SR-SIM microscopy. The contour length of the RIBEYE B-domain and RIBEYE A-domain immunolabeled synaptic ribbon was significantly reduced in RBE^{WT/KI} mice in comparison to RBE^{WT/WT} mice (Figure 25, 26).

To further support these results, I measured the height of synaptic ribbons in rod photoreceptor terminal of RBE^{WT/KI} mice at the ultrastructural level by transmission electron microscopy. TEM analysis showed

DISCUSSION

that ribbon height in the X-Y direction was significantly reduced in RBE^{WT/KI} mice in comparison to RBE^{WT/WT} mice (Figure 27).

The possible reason for the decreased ribbon size in RBE^{WT/KI} mice could be decreased expression of RIBEYE protein that translates into different ribbon sizes. Likewise, smaller synaptic ribbons were also reported in heterozygous RIBEYE knock-out mice (RBE^{WT/KO}) in comparison to wildtype mice (RBE^{WT/WT}) (Jean et al., 2018), and fish deficient in RIBEYE A-domain also have shorter ribbons (Wan et al., 2005)

5.3 RIBEYE immunofluorescence and puncta was less in the IPL of RBE^{WT/KI} mice in comparison to RBE^{WT/WT} and bipolar cells of RBE^{KI/KI} mice lacking synaptic ribbons

In the inner plexiform layer of heterozygous RIBEYE knock-in (RBE^{WT/KI}) mice I also observed a decrease in immunosignals of RIBEYE B-domain and RIBEYE A-domain in comparison to RBE^{WT/WT} mice (Figure 28B, D). I also analyzed RIBEYE B-/ RIBEYE A-domain puncta per μm^2 IPL at high magnification. I found RIBEYE puncta was significantly reduced in RBE^{WT/KI} mice in comparison to RBE^{WT/WT} mice (Figure 28C, E).

To further corroborate the reduction of RIBEYE puncta in IPL, I analyzed the ultrastructure of rod bipolar cell synapses in IPL by transmission electron microscopy, I found synaptic ribbons were completely absent from the rod bipolar synapses of RIBEYE knock-in mice in comparison to control mice (Figure 28F, G) whereas ultrastructure was comparable with control mice (RBE^{WT/WT}).

The reduction of RIBEYE puncta in the IPL of RBE^{WT/KI} mice could be because, the size of synaptic ribbons of bipolar cell synapses are smaller than the ribbons of rod photoreceptor synapses (Moser et al., 2020). Thus, further reduction in ribbon size of RBE^{WT/KI} can leads to complete disappearance of the synaptic ribbons from the rod bipolar cell synapses than rod photoreceptor synapses.

5.4 RIBEYE expression was downregulated in RIBEYE knock-in retina

From the immunofluorescence and transmission electron microscopy experiments, I found that RIBEYE B-domain is essential for the ribbon assembly. To further verify this, I checked the expression of RIBEYE by western blotting. I did not find expression of RIBEYE B-domain in the retina of RBE^{KI/KI} mice in comparison to RBE^{WT/WT} and RBE^{WT/KI} mice because it's lacking RIBEYE B-domain, but CtBP2 was expressing constantly (Figure 29 B). Although, RIBEYE A-domain is continuously expressed as a GCaMP3 fusion protein in the retina of RBE^{KI/KI} because it contains RIBEYE A/GCaMP3 allele (Figure

DISCUSSION

29 C). In contrast, immunofluorescence analysis shows a complete absence of synaptic ribbons in RIBEYE knock-in mice.

Hence, these results confirm that RIBEYE A-domain alone is not sufficient for assembly of ribbon, for that RIBEYE B-domain is required and reveals that phenotype caused by deletion of RIBEYE B-domain is as severe as complete RIBEYE deletion.

6. CONCLUSION

In conclusion, my findings determine that RIBEYE A-domain alone cannot make synaptic ribbons. This was shown by analyses of ribbon synapses of RIBEYE knock-in mice. I found that RIBEYE B-domain is also essential for the making of the synaptic ribbon in retinal and inner ear ribbon synapses. In the complete absence of RIBEYE B-domain, no ribbons were formed both in the retina as well as in the inner ear. Further analyses are needed to further validate how RIBEYE B-domain endorses the assembly of the synaptic ribbon. RIBEYE B-domain is nearly identical to the transcriptional co-repressor CtBP2. Recent studies have shown that CtBP1 and CtBP2 assembled into tetrameric complexes in a NAD(H)-dependent manner. These stable tetrameric complexes are assembled by two dimeric pairs of CtBP (Nardini et al., 2009; Madison et al., 2013; Bellesis et al., 2018; Kumar et al., 2002; Jecrois et al., 2021). Similar assemblies are likely formed at the synaptic ribbon by RIBEYE B-domain. Similar to CtBP1 and CtBP2, RIBEYE B-domain also binds with NAD(H) (Schmitz et al., 2000). Thus, RIBEYE B-domain also can be speculated to form tetrameric structures that can be controlled by the binding of NAD(H). During ribbon assembly, these oligomeric RIBEYE B-complexes could hold RIBEYE proteins together to promote assembly and the stability of the synaptic ribbon. Interestingly, the addition of NAD(H) has an impact on the size of synaptic ribbon in sensory hair cells (Wong et al., 2019; Okur et al., 2020). Also, the increase in the size of synaptic ribbons in inner hair cells was observed due to disruption of NAD⁺ / NADH homeostasis with aging in C57BL/6J mice (Peineau et al., 2021; Xiong et al., 2020). Hidden hearing loss (cochlear synaptopathy) causes damage of the sensory synapses between IHCs and spiral ganglion neurons (Wei et al., 2020). Hence, this RIBEYE knock-in mice (RBE^{KI/KI}) is an ideal mouse model for future analysis to study the physiological consequences of RIBEYE B-domain deletion on vision and hearing.

7. REFERENCES

Ackermann F, Waites CL, Garner CC (2015) Presynaptic active zones in invertebrates and vertebrates. *EMBO Reports* 16:923–938.

Airaksinen PJ, Doro S, Veijola J (2008) Conformal geometry of the retinal nerve fiber layer. *PNAS* 105:19690-19695.

Amartely H, Iosub-Amir A, Friedler A (2014) Identifying protein-protein interaction sites using peptide arrays. *J Vis Exp* 93: e52097.

Becker L, Schnee M.L, Niwa M, Sun W, Maxeiner S, Talaei S, Kachar B, Rutherford MA, Ricci AJ (2018) The presynaptic ribbon maintains vesicle populations at the hair cell afferent fiber synapse. *eLife* 7, e30242.

Bellesis AG, Jecrois AM, Hayes JA, Schiffer CA, Royer Jr WE (2018) Assembly of human C-terminal binding protein (CtBP) into tetramers. *The Journal of biological chemistry* 293: 9101-9112.

Bloom FE, Aghajanian GK (1968) Fine structural and cytochemical analysis of the staining of synaptic junctions with phosphotungstic acid. *J Ultrastruct Res* 22:361-375.

Bortolozzi M, Mammano F (2018) PMCA2 pump mutations and hereditary deafness. *Neurosci Lett* 663:18–24.

Brandstätter JH, Fletcher EL, Garner CC, Gundelfinger ED, Wässle H (1999) Differential expression of the presynaptic cytomatrix protein bassoon among ribbon synapses in the mammalian retina. *Eur J Neurosci* 11:3683-93.

Buckley K, Kelly RB (1985) Identification of a transmembrane glycoprotein specific for secretory vesicles of neuronal and endocrine cells. *J Cell Biol* 100: 1284 -1294.

Chen J, Sampath AP (2013) Structure and function of rod and cone photoreceptors. *Retina* 5th edition.1: 342-359.

Chinnadurai G (2003) CtBP family proteins: more than transcriptional corepressors. *Bioessays* 25: 9-12.

REFERENCES

Chinnadurai G (2002) CtBP, an unconventional transcriptional corepressor in development and oncogenesis. *Mol Cell* 9: 213–224.

Chinnadurai G (2007) CtBP Family proteins: unique transcriptional regulators in the nucleus with diverse cytosolic functions. Austin (TX): Landes Bioscience; 2000-2013.

Davies JN, Zamponi GW (2008) Old proteins, developing roles: The regulation of calcium channels by synaptic proteins. *Channels* 2: 130-138.

Davydova D, Marini C, King C, Klueva J, Bischof F, Romorini S, Montenegro-Venegas C, Heine M, Schneider R, Schröder MS, Altmann WD, Henneberger C, Rusakov DA, Gundelfinger ED, Fejtova A (2014) Bassoon specifically controls presynaptic P/Q-type Ca²⁺ channels via RIM-binding protein. *Neuron* 82: 181-194.

Deguchi-Tawarada M, Inoue E, Takao-Rikitsu E, Inoue M, Kitajima I, Ohtsuka T, Takai Y (2006) Active zone protein CAST is a component of conventional and ribbon synapses in mouse retina. *J Comp Neurol* 495: 480-496.

Dembla M, Kesharwani A, Natarajan S, Fecher-Trost C, Fairless R, Williams SK, Flockerzi V, Diem R, Schwarz K, Schmitz F (2018) Early auto-immune targeting of photoreceptor ribbon synapses in mouse models of multiple sclerosis. *EMBO Mol Med* 10: e8926.

De Winter JCF (2013) Using the Student's t-test with extremely small sample sizes. *Practical Assessment, Research & Evaluation* 18:10.

Dick O, Hack I, Altmann WD, Garner CC, Gundelfinger ED, Brandstätter JH (2001) Localization of the presynaptic cytomatrix protein Piccolo at ribbon and conventional synapses in the rat retina: comparison with Bassoon. *J Comp Neurol* 439: 224-234.

Dick O, Dieck S, Wilko Detlef Altmann, Josef Ammermüller, Reto Weiler, Craig Curtis Garner, Eckart Dieter Gundelfinger, Johann Helmut Brandstätter (2003) The presynaptic active zone protein bassoon is essential for photoreceptor ribbon synapse formation in the retina. *Neuron* 37:775-786.

REFERENCES

- Dieckmann–Schuppert A, Schnittler HJ (1997) A simple assay for quantification of protein in tissue sections, cell cultures, and cell homogenates, and of protein immobilized on solid surfaces. *Cell Tissue Res* 288: 119-126.
- Dowling JE, Werblin FS (1971) Synaptic organization of the vertebrate retina. *Vision Res* 3: 1-15.
- Drenckhahn D, Franz H (1986) Identification of actin-, alpha-actinin-, and vinculin-containing plaques at the lateral membrane of epithelial cells. *J Cell Biol* 102: 1843-1852.
- Euler T, Haverkamp S, Schubert T, Baden T (2014) Retinal bipolar cells: elementary building blocks of vision. *Nat Rev Neurosci* 15: 507-519.
- Fang QJ, Wu F, Chai R, Sha SH (2019) Cochlear surface preparation in the adult mouse. *J Vis Exp* 6:153.
- Fjeld CC, Birdsong WT, Goodman RH (2003) Differential binding of NAD and NADH allows the transcriptional corepressor carboxyl-terminal binding protein to serve as a metabolic sensor. *Proc Natl Acad Sci USA* 100: 9202-9207.
- Frank R (2002) The SPOT-synthesis technique. Synthetic peptide arrays on membrane supports—principles and applications. *J Immunol Methods* 267: 13-26.
- Fry KR, Spira AW (1980) An ethanolic phosphotungstic acid (EPTA) analysis of photoreceptor and synaptic ultrastructure in the guinea pig retina. *J Histochem Cytochem* 28: 142-148.
- Grabner CP, Gandini MA, Rehak R, Le Y, Zamponi GW, Schmitz F (2015) RIM1/2-mediated facilitation of Cav1.4 channel opening is required for Ca²⁺-stimulated release in mouse rod photoreceptors. *J Neurosci* 35: 13133-13147.
- Gruber T, Pan C, Contreras RE, Wiedemann T, Morgan DA, Skowronski AA, Lefort S, Murat CM, Le Thuc O, Legutko B, Ruiz-Ojeda FJ, Fuente-Fernandez M, Garcia-Villlon AL, Gonzalez-Hedstrom D, Huber M, Szigeti-Buck K, Müller TD, Ussar S, Pfluger P, Woods SC, Ertürk A, LeDc CA, Rahmouni K, Granado M, Horvath TL, Tschöp M, Barcia-Caeres C (2021) Obesity-associated hyperleptinemia alters the gliovascular interface of the hypothalamus to promote hypertension. *Cell Metab* 33: 1155-1170.

REFERENCES

- Goldberg JD, Yoshida T, Brick P (1994) Crystal structure of a NAD-dependent D-glycerate dehydrogenase at 2.4 Å resolution. *J Mol Biol* 236: 1123-1140.
- Gupta MP, Herzlich AA, Sauer T, Chan CC (2016) Retinal Anatomy and Pathology. *Dev Ophthalmol* 55: 7–17.
- Gustafsson MGL, Shao L, Carlton PM, Wang CJR, Golubovskaya IN, Cande WZ, Agard DA, Sedat JW (2008) Three-dimensional resolution doubling in wide-field fluorescence microscopy by structured illumination. *Biophys J* 94: 4957-4970.
- Harsman A, Kopp A, Wagner R, Zimmermann R, Jung M (2011) Calmodulin regulation of the calcium-leak channel Sec61 is unique to vertebrates. *Channels (Austin)* 5: 293-298.
- Heidelberger R, Thoreson WB, Witkovsky P (2005) Synaptic transmission at retinal ribbon synapses. *Prog Retin Eye Res* 24: 682-720.
- Hildebrand JD, Soriano P (2002) Overlapping and unique roles for C-terminal binding protein 1 (CtBP1) and CtBP2 during mouse development. *Mol Cell Biol* 22: 5296-5307.
- Hilpert K, Winkler DFH, Hancock REW (2007) Peptide arrays on cellulose support: SPOT synthesis, a time and cost efficient method for synthesis of large numbers of peptides in a parallel and addressable fashion *Nat Protoc* 2: 1333-1349.
- Hodges RS, Heaton RJ, Parker JM, Molday L, Molday RS (1988) Antigen-antibody interaction: synthetic peptides define linear antigenic determinants recognized by monoclonal antibodies directed to the cytoplasmic carboxy terminus of rhodopsin. *J Biol Chem* 263: 11768-11775.
- Irie M, Hata Y, Takeuchi M, Ichtchenko K, Toyoda A, Hirao K, Takai Y, Rosahl TW, Südhof TC (1997) Binding of neuroligins to PSD-95. *Science* 277: 1511-1515.
- Jean P, de la Marina DL, Michanski S, Tobón LMJ, Chakrabarti R, Picher MM, Neef J, Jung S, Gültas M, Maxeiner S, Neef A, Wichmann C, Strenzke N, Grabner C, and Moser T (2018) The synaptic ribbon is critical for sound encoding at high rates with temporal precision. *eLife* 7: e29275.

REFERENCES

Jecrois AM, Dcona MM, Deng X, Bandyopadhyay D, Grossman SR, Schiffer CA, and Royer Jr WE (2021) Cryo-EM structure of CtBP2 confirms tetrameric architecture. *Structure* 29: 310-319.

Jockusch WJ, Praefcke GJK, McMahon HT, Lagnado L (2005) Clathrin-dependent and clathrin-independent retrieval of synaptic vesicles in retinal bipolar cells. *Neuron* 46: 869-878.

Kannan M (2018) Transmission Electron Microscope – Principle, Components and Applications. A Textbook on Fundamentals and Applications of Nanotechnology. 93-101.

Kerov V, Laird JG, Joiner ML, Knecht S, Soh D, Hagen J, Gardner SH, Gutierrez W, Yoshimatsu T, Bhattarai S, Puthussery T, Artemyev NO, Drack AV, Wong RO, Baker SA, Lee A (2018) $\alpha 2\delta$ -4 is required for the molecular and structural organization of rod and cone photoreceptor synapses. *J Neurosci* 38: 6145-6160.

Khimich D, Nouvian R, Pujol R, Tom Dieck S, Egnér A, Gundelfinger ED, Moser T (2005) Hair cell synaptic ribbons are essential for synchronous auditory signalling. *Nature* 434: 889-94.

Klapper SD, Swiersy A, Bamberg E, Busskamp V (2016) Biophysical properties of optogenetic tools and their application for vision restoration approaches. *Front Syst Neurosci* 10:74.

Kolb H (2005) *Gross Anatomy of the Eye*. Salt Lake City (UT): University of Utah Health Sciences Center; 1995. PMID: 21413392.

Kolb H (2005) *Simple Anatomy of the Retina*. University of Utah Health Sciences Center; 1995. PMID: 21413391.

Kolb H (2001) *Glia cell of the Retina*. Salt Lake City (UT): University of Utah Health Sciences Center; 1995. PMID: 21413380.

Kolb H (1997) Amacrine cells of the mammalian retina: neurocircuitry and functional roles. *Eye* 11: 904-923.

Kolb H, Fernandez E, Nelson R (1995) *The Organization of the Retina and Visual System*. Salt Lake City (UT): University of Utah Health Sciences Center. PMID: 21413389.

REFERENCES

- Koulen P, Fletcher EL, Craven SE, Brecht DS, Wässle H (1998). Immunocytochemical localization of the postsynaptic density protein PSD-95 in the mammalian retina. *J Neurosci* 18:10136-10149.
- Kumar V, Carlson JE, Ohgi KA, Edwards TA, Rose DW, Escalante CR, Rosenfeld MG, Aggarwal AK (2002) Transcription Corepressor CtBP Is an NAD-Regulated Dehydrogenase. *Molecular Cell* 10: 857-869.
- Laemmli UK (1970) Cleavage of structural proteins during the assembly of the head of bacteriophage T4. *Nature* 227: 680–685.
- Lagnado L, Schmitz F (2015) Ribbon synapses and visual processing in the retina. *Annu Rev Vis Sci* 1: 235-262.
- Lee YB, Glover CP, Cosgrave AS, Bienemann A, Uney JB (2005) Optimizing regulatable gene expression using adenoviral vectors. *Exp Physiol* 90: 33-37.
- Lessard JL (1988) Two monoclonal antibodies to actin: one muscle selective and one generally reactive. *Cell Motil Cytoskeleton* 10: 349-362.
- Li P, Lin Z, An Y, Lin J, Zhang A, Wang S, Tu H, Jie Ran, Wang J, Liang Y, Liu Z, Ye C, Fu X, Gao J (2021) Piccolo is essential for the maintenance of mouse retina but not cochlear hair cell function. *Aging* 13: 11678-11695.
- Limbach C, Laue MM, Wang X, Hu B, Thiede N, Hultqvist G, Kilimann MW (2011) Molecular in situ topology of aczonin/piccolo and associated proteins at the mammalian neurotransmitter release site. *Proc Natl Acad Sci USA* 108: E392-401.
- Lin X, Brunck MGK, Yuanxiang P, Curran AW, Zhang E, Stöber F, Goldschmidt J, Gundelfinger ED, Vollmer M, Happel MFK, Herrera-Molina R, and Montag D (2021) Neuroplastin expression is essential for hearing and hair cell PMCA expression. *Brain Struct Funct* 226: 1533-1551.
- LoGiudice L, Matthews G (2007) Endocytosis at ribbon synapses. *Traffic* 8: 1123-1128.
- Lowry OH, Rosebrough NJ, Farr AL, Randall RJ (1951) Protein measurement with the Folin phenol reagent. *J Biol Chem* 193: 265-275.

REFERENCES

- Llobet A, Gallop JL, Burden JJE, Camdere G, Chandra P, Vallis Y, Hopkins CR, Lagnado L, McMahon HT (2011) Endophilin drives the fast mode of vesicle retrieval in a ribbon synapse. *J Neurosci* 31:8512-19.
- Madison DL, Wirz JA, Siess D, Lundblad JR (2013) Nicotinamide adenine dinucleotide-induced multimerization of the co-repressor CtBP1 relies on a switching tryptophan. *The Journal of biological chemistry* 288: 27836-27848.
- Magupalli VG, Schwarz K, Alpadi K, Natarajan S, Seigel GM, Schmitz F (2008) Multiple RIBEYE–RIBEYE interactions create a dynamic scaffold for the formation of synaptic ribbons. *J Neurosci* 28: 7954-7967.
- Mandell JW, Townes-Anderson E, Czernik AJ, Cameron R, Greengard P, De Camilli P (1990) Synapsins in the vertebrate retina: Absence from ribbon synapses and heterogeneous distribution among conventional synapses. *Neuron* 5:19-33.
- Mandell JW, Czernik AJ, De Camilli P, Greengard P (1992) Differential expression of synapsins I and II among rat retinal synapses. *J Neurosci* 12: 1736-1749
- Mashige KP, Oduntan OA (2016) A review of the human retina with emphasis on nerve fibre layer and macula thicknesses. *African Vision Eye Health* 75: a330.
- Masland RH (2012) The neuronal organization of the retina. *Neuron* 76: 266-280.
- Matthews G, Fuchs P (2010) The diverse roles of ribbon synapses in sensory neurotransmission. *Nat Rev Neurosci*. 11: 812-822.
- Maxeiner S, Luo F, Tan A, Schmitz F, Südhof TC (2016) How to make a synaptic ribbon: RIBEYE deletion abolishes ribbons in retinal synapses and disrupts neurotransmitter release. *EMBO J* 35: 1098-1114.
- Mercer AJ, Thoreson WT (2011) The dynamic architecture of photoreceptor ribbon synapses: Cytoskeletal, extracellular matrix, and intramembrane proteins. *Vis Neurosci* 28: 453-471.

REFERENCES

- Mennerick S, Matthews G (1996) Ultrafast exocytosis elicited by calcium current in synaptic terminals of retinal bipolar neurons. *Neuron* 17: 1241-1249.
- Minsky M (1961) *Microscopy Apparatus*.
- Minsky M (1988) Memoir on inventing the Confocal Scanning Microscopy. *Scanning* 10: 128-138.
- Montgomery SC, Cox BC (2016) Whole mount dissection and immunofluorescence of the adult mouse cochlea. *J Vis Exp* 107: 53561.
- Morgans CW (2000) Neurotransmitter release at ribbon synapses in the retina. *Immunol Cell Biol* 78: 442-446.
- Moser T, Grabner CP, Schmitz F (2020) Sensory processing at ribbon synapses in the retina and the cochlea. *Physiol Rev* 100:103-144.
- Mukherjee A, Katiyar R, Dembla E, Dembla E, Kumar P, Belkacemi A, Jung M, Beck A, Flockerzi V, Schwarz K, Schmitz F (2020) Disturbed presynaptic Ca²⁺ signaling in photoreceptors in the EAE mouse model of multiple sclerosis. *iScience* 23: 101830.
- Müller TM, Gierke K, Joachimsthaler A, Sticht H, Izsvák Z, Hamra FK, Anna Fejtová A, Ackermann F, Garner CC, Kremers J, Brandstätter JH, Regus-Leidig H (2019) A multiple Piccolino-RIBEYE interaction supports plate-shaped synaptic ribbons in retinal neurons. *J Neurosci* 39: 2606-2619.
- Nardini M, Spanò S, Cericola C, Pesce A, Massaro A, Millo E, Luini A, Corda D, Bolognesi M (2003) CtBP/BARS: a dual-function protein involved in transcription co-repression and Golgi membrane fission. *EMBO J* 22: 3122-3130.
- Nardini M, Valente C, Ricagno S, Luini A, Corda D, Bolognesi M (2009) CtBP1/BARS Gly172--> Glu mutant structure: impairing NAD(H)-binding and dimerization. *Biochem Biophys Res Commun* 381: 70-74.
- Nelson R (2021) Ganglion cell physiology by ralph nelson. *The Organization of the Retina and Visual System*. Webvision 19.8.2021

REFERENCES

- Neves G, Lagnado L (1999) The kinetics of exocytosis and endocytosis in the synaptic terminal of goldfish retinal bipolar cells. *J Physiol* 515: 181-202.
- Okur MN, Mao B, Kimura R, Haraczy S, Fitzgerald T, Edwards-Hollingsworth K, Tian J, Osmani W, Croteau DL, Kelley MW, Bohr VA (2020) Short-term NAD⁺ supplementation prevents hearing loss in mouse models of Cockayne syndrome. *NPJ Aging Mech Dis* 6: 1.
- Pangrsic T, Singer JH, Koschak A (2018) Voltage-gated calcium channels: key players in sensory coding in the retina and the inner ear. *Physiol Rev* 98: 2063-2096.
- Park SY, Yoo YM, Jung EM, Jeung EB (2019) Distribution of and steroid hormone effects on calbindin-D_{9k} in the immature rat brain. *Brain Res Bull* 152: 225-235.
- Peineau T, Belleudy S, Pietropaolo S, Bouleau Y, Dulon D (2021) Synaptic release potentiation at aging auditory ribbon synapses. *Front. Aging Neurosci* 13: 756449.
- Piatigorsky J (2001) Dual use of the transcriptional repressor (CtBP2)/ribbon synapse (RIBEYE) gene: how prevalent are multifunctional genes? *Trends Neurosci* 24: 555-557.
- Punge A, Rizzoli SO, Jahn R, Wildanger JD, Meyer L, Schönle A, Kastrup L, Hell SW (2008) 3D reconstruction of high-resolution STED microscope images. *Microsc Res Tech* 71: 644-650.
- Purves D, Augustine GJ, Fitzpatrick D, Katz L C, LaMantia A-S, McNamara J O, Williams SM (2004) *Neuroscience*. Sunderland, MA: Sinauer Associates.
- Ramakrishnan NA, Dreschera MJ, Drescher DG (2012) The SNARE complex in neuronal and sensory cells. *Mol Cell Neurosci* 50: 58-69.
- Regus-Leidig H, Fuchs M, Löhner M, Leist SR, Leal-Ortiz S, Chiodo VA, Hauswirth WW, Garner CC, Brandstätter JH (2014) In vivo knockdown of Piccolino disrupts presynaptic ribbon morphology in mouse photoreceptor synapses. *Front Cell Neurosci* 8: 259.
- Regus-Leidig H, Ott C, Löhner M, Atorf J, Fuchs M, Sedmak T, Kremers J, Fejtová A, Gundelfinger ED, Brandstätter JH (2013) Identification and Immunocytochemical Characterization of Piccolino, a

REFERENCES

Novel Piccolo Splice Variant Selectively Expressed at Sensory Ribbon Synapses of the Eye and Ear. PLoS One 8: e70373.

Reynolds ES (1963) The use of lead citrate at high pH as an electron-opaque stain in electron microscopy. J Cell Biol 17: 208-212.

Salman A, McClements ME, MacLaren RE (2021) Insights on the Regeneration Potential of Müller Glia in the Mammalian Retina. Cells 10: 1957.

Schermelleh L, Heintzmann R, Leonhardt H (2010) A guide to super-resolution fluorescence microscopy. J Cell Biol 190: 165-175.

Schmitz F (2009) The making of synaptic ribbons: how they are built and what they do. Neuroscientist 15: 611-24.

Schmitz F, Königstorfer A, Südhof TC (2000) RIBEYE, a component of synaptic ribbons: A protein's journey through evolution provides insight into synaptic ribbon function. Neuron 28: 857-872.

Shankhwar S, Schwarz K, Katiyar R, Jung M, Maxeiner S, Südhof TC, Schmitz F (2022) RIBEYE B-Domain Is Essential for RIBEYE A-Domain Stability and Assembly of Synaptic Ribbons. Front Mol Neurosci 15: 838311.

Sheets L, Hagen MW, Nicolson T (2014) Characterization of Ribeye subunits in zebrafish hair cells reveals that exogenous Ribeye B-domain and CtBP1 localize to the basal ends of synaptic ribbons. PLoS One 9: e107256.

Shekhar K, Lapan SW, Whitney IE, Tran NM, Macosko EZ, Kowalczyk M, Adiconis X, Levin JZ, Nemesh J, Goldman M, McCarroll SA, Cepko CL, Regev A, Sanes JR (2016) Comprehensive classification of retinal bipolar neurons by single-cell transcriptomics. Cell 166: 1308-1323.

Shi Y, Sawada J, Sui G, Affar el B, Whetstone JR, Lan F, Ogawa H, Po-Shan Luke M, Nakatani Y, Shi Y (2003) Coordinated histone modifications mediated by a CtBP co-repressor complex. Nature 422: 735-738.

REFERENCES

- Shichida Y, Matsuyama T (2009) Evolution of opsins and phototransduction. *Philos Trans R Soc Lond B Biol Sci* 364: 2881-2895.
- Snellman J, Mehta B, Babai N, Bartoletti TM, Akmentin W, Francis A, Matthews G, Thoreson W, Zenisek D (2011) Acute destruction of the synaptic ribbon reveals a role for the ribbon in vesicle priming. *Nat Neurosci* 14: 1135-1141.
- Sterling P, Matthews G (2005) Structure and function of ribbon synapses. *Trends Neurosci* 28: 20-29.
- Stoll VS, Kimber MS, Pai EF (1996) Insights into substrate binding by D-2-ketoacid dehydrogenases from the structure of *Lactobacillus pentosus* D-lactate dehydrogenase. *Structure* 4: 437-447.
- Südhof TC (2004) The synaptic vesicle cycle. *Annu Rev Neurosci* 27: 509-547.
- Südhof TC (2014) The molecular machinery of neurotransmitter release (Nobel Lecture). *Angew Chem Int Ed* 53: 12696-12717.
- Sung CH., Chuang JZ (2010) The cell biology of vision. *J Cell Biol* 190: 953-963.
- Tian L, Hires SA, Mao T, Huber D, Chiappe ME, Chalasani SH, Petreanu L, Akerboom J, McKinney SA, Schreier ER, Bargmann CI, Jayaraman V, Svoboda K, Looger LL (2009) Imaging neural activity in worms, flies and mice with improved GCaMP calcium indicators. *Nat Methods* 6: 875-81.
- Tsukamoto Y, Omi N (2017) Classification of Mouse Retinal Bipolar Cells: Type-Specific Connectivity with Special Reference to Rod-Driven AII Amacrine Pathways. *Front Neuroanat* 11: 92.
- tom Dieck S, Brandstätter JH (2006) Ribbon synapses of the retina. *Cell Tissue Res* 326: 339-346.
- tom Dieck S, Altrock WD, Kessels MM, Qualmann B, Regus H, Brauner D, Fejtová A, Bracko O, Gundelfinger ED, Brandstätter JH (2005) Molecular dissection of the photoreceptor ribbon synapse: physical interaction of Bassoon and RIBEYE is essential for the assembly of the ribbon complex. *J Cell Bio* 168: 825-836.
- Vaithianathan T, Wollmuth LP, Henry D, Zenisek D, Matthews G (2019) Tracking newly released synaptic vesicle proteins at ribbon active zones. *iScience* 17: 10-23.

REFERENCES

- von Gersdorff H (2001) Synaptic ribbons: versatile signal transducers. *Neuron* 29: 7-10.
- von Gersdorff H, Matthews G (1994) Dynamics of synaptic vesicle fusion and membrane retrieval in synaptic terminals. *Nature* 367: 735-39.
- Wässle H, Boycott BB (1991) Functional architecture of the mammalian retina. *physiol rev* 71: 447-480.
- Wan L, Almers W, Chen W (2005) Two ribeye genes in teleosts: the role of ribeye in ribbon formation and bipolar cell development. *J Neurosci* 25: 941-949.
- Wahl S, Katiyar R, Schmitz F (2013) A local, periaxonal zone endocytic machinery at photoreceptor synapses in close vicinity to synaptic ribbons. *J Neurosci* 33: 10278-10300.
- Wan QF, Heidelberger R (2011) Synaptic release at mammalian bipolar cell terminals. *Vis Neurosci* 28:109-119.
- Watson CJ, Temple BL (2013) A new ATP2B2 deafwaddler allele, dfw(i5), interacts strongly with Cdh23 and other auditory modifiers. *Hear Res* 304: 41-48.
- Winey M, Meehl JB, Toole ETO, Giddings Jr TH (2014) Conventional transmission electron microscopy. *Mol Biol Cell* 25: 319-323.
- Weichselbaum T E (1946) An accurate and rapid method for the determination of proteins in small amounts of blood serum and plasma. *Am J Clin Pathol* 16: 40-49.
- Wei M, Wang W, Liu Y, Mao X, Chen TS, Lin P (2020) Protection of Cochlear Ribbon Synapses and Prevention of Hidden Hearing Loss. *Neural Plast* 2020: 8815990.
- Wong HC, Zhang Q, Beirl AJ, Petralia RS, Wang YX, Kindt K (2019) Synaptic mitochondria regulate hair-cell synapse size and function. *eLife* 8: e48914.
- Xiong W, Yu S, Liu K, Gong S (2020) Loss of cochlear ribbon synapses in the early stage of aging causes initial hearing impairment. *Am J Transl Res* 12: 7354-7366.

REFERENCES

Yuan L, Song X, Zhang L, Yu Y, Liang Z, Lei Y, Ruan J, Tan B, Liu J, Li C (2021) The transcriptional repressors VAL1 and VAL2 recruit PRC2 for genome-wide Polycomb silencing in Arabidopsis. *Nucleic Acids Res* 49: 98-113.

Zenisek D, Steyer JA, Almers W (2000) Transport, capture and exocytosis of synaptic vesicles at active zones. *Nature* 406: 849-854.

Zamponi GW (2003) Regulation of presynaptic calcium channels by synaptic proteins. *J Pharmacol Sci* 92: 79-83.

Zhu J, Zhang E, Rio-Tsonis KD (2012) *Eye Anatomy*, eLS & John Wiley & Sons, Ltd. www.els.net.

8. LIST OF FIGURES

Figure 1. Drawing of a sagittal section through the adult human eye	6
Figure 2. Schematic illustration of major retinal layers and cells of the adult human retina	8
Figure 3. Structural differences between rod and cone photoreceptors	9
Figure 4. The phototransduction cascade in vertebrate photoreceptors	10
Figure 5. Schematic representation of primary cells and their connection patterns in the mouse retina	11
Figure 6. Schematic diagram of rod photoreceptor synapse	13
Figure 7. Ultrastructure of rod photoreceptor ribbon synapse.....	15
Figure 8. Diversity of the ribbon synapse in the retina and the inner ear.....	16
Figure 9. Retinal ribbon synapse associated proteins.....	18
Figure 10. The vesicles fusion machinery in neuronal and sensory cells.....	20
Figure 11. Schematic domain structure of RIBEYE and CtBP2.....	22
Figure 12. Diagrammatic representation of RIBEYE/CtBP2 gene	23
Figure 13. RIBEYE is a main structural protein of the synaptic ribbons	24
Figure 14. Schematic representation of CtBP tetramerization	26
Figure 15. Schematic diagram of the absence of synaptic ribbon in RIBEYE KO mice	27
Figure 16. Schematic representation of targeting vector	28
Figure 17. Diagrammatic representation of heterozygous mice breeding and genotyping	41
Figure 18. RIBEYE KI does not alter the organization of the retina	58
Figure 19. RIBEYE B-domain immunostaining is absent in the retinal semithin sections of RBE ^{KI/KI} mice	60
Figure 20. RIBEYE B-domain puncta in the OPL are unchanged between RBE ^{WT/WT} and RBE ^{WT/KI} .	61
Figure 21. RIBEYE A-domain immunostaining is absent in the retina of RBE ^{KI/KI}	63
Figure 22. Verification of absence of RIBEYE A-domain immunoreactivity in RBE ^{KI/KI} retina, using novel mouse monoclonal antibody (6F4) against RIBEYE A-domain	65
Figure 23. RIBEYE A-domain puncta in the OPL are unchanged between RBE ^{WT/WT} and RBE ^{WT/KI} .	67
Figure 24. RIBEYE knock-in causes loss of synaptic ribbons at the active zone of rod photoreceptor terminal determined by transmission electron microscopy	69
Figure 25. Contour length of synaptic ribbon labeled with anti-RIBEYE B-domain antibody is decreased in the photoreceptor synapses of RBE ^{WT/KI} mice in comparison to RBE ^{WT/WT} mice.....	71
Figure 26. Contour length of synaptic ribbon labeled with anti-RIBEYE A-domain antibody is decreased in the photoreceptor synapses of RBE ^{WT/KI} mice in comparison to RBE ^{WT/WT} mice.....	72
Figure 27. The height of the synaptic ribbon in rod photoreceptor synapses is shorter in RBE ^{WT/KI} mice determined by transmission electron microscopy	73

LIST OF FIGURES

Figure 28. RIBEYE KI causes the absence of ribbons from the cone synapses and quantification of RIBEYE A-/ RIBEYE B-domain immunosignals and puncta in the IPL and ultrastructural analysis of rod bipolar cell terminals.....	75
Figure 29. Licor blot analysis of retinal lysates from RBE ^{WT/WT} , RBE ^{WT/KI} , RBE ^{KI/KI}	77
Figure 30. RIBEYE B-domain and RIBEYE A-domain immunosignal are absent in the inner ear of RBE ^{KI/KI} mice	79

9. LIST OF ABBREVIATIONS

μl	microlitre
μM	micromolar
μm	micrometre
°C	degree Celsius
A/AC	amacrine cells
ad	arciform density
ADP	adenosine diphosphate
APS	ammonium persulfate
ATP	adenosine triphosphate
AZ	active zone
BARS	brefeldin A adenosine di phosphate ribosylated substrate
BC/bi	rod bipolar cells
BSA	bovine serumalbumin
Ca ²⁺	calcium-ion
CaBP4	calcium binding protein 4
CAST1	CAZ-associated structural protein 1
CAZ	cytomatrix active zone
CB	cone bipolar cells
cDNA	complementary DNA
cGMP	cyclic guanosinemonophosphate
CME	chromatin modifying enzyme
C-terminal	carboxy terminal
CtBP1	C-terminal Binding protein 1
CtBP2	C-terminal Binding protein 2
CTD	carboxyterminal domain
CtIP	c-terminal interacting protein
DDSA	Dodecenyl Succinic anhydride
ddH ₂ O	distilled water
DMSO	dimethyl sulfoxide
DNA	deoxyribonucleic acid
dNTPs	deoxynucleotide triphosphate
ECL	Enhanced chemiluminescence
EDTA	ethylene diamine tetra-acetic acid
ELKS	Rab6-interacting/CAST family

LIST OF ABBREVIATIONS

E-PTA	ethanolic phosphotungstic acid
ERC2	ELKS/Rab6-interacting/CAST family
FALI	fluorophore assisted light inactivation
G/GC	ganglion cell
GCaMP3	genetically encoded calcium sensor
GCL	ganglion cell layer
GFP	green fluorescent protein
Glu	glutamate
GMP/GDP/GTP	guanosine mono/ di/ triphosphate
H/HC/ho	horizontal cells
HRP	horseradish peroxidase
hrs	hours
IHC	inner hair cells
ILM	inner limiting membrane
INL	inner nuclear layer
igluR	ionotropic glutamate receptor
IPL	inner plexiform layer
IS	inner segments
KCl	potassium chloride
kDa	kilo Dalton
KIF3A	kinesin motor protein
KI	knock-in
KO	knock-out
L	liter
M	molar
mbar	millibar
MG	müller glial cell
mM	millimolar
MALS	multi angle light scattering
Mg	milligram
MgCl ₂	magnesium chloride
min	minutes
ml	milliliter
mV	millivolt
mgluR6	metabotropic glutamate

LIST OF ABBREVIATIONS

N	normality
Na ⁺	sodium-ion
NAD(H)	nicotinamide adenine dinucleotide hydrogen
NBD	NADH binding domain
NFL	nerve fiber layer
ng	nanogram
NIH	national institute of health
N-terminal	amino terminal
NPG	n-Propylgallate
NSF	N-ethylmaleimide sensitive fusion
nm	nano meter
ns	not significant
OHC	outer hair cells
OLM	outer limiting membrane
ONL	outer nuclearlayer
OPL	outer plexiformlayer
OS	outer segments
PAGE	polyacrylamide gel electrophoresis
PBS	phosphate buffer saline
PFA	paraformaldehyde
PCR	polymerase chain reaction
PDE	phosphodiesterase
PGK	phosphoglycerate kinase
pH	potential hydrogen
PMCA	plasma membrane calcium ATPases
PMT	photo multipliertube
PNA	peanut agglutinin
Pre	presynaptic terminal
RB	rod bipolar cells
RBE	RIBEYE
RBE ^{WT/WT}	wildtype
RBE ^{WT/KI}	heterozygous knock-in
RBE ^{KI/KI}	homozygous knock-in
RBE ^{WT/KO}	heterozygous knock-out
RBE ^{KO/KO}	homozygous knock-out

LIST OF ABBREVIATIONS

RIM	Rab3 interacting molecule
ROI	region of interest
RPE	retinal pigment epithelium
RRP	readily releasable pool
RT	room temperature
sec	second
SEM	standard error of mean
SDS	sodium dodecyl sulphate
SV	synaptic vesicles
SR	synaptic ribbon
SR-SIM	super resolution structure illuminated
T	transducing
TEMED	tetramethyl ethylenediamine
TEM	transmission electron microscopy
t-SNARE	target-Soluble (NSF Attachment Protein)
v-SNARE	vesicle-Soluble (NSF Attachment Protein)
WPRE	posttranscriptional regulatory element WPRE of woodchuck hepatitis virus

10. CV AND PUBLICATIONS

“The curriculum vitae was removed from the electronic version of the doctoral thesis for reasons of data protection.”

„Aus datenschutzrechtlichen Gründen wird der Lebenslauf in der elektronischen Fassung der Dissertation nicht veröffentlicht.“

Publication:

- **Soni Shankhwar**, Karin Schwarz, Rashmi Katiyar, Martin Jung, Stephan Maxeiner, Thomas C Südhof, Frank Schmitz, “**RIBEYE B-Domain Is Essential for RIBEYE A-Domain Stability and Assembly of Synaptic Ribbons**” *Front Mol Neurosci* 15, 838311, 2022.
- Rashmi Katiyar R, Renate Lewis, Linda Madisen, Karin Schwarz, Ulf Matti, Shweta Suiwal, **Soni Shankhwar**, Chad P. Grabner et al., “**An unexpected positive feedback GABA enhances presynaptic Ca²⁺ release from an endogenous Ca²⁺-store close to the synaptic ribbon in mouse rod photoreceptor synapses**” (Manuscript under preparation).
- **Soni Shankhwar**, Mulayam Singh Gaur, “**Simple approach of synthesis of stable Gold nanoparticles, characterization and study of various parameters for arsenic detection**” *NBL-2016* Vol. 3, No. 1, p. 295 doi:10.3850/978-981-09-7519-7nbl16-rps-295.
- **Soni Shankhwar**, Mulayam Singh Gaur, Amit Kumar Sharma, Rajni Yadav, Boris B. Dzantiev, “**Novel Preparation of Gold Nanoparticles with Application for the Amperometric Determination of Arsenic**”, *analytical letter* 49(9) 1388-1397, 2016.
- Amit Kumar Sharma, **Soni Shankhwar**, Mulayam Singh Gaur, “**PEI-Conjugated AuNPs as a Sensing Platform for Arsenic (AS-III)**”, *Journal of experimental nanoscience*, 9(9) 892-905, 2013.

Conferences/ Presentations/ Workshops

- Attended ribbon synapses symposium 2017, Institute for Auditory Neuroscience, University Medical Center Göttingen, Germany
- Oral research paper presentation “**Binding of chemically synthesized spherical gold nanoparticles with arsenic**” at *National Conference Engineering, Science & Management: Innovation & Challenges, 10-11th March 2016* organized by Delhi Technical Campus, Greater Noida, India.
- Presented a poster on “**Extraction and purification of Tyrosine Hydroxylase from leaves of *Mucuna pruriens***”, at *9th Symposium on Frontiers in Biomedical Research, 14-16th April 2014* organized by Dr. B.R. Ambedkar Center for Biomedical Research, University of Delhi North Campus, India.
- Presented a poster on “**Synthesis and Characterization of GNPs synthesized by triple reducing agent**”, at *National Conference/ workshop on synthesis, characterization and application of advanced nanomaterials, 17-19th January 2014* organized by Hindustan College of Science and Technology, Mathura, India.
- Presented a poster on “**Binding of chemically synthesized spherical gold nanoparticles with arsenic**”, at *International Conference on Emerging Technologies: Micro to Nano 2013 (ETMN-2013), February 23-24, 2013* organized by BITS Pilani, KK Birla Goa Campus India.
- Presented a poster on “**Design of colorimetric methodology for detection of arsenic in water samples at nanogram level**” *National Symposium on “Recent advances in Nanoscience, Engineering & Technology (RANET-11), November 19-20, 2011”* CNTL (Computational Nanoscience & Technology Lab) IITM, Gwalior India.
- Instructional workshop on Proteomics and Proteogenomics: **Hands-on Protein Identification and Gene Discovery from Mass Spectrometry Data** to be held from October 10-12, 2015 at Web Facilitation Centre, Acharya Narendra Dev College, University of Delhi.
- 32nd Annual convention of Indian Association of cancer research on “Emerging trends in cancer research Road to prevent and cure” **and International Symposium on Infection and cancer, 13-16 February 2013** organized by Dr. B. R. Ambedkar Center for Biomedical Research, University of Delhi North Campus, India.



RIBEYE B-Domain Is Essential for RIBEYE A-Domain Stability and Assembly of Synaptic Ribbons

Soni Shankhwar^{1*}, Karin Schwarz¹, Rashmi Katiyar¹, Martin Jung², Stephan Maxeiner¹, Thomas C. Südhof³ and Frank Schmitz^{1*}

¹Institute of Anatomy and Cell Biology, Saarland University, Medical School, Homburg, Germany, ²Institute of Medical Biochemistry and Molecular Biology, Saarland University, Medical School, Homburg, Germany, ³Department of Molecular and Cellular Physiology, Stanford University School of Medicine, Stanford, CA, United States

OPEN ACCESS

Edited by:

Jaewon Ko,
Daegu Gyeongbuk Institute of
Science and Technology (DGIST),
South Korea

Reviewed by:

Wallace B. Thoreson,
University of Nebraska Medical
Center,
United States
Didier Dulon,
Institut Pasteur, France

*Correspondence:

Soni Shankhwar
sonikk27@gmail.com
Frank Schmitz
frank.schmitz@uks.eu

Specialty section:

This article was submitted to
Molecular Signalling and Pathways,
a section of the journal
Frontiers in Molecular Neuroscience

Received: 17 December 2021

Accepted: 03 January 2022

Published: 28 January 2022

Citation:

Shankhwar S, Schwarz K, Katiyar R,
Jung M, Maxeiner S, Südhof TC and
Schmitz F (2022) RIBEYE B-Domain
Is Essential for RIBEYE A-Domain
Stability and Assembly of Synaptic
Ribbons.
Front. Mol. Neurosci. 15:838311.
doi: 10.3389/fnmol.2022.838311

Synaptic ribbons are presynaptic specializations that define eponymous ribbon synapses. Synaptic ribbons are largely composed of RIBEYE, a protein containing an N-terminal A-domain and a carboxyterminal B-domain that is identical with CtBP2, a NAD(H)-binding transcriptional co-repressor. Previously we showed that synaptic ribbons are completely absent in RIBEYE knockout mice in which the RIBEYE A-domain-encoding exon had been deleted, but CtBP2 is still made, demonstrating that the A-domain is required for synaptic ribbon assembly. In the present study, we asked whether the RIBEYE B-domain also has an essential role in the assembly of synaptic ribbons. For this purpose, we made use of RIBEYE knockin mice in which the RIBEYE B-domain was replaced by a fluorescent protein domain, whereas the RIBEYE A-domain was retained unchanged. We found that replacing the RIBEYE B-domain with a fluorescent protein module destabilizes the resulting hybrid protein and causes a complete loss of synaptic ribbons. Our results thus demonstrate an essential role of the RIBEYE B-domain in enabling RIBEYE assembly into synaptic ribbons, reinforcing the notion that RIBEYE is the central organizer of synaptic ribbons.

Keywords: retina, inner ear, ribbon synapse, synaptic ribbon, RIBEYE A-domain, RIBEYE B-domain, CtBP2, presynaptic active zone

INTRODUCTION

Ribbon synapses are specialized chemical synapses found in the retina, inner ear, and pineal gland (Matthews and Fuchs, 2010; Moser et al., 2020). These synapses are continuously active and possess specialized active zones that allow fast, precisely timed signaling for prolonged periods of time. Exocytosis of synaptic vesicles occurs at the active zones close to the voltage-gated Ca²⁺-channels (Cav-channels) (Zenisek et al., 2000; Grabner and Moser, 2021). The active zones of ribbon synapses associate with large, electron-dense presynaptic specializations, the synaptic ribbons, that tether and deliver large numbers of synaptic vesicles to the active zone similar to an assembly line (Vaithianathan et al., 2019; Joselevitch and Zenisek, 2020). The ribbon-associated docked vesicles close to the active zone represent the vesicle pool that fuses with the fastest release kinetics (Moser et al., 2020; Grabner and Moser, 2021). Synaptic vesicles associated with more distant parts of the ribbon away from the active zone refill vacated release sites and promote continuous signaling (Zenisek et al., 2000; Vaithianathan et al., 2019; Joselevitch and Zenisek, 2020).

Synaptic ribbons are large presynaptic structures with a complex three-dimensional (3D) shape (Moser et al., 2020). The 3D shape and size of the ribbon are relevant for synaptic transmission/signaling because the ribbon geometry

determines the pool size of ribbon-associated vesicles (Moser et al., 2020; Kesharwani et al., 2021). The photoreceptor synapse as the first synapse in the visual system transmits light stimuli to the inner retina. In the mouse retina, rod photoreceptors represent the major type of photoreceptors (95% of photoreceptors; Moser et al., 2020). Rod photoreceptor synapses are built in a fairly uniform manner. They contain a single, large active zone with a single large, horseshoe-shaped synaptic ribbon (Schmitz, 2009; Moser et al., 2020). Due to their large size and conspicuous horseshoe-shaped morphology, rod ribbons are particularly suitable for imaging analyses. In the inner retina, bipolar cell terminals possess multiple active zones with smaller synaptic ribbons that are morphologically and functionally more diverse than rod photoreceptor synapses in the outer retina (Moser et al., 2020).

Despite differences in size and shape, all ribbons contain the ribbon-specific protein RIBEYE (Schmitz et al., 2000; Moser et al., 2020), the core protein of all synaptic ribbons (Schmitz et al., 2000; Maxeiner et al., 2016; Becker et al., 2018; Jean et al., 2018). RIBEYE is evolutionarily conserved in vertebrates, and also serves as a major building block of synaptic ribbons in zebrafish (Lv et al., 2016; Sheets et al., 2017). Structurally, RIBEYE consists of a unique N-terminal, proline-rich A-domain, and a carboxyterminal B-domain that is identical (except for the N-terminal 20 amino acids) to the nuclear transcriptional co-repressor CtBP2 (Schmitz et al., 2000; Piatigorski, 2001). The RIBEYE B-domain/CtBP2 emerged from a family of D isomer-specific 2-hydroxyacid dehydrogenases (Goldberg et al., 1994). RIBEYE has multiple binding sites for other RIBEYE proteins both in the A- and B-domain of RIBEYE (Magupalli et al., 2008; Madison et al., 2013; Bellesis et al., 2018; Jecrois et al., 2021). However, the contribution of the RIBEYE A- and B-domains to the formation of synaptic ribbons remains unclear. Based on cell transfection experiments, the RIBEYE A-domain appears to serve mainly as a structural component of the synaptic ribbon scaffold (Schmitz et al., 2000; Magupalli et al., 2008), but it is unknown whether the RIBEYE A-domain alone is sufficient for the assembly of synaptic ribbons *in-situ* or whether this process also depends on RIBEYE B-domain.

In order to understand whether RIBEYE B-domain plays a role in the assembly of synaptic ribbons, we made use of RIBEYE^{KI} knockin (KI) mice (Maxeiner et al., 2016). In these KI mice, RIBEYE B-domain has been replaced by GCaMP3 in the KI allele, thus making these animals an ideal tool to study the role of the RIBEYE B-domain. We found that in the absence of the RIBEYE B-domain, synaptic ribbons are not assembled and the RIBEYE A-domain/GCaMP3 fusion protein is destabilized. Thus, the RIBEYE B-domain is essential for the assembly of synaptic ribbons.

MATERIALS AND METHODS

Mice

All animal care and use procedures were reviewed and approved by the local animal authorities (Landesamt für Verbraucherschutz; Geschäftsbereich 3; 66115 Saarbrücken,

Germany; GB 3-2.4.1.1-K110/180-07). Mice were anesthetized with isoflurane and killed by cervical dislocation in ambient light before organ collection. The RIBEYE knockin (KI) mice that were analyzed in the present study were generated by Maxeiner et al. (2016). In the RIBEYE KI, the alternative exon 1b of the mouse CtBP2/RIBEYE gene encoding RIBEYE A-domain was fused in frame with cDNA encoding for the Ca²⁺-indicator GCaMP3 (Tian et al., 2009) concluded by a STOP codon. As a consequence, the RIBEYE B-domain was replaced by GCaMP3 in the recombinant RIBEYE KI allele (Maxeiner et al., 2016). All possible genotypes at the recombinant RIBEYE locus (WT: RBE^{WT/WT}; heterozygous KI: RBE^{WT/KI} and homozygous KI: RBE^{KI/KI}) were analyzed in the RIBEYE KI mice as indicated in the respective experiments/figures. The genotypes were obtained by breeding heterozygous mice with each other (RBE^{WT/KI} X RBE^{WT/KI}). Mice were kept under standard light/dark cycle and supported with standard food and water *ad libitum*.

Methods

Embedding of Retinas and Immunocytochemistry on Semi-thin Retina Sections

Retina samples were processed for immunofluorescence microscopy (on resin sections) as previously described (Wahl et al., 2013, 2016; Dembla et al., 2014, 2018, 2020; Mukherjee et al., 2020). In brief, mice were anesthetized with isoflurane and killed by cervical dislocation. Eyes were enucleated within 5 min *post-mortem*. The anterior eyecup including the lens was removed by puncturing the isolated eye at the equatorial plane of the eye with a 20 Gauge needle and cutting along the equatorial plane with fine dissection scissors (FST, Heidelberg, Germany; No. 15024-10). The posterior eyecup with the attached retina was flash-frozen in liquid nitrogen-cooled isopentane. Lyophilization of the tissue was performed for ≈48 h with the tissue being continuously cooled by liquid nitrogen. Lyophilization of the samples was performed at a vacuum of ≈10⁻⁷ mbar using a TCP270 turbomolecular pump (Arthur-Pfeiffer-Vacuumtechnik, Wetzlar/Aßlar, Germany) controlled by a PKG020 Pirani-gold cathode gauge control unit and an oil diffusion pump (type DUO 004B; Arthur-Pfeiffer-Vacuumtechnik, Wetzlar/Aßlar, Germany). After lyophilization, samples were equilibrated to room temperature and infiltrated with Epon resin. For better infiltration with Epon, samples were equilibrated with Epon on a rotor (≈10 rpm) at 28°C for ≈24 h. Afterward, samples were degassed for 30 min in a vacuum chamber and were polymerized at 60°C for ≈24 h.

From the polymerized tissue blocks, 0.5 μm-thin (semi-thin) sections were cut with a Reichert ultramicrotome and collected on glass cover-slips, as previously described (Wahl et al., 2013, 2016). 0.5 μm-thin sections provide higher resolution compared to paraffin-embedded sections and cryosections (Punge et al., 2008). Epon resin was removed as described previously (Wahl et al., 2013, 2016; Dembla et al., 2018, 2020; Mukherjee et al., 2020). In brief, the Epon was removed from the 0.5 μm-thin resin sections by incubating the sections in the following solutions: sodium methanolate (30% solution in methanol; Sigma-Aldrich #8.18194) for 10 min; 1:1 mixture of xylol/methanol (10 min);

Antibodies

Primary Antibodies

Antibody	Source	Reference	Dilution
RIBEYE A-domain (6F4), mouse monoclonal IgG1 antibody(stock≈0.8 mg/ml)	Generated in the present study	Raised against a GST fusion protein encoding mouse RIBEYE(A): amino acids 83–211 (NP001164215)	1:100 (IF, WB) 1:500 (Cryo) 1:50 (EM)
RIBEYE(A), rabbit polyclonal (tau)	Lab-made	Maxeiner et al. (2016)	1:500 (IF)
RIBEYE(A)/ SySy, rabbit polyclonal	Synaptic Systems; Göttingen, Germany; 192103	Kerov et al. (2018)	1:500 (Licor)
RIBEYE B-domain (2D9), mouse monoclonal IgG2b antibody	Lab-made	Dembla et al. (2018)	1:200 (IF, Licor, WB)
Rhodopsin 1D4, mouse monoclonal	Gift: Dr. R.S. Molday	Hodges et al. (1988)	1:100 (IF)
PSD95, rabbit polyclonal (L667)	Dr. T.C. Südhof	Irie et al. (1997)	1:500 (IF)
Calbindin-D-28K (KD-15), rabbit polyclonal	Sigma; Darmstadt, Germany; C7354	Park et al. (2019)	1:100 (IF)
Glial Fibrillary Acidic Protein (GFAP), rabbit polyclonal	DaKo; Glostrup, Denmark; Z0334	Gruber et al. (2021)	1:500 (IF)
SV2, mouse monoclonal	Develop. Studies Hybridoma Bank; Univ. Iowa; Iowa City, IA, USA	Buckley and Kelly (1985)	1:20 (IF)
GFP, rabbit polyclonal	Abcam; Cambridge, UK; ab290	Yuan et al. (2021)	1:2,000 (Licor)
Actin, mouse monoclonal (clone C4)	Millipore; Molsheim, France (MAB1501)	Lessard (1988) and Mukherjee et al. (2020)	1:3,000 (WB, Licor)
PMCA2 ATPase, rabbit polyclonal	Thermo Fisher; Rockford, USA; PA1-915	Lin et al. (2021)	1:500 (IF)

Secondary Antibodies

Antibody	Source	Dilution
Donkey anti-mouse Alexa 568	Invitrogen; Karlsruhe, Germany; A-10037	1:1,000 (IF)
Donkey anti-mouse Alexa 488	Invitrogen; Karlsruhe, Germany; A-21202	1:1,000 (Cryo)
Chicken anti-rabbit Alexa 488	Invitrogen; Karlsruhe, Germany; A-21441	1:500 (IF)
Donkey anti-rabbit IRDye 800CW	LI-COR Biosciences; Bad Homburg, Germany; #92532213	1:5,000 (Licor)
Donkey anti-mouse IRDye 680LT	LI-COR Biosciences; Bad Homburg, Germany; #92568022	1:5,000 (Licor)
Goat anti-mouse peroxidase-conjugate (POX)	Sigma; Taufkirchen, Germany; A3673	1:3,000 (WB)
Goat anti-mouse conjugated to 10 nm colloidal gold	Sigma; Taufkirchen, Germany; G7652	1:100 (EM)

Abbreviations: IF, Immunofluorescence on semi-thin resin sections; Cryo, Immunofluorescence on cryostat sections; Licor, Li-Cor Western blot; ECL, Western blot with enhanced chemiluminescence detection, EM, Electron microscopy. Miscellaneous reagents: Chameleon pre-stained protein ladder (Li-Cor Biosciences; Bad Homburg, Germany; #978-16526); Lectin PNA conjugated to Alexa 568 (Invitrogen; Karlsruhe, Germany; L32458).

acetone (2 × 10 min), tap water (1 min, 5×), PBS (1 min, 5×). For 3D SR-SIM analyses, 1.5 μm-thick sections instead of 0.5 μm-thin were used. The 1.5 μm-thick sections were treated for 12 min with sodium methanolate (instead of 10 min).

After resin removal, 0.5 μm-thin sections were incubated simultaneously with the indicated two primary antibodies that were generated in different animal species (mouse and rabbit) overnight at 4°C, as previously described (Wahl et al., 2013, 2016; Dembla et al., 2014, 2018). The next day, sections were washed several times with PBS to remove unbound primary antibodies and incubated with the corresponding fluorophore-conjugated secondary antibodies for 3 h at RT. After this incubation, sections were washed several times with PBS and mounted with an anti-fading solution, as previously described (Wahl et al., 2013, 2016; Dembla et al., 2018, 2020; Mukherjee et al., 2020). In control incubations, sections were incubated without primary antibody with

the rest of the immunolabeling procedure remaining the same. Further controls were performed for the double immunolabeling experiments by setting individual laser power lines to zero with unchanged detection settings. These controls were done to make sure that the immunosignal in the channel of interest does not result from the neighboring detection channels (“bleed through controls”). Immunolabeled sections were analyzed by confocal microscopy, as described below.

Confocal Microscopy and Quantification of RIBEYE Immunofluorescence Signals and RIBEYE Puncta in the OPL

Confocal microscopy was performed with an A1R confocal microscope (Nikon), as previously described (Wahl et al., 2013, 2016; Eich et al., 2017; Dembla et al., 2018; Mukherjee et al., 2020). Image acquisition was performed in a blinded manner

with the experimenter not knowing the identity (genotype) of the samples. Images were acquired with $60\times/1.40$ N.A. oil objective using laser excitation lines 488 nm and 561 nm under the control of the NIS Elements software (NIS Elements AR 3.2, 64 bit; Nikon). Identical conditions were maintained for confocal image acquisition using the “re-use” settings option of NIS Elements software for the comparative analyses of the different genotypes (RBE^{WT/WT}, RBE^{WT/KI}, and RBE^{KI/KI}). For quantification of immunolabeled sections, NIH ImageJ software (“Fiji”) was used (Schindelin et al., 2012; Schneider et al., 2012).

For quantification of fluorescence intensities, the OPL was marked as the region of interest (ROI) by using the SV2- and PSD95 immunosignals as reference for the correct placement of the ROI. SV2 and PSD95 are well-characterized markers for photoreceptor synapses and produce a very typical staining pattern in the OPL (Buckley and Kelly, 1985; Koulen et al., 1998; Maxeiner et al., 2016). ROIs were managed with the Analyze-Tools-ROI Manager in NIH ImageJ. To analyze the fluorescence integrated density, a rectangular ROI was drawn around the entire OPL. The fluorescence intensity of the immunolabeled synaptic protein of OPL was determined as integrated density. The identical OPL-ROI was used for the analysis of immunolabeled sections of all genotypes. Quantifications were done blindly. Average integrated values were normalized. For this purpose, wild-type [RBE^{WT/WT}] values were set to 100%, and heterozygous mice [RBE^{WT/KI}], and homozygous knockin mice [RBE^{KI/KI}] were related to wildtype values. Integrated density data were analyzed with Microsoft Excel. Individual datapoints were plotted as box and whisker plots in Origin Pro 2019b software. Statistical analyses for significance were performed as described below.

For counting the number of immunolabeled RIBEYE puncta per μm OPL, the length of OPL was derived from confocal NIS Elements software by using a known length distance for calibration. Confocal images were opened in ImageJ and the same OPL ROI was used for the integrated density measurements. After that, the image was duplicated (using the Image-Duplicate option of ImageJ) and puncta were counted automatically using the Process/Find Maxima-Point selection plugin (prominence 25, output/point selection including edge maxima), as described (Dembla et al., 2018). The average number of RIBEYE puncta was plotted as RIBEYE puncta per 100 μm length of OPL. Average puncta values for RBE^{WT/WT}, RBE^{WT/KI}, and RBE^{KI/KI} were plotted in Excel and data distribution was plotted in a box and whisker plot in Origin Pro 2019b software. Statistical analyses for significance were performed as described below.

Quantification of RIBEYE Immunosignals and RIBEYE Puncta Count in the IPL

For the analysis of fluorescence intensity of RIBEYE immunosignals in the IPL, integrated density measurements were performed on the acquired confocal images using Fiji NIH ImageJ (Schindelin et al., 2012; Schneider et al., 2012). The region of interest (ROI), i.e., the IPL, was selected with the help of the SV2- and PSD95 immunosignals (as described above for the OPL). A rectangular ROI was drawn around the

SV2/PSD95 immunosignals in the IPL that served as a reference for the outline of the IPL. The size of the rectangular ROI was calibrated by using known distances that were measured by the confocal imaging and NIS Elements software. The same ROI was used for determining the RIBEYE puncta in the respective double-immunolabeled sections. The size of the IPL ROIs was kept identical for all genotypes. Integrated density was measured as described above for the OPL.

The average integrated values of RIBEYE A-domain and RIBEYE B-domain immunosignals in the IPL were normalized. The mean of the RBE^{WT/WT} values was set to 100% and RBE^{WT/KI}, and RBE^{KI/KI} were compared with RBE^{WT/WT} wildtype values. Integrated density values were calculated in Microsoft Excel and individual data distribution was plotted as box and whisker plot with Origin Pro 2019b software. Statistical analysis was performed using Mann-Whitney *U*-test in Origin Pro 2019b or online Mann-Whitney *U*-test¹ because data were non-normally distributed.

The number of immunolabeled RIBEYE A- and RIBEYE B-puncta in the IPL were counted automatically using the point selection plugin of ImageJ, as described above for the OPL. The puncta were counted in a rectangular area of $3,000 \mu\text{m}^2$ of an immunolabeled retina cross-section. Average RIBEYE puncta of RBE^{WT/WT}, RBE^{WT/KI}, and RBE^{KI/KI} retinas were plotted in Excel and individual data distribution was plotted in a box and whisker plot in Origin Pro 2019b software. Statistical analyses were done as described below.

3D Super-Resolution Structured Illuminated Microscopy (3D SR-SIM) and Measurement and Quantification of Ribbon Contour Length

3D SR-SIM microscopy resolves immunolabeled objects beyond the diffraction limit of light (Schermelleh et al., 2010). For 3D SR-SIM microscopy, images were acquired from 1.5 μm -thick immunolabeled retina sections using the ELYRA PS1 setup (Carl Zeiss Microscopy GmbH), largely as previously described (Dembla et al., 2020; Mukherjee et al., 2020; Kesharwani et al., 2021). The 1.5 μm -thick sections, which were processed for 3D SR-SIM, were labeled only with a single primary antibody (anti-RIBEYE A-domain: 6F4 or anti-RIBEYE B-domain: 2D9, as described in the respective figures) and processed for indirect immunofluorescence microscopy as described above. Images were acquired with a $63\times/1.4$ NA oil (DIC) objective using the 561 nm laser line collected by an Andor iXon EM-CCD camera (100 ms exposure time), as previously described (Wahl et al., 2013, 2016; Dembla et al., 2020; Mukherjee et al., 2020; Kesharwani et al., 2021). For obtaining 3D SR-SIM images, z-stack images were taken at 125 nm intervals by using Zen 2012 software (black version). The entire thickness of the retinal section was scanned, and images were then processed for 3D SR-SIM. Single cropped anti-RIBEYE-immunolabeled synaptic ribbons were iteratively scanned to ensure that the entire immunolabeled synaptic ribbon was completely captured by the scans using ZEN 2.3 SP1 software (black version). From the z-stacks, the 3D views were created in transparent mode

¹<https://astatsa.com/WilcoxonTest/>

with ZEN 2.3 SP1 software. Maximum 2D projection images were generated from the 3D images of single, cropped synaptic ribbons, as previously described (Dembla et al., 2020; Mukherjee et al., 2020). The contour length of the maximum 2D projections was measured using the open polyline tool (Dembla et al., 2020; Mukherjee et al., 2020; Kesharwani et al., 2021). Average values were calculated and plotted in Microsoft Excel. Box and whisker plots were generated using Origin Pro 2019b software. Statistical analyses were performed as described below.

Immunolabeling of PNA-Stained Cone Synapses on Cryostat Sections of the Mouse Retina

Visualization of cone synapses with the fluorescent lectin PNA Alexa 568 and immunostaining of cone synapses was performed on ≈ 10 μm -thick cryostat sections, as previously described (Grabner et al., 2015). Cryostat sections were obtained from the retinas of RBE^{WT/WT} and RBE^{KI/KI} mice. For immunostaining/cone staining, cryo-sections were first heat fixed (10 min, 50°C) and then incubated with blocking buffer (0.5% BSA in PBS), for 1 h at RT. Next, sections were incubated with primary antibodies 6F4 (1:500 in blocking buffer, overnight, 4°C). Sections were washed three-four times with PBS and incubated simultaneously with donkey anti-mouse Alexa 488 secondary antibody (1:1,000 in blocking buffer) and PNA Alexa 568 (1:200 in blocking buffer) for 3 h at RT. After several washes with PBS, sections were mounted with anti-fading solution, as described above.

Isolation of the Mouse Inner Ear and Whole-Mount Immunostaining of the Organ of Corti

For the dissection of the mouse cochlea, 4–8 weeks old RBE^{WT/WT} and RBE^{KI/KI} mice were used. Mice were anesthetized with isoflurane and killed by cervical dislocation/decapitation. After decapitation, mice heads were chilled for 15 min on ice. Isolation of the cochlea was performed, largely as described previously (Montgomery and Cox, 2016; Fang et al., 2019). In brief, first, the skull bone was removed after making a cut along the sagittal suture. The brain was removed and the cranial nerves were scrapped away from the temporal bone with an anatomical forceps (Schreiber Instrument, Fridingen Germany; SI Line; SI-14-1531). The petrous part of the temporal bone was transferred to a 2 ml microcentrifuge tube containing 4% PFA in PBS (pH 7.4) and incubated overnight at 4°C on a shaker. After several washes with PBS, the temporal bone was decalcified with a solution containing 120 mM ethylenediamine-tetraacetic acid (EDTA) in PBS, pH 7.4 (for 3 days, 4°C). EDTA solution was changed two times a day (after ≈ 8 h) (Montgomery and Cox, 2016). After decalcification, the temporal bone was washed again four-five times with PBS. The organ of Corti was isolated from the decalcified temporal bone as described previously (Montgomery and Cox, 2016; Fang et al., 2019). In brief, the vestibular portion of the petrous part of the temporal bone was held with forceps and cut away from the cochlea by a cut through the oval window and round window with a scalpel. After that, the bony capsule was removed and the cochlear turns were dissected. The isolated organs of Corti dissected from the

basal, middle, and apical turn were placed in 24-well plates filled with PBS.

For immunostaining, samples were incubated with 300 μl blocking/permeabilization solution (0.5% BSA, 1% Triton X-100 in PBS; 1 h 30 min, RT, rotary shaker). Afterward, samples of the cochlea were double-immunolabeled with the indicated primary antibodies overnight at 4°C on a shaker. Antibodies were diluted in 0.5% BSA, 1%, Triton X-100 in PBS. After removing the unbound primary antibody with several washes in PBS, samples were incubated with corresponding secondary antibodies diluted in PBS containing 0.5% BSA and 1% Triton X-100 (3 h at RT on a shaker). After several washes with PBS, the immunolabeled cochleas were analyzed by confocal microscopy using a 60 \times water objective (Nikon NR Apo 60 \times /1.0W DIC N2). Z-stacks were acquired from the immunolabeled inner ear wholemounts and processed for maximum projection. Representative maximum projections are shown in **Figure 13**.

Transmission Electron Microscopy (TEM)

Embedding of Retinas for Transmission Electron Microscopy

RBE^{WT/WT} wild-type, heterozygous RBE^{WT/KI}, and homozygous RBE^{KI/KI} littermate mice were used for the comparative ultrastructural analyses of retinal synapses by transmission electron microscopy (TEM). Retina samples were processed and embedded for TEM, largely as previously described (Maxeiner et al., 2016). In brief, eyes were enucleated within 5 min *post-mortem*. Isolated eyes were hemisected coronally and the anterior eyecup, including the lens, was removed. The posterior eyecups with the attached retina were fixed with 4% (wt/vol) paraformaldehyde (in PBS, pH 7.4) and 2.5% (vol/vol) glutaraldehyde (in PBS) for 12 h each (at 4°C with constant gentle shaking). Retina samples were postfixed with 1% (wt/vol) OsO₄, 1.5% (wt/vol) K₄[Fe(CN)₆] \times 3H₂O in 100 mM cacodylate buffer, pH 7.4 for 1 h (at 4°C on a rotating shaker). After three washes with 100 mM cacodylate buffer, pH 7.4, H₂O and 50 mM Na-maleate in H₂O (pH 5.0), samples were contrasted with 2% (wt/vol) uranyl acetate (UA) in 50 mM Na-maleate (pH 5.0) for 3 h (at 4°C on an orbital shaker). After several washes with maleate buffer and H₂O, samples were dehydrated in an ascending, graded series of ethanol (30%, 50%, 70%, 80%, 90%, 99%) and pure acetone (15 min, each step at RT). Acetone was gradually replaced by a mixture of acetone and increasing volumes of Epon resin (3/1, 1/1, 1/3 (v/v); 1 h each, RT). Finally, samples were infiltrated with pure Epon resin overnight (RT, mild agitation). Epon-infiltrated samples were transferred to Silica embedding molds for polymerization. Polymerization was performed at $\approx 60^\circ\text{C}$ for ≈ 24 h. Ultrathin sections (≈ 70 nm in thickness) were cut with a Reichert UCT ultramicrotome (Reichert-Jung). Sections were analyzed with a Tecnai Biotwin12 digital transmission electron microscope (FEI) equipped with a Megaview III digital camera (Gatan) and controlled by iTEM acquisition software (Olympus, Hamburg, Germany). The TEM microscope was operated at 100 kV.

Rod photoreceptor synapses in the outer plexiform layer (OPL) of the retina have a very typical ultrastructural appearance

and can be clearly identified in the OPL by their typical appearance (Lagnado and Schmitz, 2015; Moser et al., 2020). The mouse retina is a rod-dominated retina. About 95% of photoreceptor synapses are made by rod photoreceptors. Rod photoreceptors possess a single large active zone that is typically occupied by a single large synaptic ribbon (Lagnado and Schmitz, 2015; Moser et al., 2020). Cone synapses are larger in size and possess multiple active zones with smaller synaptic ribbons (Lagnado and Schmitz, 2015; Moser et al., 2020). Ribbon synapses are also present in the inner plexiform layer (IPL) of the retina. Ribbons are present in most of the presynaptic terminals of retinal bipolar cells (Okawa et al., 2019). In general, synaptic ribbons in the IPL are smaller in size than in the OPL (Moser et al., 2020).

Staining of Retina Samples With Ethanolic Phosphotungstic Acid (E-PTA) for TEM

Ethanolic phosphotungstic acid (E-PTA) staining for TEM was performed as previously described (Bloom and Aghajanian, 1968; Limbach et al., 2011). For E-PTA electron microscopy, 4–5 months old littermate mice (RBE^{WT/WT}, RBE^{WT/KI}, and RBE^{KI/KI}) were used for the analyses. The posterior eye-cups with the attached retina were immersed in 4% paraformaldehyde (PFA) in PBS (pH 7.4) (overnight at 4°C with mild shaking). After several washes with PBS, samples were dehydrated with an ascending ethanol concentration series (30%, 50%, 70%, 80%, 90%, 99%), 15 mins each step at RT. Next, samples were treated for 10 mins with absolute ethanol (100%) before samples were stained for 1.5 h in 1% phosphotungstic acid (w/v) in absolute ethanol that contained 5 drops of 95% absolute ethanol per 10 ml of staining solution (Bloom and Aghajanian, 1968; Limbach et al., 2011). Staining with E-PTA solution was performed for 1.5 h at RT on an orbital shaker. After removal of the E-PTA solution, retina samples were treated with ice-cold propylene oxide to avoid a strong exothermic reaction (Fry and Spira, 1980; Limbach et al., 2011). Propylene oxide was changed once and samples were subsequently incubated in propylene oxide for 30 min. Tissue was immersed in Epon solutions and embedded in Epon, as described above. Ultrathin sections were cut from the polymerized sample blocks and mounted on 100 mesh copper grids. Sections from E-PTA-stained samples were not further contrasted with UA or lead citrate and viewed with a Tecnai Biotwin12 (FEI) transmission electron microscope, as described above.

Quantification of the Presence of Synaptic Ribbons in Rod Photoreceptor Synapses and Determination of Ribbon Height Using TEM

The number of ribbons per rod terminal and ribbon height measurement in RBE^{WT/WT}, RBE^{WT/KI}, and RBE^{KI/KI} littermates were analyzed with TEM images from rod terminals acquired at a magnification of 43,000×. Only cross-sectioned rod terminals with a clearly visible active zone were included in the analyses. The average ratios of ribbon per rod terminal and ribbon height of RBE^{WT/WT}, RBE^{WT/KI}, and RBE^{KI/KI} mice were calculated and plotted in Microsoft Excel. For the analyses of ribbon number per rod terminal, RBE^{WT/WT} values were normalized to 1, and

RBE^{WT/KI}, RBE^{KI/KI} values were compared with RBE^{WT/WT}. Box and whiskers were plotted in OriginPro 2019b software.

For measurement of synaptic ribbon height in rod photoreceptor synapses, only rod photoreceptor synapses of RBE^{WT/WT} and RBE^{WT/KI} mice were analyzed in which the active zone could be clearly visualized and in which the typical postsynaptic configuration consisting of horizontal and bipolar cells was visible (postsynaptic triad/tetrad). Ribbon height in the rod photoreceptor terminal was measured at a magnification of 43,000× by drawing a straight line from the base of the ribbon to the top of the ribbon using iTEM software. The length of the scale bar on the exported TEM images was used as a reference for length calibration.

Embedding of Retina Samples in LR Gold for Post-embedding Immunogold Electron Microscopy

Embedding of mouse retina and processing for immunogold labeling was performed as previously described (Schmitz et al., 2000; Wahl et al., 2013) with some modifications. Briefly, freshly isolated retinas were overnight fixed in 2% paraformaldehyde (in PBS, pH 7.4) at 4°C then 3× washed with PBS. Afterward, samples were dehydrated with increasing concentration of ethanol (30% ethanol 4°C, 10 min; pre-cooled 50%, 70%, 80% to 99% ethanol, 1 h at –20°C with mild agitation using a spinning wheel rotator). Samples were infiltrated with an increasing volume of LR gold (2/1, 1/2 (v/v); 1 h each, at –20°C) and then with pure LR gold overnight –20°C. After infiltrating samples with LR Gold that contained 0.1% benzil (w/v), samples were polymerized under UV light for 48 h at –20°C. After polymerization, ultrathin sections (≈70 nm in thickness) were cut with a Reichert-Jung ultramicrotome and collected on 100 mesh gold grids.

Post-embedding Immunogold Labeling

Post-embedding immunogold labeling was performed largely as previously described (Schmitz et al., 2000; Wahl et al., 2013). For immunolabeling, ultrathin sections of LR Gold-embedded tissue were first treated with 0.5% bovine serum albumin (BSA) in PBS, pH 7.4 (45 min, RT) to block nonspecific protein binding sites (Wahl et al., 2013). Then, sections were incubated with RIBEYE A-domain (6F4) primary antibody diluted 1:50 in blocking buffer (overnight at 4°C). After several washes with PBS, sections were incubated with goat anti-mouse secondary antibody conjugated to 10 nm gold particles (1:100 in blocking buffer, 1 h, RT). After several washes with PBS, immune complexes were fixed with 2.5% glutaraldehyde in PBS (15 min, RT). After removal of the PBS, sections were contrasted with 2% uranyl acetate (in H₂O, 15 min, RT). As negative controls, primary antibodies were omitted with the rest of the immunogold labeling procedure remaining the same. Immunolabeled ultrathin sections were analyzed with a Tecnai Biotwin digital transmission electron microscope (FEI/ThermoFisher; Eindhoven, Netherlands), as described above.

Western Blot Analyses

Retinas from littermate mice of the indicated genotypes were isolated within 5 min *post-mortem* and dissolved in 200 μl Laemmli buffer. Protein lysates were solubilized by

homogenization by up-/down pipetting in a 100 μ l tip in Laemmli buffer and heated at 96°C for 10 min. The protein concentration of retina samples dissolved in the Laemmli buffer was determined with an amido black-based quantification method, as described (Dieckmann-Schuppert and Schnittler, 1997). Fifty microgram of retinal lysate was loaded per lane and separated by 10% acrylamide SDS PAGE. Proteins were electrotransferred to nitrocellulose membrane (Protran 0.45 μ m) at 50 V for 5 h (4°C). For quantitative immunoblotting, the Li-Cor Western blot (WB) fluorescence detection system was used because of its wide dynamic range and high accuracy of quantitative WB measurements (Pillai-Kastoori et al., 2020). WB membranes were treated with 5% skimmed milk in PBS (blocking buffer) for 1 h at RT to block unspecific protein binding sites. The indicated primary antibodies were incubated overnight (at 4°C) at the indicated dilutions (in 3% skimmed milk in PBS). After several washes with PBS, WB membranes were probed with secondary antibody (donkey anti-rabbit IRDye 800CW, donkey anti-mouse IRDye 680 LT) diluted 1:5,000 in 3% skimmed milk in PBS (3 h, RT). After several washes, fluorescence signals were detected with Odyssey Infrared scanner and Odyssey software (Li-Cor Biosciences; Bad Homburg, Germany). The band intensities were quantified by using densitometry in Image Studio Lite software (Image Studio Lite 5.2 software; Li-Cor). The band density of the protein of interest was normalized to the actin signal density, that served as a loading control, in the same lane. For the quantitative analysis of RIBEYE A-domain and RIBEYE B-domain WB signals, RBE^{WT/WT} wild-type values were set to 100%, and RBE^{WT/KI} and RBE^{KI/KI} were compared to the respective wild-type values. For the analysis of GFP WB signals, RIBEYE^{KI/KI} values were set to 100%, and RBE^{WT/KI} and RBE^{WT/WT} values were related to this reference. The correlation coefficient of the results in the different experiments was calculated in Microsoft Excel. The correlation coefficient was high ($r \geq 0.8$). Therefore, according to De Winter (2013), two-sample Student's *t*-test for non-equal variance was performed for determining the statistical significance. Normalized band signal graph was plotted in Microsoft Excel and statistical analysis was performed with OriginPro 2019b. In indicated experiments, Western blots were also processed for enhanced chemoluminescence (ECL) detection. In these cases, HRP-conjugated secondary antibodies were used (as summarized above). The respective ECL signals were scanned with a ChemiDocTM XRS Gel Doc system (Bio-Rad; Feldkirchen, Germany).

Peptide Arrays for Epitope Mapping

For antibody epitope mapping of RIBEYE A-domain monoclonal antibody 6F4, peptides of RIBEYE A-domain covering the N-terminus (amino acids 83–211 of mouse RIBEYE) with a length of 20 amino acids each and an overlap of five amino acids were synthesized on a hardened cellulose membrane with a ResPepSL-Synthesizer (Intavis Bioanalytical Instruments; Cologne, Germany), as described (Frank, 2002; Hilpert et al., 2007; Harsman et al., 2011). The membrane with the immobilized peptides was activated with methanol for 1 min at RT. After two brief washes with H₂O, the membrane was

equilibrated for 2 h with binding buffer (50 mM Tris-HCl, pH 7.5, 150 mM NaCl, 0.1% Triton X-100) with mild shaking at RT. Unspecific protein binding sites of the membrane were blocked by incubating membranes in a binding buffer containing 1 μ M BSA (1 h, RT). Next, the membrane was incubated with primary antibody (6F4; 1:20,000 dilution in binding buffer, overnight, 4°C). Thereafter, the membrane was washed 3 \times 10 min with binding buffer and incubated with HRP-conjugated goat anti-mouse antibody (1:10,000 in binding buffer) for 1 h at RT on a shaker. The bound antibody was visualized by enhanced chemoluminescence using a ChemiDocTM XRS Gel Doc apparatus (Bio-Rad, Feldkirchen, Germany). For the visualization of all peptide spots, the membrane was illuminated by UV light on the Bio-Rad GelDoc system.

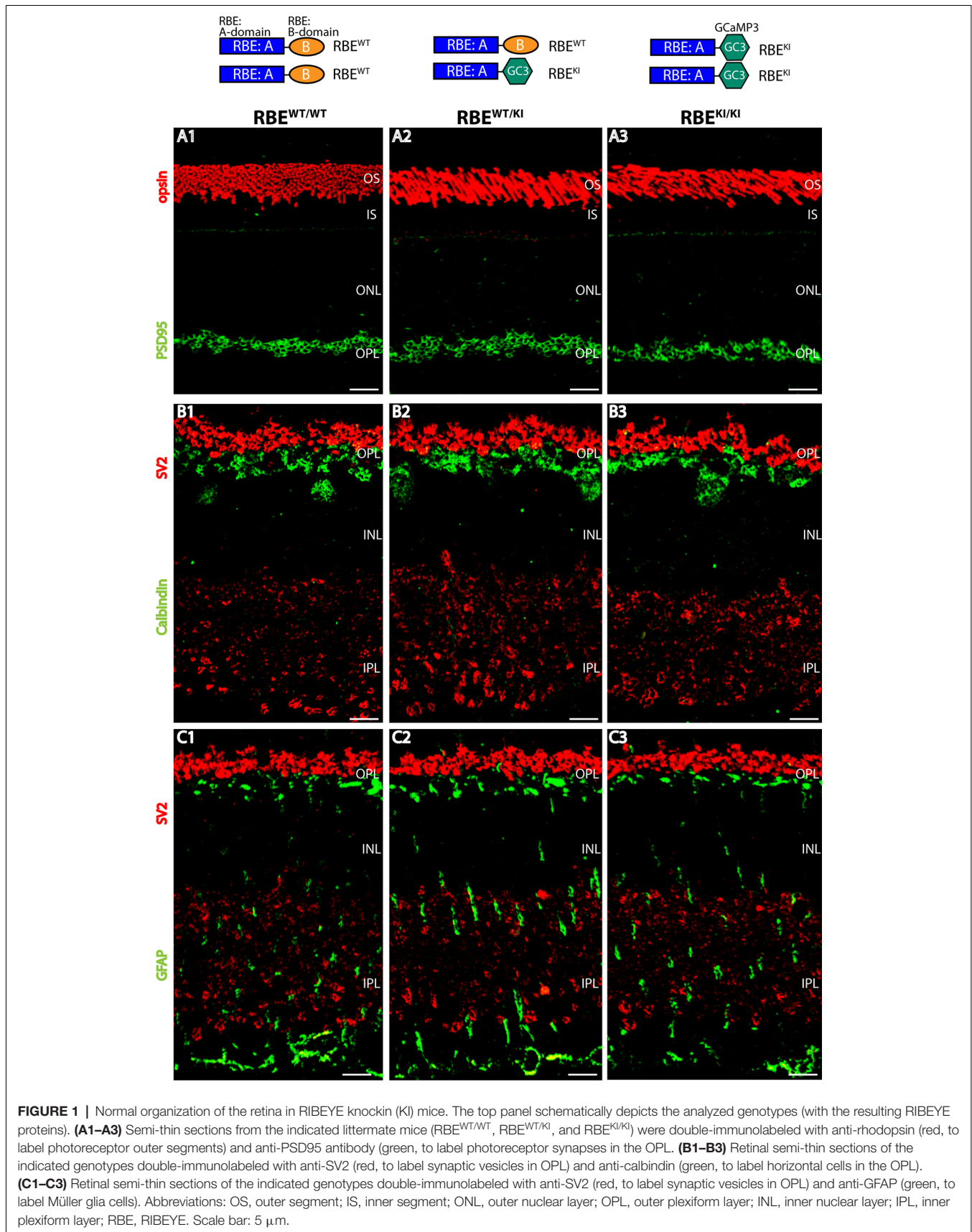
Statistical Methods

Statistical analyses were performed using OriginPro 2019b software and GraphPad Prism 8.4.3. For all analyses, at least three independent experiments were performed for each experimental group, as indicated in the respective experiments. First, we tested whether the data from individual experiments could be pooled. For this purpose, data from the individual experiments of an experimental group were checked for normality test using the Shapiro-Wilk test. Depending on the results of the Shapiro-Wilk tests, data from the individual experiments were processed for different multiple comparison analyses. For normally distributed data, ANOVA with Bonferroni's *post hoc* tests were performed; Kruskal-Wallis ANOVA test with Dunn's *post-hoc* tests were performed for non-normally distributed data at a significance level of 0.05. When multiple comparisons within the same group did not differ significantly, the data within the same was pooled. If the data within the groups were significantly different, the mean values of the individual experiments were kept and used for comparison between groups. Then data were tested for significance test between two groups. When data were normally distributed, a two-sample Student's *t*-test (with equal/non-equal variance) was used. Variance was analyzed with a two sample test for variances (OriginPro) in order to select the appropriate Student's *t*-test (equal or non-equal variances). For non-normally distributed data, nonparametric Mann-Whitney *U*-test and the two-sample Kolmogorov-Smirnov test were used, as indicated in the respective figures. Online Mann-Whitney *U*-test was performed at <https://astatsa.com/WilcoxonTest/>. Differences were considered to be statistically different with $p < 0.05$.

RESULTS

In the current study, we analyzed RIBEYE knockin (KI) mice, RBE^{KI} (Maxeiner et al., 2016) to study whether RIBEYE B-domain has a role in the assembly of synaptic ribbons. In the RIBEYE KI mice, RIBEYE B-domain has been replaced by the cDNA of GCaMP3 in the knockin (KI) allele (Maxeiner et al., 2016), making these KI mice an ideal model to study the function of the RIBEYE B-domain.

First, we checked whether the overall organization of the RBE^{KI/KI} retina is altered in comparison to littermate control



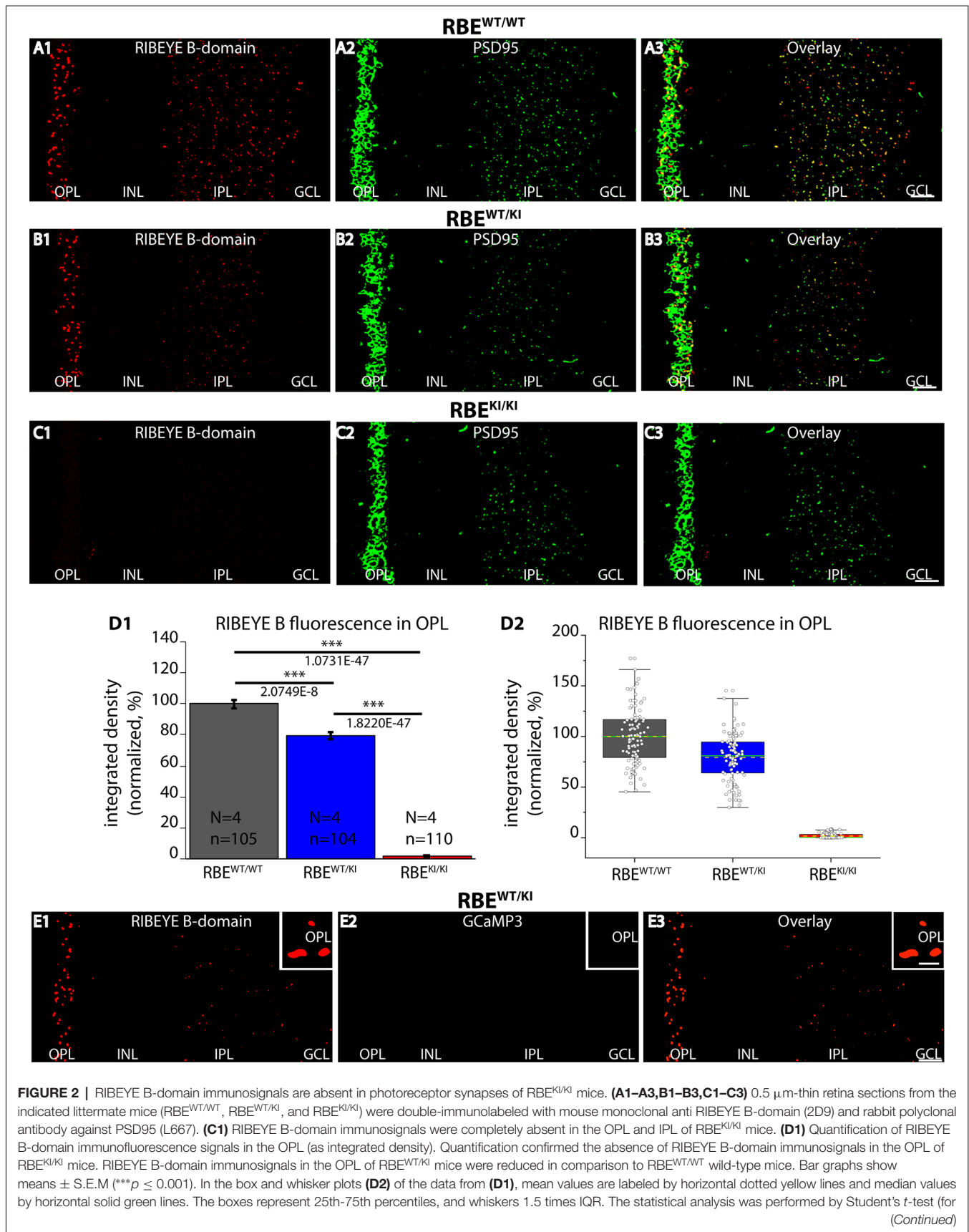


FIGURE 2 | Continued

comparison of significance between $RBE^{WT/WT}$ and $RBE^{WT/KI}$ because data were normally distributed) and Kolmogorov-Smirnov test (for comparison between $RBE^{WT/KI}$ and $RBE^{KI/KI}$ and between $RBE^{WT/WT}$ and $RBE^{KI/KI}$ because $RBE^{KI/KI}$ data were non-normally distributed). (**E1–E3**) 0.5 μm -thin retina sections from heterozygous $RBE^{WT/KI}$ mice immunolabeled with anti-RIBEYE B-domain and visualized in the red channel (**E1**). No GCaMP3 signal (direct fluorescence) is visible in the green channel in the immunolabeled semi-thin sections (**E2**). Red and green channels were merged in (**E3**). The insets show magnified regions of the OPL and confirm the absence of GCaMP3 signals at the ribbons in the OPL in semi-thin resin sections of the retina. Abbreviations: OPL, outer plexiform layer; INL, inner nuclear layer; IPL, inner plexiform layer; GCL, ganglion cell layer; RBE, RIBEYE; S.E.M., standard error of the mean; IQR, interquartile range; N = number of mice; n = number of analyzed confocal images. Scale bar: 5 μm .

mice. For this purpose, we double-immunostained retina sections obtained from mice with different RIBEYE genotypes (wildtype: $RBE^{WT/WT}$; heterozygous knockin: $RBE^{WT/KI}$ and homozygous knockin $RBE^{KI/KI}$) with various antibodies, including antibodies against opsin, to label photoreceptor outer segments (**Figure 1A**), SV2 (**Figures 1B,C**) and PSD95 (**Figure 1A**) to label retinal synapses, GFAP (**Figure 1C**) to label retinal Müller glia cells, and calbindin (**Figure 1B**) to mark horizontal cells. Using these markers, we did not observe gross alterations/differences in the retinal organization in mice with different RIBEYE genotypes ($RBE^{WT/WT}$; $RBE^{WT/KI}$, and $RBE^{KI/KI}$), arguing that the RBE^{KI} allele does not grossly affect the retinal organization. Similarly, the retinas of RIBEYE knockout mice, in which the RIBEYE protein was completely deleted, did not show gross alterations in retinal morphology and organization (Maxeiner et al., 2016).

Next, we checked for the expression of the RIBEYE B-domain in the RBE^{KI} mice (**Figure 2**) using a well-characterized mouse monoclonal antibody (clone 2D9) against the RIBEYE B-domain (Dembla et al., 2018). Both in wild-type $RBE^{WT/WT}$ mice and in heterozygous $RBE^{WT/KI}$ littermate mice, we observed strong punctate, ribbon-typical RIBEYE B-domain immunosignals in both synaptic layers (OPL and IPL) of the retina (**Figure 2**). The RIBEYE B-domain immunosignal was completely absent in the OPL and IPL of homozygous $RBE^{KI/KI}$ mice (**Figure 2C1**). The absence of RIBEYE B-domain immunosignals in the homozygous $RBE^{KI/KI}$ was expected because the RIBEYE B-domain was replaced in the RIBEYE KI allele by GCaMP3. Particularly strong RIBEYE B-domain immunosignals were observed in the OPL (**Figure 2**) of wildtype $RBE^{WT/WT}$ mice and heterozygous $RBE^{WT/KI}$ littermate mice because synaptic ribbons in rod synapses of the OPL are particularly large (Moser et al., 2020). For quantitative analyses, we thus first focused on the OPL of the retina in which the photoreceptor ribbon synapses are located.

Quantification of immunosignals in the OPL revealed that the RIBEYE B-domain immunosignals in the OPL were weaker in heterozygous $RBE^{WT/KI}$ mice compared to littermate wildtype $RBE^{WT/WT}$, and confirmed the complete absence of RIBEYE B-domain immuno-signals in $RBE^{KI/KI}$ mice (**Figure 2D**). Of note, the GCaMP3 moiety in the RIBEYE KI allele does not generate any fluorescence signals in resin sections of

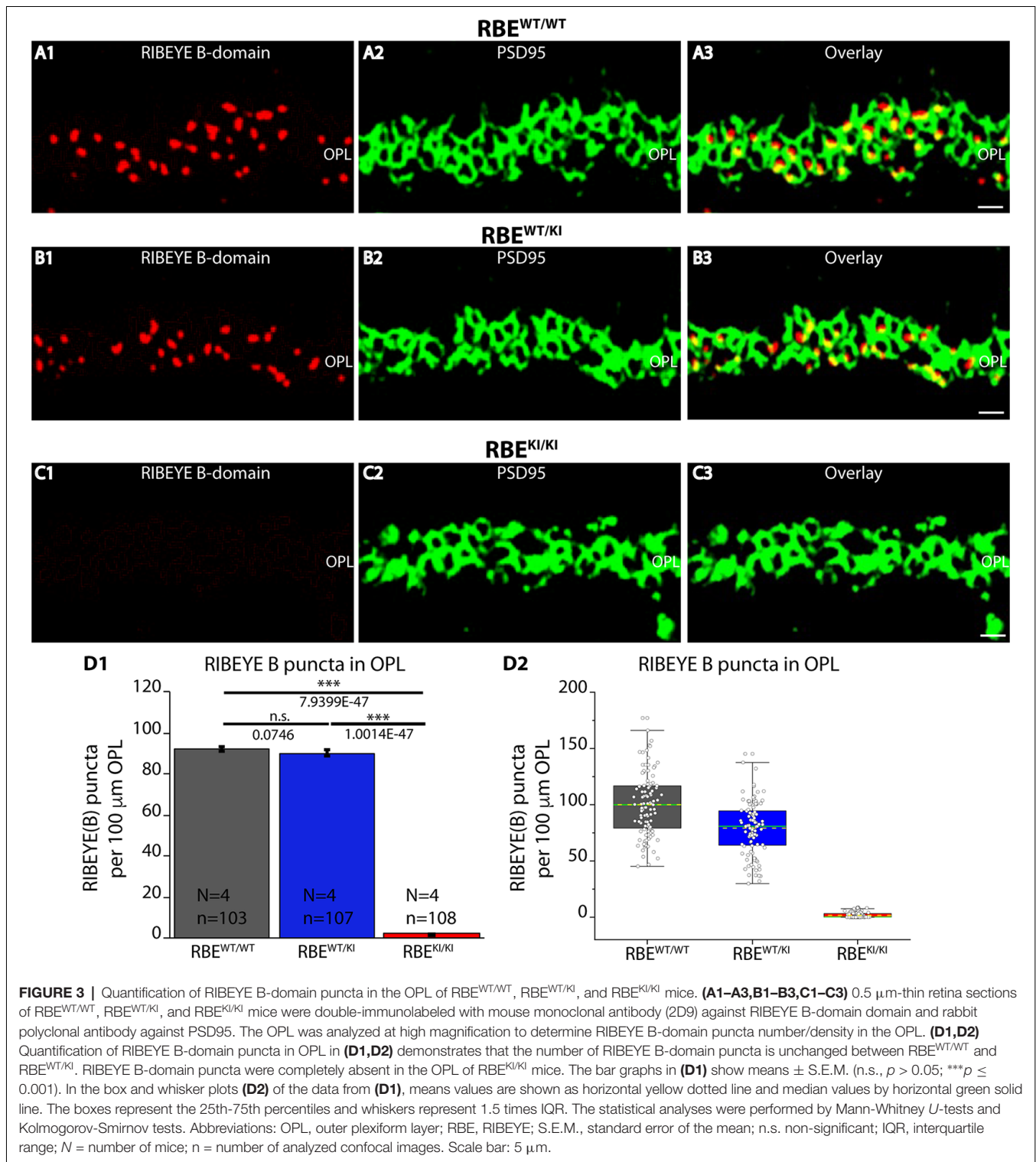
the immunolabeled retinas as shown by control incubations (**Figure 2E**).

The number and density of RIBEYE B-domain positive puncta in the OPL were determined on RIBEYE B-domain immunolabeled sections at higher magnifications that allow clear identification of single puncta (**Figures 3A–C**). Quantitative analyses revealed that the number of RIBEYE B-domain-positive puncta in the OPL were indistinguishable between $RBE^{WT/WT}$ and heterozygous $RBE^{WT/KI}$ mice (**Figure 3D**), but were completely absent from the OPL of homozygous $RBE^{KI/KI}$ mice as expected (**Figure 3D**).

The RIBEYE B-domain antibody 2D9 also detects CtBP2 that is ubiquitously expressed as a nuclear co-repressor (Dembla et al., 2018). In the 0.5 μm thin retina sections, we did not observe a nuclear staining, similar to other studies (Dembla et al., 2018; Kesharwani et al., 2021), most likely because the focal concentration of CtBP2 in the nucleus is too low.

Is the RIBEYE A-domain still assembled into ribbon-like structures in RBE^{KI} mice? To address this question, we stained retinal sections with a polyclonal antibody against RIBEYE A-domain (Maxeiner et al., 2016). As mentioned above, the RIBEYE A-domain is still present on the RBE KI allele, in contrast to the RIBEYE B-domain that has been replaced. In wildtype $RBE^{WT/WT}$ mice and heterozygous $RBE^{WT/KI}$ littermate mice, we observed a strong punctate ribbon-typical RIBEYE A-domain immunosignal in both synaptic layers of the retina (OPL and IPL) (**Figures 4A–C**). Surprisingly, the RIBEYE A-domain signal was completely absent in the OPL of $RBE^{KI/KI}$ mice (**Figures 4C,D**). Immunolabeling with an anti-SV2 antibody served as a control (**Figure 4**), demonstrating that synapses were still present as the SV2 immunosignals were unchanged in all genotypes (**Figure 4**).

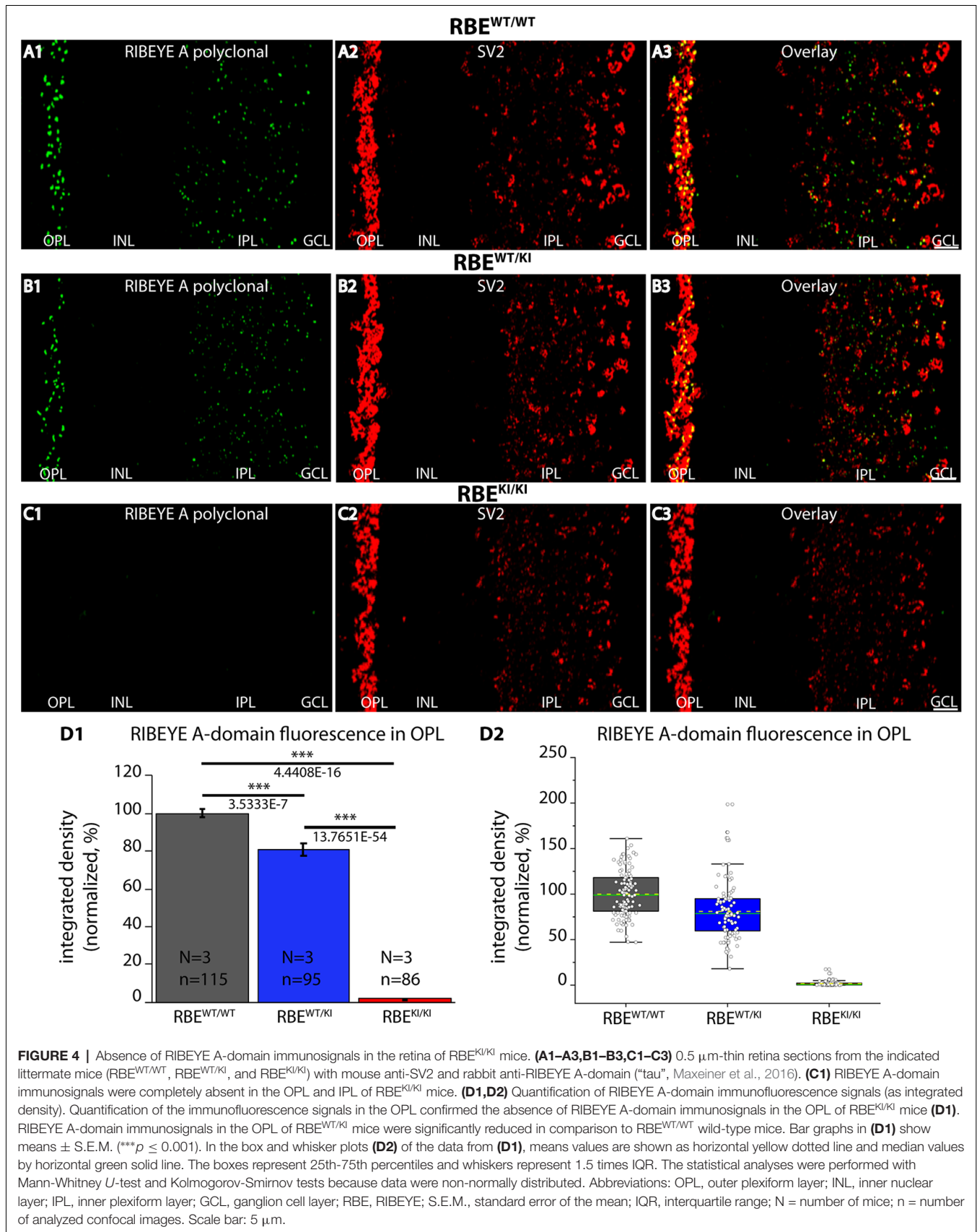
The results obtained with the rabbit polyclonal antibody against the RIBEYE A-domain (**Figures 4A–C**) were confirmed with a newly generated mouse monoclonal RIBEYE A-domain antibody, clone 6F4 (**Figure 5**). The immunostaining pattern obtained with this antibody was indistinguishable from that produced with the polyclonal RIBEYE A-domain antibody, validating the absence of RIBEYE A-domain-positive puncta in the OPL and IPL of $RBE^{KI/KI}$ mice (**Figure 5C**). In contrast, the RIBEYE A-domain immunostaining in the OPL and IPL of heterozygous $RBE^{WT/KI}$ and wildtype $RBE^{WT/WT}$ mice appeared unchanged. The newly generated mouse monoclonal RIBEYE A-domain antibody 6F4 is directed against a peptide stretch in the A-domain of RIBEYE (amino acid 83–amino acid 211 of mouse RIBEYE). The precise binding site of the antibody was determined by overlapping peptide dot blot experiments (**Figure 5F**). The specificity of the 6F4 antibody for RIBEYE was further demonstrated by Western blotting and immunofluorescence experiments on RIBEYE knockout mouse retina samples (**Figures 5D,G,H**). For the Western blotting experiments, the RIBEYE B-domain 2D9 monoclonal antibody was used for comparison. Both antibodies detected the full-length RIBEYE band at ≈ 120 kDa in control retinas, but not in retinas obtained from RIBEYE knockout mice (**Figures 5D1,E1**). The RIBEYE B-domain antibody 2D9 also detected CtBP2 at ≈ 50 kDa in control and RIBEYE knockout



retinas (Figure 5E1). CtBP2 is largely unaffected by the RIBEYE deletion in the RIBEYE knockout mice, as previously demonstrated (Dembla et al., 2018). The specificity of the RIBEYE A-domain antibody 6F4 was further confirmed by post-embedding immunogold labeling (Figure 5I). 6F4 antibody labeled synaptic ribbons in the control retina (Figure 5I1),

but not in photoreceptor synapses of RIBEYE knockout retinas (Figure 5I4).

RIBEYE A-domain puncta densities in the OPL were determined using RIBEYE A-domain immunolabeled sections at higher magnifications that allow clear identification of single, immunolabeled puncta (Figures 6A–C,E), as described



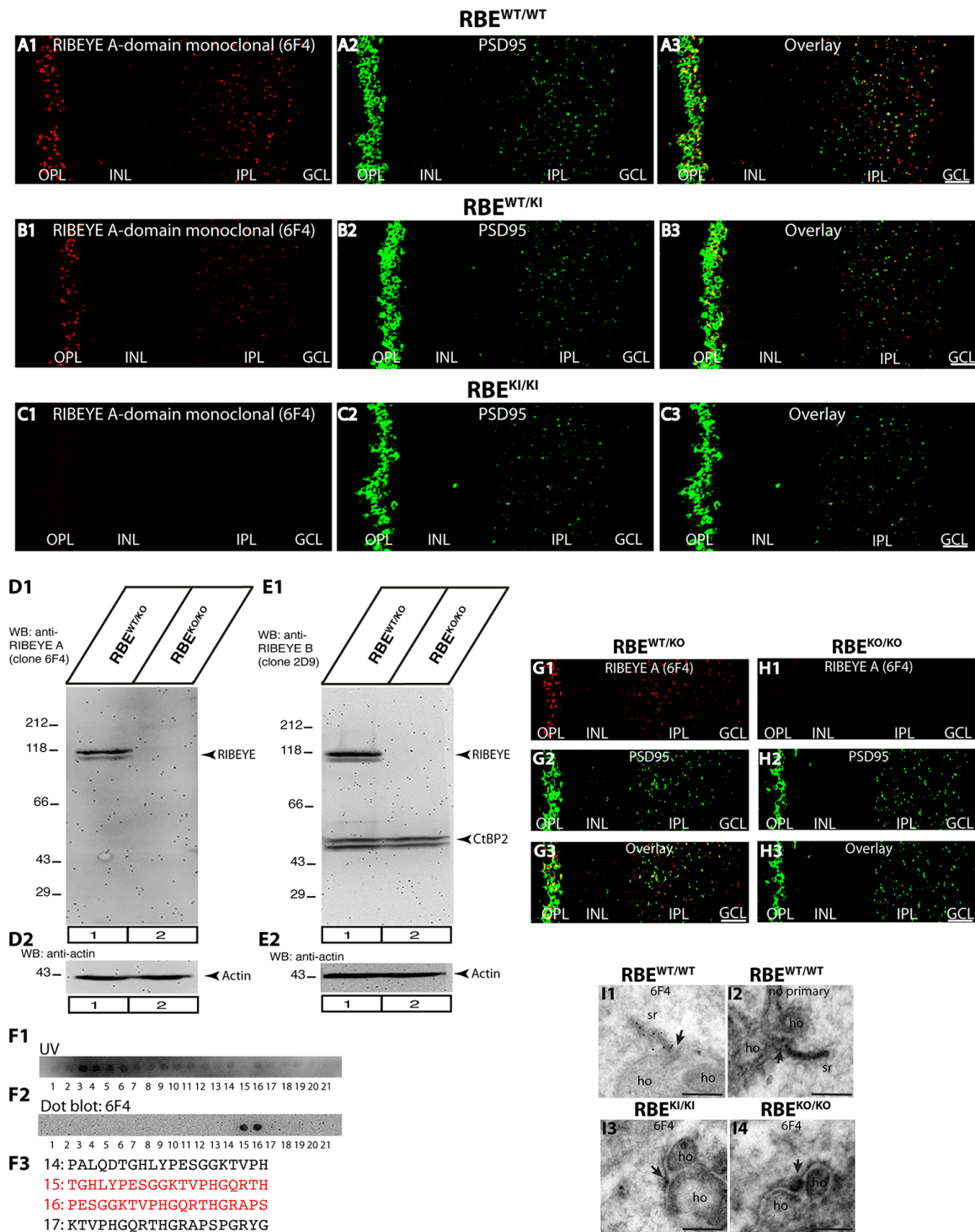


FIGURE 5 | Confirmation of absence of RIBEYE A-domain immunosignals in the retina of RBE^{KI/KI} mice with a novel mouse monoclonal antibody against RIBEYE A-domain (6F4). **(A1–A3,B1–B3,C1–C3)** 0.5 μ m-thin retina sections from the indicated littermate mice (RBE^{WT/WT}, RBE^{WT/KI}, and RBE^{KI/KI}) with mouse anti-RIBEYE A-domain (clone 6F4) and rabbit anti-PSD95. **(C1)** RIBEYE A-domain immunosignals were completely absent in the OPL and IPL of RBE^{KI/KI} mice. The specificity of the novel anti-RIBEYE A-domain antibody 6F4 was verified by different experiments. **(D1,D2)** Retinal lysate from RBE^{WT/KO} and RBE^{KO/KO} mice were probed by WB analyses with anti-RIBEYE A-domain antibody 6F4 **(D1)** and anti-actin **(D2)**. Anti-actin signals were used as a loading control. **(E1,E2)** For comparison, retinal lysate from RBE^{WT/KO} and RBE^{KO/KO} mice were also probed by WB analyses with anti-RIBEYE B-domain antibody 2D9 **(E1)** and anti-actin **(E2)**, as previously described (Dembla et al., 2018). The anti-actin signals were used as loading controls. **(F1,F2)** Overlapping peptide spots, that cover the RIBEYE A-domain fusion protein

(Continued)

FIGURE 5 | Continued

against which the antibody was generated, were probed with RIBEYE A-domain 6F4 monoclonal antibody to map the precise binding site. **(F1)** Peptide spot array trans-illuminated with UV light to visualize the location of all peptide spots. **(F2)** Peptide spot array immunolabeled with anti-RIBEYE A-domain 6F4 antibody. The binding of the antibody was visualized by enhanced chemiluminescence. Peptide spots #15 and #16 were strongly immunoreactive with 6F4 antibodies. **(F3)** Peptide sequence of peptide spots #15 and #16 that strongly reacts with 6F4 antibody are highlighted in red in **(F3)**. **(G1–G3, H1–H3)** 0.5 μm -thin retina sections from RIBEYE knockout mice ($\text{RBE}^{\text{KO/KO}}$) and control mice ($\text{RBE}^{\text{WT/KO}}$) with mouse anti-RIBEYE A-domain (clone 6F4) and rabbit anti-PSD95. The 6F4 RIBEYE antibody generated a ribbon-typical immunostaining pattern only in the retina of the control mouse **(G1)** but not in the RIBEYE knockout mouse **(H1)** demonstrating the specificity of the 6F4 monoclonal antibody for RIBEYE. The PSD95 immunostaining is unchanged in both genotypes **(G2, H2, G3, H3)**. **(I1–I4)** Post-embedding immunogold labeling of rod photoreceptor synapses of the indicated genotype with anti-RIBEYE A-domain 6F4 monoclonal antibody. Arrowhead points to the active zone of photoreceptor ribbon synapses. Abbreviations: OPL, outer plexiform layer; INL, inner nuclear layer; IPL, inner plexiform layer; GCL, ganglion cell layer; sr, synaptic ribbon; ho, horizontal cells; RBE, RIBEYE. Scale bars: 5 μm **(A–C; G–H)**; 300 nm **(I)**.

above for RIBEYE B-domain puncta density quantifications. Quantitative analyses revealed that the number of RIBEYE A-domain puncta in the OPL were indistinguishable between $\text{RBE}^{\text{WT/WT}}$ and heterozygous $\text{RBE}^{\text{WT/KI}}$ mice (**Figure 6D**). In contrast, RIBEYE A-domain puncta were completely absent from the OPL of $\text{RBE}^{\text{KI/KI}}$ mice (**Figure 6D**). The results obtained with the rabbit polyclonal antibody against RIBEYE A-domain (**Figures 6A–C**) were confirmed by immunolabeling experiments with the monoclonal RIBEYE A-domain antibody 6F4 that also demonstrated the absence of RIBEYE A-domain puncta in the OPL (**Figure 6E**).

These immunolabeling results, i.e., the absence of RIBEYE A-/RIBEYE B-immunolabeled puncta in the OPL of $\text{RBE}^{\text{KI/KI}}$ mice, that we consistently obtained with anti-RIBEYE B-domain (**Figures 2, 3**) and anti-RIBEYE A-domain antibodies (6F4 and tau; **Figures 4–6**) indicate that no structures resembling synaptic ribbons are formed in photoreceptor synapses of $\text{RBE}^{\text{KI/KI}}$ mice. To further test this conclusion, we performed ultrastructural analyses on rod photoreceptor synapses of the retinas from littermate $\text{RBE}^{\text{WT/WT}}$, $\text{RBE}^{\text{WT/KI}}$, and $\text{RBE}^{\text{KI/KI}}$ mice by transmission electron microscopy (TEM; **Figure 7**).

TEM confirmed the absence of synaptic ribbons in photoreceptor synapses of $\text{RBE}^{\text{KI/KI}}$ mice (**Figures 7C1, C2**), whereas synaptic ribbons were clearly present in $\text{RBE}^{\text{WT/WT}}$ mice (**Figures 7A1, A2**) and heterozygous $\text{RBE}^{\text{WT/KI}}$ (**Figures 7B1, B2**) (for quantification, see **Figure 7D**). Also, E-PTA-stained samples confirmed the absence of synaptic ribbons from the active zone of rod synapses in $\text{RBE}^{\text{KI/KI}}$ mice (**Figure 7C3**). Synaptic ribbons were clearly present in E-PTA-stained rod photoreceptor synapses of $\text{RBE}^{\text{WT/WT}}$ mice and heterozygous $\text{RBE}^{\text{WT/KI}}$ mice (**Figures 7A3, B3**). From these experiments, we conclude that the RIBEYE B-domain is essential for the formation of synaptic ribbons in photoreceptor synapses.

As shown above, RIBEYE A- and B-domain immunosignals in the OPL were consistently weaker in heterozygous $\text{RBE}^{\text{WT/KI}}$ mice in comparison to wild-type $\text{RBE}^{\text{WT/WT}}$ mice (**Figures 2, 4**),

whereas the ribbon density in the OPL was identical (**Figures 3, 6**). In order to identify possible reasons for the decreased RIBEYE immunosignals in the OPL of $\text{RBE}^{\text{WT/KI}}$ mice in comparison to $\text{RBE}^{\text{WT/WT}}$ mice, we measured the length of individual rod synaptic ribbons by 3D SR-SIM, as previously described (Dembla et al., 2020; Mukherjee et al., 2020; Kesharwani et al., 2021). For contour length measurements by 3D SR-SIM, rod synaptic ribbons were immunolabeled with either anti-RIBEYE B-domain (**Figure 8**) or anti-RIBEYE A-domain antibodies (**Figure 9**). By applying quantitative 3D SR-SIM analyses, we found that the contour length of synaptic ribbons was smaller in heterozygous $\text{RBE}^{\text{WT/KI}}$ compared to $\text{RBE}^{\text{WT/WT}}$ mice. This was consistently observed with both antibodies against RIBEYE (**Figures 8, 9**). This finding suggests that a decrease in the gene dosage of functional RIBEYE causes a decrease in the ribbon size, raising the exciting possibility that the ribbon size depends, among others, on the RIBEYE concentration.

In order to further characterize and confirm these light-microscopical alterations of synaptic ribbon size in photoreceptor synapses of $\text{RBE}^{\text{WT/KI}}$ mice, we performed ultrastructural analyses by using TEM. We determined the height of synaptic ribbons in cross-sections of rod photoreceptor synapses of $\text{RBE}^{\text{WT/WT}}$ mice and $\text{RBE}^{\text{WT/KI}}$ mice. The height of cross-sectioned ribbons was measured from its anchorage site in the active zone to the free cytosolic end. For the determination of ribbon height, we applied the same criteria as previously defined (Kesharwani et al., 2021). Only rod photoreceptor synaptic ribbons were included that were anchored to a clearly visible active zone and were opposed by clearly visible postsynaptic triads. This procedure was applied to exclude those tangentially sectioned ribbons (sectioned parallel to the active zone) that were erroneously included in the analyses. We found that the ribbon height in rod photoreceptor synapses of heterozygous $\text{RBE}^{\text{WT/KI}}$ mice was significantly lower ($\approx 28\%$) than in $\text{RBE}^{\text{WT/WT}}$ mice (**Figures 10A, B**; for quantification, **Figure 10C**).

The previous experiments consistently showed the absence of RIBEYE immunosignals in the OPL of $\text{RBE}^{\text{KI/KI}}$ mice (**Figures 2–6**). As mentioned above, the OPL of the mouse retina contains mostly rod synapses, but also the less abundant cone synapses. In order to exclude the possibility that cone synapses might have escaped our attention in the immunolabeling experiments, we directly visualized cone terminals in the OPL by staining with fluorescent PNA lectin (Grabner et al., 2015) and analyzed with anti-RIBEYE 6F4 whether the cone terminals show RIBEYE immunosignals (**Figures 11A1, A2**). Despite the presence of PNA-positive cone terminals, no RIBEYE signals were observed in the OPL of $\text{RBE}^{\text{KI/KI}}$ mice (**Figure 11A2**). The OPL of $\text{RBE}^{\text{WT/WT}}$ mice served as a positive control in these experiments (**Figure 11A1**). Ribbons could be readily detected in the cone terminals of $\text{RBE}^{\text{WT/WT}}$ mice (**Figure 11A1**) but not in the cone terminals of $\text{RBE}^{\text{KI/KI}}$ mice (**Figure 11A2**) indicating the absence of synaptic ribbons also in cone synapses, similar to rod synapses.

To complement these analyses in the OPL, we analyzed synaptic ribbons in the inner plexiform layer (IPL) of the retinas from $\text{RBE}^{\text{WT/WT}}$, $\text{RBE}^{\text{WT/KI}}$, and $\text{RBE}^{\text{KI/KI}}$ mice. For this purpose, we made use of the immunolabeling experiments that were

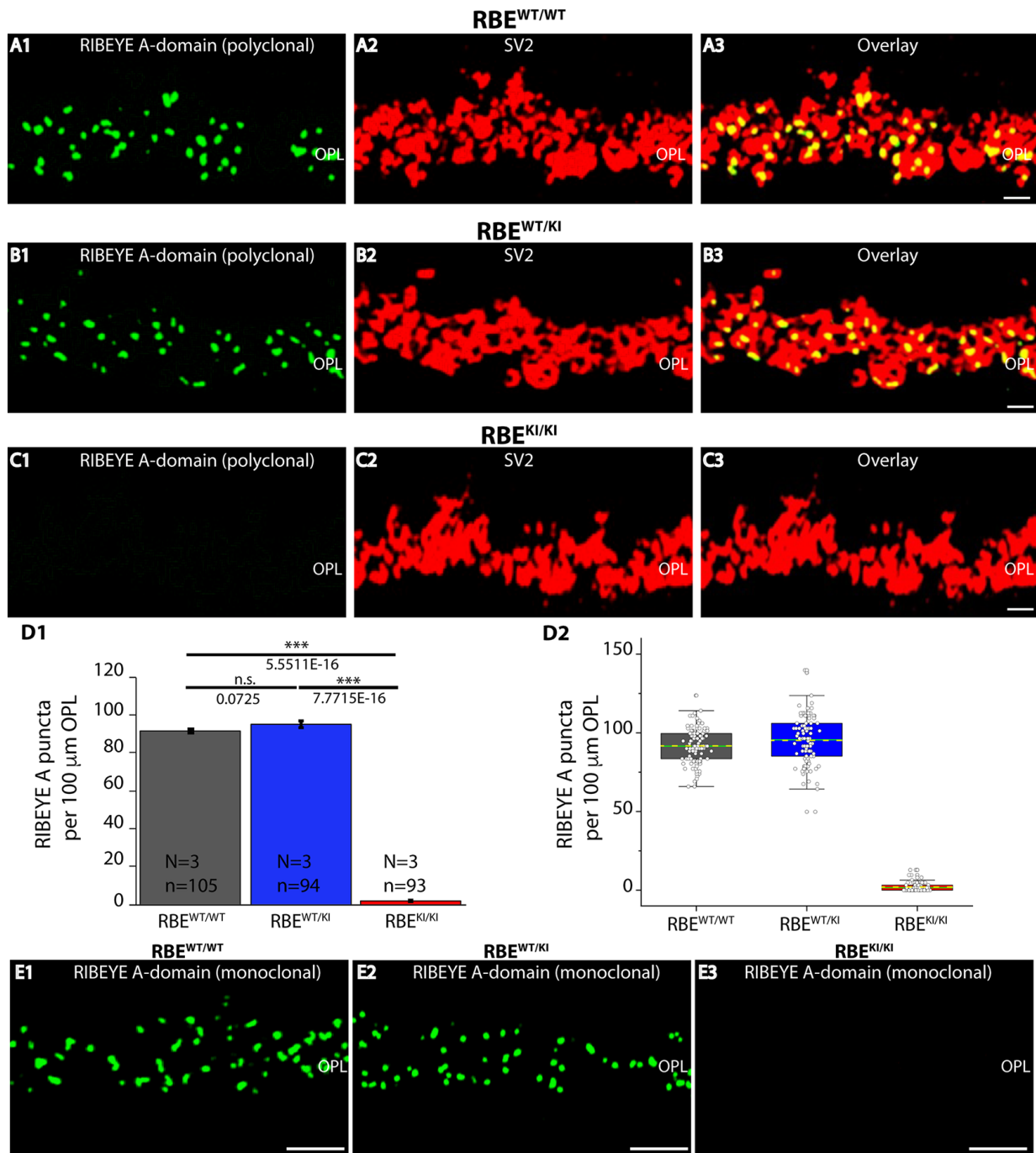


FIGURE 6 | Quantification of RIBEYE A-domain puncta in the OPL of RBE^{WT/WT}, RBE^{WT/KI}, and RBE^{KI/KI} mice. **(A1–A3, B1–B3, C1–C3)** 0.5 μm -thin retina sections of RBE^{WT/WT}, RBE^{WT/KI}, RBE^{KI/KI} mice were double-immunolabeled with mouse monoclonal anti-SV2 and rabbit polyclonal antibody against RIBEYE A-domain (tau; Maxeiner et al., 2016). The OPL was analyzed at high magnification to determine RIBEYE A-domain puncta number/density in the OPL. **(D1, D2)** Quantification of RIBEYE A-domain puncta in OPL in **(D1, D2)** demonstrates that the number of RIBEYE A-domain puncta is unchanged between RBE^{WT/WT} and RBE^{WT/KI}. RIBEYE B-domain puncta were completely absent in the OPL of RBE^{KI/KI} mice. The bar graphs in **(D1)** show means \pm S.E.M. (n.s., $p > 0.05$; *** $p \leq 0.001$). In the box and whisker plots **(D2)** of the data from **(D1)**, means values are shown as horizontal yellow dotted line and median values by horizontal green solid line. The boxes represent the 25th–75th percentiles and whiskers represent 1.5 times IQR. The statistical analysis was performed by Student's *t*-test for RBE^{WT/WT}/RBE^{WT/KI} comparison because data were normally distributed. Kolmogorov-Smirnov tests were used for RBE^{WT/WT}/RBE^{KI/KI} and RBE^{WT/KI}/RBE^{KI/KI} comparisons because RBE^{KI/KI} data were non-normally distributed. **(E1–E3)** 0.5 μm -thin retina sections of RBE^{WT/WT}, RBE^{WT/KI}, and RBE^{KI/KI} mice were single-immunolabeled with mouse monoclonal antibody against RIBEYE A-domain clone 6F4. The two RIBEYE A-domain antibodies (monoclonal 6F4, polyclonal tau) produced very similar immunolabeling patterns also at the higher magnifications shown in **Figure 6**. Abbreviations: OPL, outer plexiform layer; RBE, RIBEYE; S.E.M., standard error of the mean; IQR, interquartile range; n.s., non significant; N = number of mice; n = number of analyzed confocal images. Scale bar: 5 μm .

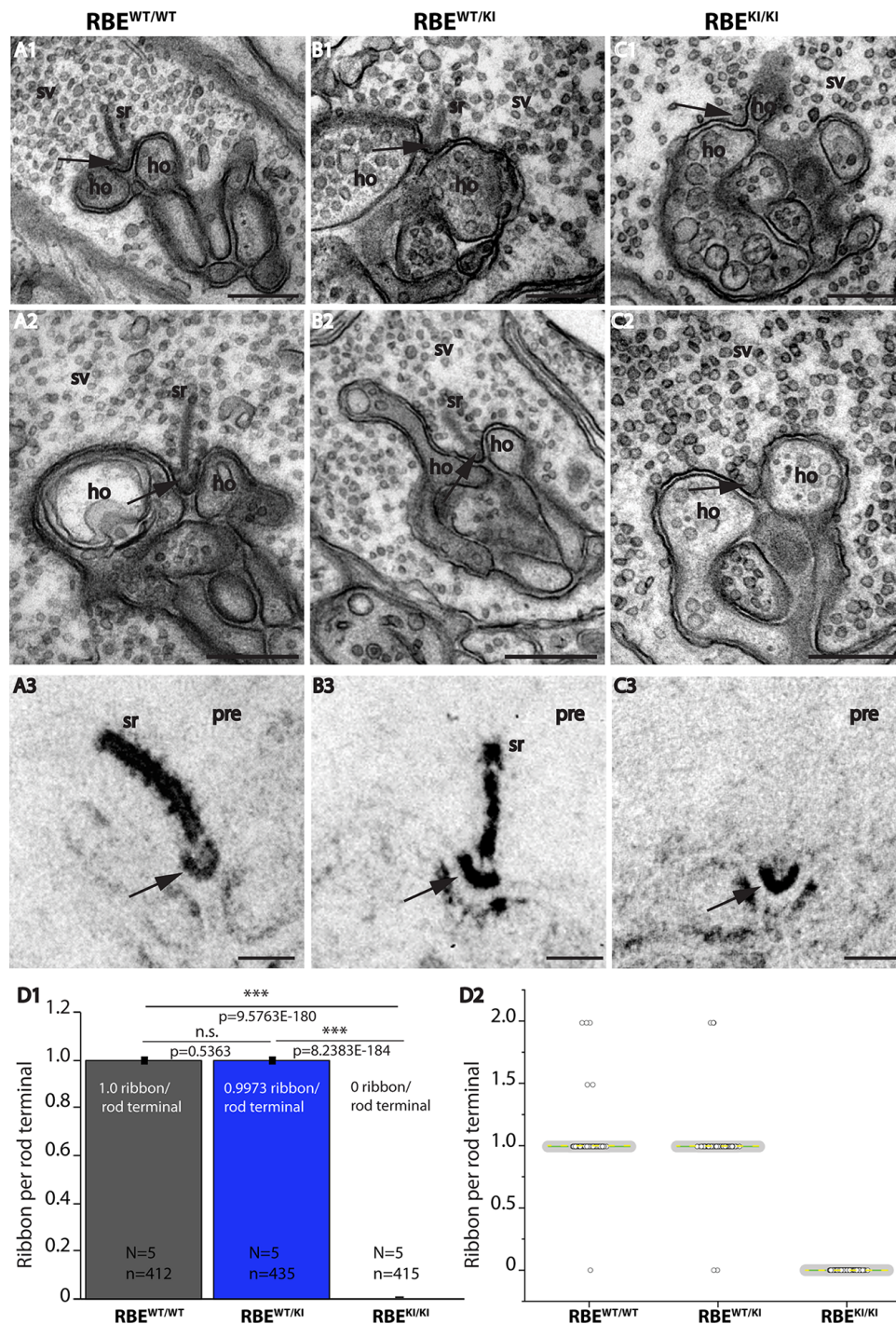


FIGURE 7 | Absence of synaptic ribbons at the active zone of rod photoreceptor terminal from RBE^{KI/KI} mice as demonstrated by transmission electron microscopy. **(A–C)** Representative transmission EM (TEM) images of rod photoreceptor terminal RBE^{WT/WT}, RBE^{WT/KI}, and RBE^{KI/KI} mice. Panels **(A1,A2,B1,B2,C1,C2)** show conventional TEM images; panels **(A3,B3,C3)** show TEM images of E-PTA-stained samples. Arrows indicate the active zone of rod synapses. **(C1,C2,C3)** Synaptic ribbons are present at the active zone of RBE^{WT/WT} and RBE^{WT/KI} mice, but completely absent from the active zone of RBE^{KI/KI} mice. Except for the absence of synaptic ribbons, the ultrastructure of the rod photoreceptor synapses of RBE^{KI/KI} mice is comparable with control. **(D)** Quantification of the number of ribbons per rod terminal. Values in **(D1)** are means ± S.E.M. (n.s., $p > 0.05$; *** $p \leq 0.001$). In the box and whisker plots **(D2)** of the data from **(D1)**, mean values are labeled by horizontal yellow dotted line and median values by horizontal green solid line. The box represents 25th–75th percentile, and whiskers represent 1.5 times of interquartile range. Statistical significance analyses were performed by Mann-Whitney *U*-tests and Kolmogorov-Smirnov tests. Abbreviations: sr, synaptic ribbon; ho, horizontal cells; SV, synaptic vesicles; pre, presynaptic; RBE, RIBEYE; S.E.M., standard error of the mean; N = number of mice, n = number of analyzed images; n.s., non-significant. Scale bar: 200 nm.

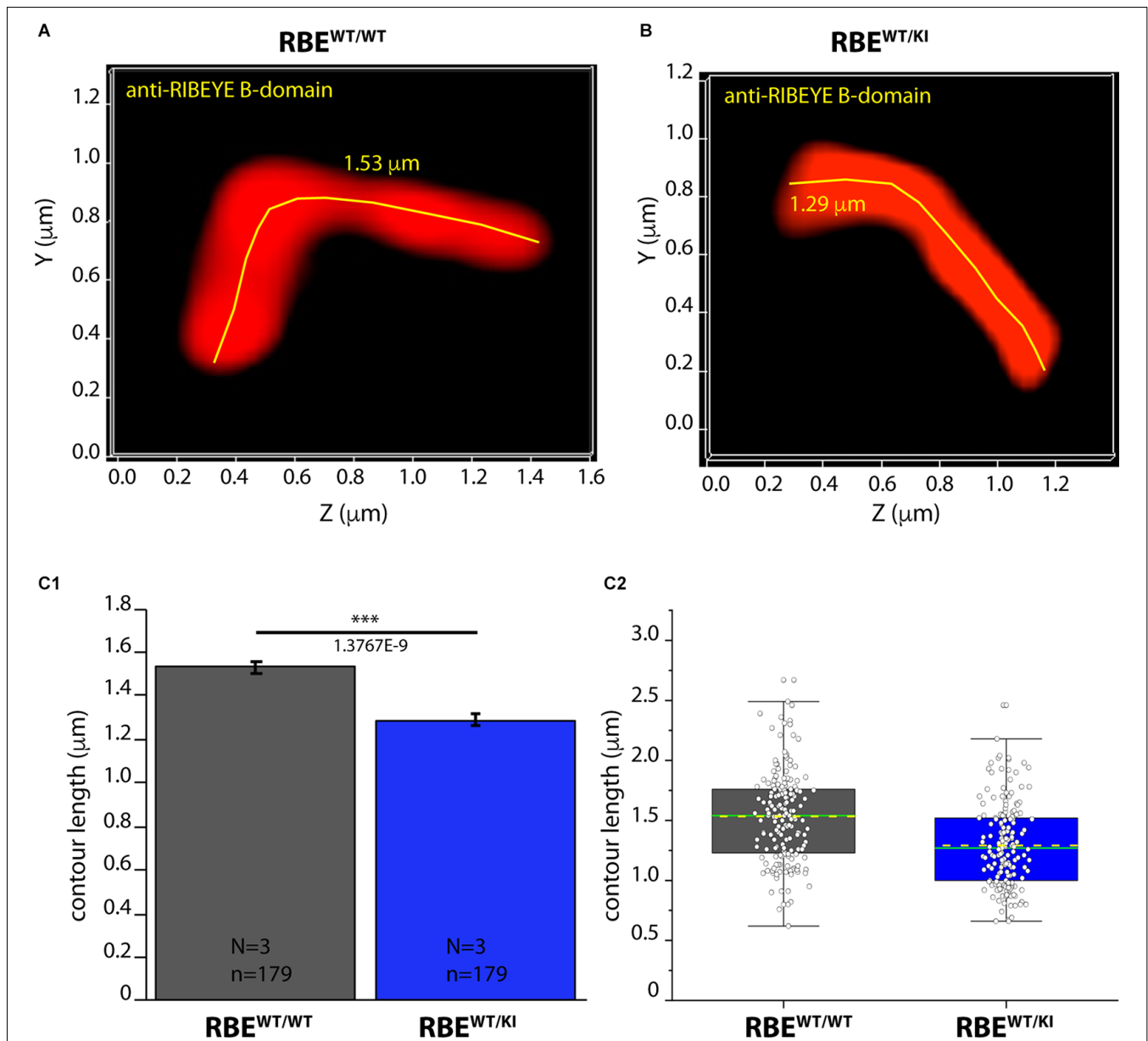
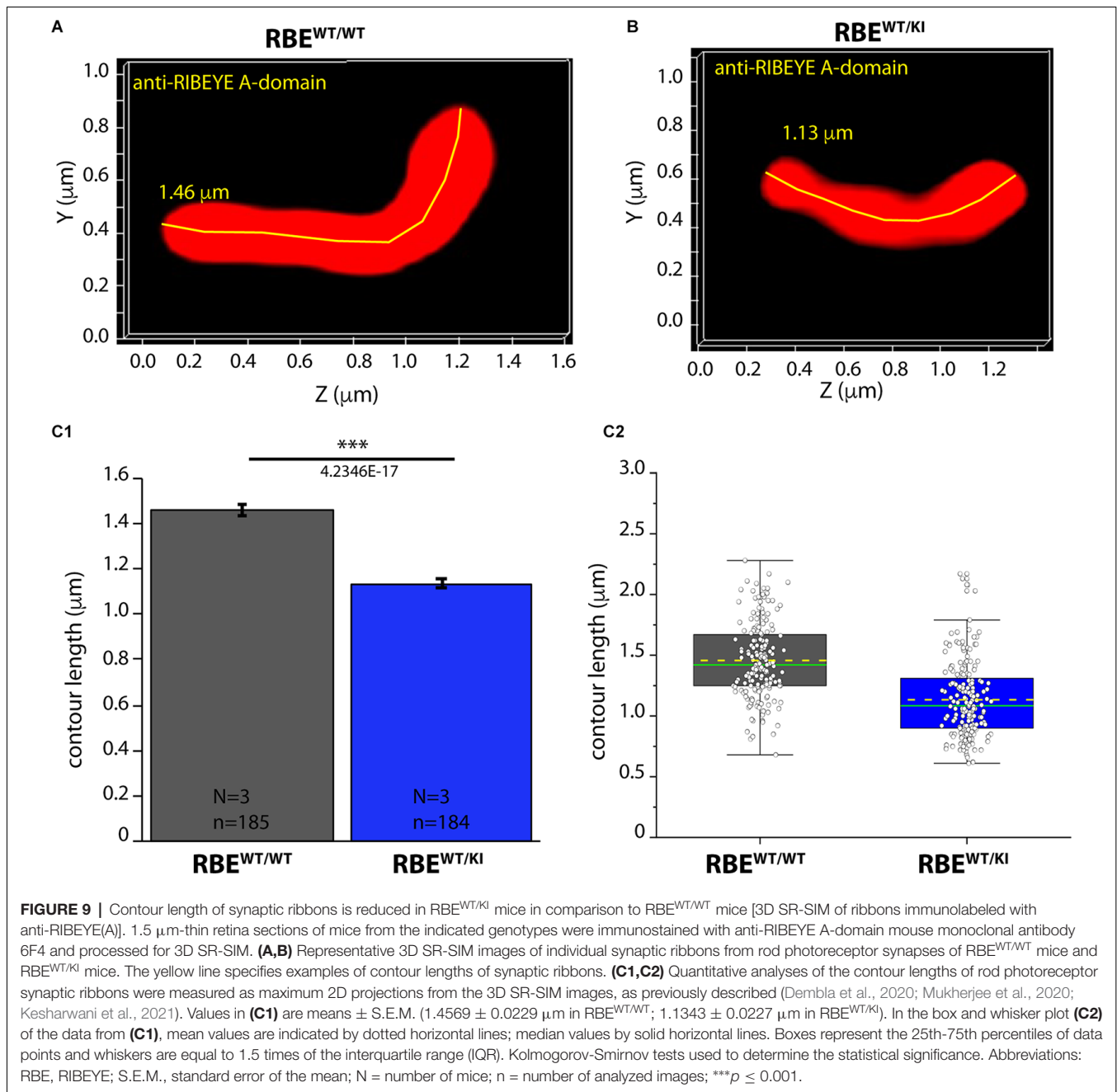


FIGURE 8 | Contour length of synaptic ribbons is reduced in RBE^{WT/KI} mice in comparison to RBE^{WT/WT} mice [3D SR-SIM of ribbons immunolabeled with anti-RIBEYE(B)]. 1.5 μm -thin retina sections of mice from the indicated genotypes were immunostained with anti-RIBEYE B-domain antibody (2D9) and processed for 3D SR-SIM. **(A,B)** Representative 3D SR-SIM images of individual synaptic ribbons from rod photoreceptor synapses of RBE^{WT/WT} mice and RBE^{WT/KI} mice. The yellow lines specify examples of the contour length of rod synaptic ribbons. **(C1,C2)** Quantitative analysis of the contour lengths of rod photoreceptor synaptic ribbons were measured as maximum 2D projections from the 3D SR-SIM images, as previously described (Dembla et al., 2020; Mukherjee et al., 2020; Kesharwani et al., 2021). Values in **(C1)** are means \pm S.E.M. (1.5336 \pm 0.0281 μm in RBE^{WT/WT}; 1.2908 \pm 0.0258 μm in RBE^{WT/KI}). In the box and whisker plot **(C2)** of the data from **(C1)**, mean values are indicated by dotted horizontal lines; median values by solid horizontal lines. Boxes represent the 25th-75th percentiles of data points and whiskers are equal to 1.5 times of the interquartile range (IQR). Mann-Whitney *U*-test was used to determine the statistical significance. Abbreviations: RBE, RIBEYE; S.E.M., standard error of the mean; N = number of mice; n = number of analyzed images; *** $p \leq 0.001$.

shown in **Figures 2, 4**. In the IPL, 15 different types of retinal bipolar cells (Shekhar et al., 2016) form a morphologically and functionally heterogeneous population of synapses (Moser et al., 2020) that mostly contain synaptic ribbons at their active zone (Okawa et al., 2019). Synaptic ribbons are typically smaller in the IPL than in the OPL and exhibit different shapes, ranging from bar-shaped to ovoid (Moser et al., 2020). In agreement with

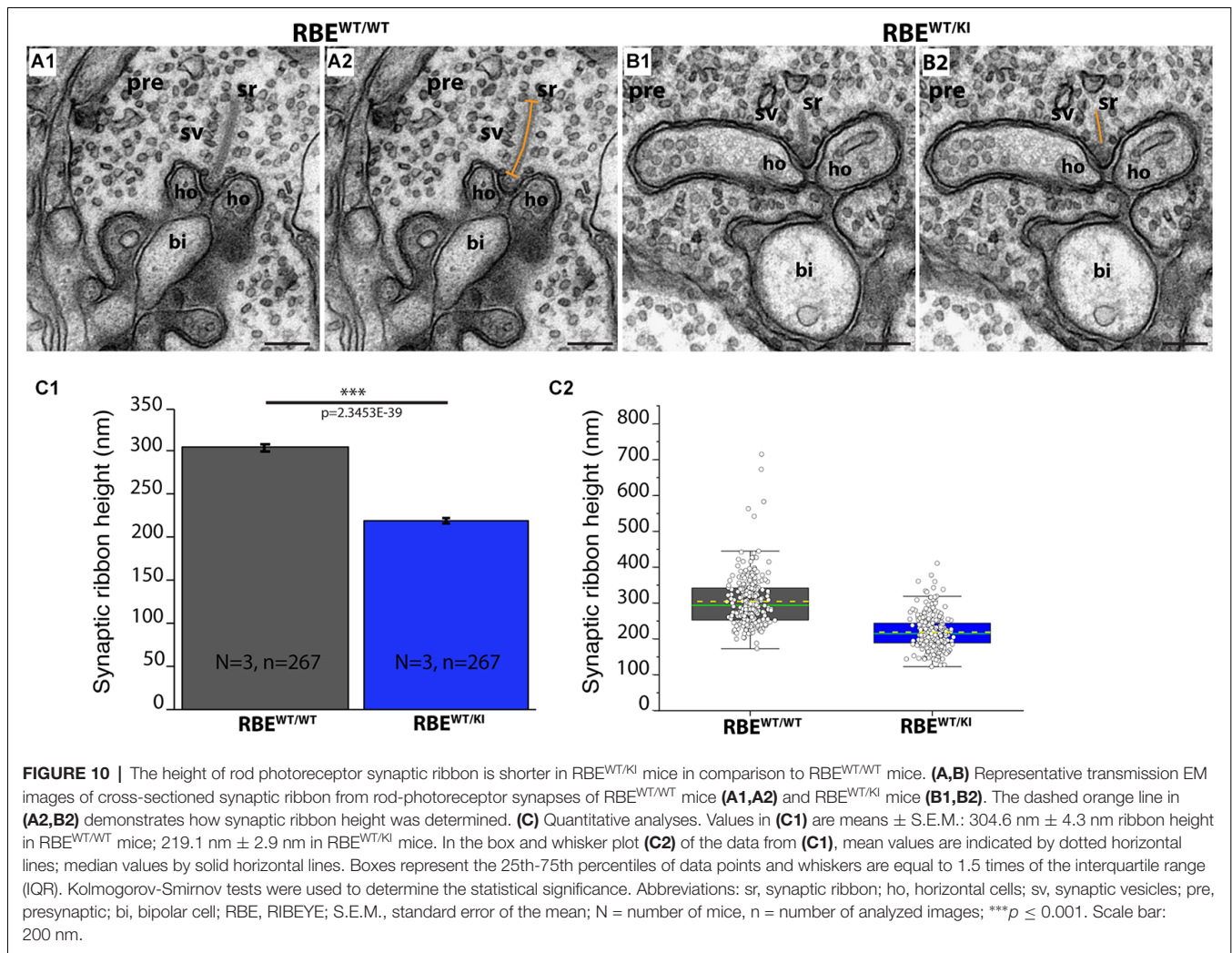
the findings in the OPL, we observed a complete lack of both RIBEYE A-domain and RIBEYE B-domain immunosignals in the IPL of RBE^{KI/KI} mice in comparison to RBE^{WT/KI} and RBE^{WT/WT} mice (**Figures 2, 4, 11B–E**). We detected no RIBEYE fluorescence signals in the IPL of RBE^{KI/KI} mice (**Figure 11**) as expected. Electron microscopy confirmed the absence of synaptic ribbons in retinal bipolar cells, as shown by exemplary representative



EM images of rod bipolar cells in **Figures 11F–G**. In RBE^{WT/KI} mice, RIBEYE fluorescence signals were again less intense than in the RBE^{WT/WT} mice, and RIBEYE puncta were also slightly, but highly significantly reduced (≈9% RIBEYE B puncta, ≈12% for RIBEYE A puncta) in comparison to homozygous RBE^{WT/WT} littermate control mice (for quantification, **Figures 11B–E**).

In order to determine whether deletion of the RIBEYE B-domain in RBE^{KI} mice has an impact on the expression levels of RIBEYE proteins, we performed Western blotting analyses on retinal lysates obtained from RBE^{WT/WT}, RBE^{WT/KI}, and RBE^{KI/KI} mice with the indicated primary antibodies using the Li-Cor system (**Figure 12**). As expected, we did

not observe any RIBEYE band at ≈120 kDa with the anti-RIBEYE B-domain antibody in RBE^{KI/KI} mice (**Figure 12B**; for quantification, **Figure 12F**) because the RIBEYE B-domain is absent in RBE^{KI/KI} mice. In contrast, the RIBEYE band was clearly present in the lysates from littermate RBE^{WT/WT} and RBE^{WT/KI} mice (**Figure 12B**, arrowhead). With the anti-RIBEYE A-domain antibody, a RIBEYE A-domain-positive immunoblotting band was clearly present in retinal lysates from RBE^{KI/KI} mice, although the amount was less than in RBE^{WT/WT} mice and RBE^{WT/KI} mice (**Figure 12C** arrowhead; for quantification, **Figure 12G**). Antibodies against GFP were used to detect the expression of RIBEYE-GCaMP3 expression



construct (**Figure 12A**, arrowhead). For normalization, the intensity of the respective bands obtained in the Li-Cor system was normalized to actin that served as a loading control. Importantly, the immunoblotting experiments revealed that the RIBEYE A-domain/GCaMP3 fusion protein was clearly produced in the RBE^{KI/KI} mice, but that the levels of the fusion protein were $\approx 31\%$ of the wild-type RIBEYE levels (**Figures 12C,G1,G2**). These results suggest that the RIBEYE A-domain/GCaMP3 fusion protein may be unstable, possibly because it cannot be assembled into synaptic ribbons in the absence of the B-domain. The absence of synaptic ribbons in RBE^{KI/KI} mice is thus not due to a lack of RIBEYE protein synthesis but caused by the deletion of the B-domain.

Finally, we also analyzed synaptic ribbons in inner and outer hair cells (IHC and OHCs) in the organ of Corti of the inner ear. Synaptic ribbons were clearly visible in the IHCs and OHCs of RBE^{WT/WT} mice but completely absent in the IHCs and OHCs of RBE^{KI/KI} mice (**Figure 13**). This was consistently observed with both antibodies against RIBEYE B-domain (**Figures 13A,B**) as well as with antibodies against RIBEYE A-domain (**Figures 13C,D**).

Thus, synaptic ribbons were consistently absent in retinal synapses, both in the OPL and IPL, as well as in ribbon synapses in the IHCs and OHCs of the organ of Corti. These data show that the RIBEYE B-domain is essential for the assembly of synaptic ribbons.

DISCUSSION

RIBEYE is the defining protein component of synaptic ribbons that is essential for the formation of synaptic ribbons, as most directly shown with RIBEYE knockout mice in which deletion of RIBEYE leads to a complete absence of synaptic ribbons (Maxeiner et al., 2016; Becker et al., 2018; Jean et al., 2018). Although the fundamental role of RIBEYE in synaptic ribbons is thus well documented, the contribution of its individual protein domains and the mechanism of its action in ribbon assembly remains unclear. RIBEYE consists of a unique, proline-rich N-terminal RIBEYE A-domain and a C-terminal B-domain that is identical to CtBP2, a ubiquitously expressed transcriptional co-repressor. In support of the role of RIBEYE as a central building block of synaptic ribbons, multiple binding sites were

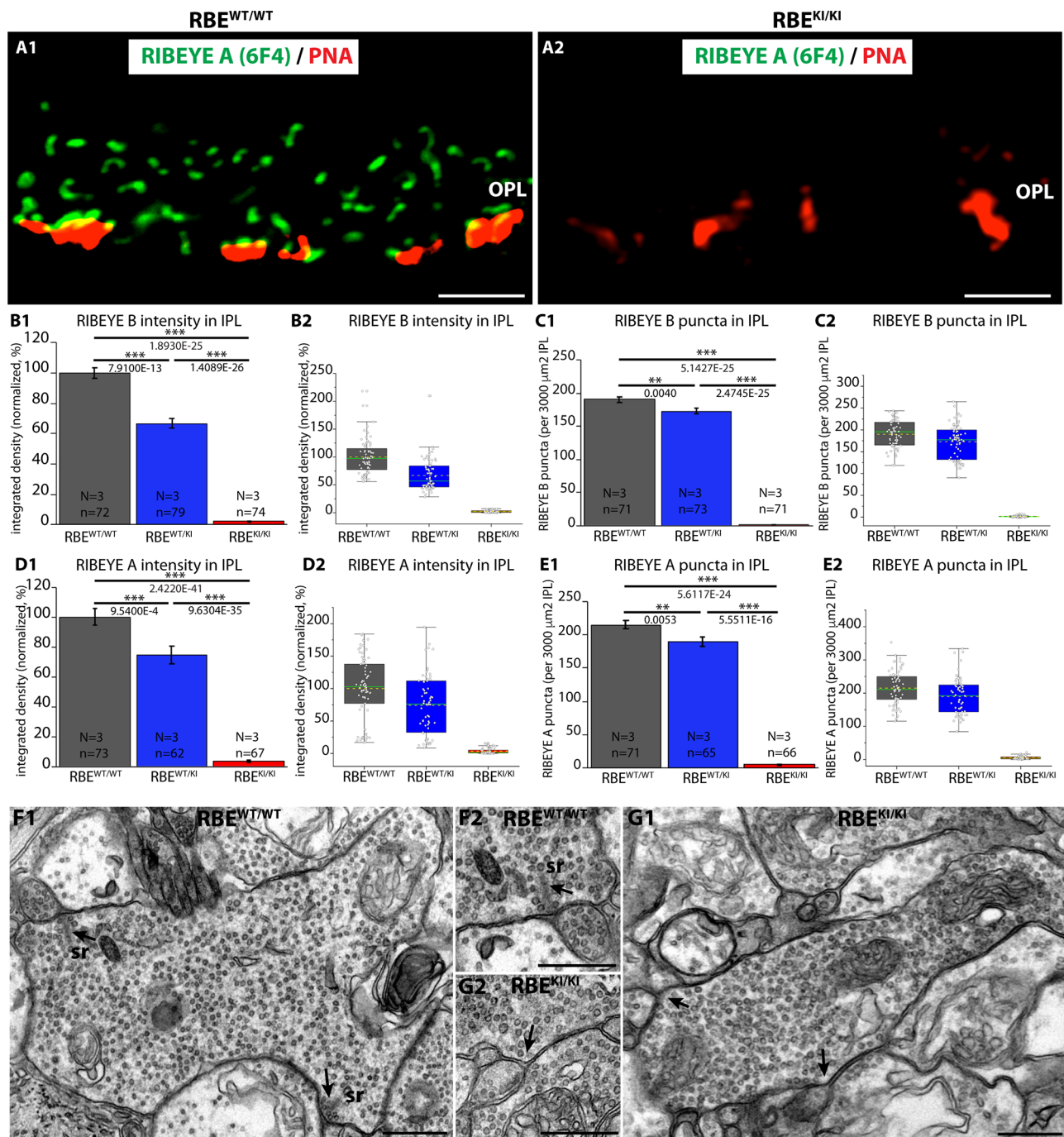


FIGURE 11 | Absence of ribbons in cone synapses of RBE^{KI/KI} mice and quantification of RIBEYE immunosignals and RIBEYE puncta in the IPL of RBE^{WT/WT}, RBE^{WT/KI}, and RBE^{KI/KI} mice. (A1,A2) Cryostat sections of retinas obtained from the indicated genotypes were stained with PNA lectin Alexa 568 to visualize cone synapses in the OPL and immunolabeled with anti-RIBEYE 6F4 to visualize ribbons. Despite the clear presence of PNA-positive cone terminals, no ribbons were present in the OPL of RBE^{KI/KI} mice (Figure 11A). RBE^{WT/WT} mice served as controls (Figure 11A). (B1,B2,C1,C2,D1,D2,E1,E2) RIBEYE(B)/RIBEYE A-domain immunosignals and RIBEYE(B)/RIBEYE A-domain puncta in the inner plexiform layer that was double-immunolabeled with antibodies against RIBEYE(B)/PSD95 (Figures 2, 3) and antibodies against RIBEYE(A)/SV2 (Figures 4, 6). (B1,B2,D1,D2) RIBEYE B-domain and RIBEYE A-domain immunosignals were completely absent in the IPL of RBE^{KI/KI} mice. In RBE^{WT/KI} mice, levels were in between the levels of RBE^{WT/WT} and RBE^{KI/KI} mice. (C1,C2,E1,E2) RIBEYE(B)/RIBEYE A-domain puncta were also completely absent in the IPL of RBE^{KI/KI} mice. In RBE^{WT/KI} mice, RIBEYE puncta (RIBEYE B-domain puncta and RIBEYE A-domain puncta) were between the levels of RBE^{WT/WT} and RBE^{KI/KI} mice. (C1) RIBEYE B-domain puncta in IPL: 190.1 ± 3.7 (mean ± S.E.M.) in RBE^{WT/WT}, 172.9 ± 4.6 (mean ± S.E.M.) in RBE^{WT/KI} and 1.5 ± 0.2 (mean ± S.E.M.) in RBE^{KI/KI} mice. (E1) RIBEYE A-domain puncta in IPL: 215.0 ± 6.1 (mean ± S.E.M.) in RBE^{WT/WT}, 189.5 ± 6.9 (mean ± S.E.M.) in RBE^{WT/KI} and 5.5 ± 0.6 (mean ± S.E.M.) in RBE^{KI/KI}. Values in (B1,C1,D1,E1) are means ± S.E.M. In the box and whiskers plot (B2,C2,D2,E2) (Continued)

FIGURE 11 | Continued

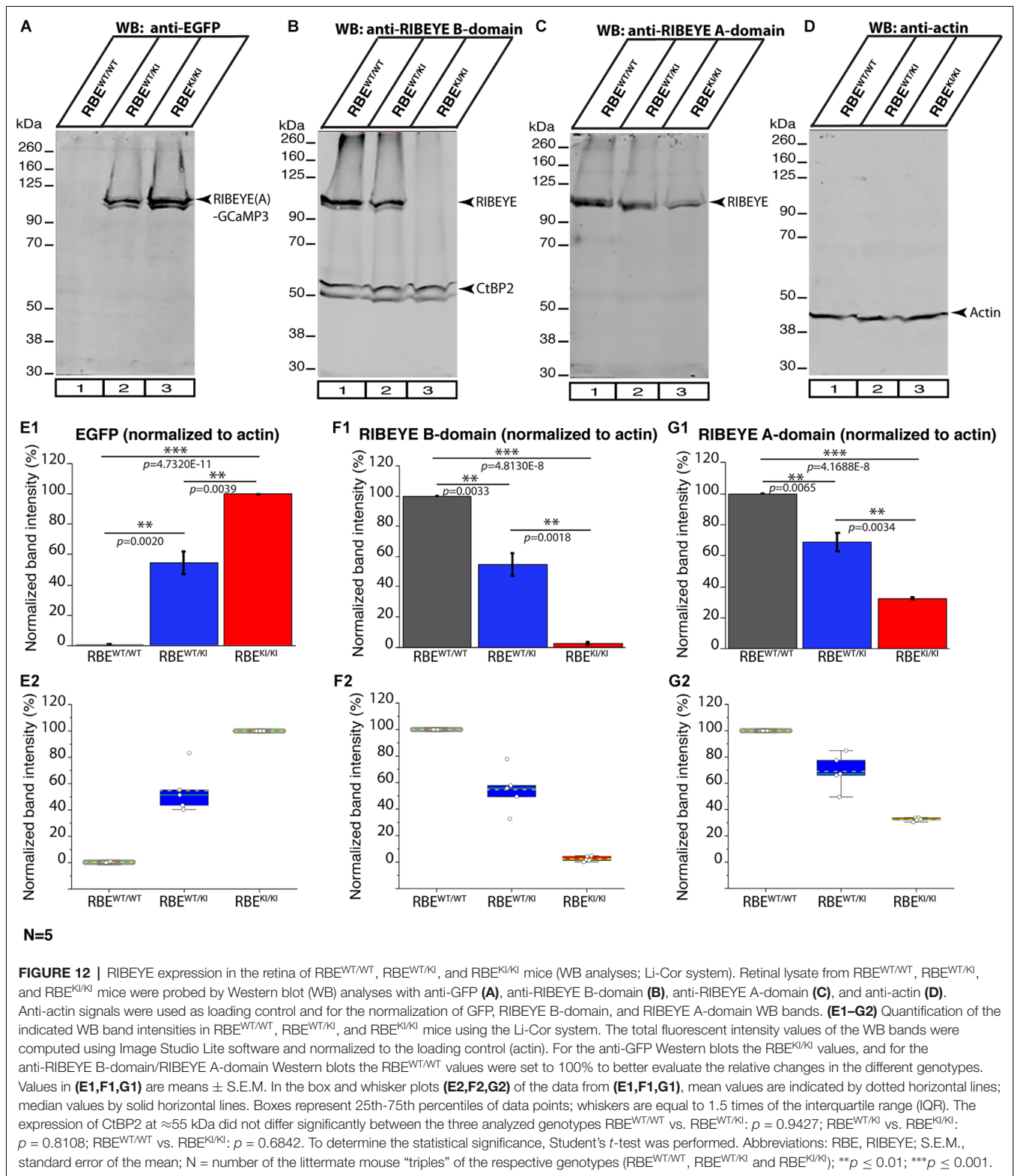
of the data from **(B1,C1,D1,E1)**, mean values are indicated by dotted horizontal lines; median values by solid horizontal lines. Boxes represent the 25th–75th percentiles of data points and whiskers are equal to 1.5 times of the interquartile range (IQR). To determine statistical significance, Mann-Whitney *U*-tests were performed for all comparisons of integrated densities. For RIBEYE B-domain puncta count, Student's *t*-test was performed for RBE^{WT/WT} / RBE^{WT/KI} comparison because data were normally distributed; Mann-Whitney *U*-tests were performed for RBE^{WT/WT} / RBE^{KI/KI} and RBE^{WT/KI} / RBE^{KI/KI}. For RIBEYE A-domain puncta count, Mann-Whitney *U*-tests were performed for RBE^{WT/WT} / RBE^{WT/KI}, RBE^{WT/WT} / RBE^{KI/KI} comparisons, Kolmogorov-Smirnov test for RBE^{WT/KI} / RBE^{KI/KI} because data were non-normally distributed. **(F,G)** Representative transmission EM images of cross-sectioned synaptic ribbons from rod bipolar synapses of RBE^{WT/WT} mice **(F1,F2)** and RBE^{KI/KI} mice **(G1,G2)**. Abbreviations: sr, synaptic ribbon; RBE, RIBEYE; S.E.M., standard error of the mean; N = number of mice, n = number of analyzed images; ***p* ≤ 0.01; ****p* ≤ 0.001. The arrows in **(F1,F2,G1,G2)** point to the active zones. Scale bar: 500 nm.

identified in RIBEYE that mediate assembly RIBEYE multimers. In particular, several interaction sites were found in the RIBEYE A-domain that enable binding of the A-domain to other A-domains and to B-domains, which may be involved in ribbon assembly (Magupalli et al., 2008). Moreover, the RIBEYE B-domain/CtBP2 was shown to also interact with other B-domains and assemble into oligomeric structures (Kumar et al., 2002; Balasubramanian et al., 2003; Nardini et al., 2003; Madison et al., 2013; Bellesis et al., 2018; Jecrois et al., 2021). It seems likely that the RIBEYE A-domain constitutes the core assembly domain of the synaptic ribbon (Schmitz et al., 2000), but the role of the RIBEYE B-domain with its NAD(H) binding site in synaptic ribbons remains unknown. Indeed, it is even unclear whether the B-domain is required for synaptic ribbon assembly, or performs a different function associated with synaptic ribbons. For example, it is conceivable that the RIBEYE A-domain solely mediates the assembly of synaptic ribbons, and that the B-domain performs a peripheral function in tethering vesicles to the ribbon, an exciting possibility in view of the current lack of information on how synaptic ribbons organize continuous neurotransmitter exocytosis.

In the present study, we tested the basic role of the RIBEYE B-domain in mice. Using a genetic approach, we found that the RIBEYE B-domain is essential for the assembly of synaptic ribbons. Analysis of RIBEYE knockin (RBE^{KI}) mice in which the B-domain of RIBEYE was replaced by an unrelated protein (the Ca²⁺-sensor GCaMP3) revealed a complete absence of synaptic ribbons even though the RIBEYE A-domain continues to be expressed as a GCaMP3 fusion protein. Thus, the RIBEYE A-domain is not sufficient for ribbon assembly, and the phenotype caused by the deletion of the B-domain is as severe as that of the complete RIBEYE deletion (Maxeiner et al., 2016). Moreover, our data confirm that RIBEYE functions universally in all synaptic ribbons as previously suggested (Schmitz et al., 2000; Maxeiner et al., 2016; Becker et al., 2018; Jean et al., 2018), since, in RBE^{KI/KI} mice, synaptic ribbons were completely absent not only in the retina but also in the inner and outer hair cells of the organ of Corti (Figure 13).

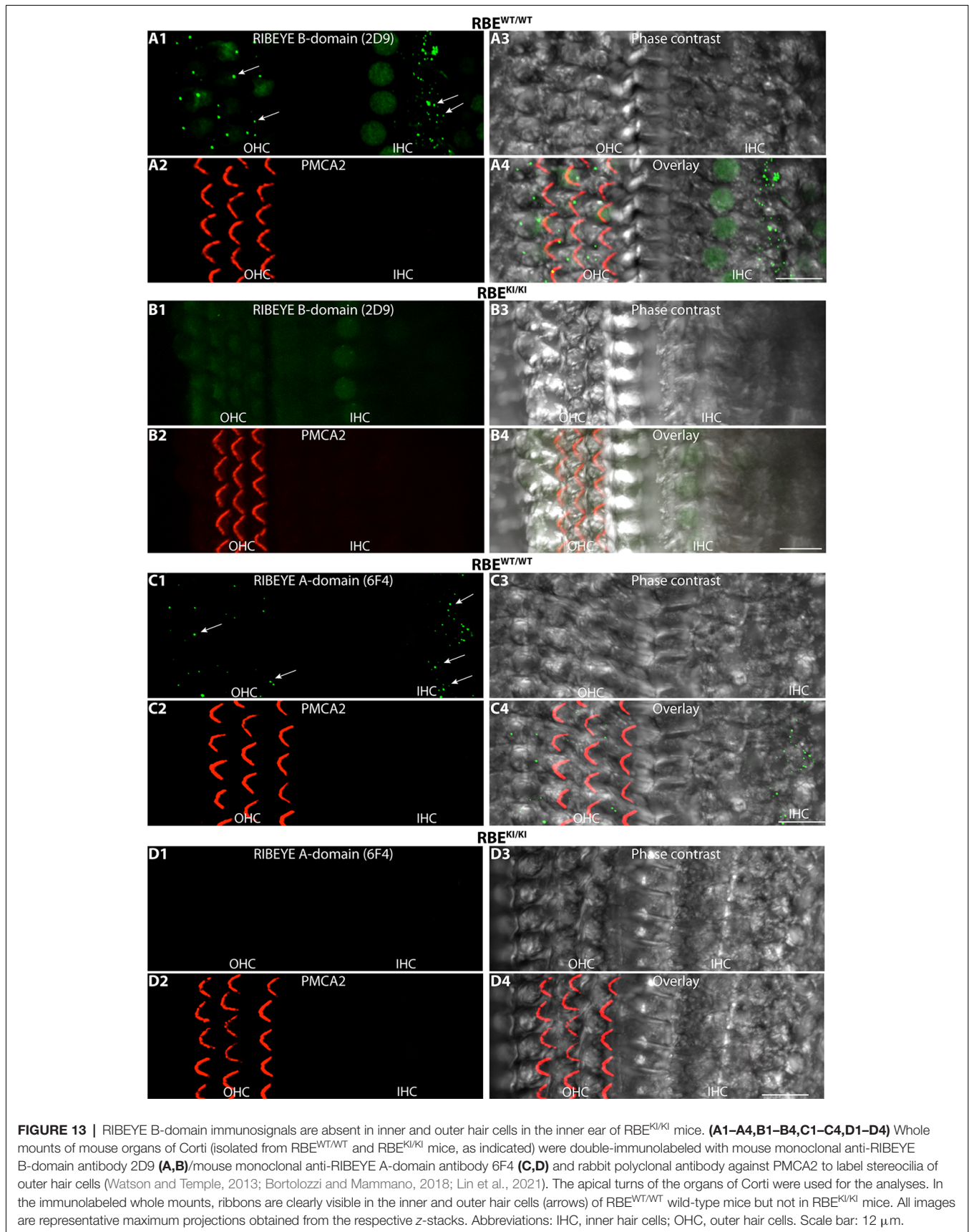
Interestingly, we show that one genomic copy of RIBEYE B-domain is largely sufficient to enable the assembly of synaptic ribbons, but that the ribbons in heterozygous RIBEYE^{WT/KI} mice are smaller. In photoreceptor synapses, the number of ribbons (ribbon density) were unchanged in the heterozygous RIBEYE^{WT/KI} mice but decreased in size in comparison to RIBEYE^{WT/WT} mice (as judged by quantitative 3D SR-SIM and EM measurements; Figures 8–10). This decrease in ribbon size in heterozygous RIBEYE^{WT/KI} could be explained by two alternative hypotheses. It is possible that the decreased expression of RIBEYE protein in the retina of RIBEYE^{WT/KI} mice in comparison to RIBEYE^{WT/WT} mice translates into a difference in ribbon size. This would imply that the ribbon size is determined by the RIBEYE concentration similar to a mass-action-law. Alternatively, it is possible that trace amounts of the RIBEYE A-domain/GCaMP3 fusion protein are incorporated into the ribbons, and that they hinder the full assembly of the ribbons. However, the fact that smaller synaptic ribbons were also reported in heterozygous RIBEYE knockout mice (RBE^{WT/KO}) compared to RIBEYE WT mice (RBE^{WT/WT}) (Jean et al., 2018) strongly supports the first hypothesis. In further support of this hypothesis, moreover, transgenic overexpression of RIBEYE protein in zebrafish results in particularly large, oversized synaptic ribbons (Sheets et al., 2011, 2017). In the IPL of the inner retina, the fluorescence intensity of RIBEYE immunosignals was decreased in RIBEYE^{WT/KI} mice in comparison to RIBEYE^{WT/WT} mice. In the IPL, the number of synaptic ribbons/per IPL area was smaller in heterozygous RIBEYE^{WT/KI} mice in comparison to RIBEYE^{WT/WT} mice. This is probably based on the fact that synaptic ribbons in bipolar terminals in the IPL are typically smaller in size than in rod photoreceptor terminals (Moser et al., 2020). A further reduction in size in heterozygous RIBEYE^{WT/KI} mice thus can more easily result in their complete disappearance in bipolar cell synapses than in rod photoreceptor synapses in which synaptic ribbons are bigger.

In summary, our results demonstrate that the RIBEYE B-domain is essential for the assembly of synaptic ribbons and that the RIBEYE A-domain alone cannot build synaptic ribbons in the synaptic terminals of the retina and in sensory hair cells of the inner ear. How the RIBEYE B-domain promotes ribbon assembly needs to be further analyzed, but it seems likely that it acts as more than a structural component. Recent biochemical and structural analyses on CtBP1 and CtBP2, that is largely identical to the RIBEYE B-domain, can give important hints (Nardini et al., 2009; Madison et al., 2013; Bellesis et al., 2018; Jecrois et al., 2021). These data showed that CtBP2 forms tetrameric complexes via dimeric intermediates (Madison et al., 2013; Nichols et al., 2021). The assembly of these complexes is enhanced by NAD(H) (Madison et al., 2013; Jecrois et al., 2021; Nichols et al., 2021). Interestingly, NAD(H) has been shown to influence the size of synaptic ribbons in sensory hair cells (Wong et al., 2019; Okur et al., 2020). The size of auditory hair cell ribbon synapses also strongly increases with aging in C57BL/6J mice (Peineau et al., 2021). Based on the CtBP1/CtBP2 structural data (Balasubramanian et al., 2003; Madison et al., 2013; Jecrois et al., 2021; Nichols et al., 2021), the RIBEYE B-domain can



be expected to also assemble into tetrameric complexes that are controlled by NAD. These oligomeric RIBEYE B-complexes could link different RIBEYE units to each other during ribbon

assembly and/or mediate stability to the synaptic ribbon. The functional properties of ribbon synapses in $RBE^{KI/KI}$ mice and the physiological consequences of RIBEYE B-domain deletion in



the RBE^{KI/KI} mice for vision and hearing need to be analyzed by future analyses.

DATA AVAILABILITY STATEMENT

The original contributions presented in the study are included in the article, further inquiries can be directed to the corresponding author/s.

ETHICS STATEMENT

The animal study was reviewed and approved by Landesamt für Verbraucherschutz; Geschäftsbereich 3; 66115 Saarbrücken, Germany; GB 3-2.4.1.1-K110/180-07.

AUTHOR CONTRIBUTIONS

SS performed all experiments and analyses shown in Figures 1–13 and wrote the article together with FS and TS. KS performed embeddings and provided help with experiments and statistical procedures. RK introduced SS to confocal microscopy and provided help with analyses. MJ generated the peptide arrays

and provided important advice. SM generated knockin and knockout mice and provided help with analyses. TS designed knockin strategy, organized KI and KO mouse generation and provided essential support. FS designed and supervised the study and wrote the article together with SS and TS. All authors contributed to the article and approved the submitted version.

FUNDING

Work of the authors was supported by the Dr. Rolf M. Schwiete foundation (2020-002) and the Deutsche Forschungsgemeinschaft (Schm797/8-1 and SFB894 TP A7 and P3).

ACKNOWLEDGMENTS

We thank Robert S. Molday for the kind gift of opsin antibody; Bianca Schrul (PZMS Homburg) for access to the Li-Cor Odyssey system; Kheertana Ravichandran/Elmar Krause/Jens Rettig (CIPMM Homburg) for help and access to the SR-SIM microscope; Gabriele Kiefer and Sabine Schmidt for excellent technical assistance.

REFERENCES

- Balasubramanian, P., Zhao, L.J., and Chinnadurai, G. (2003). Nicotinamide adenine dinucleotide stimulates oligomerization, interaction with adenovirus E1A and an intrinsic dehydrogenase activity of CtBP. *FEBS Lett.* 537, 157–160. doi: 10.1016/s0014-5793(03)00119-4
- Becker, L., Schnee, M. L., Niwa, M., Sun, W., Maxeiner, S., Talaei, S., et al. (2018). The presynaptic ribbon maintains vesicle populations at the hair cell afferent fiber synapse. *eLife* 7:e30242. doi: 10.7554/eLife.30241
- Bellesis, A. G., Jecrois, A. M., Hayes, J. A., Schiffer, C. A., and Royer, W. E., Jr. (2018). Assembly of human C-terminal binding protein into tetramers. *J. Biol. Chem.* 293, 9101–9112. doi: 10.1074/jbc.RA118.002514
- Bloom, F. E., and Aghajanian, G. K. (1968). Fine structural and cytochemical analysis of the staining of synaptic junctions with phosphotungstic acid. *J. Ultrastruct. Res.* 22, 361–375. doi: 10.1016/s0022-5320(68)90027-0
- Bortolozzi, M., and Mammano, F. (2018). PMCA2 pump mutations and hereditary deafness. *Neurosci. Lett.* 663, 18–24. doi: 10.1016/j.neulet.2017.09.059
- Buckley, K., and Kelly, R. B. (1985). Identification of a transmembrane glycoprotein specific for secretory vesicles of neuronal and endocrine cells. *J. Cell. Biol.* 100, 1284–1294. doi: 10.1083/jcb.100.4.1284
- De Winter, J. C. F. (2013). Using the Student's t-test with extremely small sample sizes. *Pract. Assess. Res. Eval.* 18:10. doi: 10.7275/e4r6-dj05
- Dembla, E., Dembla, M., Maxeiner, S., and Schmitz, F. (2020). Synaptic ribbons foster active zone stability and illumination-dependent active zone enrichment of RIM2 and Cav1.4. *Sci. Rep.* 10:5957. doi: 10.1038/s41598-020-62734-0
- Dembla, M., Kesharwani, A., Natarajan, S., Fecher-Trost, C., Fairless, R., Williams, S. K., et al. (2018). Early auto-immune targeting of photoreceptor ribbon synapses in mouse models of multiple sclerosis. *EMBO Mol. Med.* 10:e8926. doi: 10.15252/emmm.201808926
- Dembla, M., Wahl, S., Katiyar, R., and Schmitz, F. (2014). ArfGAP3 is a component of the photoreceptor synaptic ribbon complex and forms an NAD(H)-regulated, redox-sensitive complex with RIBEYE that is important for endocytosis. *J. Neurosci.* 34, 5245–5260. doi: 10.1523/JNEUROSCI.3837-13.2014
- Dieckmann-Schuppert, A., and Schnittler, H. J. (1997). A simple assay for quantification of protein in tissue sections, cell cultures and cell homogenates and of protein immobilized on solid surfaces. *Cell Tissue Res.* 288, 119–126. doi: 10.1007/s004410050799
- Eich, M. L., Dembla, E., Wahl, S., Schwarz, K., and Schmitz, F. (2017). The calcineurin-binding, activity-dependent splice variant dynamin1xb is highly enriched in synapses in various regions of the central nervous system. *Front. Mol. Neurosci.* 10:230. doi: 10.3389/fnmol.2017.00230
- Fang, Q. J., Wu, F., Chai, R., and Sha, S. H. (2019). Cochlear surface preparation in the adult mouse. *J. Vis. Exp.* 153:e60299. doi: 10.3791/60299
- Frank, R. (2002). The SPOT-synthesis technique. Synthetic peptide arrays on membrane supports-principles and applications. *J. Immunol. Methods* 267, 13–26. doi: 10.1016/s0022-1759(02)00137-0
- Fry, K. R., and Spira, A. W. (1980). An Ethanolic Phosphotungstic Acid (EPTA) analysis of photoreceptor and synaptic ultrastructure in the guinea pig retina. *J. Histochem. Cytochem.* 28, 142–148. doi: 10.1177/28.2.6153396
- Goldberg, J. D., Yoshida, T., and Brick, P. (1994). Crystal structure of a NAD-dependent D-glycerate dehydrogenase at 2.4 Å resolution. *J. Mol. Biol.* 236, 1123–1140. doi: 10.1016/0022-2836(94)90016-7
- Grabner, C. P., Gandini, M. A., Rehak, R., Le, Y., Zamponi, G. W., and Schmitz, F. (2015). RIM1/2-mediated facilitation of Cav1.4 channel opening is required for Ca²⁺-stimulated release in mouse rod photoreceptors. *J. Neurosci.* 35, 13133–13147. doi: 10.1523/JNEUROSCI.0658-15.2015
- Grabner, C. P., and Moser, T. (2021). The mammalian rod synaptic ribbon is essential for Cav channel facilitation and ultrafast vesicle fusion. *eLife* 10:e63844. doi: 10.7554/eLife.63844
- Gruber, T., Pan, C., Contreras, R. E., Wiedemann, T., Morgan, D. A., Skowronski, A. A., et al. (2021). Obesity-associated hyperleptinemia alters the gliovascular interface of the hypothalamus to promote hypertension. *Cell Metab.* 33, 1155–1170.e10. doi: 10.1016/j.cmet.2021.04.007
- Harsman, A., Kopp, A., Wagner, R., Zimmermann, R., and Jung, M. (2011). Calmodulin regulation of the calcium-leak channel Sec61 is unique to vertebrates. *Channels (Austin)* 5, 293–298. doi: 10.4161/chan.5.4.16160
- Hilpert, K., Winkler, D. F. H., and Hancock, R. E. W. (2007). Peptide arrays on cellulose support: SPOT synthesis, a time and cost-efficient method for synthesis of large numbers of peptides in a parallel and addressable fashion. *Nat. Protoc.* 2, 1333–1349. doi: 10.1038/nprot.2007.160
- Hodges, R. S., Heaton, R. J., Parker, J. M., Molday, L., and Molday, R. S. (1988). Antigen-antibody interaction: synthetic peptides define linear antigenic determinants recognized by monoclonal antibodies directed to the cytoplasmic carboxy terminus of rhodopsin. *J. Biol. Chem.* 263, 11768–11775. doi: 10.1016/S0021-9258(18)37850-5

- Irie, M., Hata, Y., Takeuchi, M., Ichtchenko, K., Toyoda, A., Hirao, K., et al. (1997). Binding of neuroligins to PSD-95. *Science* 277, 1511–1515. doi: 10.1126/science.277.5331.1511
- Jean, P., de la Marina, D. L., Michanski, S., Tobón, L. M. J., Chakrabarti, R., Picher, M. M., et al. (2018). The synaptic ribbon is critical for sound encoding at high rates with temporal precision. *eLife* 7:e29275. doi: 10.7554/eLife.29275
- Jecrois, A. M., Dcona, M. M., Deng, X., Bandyopadhyay, D., Grossman, S. R., Schiffer, C. A., et al. (2021). Cryo-EM structure of CtBP2 confirms tetrameric architecture. *Structure* 29, 310–319.e5. doi: 10.1016/j.str.2020.11.008
- Joselevitch, C., and Zenisek, D. (2020). Direct observation of vesicle transport on the synaptic ribbon provides evidence that vesicles are mobilized and prepared rapidly for release. *J. Neurosci.* 40, 7390–7404. doi: 10.1523/JNEUROSCI.0605-20.2020
- Kerov, V., Laird, J. G., Joiner, M. L., Knecht, S., Soh, D., Hagen, J., et al. (2018). $\alpha 28-4$ is required for the molecular and structural organization of rod and cone photoreceptor synapses. *J. Neurosci.* 38, 6145–6160. doi: 10.1523/JNEUROSCI.3818-16.2018
- Kesharwani, A., Schwarz, K., Dembla, E., Dembla, M., and Schmitz, F. (2021). Early changes in exo- and endocytosis in the EAE mouse model of multiple sclerosis correlate with decreased synaptic ribbon size and reduced ribbon-associated vesicle pools in rod photoreceptor synapses. *Int. J. Mol. Sci.* 22:10789. doi: 10.3390/ijms221910789
- Koulen, P., Fletcher, E. L., Craven, S. E., Brecht, D. S., and Wässle, H. (1998). Immunocytochemical localization of the postsynaptic density protein PSD-95 in the mammalian retina. *J. Neurosci.* 18, 10136–10149. doi: 10.1523/JNEUROSCI.18-23-10136.1998
- Kumar, V., Carlson, J. E., Ohgi, K. A., Edwards, T. A., Rose, D. W., Escalante, C. R., et al. (2002). Transcriptional corepressor CtBP is an NAD(+)-regulated dehydrogenase. *Mol. Cell* 10, 857–869. doi: 10.1016/s1097-2765(02)00650-0
- Lagnado, L., and Schmitz, F. (2015). Ribbon synapses and visual processing in the retina. *Annu. Rev. Vis. Sci.* 1, 235–262. doi: 10.1146/annurev-vision-082114-035709
- Lessard, J. L. (1988). Two monoclonal antibodies to actin: one muscle selective and one generally reactive. *Cell Motil. Cytoskeleton* 10, 349–362. doi: 10.1002/cm.970100302
- Limbach, C., Laue, M. M., Wang, X., Hu, B., Thiede, N., Hultqvist, G., et al. (2011). Molecular in situ topology of aczonin/piccolo and associated proteins at the mammalian neurotransmitter release site. *Proc. Natl. Acad. Sci. U S A* 108, E392–E401. doi: 10.1073/pnas.1101707108
- Lin, X., Brunck, M. G. K., Yuanxiang, P., Curran, A. W., Zhang, E., Stöber, F., et al. (2021). Neuroplastin expression is essential for hearing and hair cell PMCA expression. *Brain Struct. Funct.* 226, 1533–1551. doi: 10.1007/s00429-021-02269-w
- Lv, C., Stewart, W. J., Akanyeti, O., Frederick, C., Zhu, J., Santos-Sacchi, J., et al. (2016). Synaptic ribbons require Ribeye for electron density, proper synaptic localization and recruitment of calcium channels. *Cell Rep.* 15, 2784–2795. doi: 10.1016/j.celrep.2016.05.045
- Madison, D. L., Wirz, J. A., Siess, D., and Lundblad, J. R. (2013). Nicotinamide adenine dinucleotide-induced multimerization of the co-repressor CtBP1 relies on a switching tryptophan. *J. Biol. Chem.* 288, 27836–27848. doi: 10.1074/jbc.M113.493569
- Magupalli, V. G., Schwarz, K., Alpadi, K., Natarajan, S., Seigel, G. M., and Schmitz, F. (2008). Multiple RIBEYE-RIBEYE interactions create a dynamic scaffold for the formation of synaptic ribbons. *J. Neurosci.* 28, 7954–7967. doi: 10.1523/JNEUROSCI.1964-08.2008
- Matthews, G., and Fuchs, P. (2010). The diverse roles of ribbon synapses in sensory neurotransmission. *Nat. Rev. Neurosci.* 11, 812–822. doi: 10.1038/nrn2924
- Maxeiner, S., Luo, F., Tan, A., Schmitz, F., and Südhof, T. C. (2016). How to make a synaptic ribbon: RIBEYE deletion abolishes ribbons in retinal synapses and disrupts neurotransmitter release. *EMBO J.* 35, 1098–1114. doi: 10.15252/embj.201592701
- Montgomery, S. C., and Cox, B. C. (2016). Whole mount dissection and immunofluorescence of the adult mouse cochlea. *J. Vis. Exp.* 107:53561. doi: 10.3791/53561
- Moser, T., Grabner, C. P., and Schmitz, F. (2020). Sensory processing in the retina and the inner ear. *Physiol. Rev.* 100, 103–144. doi: 10.1152/physrev.00026.2018
- Mukherjee, A., Katiyar, R., Dembla, E., Dembla, E., Kumar, P., Belkacemi, A., et al. (2020). Disturbed presynaptic Ca^{2+} signaling in photoreceptors in the EAE mouse model of multiple sclerosis. *iScience* 23:101830. doi: 10.1016/j.isci.2020.101830
- Nardini, M., Spano, S., Cericola, C., Pesce, A., Massaro, A., Millo, E., et al. (2003). CtBP/BARS: a dual-function protein involved in transcription co-repression and Golgi membrane fission. *EMBO J.* 22, 3122–3130. doi: 10.1093/emboj/cdg283
- Nardini, M., Valente, C., Ricagno, S., Luini, A., Corda, D., and Bolognesi, M. (2009). CtBP1/BARS Gly172—Glu mutant structure: impairing NAD(H)-binding and dimerization. *Biochem. Biophys. Res. Commun.* 381, 70–74. doi: 10.1016/j.bbrc.2009.02.010
- Nichols, J. C., Schiffer, C. A., and Royer, W. E., Jr. (2021). NAD(H) phosphates mediate tetramer assembly of human C-terminal binding protein. *J. Biol. Chem.* 296:100351. doi: 10.1016/j.jbc.2021.100351
- Okawa, H., Yu, W. Q., Matti, U., Schwarz, K., Odermatt, B., Zhong, H., et al. (2019). Dynamic assembly of ribbon synapses and circuit maintenance in a vertebrate sensory system. *Nat. Commun.* 10:2167. doi: 10.1038/s41467-019-10123-1
- Okur, M. N., Mao, B., Kimura, R., Haracz, S., Fitzgerald, T., Edwards-Hollingsworth, K., et al. (2020). Short-term NAD⁺ supplementation prevents hearing loss in mouse models of Cockayne syndrome. *NPJ Aging Mech. Dis.* 6:1. doi: 10.1038/s41514-019-0040-z
- Park, S. Y., Yoo, Y. M., Jung, E. M., and Jeung, E. B. (2019). Distribution of and steroid hormone effects on calbindin- D_{9k} in the immature rat brain. *Brain Res. Bull.* 152, 225–235. doi: 10.1016/j.brainresbull.2019.07.028
- Peineau, T., Belleudy, S., Pietropaolo, S., Bouleau, Y., and Dulon, D. (2021). Synaptic release potentiation at aging auditory ribbon synapses. *Front. Aging Neurosci.* 13:756449. doi: 10.3389/fnagi.2021.756449
- Piatigorski, J. (2001). Dual use of the transcriptional repressor (CtBP2/ ribbon synapse (RIBEYE) gene: how prevalent are multifunctional genes? *Trends Neurosci.* 24, 555–557. doi: 10.1016/s0166-2236(00)01894-4
- Pillai-Kastoori, L., Schutz-Geschwender, A. R., and Harford, J. A. (2020). A systematic approach to quantitative Western blot analysis. *Anal. Biochem.* 593:113608. doi: 10.1016/j.ab.2020.113608
- Punge, A., Rizzoli, S. O., Jahn, R., Wildanger, J. D., Meyer, L., Schönlé, A., et al. (2008). 3D reconstruction of high-resolution STED microscope images. *Microsc. Res. Tech.* 71, 644–650. doi: 10.1002/jemt.20602
- Schermele, L., Heintzmann, R., and Leonhardt, H. (2010). A guide to super-resolution fluorescence microscopy. *J. Cell Biol.* 190, 165–175. doi: 10.1083/jcb.201002018
- Schindelin, J., Arganda-Carreras, I., Frise, E., Kaynig, V., Longair, M., Pietzsch, T., et al. (2012). Fiji: an open-source platform for biological-image analysis. *Nat. Methods* 9, 676–682. doi: 10.1038/nmeth.2019
- Schmitz, F. (2009). The making of synaptic ribbons: how they are built and what they do. *Neuroscientist* 15, 611–624. doi: 10.1177/1073858409340253
- Schmitz, F., Königstorfer, A., and Südhof, T. C. (2000). RIBEYE, a component of synaptic ribbons. A protein's journey through evolution provides insight into synaptic ribbon function. *Neuron* 28, 857–872. doi: 10.1016/s0896-6273(00)00159-8
- Schneider, C. A., Rasband, W. S., and Eliceiri, K. W. (2012). NIH Image to ImageJ: 25 years of image analysis. *Nat. Methods* 9, 671–675. doi: 10.1038/nmeth.2089
- Sheets, L., He, X. J., Olt, J., Schreck, M., Petralia, R. S., Wang, Y. X., et al. (2017). Enlargement of ribbons in zebrafish hair cells increases calcium currents but disrupts afferent spontaneous activity and timing of stimulus onset. *J. Neurosci.* 37, 6299–6313. doi: 10.1523/JNEUROSCI.2878-16.2017
- Sheets, L., Trapani, J. G., Mo, W., Obholzer, N., and Nicolson, T. (2011). Ribeye is required for presynaptic Cav1.3a channel localization and afferent innervation of sensory hair cells. *Development* 138, 1309–1319. doi: 10.1242/dev.059451
- Shekhar, K., Lapan, S. W., Whitney, I. E., Tran, N. M., Macosko, E. Z., Kowalczyk, M., et al. (2016). Comprehensive classification of retinal bipolar neurons by single-cell transcriptomics. *Cell* 166, 1308–1323.e30. doi: 10.1016/j.cell.2016.07.054
- Tian, L., Hires, S. A., Mao, T., Huber, D., Chiappe, M. E., Chalasani, S. H., et al. (2009). Imaging neural activity in worms, flies and mice with improved GCaMP calcium indicators. *Nat. Methods* 6, 875–881. doi: 10.1038/nmeth.1398

- Vaithianathan, T., Wollmuth, L. P., Henry, D., Zenisek, D., and Matthews, G. (2019). Tracking newly released synaptic vesicle proteins at ribbon active zones. *iScience* 17, 10–23. doi: 10.1016/j.isci.2019.06.015
- Wahl, S., Katiyar, R., and Schmitz, F. (2013). A local, periaxonal zone endocytic machinery at photoreceptor synapses in close vicinity to synaptic ribbons. *J. Neurosci.* 33, 10278–10300. doi: 10.1523/JNEUROSCI.5048-12.2013
- Wahl, S., Magupalli, V. G., Dembla, M., Katiyar, R., Schwarz, K., Köblitz, L., et al. (2016). The disease protein tulp1 is essential for periaxonal zone endocytosis in photoreceptor ribbon synapses. *J. Neurosci.* 36, 2473–2493. doi: 10.1523/JNEUROSCI.2275-15.2016
- Watson, C. J., and Temple, B. L. (2013). A new ATP2B2 deafwaddler allele, dfw(i5), interacts strongly with Cdh23 and other auditory modifiers. *Hear. Res.* 304, 41–48. doi: 10.1016/j.heares.2013.06.003
- Wong, H. C., Zhang, Q., Beirl, A. J., Petralia, R. S., Wang, Y. X., and Kindt, K. (2019). Synaptic mitochondria regulate hair-cell synapse size and function. *eLife* 8:e48914. doi: 10.7554/eLife.48914
- Yuan, L., Song, X., Zhang, L., Yu, Y., Liang, Z., Lei, Y., et al. (2021). The transcriptional repressors VAL1 and VAL2 recruit PRC2 for genome-wide Polycomb silencing in *Arabidopsis*. *Nucleic Acids. Res.* 49, 98–113. doi: 10.1093/nar/gkaa1129
- Zenisek, D., Steyer, J. A., and Almers, W. (2000). Transport, capture and exocytosis of single synaptic vesicles at the active zone. *Nature* 406, 849–854. doi: 10.1038/35022500

Conflict of Interest: The authors declare that the research was conducted in the absence of any commercial or financial relationships that could be construed as a potential conflict of interest.

Publisher's Note: All claims expressed in this article are solely those of the authors and do not necessarily represent those of their affiliated organizations, or those of the publisher, the editors and the reviewers. Any product that may be evaluated in this article, or claim that may be made by its manufacturer, is not guaranteed or endorsed by the publisher.

Copyright © 2022 Shankhwar, Schwarz, Katiyar, Jung, Maxeiner, Südhof and Schmitz. This is an open-access article distributed under the terms of the Creative Commons Attribution License (CC BY). The use, distribution or reproduction in other forums is permitted, provided the original author(s) and the copyright owner(s) are credited and that the original publication in this journal is cited, in accordance with accepted academic practice. No use, distribution or reproduction is permitted which does not comply with these terms.